Assessment of Magnesium Potassium Phosphate Cement Systems for Radioactive Waste Encapsulation

Laura Jane Gardner

A thesis submitted in partial fulfilment for the degree of Doctor of Philosophy

Immobilisation Science Laboratory

Department of Materials Science and Engineering

The University of Sheffield

September 2016

Abstract

In the UK, the current stabilisation/solidification technique for intermediate level waste (ILW) is for encapsulation in a Portland cement (PC) composite, which have desirable physical and chemical interactions with ILWs. However, niche waste streams such as reactive metals are known to corrode in the high pH and high free water environment of PCs. Corrosion can lead to the formation of expansive products and the generation of hydrogen. Consequently, there is a growing demand for tailored encapsulant grouts that can be chosen based on the chemical compatibility with the waste streams. Magnesium potassium phosphate cements (MKPCs) formed via an acid-base reaction, with a near-neutral pH and low water demand are one of the alternative encapsulants under consideration for such niche wastes.

The aim of this project was to assess MKPCs for deployment in the nuclear industry with particular focus on: formulation optimisation, chemical stability with wastes, radiation tolerance and performance in accident scenarios, i.e. thermal incident. Uranium corrosion trials revealed a reduced gas generation compared to the standard industry grout. It was also demonstrated that the inclusion of supplementary cementitious materials in MKPCs (to form FA/MKPC and GBFS/MKPC) can lead to the formation of secondary reaction products, likely to be potassium aluminosilicates. The high temperature behaviour (i.e. thermal incident) and the radiation tolerance of blended MKPC binders were chosen to demonstrate the suitability of these binders for the UK nuclear industry. The high temperature performance indicated substantial phase assemblage changes occurred up to 1200 °C, however no cracking or spalling of the pellets exposed to high temperatures was observed, which is an important physical property and could to avoid/limit the radioactivity release in a fire scenario. Whilst, the irradiation experiments (up to 10 MGy) revealed that blended MKPC binders exhibit considerable gamma radiation tolerance (regardless of dose rate). The work demonstrated in this thesis indicates that MKPC binders could be a suitable encapsulant for use in the UK but further work involving scaled up experiments are still needed to provide an in-depth safety case.

Acknowledgments

First of all, I would like to express my gratitude to Prof. Neil Hyatt and Dr. Claire Corkhill for their continued support, patience and encouragement throughout the entirety of this research project. A special thanks to Prof. John Provis and Dr. Susan Bernal-López, who became unofficial supervisors (willingly…I hope) and were always available to offer their support, time and knowledge. I feel very luckily to have had this team of supervisors throughout my Ph.D., again thank you very much!

A special thanks to Prof. Simon Pimblott and Ruth Edge based at the Dalton Cumbrian Facility, University of Manchester, who undertook the role of irradiating the MKPC samples in the Co-60 irradiator. I would like to express my appreciation to my family and friends who have shown their constant love, encouragement and moral support over the last few years.

I want to say a big thank you to Dr. Claire Corkhill, Dr. Samuel Walling, Ruth Bradley and Valentin Lejeune who looked after my two-year uranium corrosion experiments at times when I was absent from the university. I would also like to thank the Immobilisation Science Laboratory group (ISL) for making it an exciting and dynamic place to complete this research project, particularly Dr. Martin Stennett, Dr. Nik Reeves, Dr. Oday Hussain and Andrew Mould for all your help.

Finally, I would like to thank the Nuclear Decommissioning Authority for funding this studentship and giving me the opportunity to further my academic career.

Publications

The author has contributed to the following peer-reviewed publications during this body of research:

1. L.J. Gardner, V. Lejeune, C.L. Corkhill, S.A. Bernal, J.L. Provis, M.C. Stennett, N.C. Hyatt, Evolution of the phase assemblage in magnesium potassium phosphate cement binders at 200 and 1000 °C, *Advances in Applied Ceramics (invited response)*, **2015***, vol. 114, pp. 386-392.*
2. L.J. Gardner, S.A. Bernal, S.A. Walling, C.L. Corkhill, J.L. Provis, N.C. Hyatt, Characterisation of magnesium potassium phosphate cements blended with fly ash and blast furnace slag, *Cement and Concrete Research*, **2015**, vol. 74, pp. 78-87.
3. C.L. Corkhill, J.W. Bridge, P. Hillel, L.J. Gardner, S.A. Banwart, N.C. Hyatt, Technetium-99m Transport and Immobilisation in Porous Media: Development of a Novel Nuclear Imaging Technique, *MRS Online Proceedings Library*, **2013**, vol. 1518, pp. 123-129.

Oral Presentations

1. L.J. Gardner, V. Lejeune, C.L. Corkhill, S.A. Bernal, S.A. Walling, J.L. Provis, N.C. Hyatt, High temperature study of FA/MKPC binders for nuclear waste encapsulation, *34th Cement and Concrete Science Conference and Workshop of Waste Cementation*; Sheffield, UK, Sept 14-17, **2014**, printed proceedings, pp. 381-385.
2. L.J. Gardner, C.L. Corkhill, S.A. Bernal, N.C. Collier, J.L. Provis, N.C. Hyatt, Assessment of magnesium potassium phosphate cement as an encapsulant for radioactive waste: 1, immobilisation of ^{99}Tc, *33rd Cement and Concrete Science Conference*; Portsmouth, UK, Sept 2-3, **2013**, printed proceedings, pp. 74-78.

Poster Presentations

1. L.J. Gardner, V. Lejeune, C.L. Corkhill, S.A. Bernal, S.A. Walling, J.L. Provis, N.C. Hyatt, High resolution multi-nuclear NMR characterisation of a novel GBFS/MKPC binder for nuclear waste encapsulation, *34th Cement and Concrete Science Conference and Workshop of Waste Cementation;* Sheffield, UK, Sept 14-17; **2014**, printed proceedings, pp. 499-502.
2. L.J. Gardner, C.L. Corkhill, S.A. Bernal, S.A. Walling, V. Lejeune, J.L. Provis, S.M. Pimblott, N.C. Hyatt, Development of blended MKPC binders for radioactive waste encapsulation applications, *Nuclear Decommissioning Authority PhD seminar*; Manchester, UK, Jan 29th, **2013**.
3. L.J. Gardner, C.L. Corkhill, S.A. Bernal, N.C. Collier, J.L. Provis, N.C. Hyatt, Assessment of magnesium potassium phosphate cement as an encapsulant for radioactive waste: 1, radiation tolerance, *33rd Cement and Concrete Science Conference*; Portsmouth, UK, Sept 2-3, **2013**, printed proceedings, pp. 306-310.
4. L.J. Gardner, S.M. Pimblott, N.C. Hyatt, Defining the formulation envelope of magnesium potassium phosphate composites for waste encapsulation, *32nd Cement and Concrete Science Conference*; Belfast, UK, Sept 17-18, **2012**, printed proceedings, pp. 174-179.

Industry Events

1. L.J. Gardner, C.L. Corkhill, S.A. Bernal, S.A. Walling, V. Lejeune, J.L. Provis, S.M. Pimblott, N.C. Hyatt, Assessment of blended MKPC binders for radioactive waste encapsulation applications, 3rd *Nuclear Decommissioning Authority PhD seminar*; Manchester, UK, Jan 14th, **2015** (poster).
2. L.J. Gardner, C.L. Corkhill, S.A. Bernal, S.A. Walling, V. Lejeune, J.L. Provis, S.M. Pimblott, N.C. Hyatt, Understanding the chemical, mechanical and radiation stability of a magnesium potassium phosphate cement composite, 1st *Nuclear Decommissioning Authority PhD seminar*; Manchester, UK, Jan 29th, **2013** (abstract).

List of Abbreviations

ANL	Argonne National Laboratory
BET	Braunauer-Emmett-Teller
CAC	Calcium aluminate cement
CAP	Calcium aluminate phosphate cement
C-(A)-S-H	Al-substituted calcium silicate hydrate
CBC	Chemically bonded ceramic
CBPC	Chemically bonded phosphate ceramic
CP	Cross polarisation
CS	Compressive strength
CSA	Calcium sulphoaluminate cement
C-S-H	Calcium silicate hydrate
DBM	Dead burnt magnesia
DTA	Differential thermal analysis
DTG	Differential thermogravimetry
EDX	Energy dispersive X-ray spectroscopy
FA	Fly ash
GBFS	Ground granulated blast furnace slag
GDF	Geological disposal facility
HLW	High level waste
HTXRD	High temperature X-ray diffraction
IAEA	Internal Atomic Energy Agency
ICDD	International centre for diffraction data
IC	Isothermal calorimetry
ILW	Intermediate level waste
KDP	Potassium dihydrogen phosphate
LLW	Low level waste
LLWR	Low level waste repository
MAS	Magic angle spinning
MAP	Magnesium ammonium phosphate
MEP	Magnox encapsulation plant

Mg/P	Magnesium to phosphate molar ratio
MKPC	Magnesium potassium phosphate cement
MPC	Magnesium phosphate cement
MSSS	Magnox swarf storage silo
NDA	Nuclear Decommissioning Authority
NIST	National Institute of Standards and Technology
NMR	Nuclear magnetic resonance
NSLS	National synchrotron light source
PC	Portland cement
PSD	Particle size distribution
RWM	Radioactive Waste Management Ltd
SCM	Supplementary cementitious materials
SEM	Scanning electron microscope
SNF	Spent nuclear fuel
SRM	Standard reference material
SSC	Supersulphated cement
SXRD	Synchrotron X-ray diffraction
TGA	Thermogravimetric analysis
w/s	Water-to-solids ratio
XRD	X-ray diffraction
XRF	X-ray fluorescence

List of Equations

$Mg_{(s)} + 2H_2O_{(l)} \rightarrow Mg(OH)_{2\,(s)} + H_{2\,(g)}$ **Eq. 1**

$2Al_{(s)} + 6H_2O_{(l)} \rightarrow 2Al(OH)_{3\,(s)} + 3H_{2\,(g)}$ **Eq. 2**

$U_{(s)} + 2H_2O_{(l)} \rightarrow UO_{2\,(s)} + 2H_{2\,(g)}$ **Eq. 3**

$MgO_{(s)} + KH_2PO_{4\,(s)} + 5H_2O_{(l)} \rightarrow MgKPO_4{\cdot}6H_2O_{(s)}$ **Eq. 4**

$KH_2PO_{4\,(s)} \rightarrow H_2PO_4^-{}_{(aq)} + K^+{}_{(aq)}$ **Eq. 5**

$MgO_{(s)} + H_2O_{(l)} \rightarrow MgOH^+{}_{(aq)} + OH^-{}_{(aq)}$ **Eq. 6**

$MgOH^+{}_{(aq)} + 6H_2O_{(l)} \rightarrow [Mg(H_2O)_6]^{2+}{}_{(aq)} + OH^-{}_{(aq)}$ **Eq. 7**

$MgKPO_4{\cdot}6H_2O_{(s)} \rightarrow MgKPO_{4\,(s)} + 6H_2O_{(g)}$ **Eq. 8**

$MgO_{(s)} + NH_4H_2PO_{4\,(s)} + 5H_2O_{(l)} \rightarrow MgNH_4PO_4{\cdot}6H_2O_{(s)}$ **Eq. 9**

Contents

1 Introduction

1.1 UK nuclear waste

A substantial volume and breadth of radioactive materials has been created in the UK resulting from more than 60 years of nuclear fuel operations. Each waste stream is categorised (according to radioactivity and heat generation) into three main classifications, which are: low level waste (LLW), intermediate level waste (ILW), and high level waste (HLW) [1]. In LLW, the radioactivity must not exceed <4 GBq/t of alpha (α) activity or <12 GBq/t of beta (β)/gamma (γ) activity [1]. Typical LLW waste streams include: disposed paper, metal and protective clothing from nuclear operations and medical research facilities [2]. The bulk of LLW will be consigned to shallow ground storage in large steel containers at the low level waste repository (LLWR) [2] or treated to make very low level wastes that are not deemed radioactive and can be disposed under ordinary conditions or recycled [3].

In ILWs, the activity levels are above the upper threshold for LLWs but have a lower heat generation than HLW and as such, do not require active management during storage or final disposal [1]**.** ILWs are usually comprised of: steel, graphite, concrete, fuel cladding, reactor components and sludges [2]. Whilst HLWs include spent nuclear fuel (SNF) and reprocessed SNF (i.e. acidic liquors containing fission products) that constitute substantial radioactivity/heat generation associated with radioactive decay [3] that require substantial radiation shielding and remote handling [1]. The total estimate of current waste and the future arising of HLW is 1,770 m^3 (3,400 t) and for ILW is 286,000 m^3 (310,000 t), the latter accounts for 99.4% by volume of the total higher activity waste according to the 2013 UK radioactive waste inventory [3]. To reduce the inherent risks (e.g. environment contamination, radiological release) associated with nuclear waste, stabilisation and solidification techniques are often used [4]. The latter is associated with the physical containment of the waste, e.g. encapsulation in a cement grout, which is the treatment method for ILWs, whilst the former chemically changes the HLW in order to reduce the mobility/toxicity, e.g. immobilisation of highly active liquor into a glass matrix (vitrification) [4]. The stabilisation and solidification enable storage of ILW and HLW in a passively safe manner, which are subsequently referred to as conditioned waste packages [3].

The integration of ILW into suitable and stable wasteforms is a diverse and intricate challenge due to the high degree of variability in the physical/chemical composition and the waste condition (i.e. stored under water, inert gas, or open to air). The current baseline option for ILW encapsulation involves cementation using a composite Portland cement (PC) binder that consist of hydraulic PC and supplementary cementitious materials (SCMs) (e.g. fly ash and ground granulated blast furnace slag) [4, 5]. However, within the ILW inventory there are niche waste streams (e.g. reactive metals: Al, Mg and U) that require tailored solutions to ensure that both the durability and longevity of the conditioned wasteforms can be achieved in typical storage scenarios, due to waste-binder interactions.

1.1.1 Magnox swarf

Particularly problematic waste streams within the UK are legacy wastes arising from the reprocessing of Magnox reactor fuel. In Magnox nuclear reactors (CO_2 cooled, graphite moderated), the natural uranium fuel elements (Fig. 2.1A) are contained within Magnox cladding, which is a magnesium alloy (99 % Mg and 1 % Al). After defueling the reactor, the fuel elements are initially cooled (under water) prior to transport to the Sellafield Ltd site, where the Magnox cladding is mechanically decanned to form Magnox swarf (Fig. 1.1B) [6]. Two examples of Magnox swarf inventories identified from the 2010 UK nuclear waste inventory are waste streams 2D22 and 2D24 (referred to as Magnox cladding and miscellaneous solid waste), the compositions associated with these wastes are listed below.

- Waste stream 2D22 (1040 m^3): 21.0 wt. % Magnox swarf, 25.1 wt. % magnesium hydroxide, 8.0 wt. % natural uranium fuel, 43.8 wt. % water and 2.1 wt. % other [7]
- Waste stream 2D24 (1370 m^3): 25.3 wt. % Magnox swarf, 17.3 wt. % magnesium hydroxide, 12.6 wt. % natural uranium fuel, 44.1 wt. % water and 0.7 wt. % other [8]

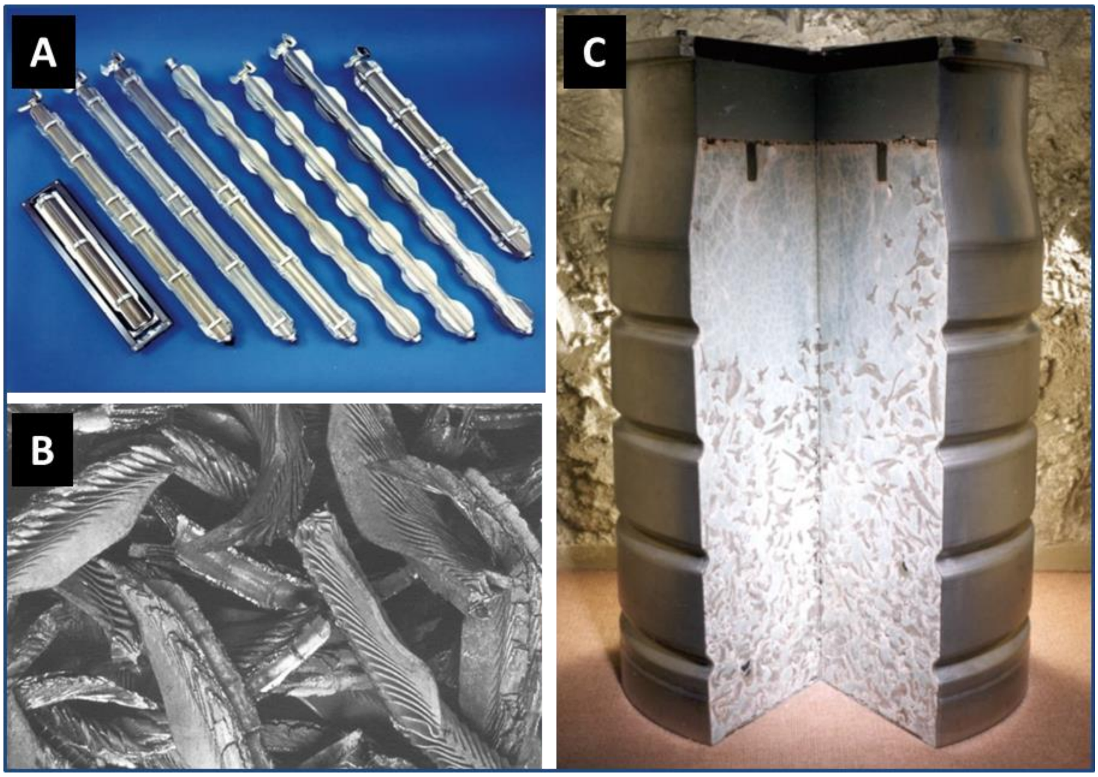

Fig. 1.1. (A) Magnox fuel elements [9], (B) Magnox swarf [10] and (C) In-drum encapsulated Magnox swarf [10]

Historically after decanning, Magnox swarf was stored in the Magnox swarf storage silo (MSSS) under water to inhibit the pyrophoric reaction of uranium hydride that reacts in air [11]. The uranium content within Magnox swarf wastes can arise from residual fuel pieces from the decanning process, this is highlighted in waste stream 2D24 where there is significant uranium content (12.6 wt. %). Since 1992, Magnox swarf is diverted to the Magnox encapsulation plant (MEP), were it is encapsulated in 500 L stainless steel drums using a PC composite grout (Fig. 2.1C) [12]. However, there is a growing concern that PC encapsulants can promote the corrosion of encapsulated reactive metals, including aluminium, magnesium [13] and uranium [14], consequently alternative encapsulants are under investigation (Chapter 2).

1.2 Geological disposal facility

In the UK, a geological disposal facility (GDF) will be designed to house the conditioned HLW and ILW inventories (Fig. 1.2A) for long term storage/final disposal [3]. The general concept for a GDF is based on a multi-barrier approach (Fig. 1.2B) at depths between 200-1000 metres [2]. Each barrier is designed for radionuclide isolation and containment, allowing for substantial radioactive decay to occur prior to reaching the environment [10]. The engineered barriers should include: a wasteform (e.g. waste encapsulated in a cement grout), which is the physical containment of the waste; a waste container (e.g. stainless steel overpack) that provides the primary structural and mechanical barrier; a buffer/backfill surrounding the packaged wasteforms, which should impede the movement of any radionuclides released by the wasteform. The final barrier is the host rock itself, where the important containment properties are stability against ground movements and a slow moving hydrogeology in order to minimise radioactivity progression towards the surface [2].

The generic safety functions for the wasteform and waste container as described by the Nuclear Decommissioning Authority (NDA) for transport and storage/disposal operations are as follows [10]: a wasteform/container should contain radionuclides during normal operations and accident scenarios (impact or fire), provide external radiation shielding, minimise the risk of criticality, prevent the build-up of internal gas pressure (for example, H_2 gas generated from metal corrosion) by gas ventilation, withstand loads for other waste containers and last but not least, provide safe handling of the conditioned waste [10]. The cement grout used for encapsulation also has several desirable properties: to physically immobilise the radioactivity, be chemically compatible with the waste, be radiation tolerant, have sufficient strength and stability, suitable flow properties to allow for complete infiltration of complex waste, and be cost effective [10]. In current surface stores, the timescale that a wasteform/waste container needs to maintain these safety functions can be up to 100 years prior to transferal into the GDF, where there is currently a 500 year safety function target [10].

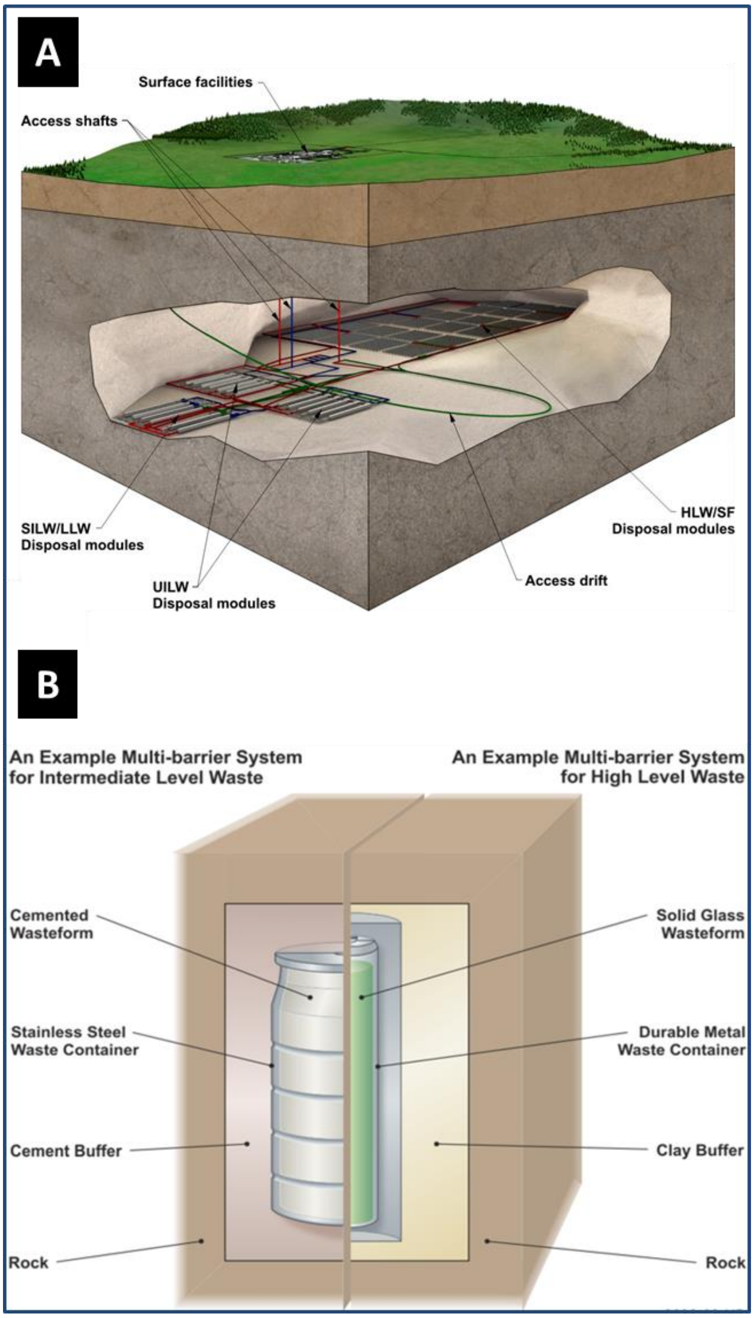

Fig. 1.2. (A) General GDF design [10] and (B) a schematic of the multi-barrier concept for the disposal of nuclear waste in the UK [2]

1.3 Project aims

In the UK, current treatment for Intermediate level wastes (ILWs) involves cementation in stainless steel drums or boxes. The typical cement used is based on Portland cement (PC) and blended with supplementary cementitious materials; fly ash (FA) and ground granulated blast furnace slag (GBFS) [4, 5]. These matrices have many advantages (e.g. inexpensive, easy to use, low technology [15]) and are suitable for a wide range of nuclear wastes. However, there are certain waste streams within the UK inventory that are unsuitable for PC encapsulation[16-18]. For example, the high pH and significant free water content of PCs can lead to the corrosion of reactive metals (uranium, Magnox swarf from Magnox fuel cladding and aluminium) [19]. Corrosion products are expansive (e.g. $Mg \rightarrow Mg(OH)_2$) and generate hydrogen gas (flammability hazard) [20] and consequently, can affect the durability of the cemented wasteforms. In line with the safety functions of wasteforms for storage and final disposal in the UK, magnesium potassium phosphate cement (MKPC) blended with FA or GBFS have been investigated as a possible alternative encapsulant for intermediate level waste streams. MKPC binders are an acid-base cement system with a near-neutral pH, low water demand, rapid setting and high early compressive strength [21]. Water is chemically bound within the struvite-K crystal structure [22], which is expected to minimise the corrosion of reactive metals.

For these reasons, this thesis will present the results of four main aims:

1. Design and optimise an MKPC formulation using FA and GBFS
2. Determine the chemistry of the optimised formulation
3. Assess the accident performance (fire) of the MKPC formulation
4. Assess the radiation tolerance of the MKPC formulation

2 Literature review

Note to reader: This thesis has been organised into chapters with respect to published papers or manuscripts in preparation, as such there may be some repetition within the chapter discussions. It is hoped that presenting the data in this way provides distinct results. The literature review will provide a simple introduction to magnesium potassium phosphate cements (MKPCs), whilst each chapter will provide more detailed literature within the chapter introduction.

2.1 Portland cement

Portland cement clinker is produced in a rotary kiln using limestone (calcite, $CaCO_3$) and clay (or shale). At temperatures ≤ 1300 °C, calcination of the calcite to lime (CaO) occurs alongside the disintegration of the clay minerals. The resulting reaction leads to the formation of: belite (Ca_2SiO_4), tricalcium aluminate (Ca_3Al_2O) and ferrite (Ca_2AlFeO_5)[23]. Upon further heating (between 1300 – 1450 °C), 20-30 % of the clinker matrix melts, this is mainly from the tricalcium aluminate and ferrite phases present [23]. A reaction between CaO, belite and the melt lead to the formation of alite (Ca_3SiO_5) and agglomeration (i.e. clinkering) of the phases. Subsequent rapid cooling of the clinker matrix leads to glass formation and crystallisation of the clinker phases: alite (50-70 %), belite (15-30 %), tricalcium aluminate (5-10 %) and ferrite (5-15 %), where the bracketed values refer to the typical composition range within PC clinker [23]. This high temperature transformation of limestone and clay to the PC clinker is shown Fig. 2.1. Upon quenching, belite undergoes a polymorph transition to the beta phase, β-Ca_2SiO_4, which is most commonly found in PCs [24]. The clinker is mixed with gypsum and finely ground using a ball mill to create the final product, Portland cement [23]. Gypsum ($CaSO_4{\cdot}2H_2O$) is included in the PC clinker as a setting-regulator that modifies the hydration of tricalcium aluminate, preventing flash setting [23]. A typical PC clinker used in the UK consists of: alite (60 %), belite (β-Ca_2SiO_4, 15 %), tricalcium aluminate (8 %), ferrite (8%) and gypsum (5 %) [15].

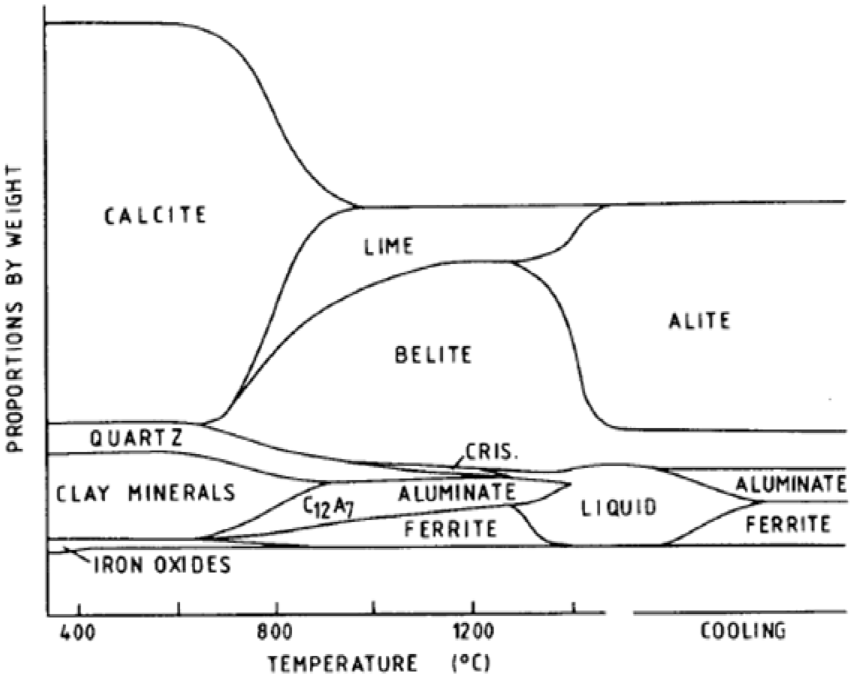

Fig. 2.1. Formation of Portland cement clinker [23]

The reaction of alite is important for the early strength development and setting properties of PC. It reacts with water to form a poorly crystalline calcium silicate hydrate (C-S-H) phase and portlandite ($CaOH_2$) [23, 24], which maintains a high alkalinity (≈ pH 13 [25]). β-belite undergoes the similar reactions, although at a much slower hydration rate, which has the benefit of enhancing the long term strength properties of PC [24]. The tricalcium aluminate and ferrite clinker phases react with gypsum to form calcium aluminate hydrated phases: ettringite ($Ca_6Al_2(SO_4)_3(OH)_{12}·26H_2O$) and monosulphoaluminate ($Ca_4Al_2(SO_4)(OH)_{12}·6H_2O$), which are dependent upon the supply of sulphate within the pore solution [24].

Portland cements form composite grouts when blended with supplementary cementitious materials (SCMs) such as, fly ash (FA) and ground granulated blast furnace slag (GBFS). The inclusion of SCMs in PCs has several advantages, it utilises industrial wastes (FA, from coal power stations) and industrial by-products (GBFS, from the steel-making process), decreases the high energy requirements of PC associated with clinker production (i.e. less clinker is required), reduces the reaction rate and exothermic output of the PC clinker and improves durability [23].

Furthermore, SCMs also have cementitious properties leading to the formation secondary C-S-H products. For example, GBFS (calcium aluminosilicate glass) is a latently hydraulic material that will react with water to form C-S-H [26]. Whilst FA (aluminosilicate glass) behaves like a pozzolanic material and will react with lime (CaO) in the presence of water to form C-S-H or C-A-S-H type phases [23, 27]

It is current practice in ILW encapsulation for the utilisation of PC blended with either FA or GBFS, to form FA/PC and GBFS/PC grouts (at up to 35 wt. % and 90 wt. % replacements, respectively) [4, 5]. The advantage of blended PCs are readily available whilst being inexpensive and durable, grout preparation is straightforward in remote operations and the cement matrix imposes a high pH environment, which can assist in the immobilisation of radionuclides (particularly actinides) through the formation of less soluble hydroxide species [15, 17]. Despite these properties, there is an increasing awareness that PC based encapsulants may not be suitable for the immobilisation/encapsulation of all ILW waste types present in the ILW inventory [16-18]. PC composites can promote the corrosion of encapsulated reactive metals, including aluminium, magnesium [13] and uranium [14]. The high pH of blended PC promotes the corrosion of Al whilst Mg and U are known to corrode in a wet environment [19]. Corrosion of reactive metals (Eq. 1-3) is considered to be problematic on two grounds: (1) the formation of expansive corrosion products (e.g. $Mg(OH)_2$) that can cause a volumetric change within the wasteform leading to the formation of stress-induced fractures and (2) formation of hydrogen gas, which presents a flammability hazard (during interim storage and disposal) and can result in pressurisation and potential distortion of the waste container [20]. Consequently, the durability of the monolithic wasteform and its ability to retain radioactivity can be deleteriously affected.

$$\mathrm{Mg}_{(s)} + 2\mathrm{H_2O}_{(l)} \rightarrow \mathrm{Mg(OH)_2}_{(s)} + \mathrm{H_2}_{(g)} \qquad \text{Eq. 1}$$

$$2\mathrm{Al}_{(s)} + 6\mathrm{H_2O}_{(l)} \rightarrow 2\mathrm{Al(OH)_3}_{(s)} + 3\mathrm{H_2}_{(g)} \qquad \text{Eq. 2}$$

$$\mathrm{U}_{(s)} + 2\mathrm{H_2O}_{(l)} \rightarrow \mathrm{UO_2}_{(s)} + 2\mathrm{H_2}_{(g)} \qquad \text{Eq. 3}$$

2.2 Alternative encapsulation grouts

In the UK, the generic waste package design for ILW cast in 500 L stainless steel drums) are subject to strict flammable gas generation limits (the hydrogen gas limit is 0.43 litres per day) compared to the total gas generation limit of 71 litres per day [28]. It is therefore essential that the corrosion rate of encapsulated reactive metals is minimised to ensure that the waste packages remain within regulatory tolerance. Therefore, there is a need to develop tailored encapsulation compatible with niche waste streams and conceptual disposal concepts. The alternative cement binders under investigation for potential encapsulation of reactive metals include: calcium aluminate cement (CAC), calcium sulphoaluminate (CSA), supersulphated cement (SSC) and magnesium potassium phosphate cement (MKPC) [17]. For reactive metal encapsulation, the principal purpose of alternative encapsulants is to decrease the pH and/or the free water availability of the system compared to PC based encapsulants in order to reduce the rate of corrosion of reactive metals and therefore, extend the longevity of the wasteform packages.

These cements also offer other useful properties, for example:

- CACs successfully maintain a high compressive strength and a low porosity at a lower pH than PC based encapsulants. Typically CACs are blended with SCMs (mainly GBFS) to reduce the negative volume changes associated with the formation of the thermodynamically favoured phases [15, 17]. Recent research has extended the scope of CACs to include phosphate modifications (calcium aluminate phosphate (CAP) cement), which resulted in a further reduction of the pH and facilitated control of the setting and mechanical properties [29].

- The major reaction product of CSAs and SSCs is ettringite ($Ca_6Al_2(SO_4)_3(OH)_{12}{\cdot}26H_2O$), which limits the amount of water available for corrosion as it is bound within the crystal structure. The formation of ettringite is beneficial for stabilisation of waste materials as it can incorporate a large range of ions within its structure [15, 17, 19, 30].

- MKPC binders are relatively less well-understood binders, their advantageous properties include: near-neutral pH, low water demand, low drying shrinkage, rapid setting and high early compressive strength [21]. Similarly to CSA/SSC systems, the water is chemically bound within the struvite-K crystal structure [22], preventing it from enhancing corrosion of any reactive metal surface present.

Although these encapsulants are passed conceptual design not all of them are currently suitable for encapsulation of radioactive wastes. The rapid setting of CACs produces a substantial exotherm, which may cause temperature problems in large scale wasteforms [17], whilst CSA is constituted of niche products primarily produced outside the UK (mainly China [17]), which has potential to produce supply continuity issues. Further data is needed on all of the alternative cementitious binders to validate their suitability for waste encapsulation in the UK and other countries. This body of work will continue to assess the suitability of MKPC binders for nuclear waste encapsulation.

2.3 Magnesium potassium phosphate cement

2.3.1 Nomenclature history

MKPCs of today emerged from early investigations by Kingery [31, 32] who developed cold setting phosphate bonds between phosphates and oxides. It was found that the reactivity of the oxide must be controlled to allow time for the formation of an organised, cohesive cement-like product. As such, weakly basic or amphoteric oxides (e.g. MgO) were favoured as they reacted slowly with phosphoric acid [32]. The term chemically bonded ceramics (CBCs) was coined by Roy [33] in relation to these new cold-setting cements that exhibited properties improved by ten-fold when compared to conventional Portland cement. It was proposed that these properties are more affiliated with those of a ceramic than a cement except that the bonding was the result of low temperature chemical reactions rather than fusion at high temperatures [33]. This term has since been further expanded to be chemically bonded phosphate ceramic (CBPC) [34]. The terms ceramic and cement are interchangeable within the literature based on magnesium phosphate systems for ease they will be referred to as cements within this body of work.

2.3.2 Acid-base reaction

MKPC binders are produced via an acid-base reaction between magnesium oxide (MgO), potassium dihydrogen phosphate (KDP; KH_2PO_4) and water, according to Eq. 4. The reaction product is struvite-K ($MgKPO_4{\cdot}6H_2O$), an analogue of struvite ($NH_4MgPO_4{\cdot}6H_2O$) [22], which is referred to as magnesium ammonium phosphate (MAP) cement. Struvite is naturally cementitious and often found in guano and kidney stones [35].[1] The acid-base reaction is based on a dissolution-precipitation mechanism where, the dissolution of KH_2PO_4 (Eq. 5) releases $H_2PO_4^-$ and K^+ ions into solution creating an acidic environment that promotes the hydration of MgO (Eq. 6) to its hydrated magnesium complex, $[Mg(H_2O)_6]^{2+}$ (Eq. 7) [36, 37].

$$\mathbf{MgO_{(s)} + KH_2PO_{4\,(s)} + 5H_2O_{(l)} \rightarrow MgKPO_4{\cdot}6H_2O_{(s)}} \qquad \textbf{Eq. 4}$$

$$\mathbf{KH_2PO_{4\,(s)} \rightarrow H_2PO_4^-{}_{(aq)} + K^+{}_{(aq)}} \qquad \textbf{Eq. 5}$$

$$\mathbf{MgO_{(s)} + H_2O_{(l)} \rightarrow MgOH^+{}_{(aq)} + OH^-{}_{(aq)}} \qquad \textbf{Eq. 6}$$

$$\mathbf{MgOH^+{}_{(aq)} + 6H_2O_{(l)} \rightarrow [Mg(H_2O)_6]^{2+}{}_{(aq)} + OH^-{}_{(aq)}} \qquad \textbf{Eq. 7}$$

---

[1] The discussions throughout this body of work often cite magnesium ammonium phosphate (MAP) cements, where struvite is the main binding phase. As only minor differences were observed in the crystal structures of struvite and struvite-K, these references were used to support MKPC binders.

The precipitation mechanism can be described to occur via either a "through solution" and or "topochemical" route. The through-solution mechanism postulates that as further Mg^{2+} ions are released into solution, the magnesium species, $[Mg(H_2O)_6]^{2+}$ react with aqueous PO_4^{3-} and K^+ ions resulting in the formation of a struvite-K cementitious gel that permeates through the solution. As the gel saturation level increases (and thus, connectivity), the gel thickens and sets around unreacted MgO particles [38, 39]. The topochemical mechanism considers the precipitation of struvite-K to occur via the adsorption of $[Mg(H_2O)_6]^{2+}$ species onto the surface of unreacted MgO particles. This process prevents the adsorption of water molecules on to the MgO surface and thus, inhibits dissolution. Additional $[Mg(H_2O)_6]^{2+}$ species are adsorbed onto the MgO surface until the particle is completely covered, at the same time available aqueous PO_4^{3-} and K^+ ions in solution react with the $[Mg(H_2O)_6]^{2+}$ species to form a struvite-K network around an unreacted MgO particle [37, 40].

2.3.3 The effect of MgO calcination

The two precipitation mechanisms discussed above infer unreacted MgO particles act as nucleation sites for the formation of struvite-K. It is reported that slow setting leads to better mechanical properties of MKPCs, as such it is important to control the reactivity of MgO [41]. MKPC formulations regularly utilise dead-burnt magnesia (DBM) sources, calcined to ≈ 1500 °C, which have an increased particle size, lower porosity and reactivity (due to a smaller surface area) compared to MgO calcined at lower temperatures [42]. This was highlighted by Kingery [32] who observed the formation of a set magnesium phosphate phase when MgO (calcined at 1280 °C) reacted with phosphoric acid. In contrast, the use of reactive MgO resulted in a violent reaction and no set magnesium phosphate phase [32]. The latent reactivity of DBM allows for a slow but constant dissolution rate [38], which is important in MKPC binders as this slow reaction rate ensures the formation of large crystallites in the magnesium phosphate binder [32]. Within MPC/MKPC systems, DBM is often used in conjunction with a set retarder (e.g. boric acid and borax) to further delay the setting reaction and enhance product workability [18, 40, 43].

2.3.4 The retardation mechanism

The retardation mechanism initially proposed for the utilisation of borax ($Na_2B_4O_7{\cdot}10H_2O$) and boric acid (H_3BO_3) in MAP (magnesium ammonium phosphate) cements described the early formation of a metastable poorly crystalline magnesium borate phase around unreacted MgO particle [40, 44], that slowly releases the Mg^{2+} ions in to solution allowing the formation of a uniform layer of struvite around the MgO particle [40]. This mechanism was further developed by Wagh *et al.* [38] who proposed that the precipitated phase was crystalline lünebergite, $Mg_3(H_2O)_6[B_2(OH)_6(PO_4)_2]$, which formed around the MgO particles [38]. This phase reduced contact between the $K^+/H_2PO_4^-$ ions in solution and the MgO particles.

The formation of lünebergite was founded on observations of a newberyite-rich ($MgHPO_4{\cdot}3H_2O$) magnesium phosphate cement (MPC), where 15 wt. % H_3BO_3 was added to calcined MgO (1300 °C) and 50 % H_3PO_4 [45]. The phases identified in the X-ray diffraction pattern (Fig. 2.3A) for this system were: newberyite, unreacted MgO and lünebergite. The latter phase was also observed in the DTA data (Fig. 2.2A) with a distinct shoulder at ≈220 °C. This feature is in agreement with the TGA/DTA behaviour of a natural lünebergite specimen described by Sen Gupta *et al.* [46]. From these findings, it is frequently stated that within magnesium phosphate cements, boric acid retards the setting of the cement *via* the formation of lünebergite, even in low-boron systems and with differing phosphates sources [14, 47-49].

The reason for this ambiguity is that the data first published by Wagh *et al.* [45] has been repeatedly published for conflicting formulations. Firstly, the H_3BO_3 additions were found to decrease from 15 wt. % [45] to 4 wt. % [50] and then 1 wt. % [38], whilst the DTA plots (Fig. 2.2B-C) remained the same, with the shoulder at ≈220 °C assigned to lünebergite. From these references, it would be possible to conclude that a decreasing boron content (from 15 – 1 wt. %) results in the same DTA response, which is unlikely to be the case. Secondly, the phosphate source was changed from H_3PO_4 to KH_2PO_4 in [36]. Potassium dihydrogen phosphate is used in the formation of magnesium potassium phosphate cements MKPC) were struvite-K ($MgKPO_4{\cdot}6H_2O$) is formed. In Fig. 2.3B, Wagh [36] reported the reaction products to be newberyite and lünebergite, which is incorrect for MKPC binders. From Fig. 2.2D and Fig. 2.3B, it is evident that the data for the MKPC system is exactly the same as published for the newberyite-rich system [45]. These disparities in results call into to question the validity of the formation of lünebergite within lower wt. % boric acid systems and within MKPC binders. Further investigation should be conducted to identify the boric acid retardation mechanism.

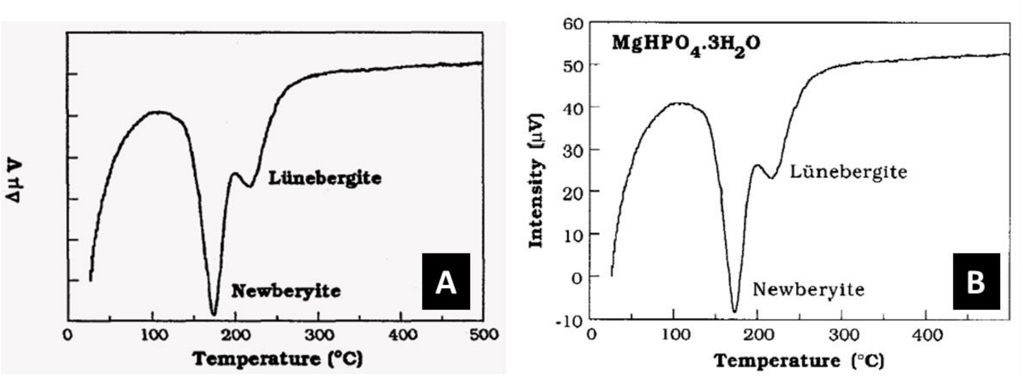

(A) MgO, H_3PO_4, 15 wt. % H_3BO_3 **(B)** MgO, H_3PO_4, 4 wt. % H_3BO_3

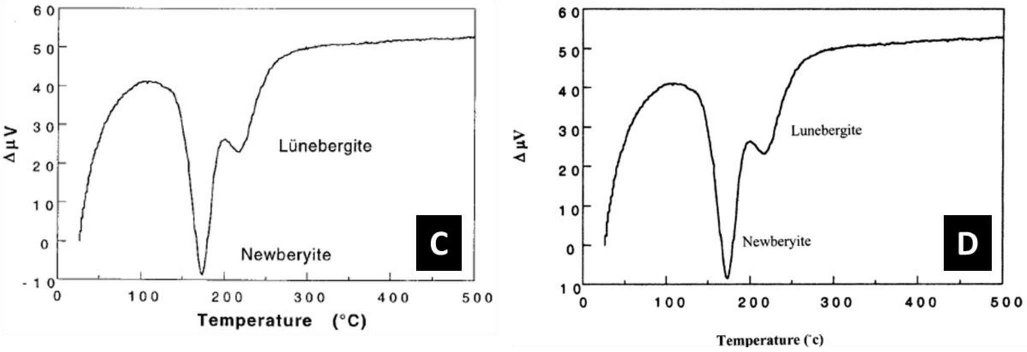

(C) MgO, H_3PO_4, 1 wt. % H_3BO_3 **(D)** MgO, KH_2PO_4, 1 wt. % H_3BO_3

Fig. 2.2. DTA thermographs published in support of the formation of lünebergite in magnesium phosphate ceramics, which were extracted from: initially (A) Wagh *et al.*, 1995 [45] and later produced in (B) Singh *et al.*, 1999 [50], (C) Wagh and Jeong, 2003 [38] and (D) Wagh, 2004 [36]

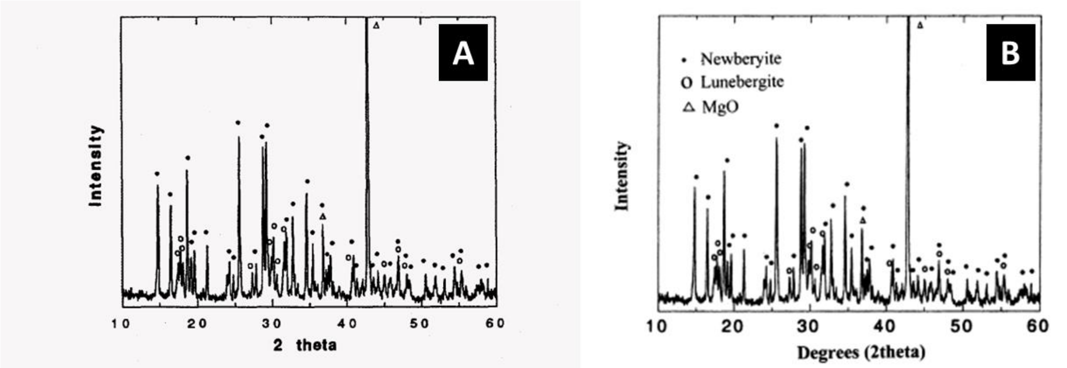

Fig. 1: X-ray diffraction output of Mg phosphate ceramic:
• newberyite, Δ MgO, ° lünebergite

X-ray diffraction output of $MgKPO_4{\cdot}6H_2O$ ceramic with boric acid.

Fig. 2.3. X-ray diffraction patterns published in support of the formation of lϋnebergite in magnesium phosphate ceramics, which were extracted from: initially (A) Wagh *et al.*, 1995 [45] and later produced in (B) Wagh, 2004 [36]

Hall *et al.* [43] reported that crystalline magnesium borate phases were unlikely to form in the initially acidic environment of MPCs. The retardation mechanism was instead thought to be associated with the adsorption of borate complexes on to the MgO particles [46] rather than the precipitation of lϋnebergite (or alternative magnesium borate phases) around unreacted MgO particles.. A recent study by Sasaki [51] examining MgO – boric acid interactions reinforced the likelihood of this theory. As precipated magneisum borate phases ($Mg_7B_4O_{13}{\cdot}7H_2O$ and $MgB_3O_3(OH)_2{\cdot}5H_2O$) were only observed in high borate conditions (>67.9 mM borate solution) under varying conditions via an intermiedate complex, $[MgB(OH)_4]^+$ [51].

2.3.5 Applications of MKPCs

Interest in magnesium phosphate cements first developed in the 1970s where the rapid setting and high early strength properties of MAP cements achieved commercial application as an emergency repair material for roads, runways, bridges, pavements [52-55]. MAP cements reduced the closure time and disturbance to high trafficked roads (e.g. motorways, runways), which could incur high costs when traditional patch repair materials are used [54]. Using traditional cementitious materials would result in a long delay in repairs, to allow for a good bonding capability to the old concrete. However, the liberation of ammonia gas during mixing and setting was an undesirable characteristic of MAP cements [39]. However, in potassium-based magnesium phosphate cement (MKPC) there is no loss during setting, which can be advantageous in waste applications (i.e. reduce gas generation). MKPC binders are often blended (up to 50 wt. % replacement) with supplementary cementitious materials (SCMs), for example, FA or GBFS to reduce the exothermic output of the acid-base reaction and reduce material costs.

In the USA, MKPC binders have been extensively researched and developed at the Argonne National Laboratory (ANL), for the management of hazardous and radioactive wastes, since the mid-1990s [56-62]. The work by ANL has resulted in commercialisation of the MKPC binder under the trademark name Ceramicrete™ [36]. ANL postulated that MKPC binders have the potential to stabilise hazardous and nuclear waste using three mechanisms: (1) chemical conversion to a less soluble phosphate product, (2) microencapsulation within the struvite-K phase and (3) macroencapsulation as part of a dense, insoluble monolith wasteform [36]. MKPC binders represent a simple and low cost technology that has been shown by ANL to stabilize a wide range of hazardous, radioactive and mixed-waste streams:

- Encapsulation of heavy metals such as Pb bricks, Pb-lined gloves, Hg contaminated light bulbs from mixed low-level waste streams. The FA/MKPC binders were found to produce dense, strong and impermeable monoliths. The microstructure identified continuous MKPC adhesion to the waste, free of air pockets, which suggest complete encapsulation of the waste materials [56].

- Stabilisation of the Hanford tank waste supernates (Cr, Pb, Ag and Cs) and sludges (Cd, Cr, Ag, Ni, Ba, Cs and Tc) separately, at respective waste loadings of 39.8 wt. % and 32 wt. % [62].

- Effective reduction of problematic long-lived radionuclide Tc-99 (half-life of 2.13×10^5 years) as a result of the addition of 2-3 wt. % $SnCl_2$, which acts as a reducing agent in the binder [59]. The redox conditions (+225 mV, pH 6.5) of FA/MKPC/$SnCl_2$ binders indicated favourable conditions to reduce and stabilise the highly mobile pertechnetate Tc(VII) species as the insoluble Tc(IV) state. This suggests that Tc-99 was chemically stabilised within the MKPC/$SnCl_2$ binder, which could potentially lead to higher waste loadings [59].

MKPC binders have been lengthily identified by ANL to have wide-reaching applications, however, in the UK, research has mainly focussed on utilising MKPC binders for the encapsulation of reactive metals (Al, U and Magnox swarf) [15, 17-19]. Corrosion trials conducted by Covill *et al.* [14] found that using natural uranium pucks in FA/MKPC binders (0.26 w/s and 0.28 w/s) have shown corrosion and gas generation rates notably lower than FA/PC grout (3:1, 0.42 w/s). After 90 days, the average hydrogen production of MKPC binders was just 5.9 vol. % of the total hydrogen production from the FA/PC grout [14]. These trial samples have indicated that there is very little chemical interaction between FA/MKPC binder and the uranium puck. Whilst work undertaken by the National Nuclear Laboratory (formerly Nexia Solutions) observed that corrosion of encapsulated aluminium was substantial reduced for FA/MKPC binders (0.31 w/s and 0.32 w/s) when compared to a GBFS/PC grout (9:1, 0.33 w/s). This suggests that the near-neutral pH of MKPC binders can assist the passivation of aluminium corrosion [19]. These trials suggest that MKPC binders appear to be suitable for encapsulation of niche intermediate level waste streams.

2.4 Summary

The current literature for MKPC binders has indicated confident results for the successful encapsulation of reactive metal waste streams. However, the UK standards for ILW wasteforms highlight that the functions of an encapsulant should include: immobilisation of radioactivity, be chemically compatible, be radiation tolerant, maintain physical integrity over the wasteform lifetime and for a range of environment conditions, have adequate strength and flow properties, and be cost effective [10]. Further research and development is needed on MKPC binders, at both the laboratory and plant scales, to provide a depth of understanding and to improve the technology readiness in order to be employed as an encapsulant. In addition to the wasteform requirements, more technical information is required to support the long-term performance of MKPC binders for example: fire performance, radionuclide retention, long-term chemical and mechanical stability, to understand the cement/waste interactions.

3 Materials and methods

3.1 Materials

The cement binder precursors were: MgO (RBH Ltd, 89 % purity) in the form of dead burnt magnesia (DBM), KH_2PO_4 (Prayon, >99 %) available as Food Grade E340 MKP, and granular H_3BO_3 (Fisher Scientific, >99.5 %). Fly ash (FA) was supplied by CEMEX as PFA BS EN 450-1 S [63]. Ground granulated blast furnace slag (GBFS) was supplied by Hanson Cements in accordance with established Sellafield Limited specifications for the UK nuclear industry, and is a blend of fine and coarse ground materials. The characterisation and chemical compositions of MgO, FA and GBFS presented in Tables 3.1 and 3.2 were determined using: a Malvern Mastersizer 3000 for the particle size distribution (PSD), powder fineness was measured using Controls 62-L0041/A Blaine fineness apparatus calibrated using NIST SRM material 114q, all samples were prepared according to BS EN 196-9:2010 [64]. Braunauer-Emmett-Teller (BET) surface area measurements were carried out using a Coulter SA 3100 instrument, density was measured using a Micromeritics AccuPyc II 1340 instrument, and the oxide compositions were determined using X-ray fluorescence (XRF) analysis. The XRF analysis was externally performed by AMG Superalloys UK (formally London & Scandinavian Metallurgical Co. Ltd) using the fuse-bead method.

Table 3.1. Characterisation of raw materials using PSD, Blaine fineness, BET surface area and density measurements

	d_{10} (µm)	d_{50} (µm)	d_{90} (µm)	Blaine fineness (m^2/kg)	BET (m^2/kg)	Density (kg/m^3)
MgO	3.2 ± 0.1	24.4 ± 0.3	63.8 ± 0.6	329 ± 16	563 ± 72	3471 ± 1
FA	2.7 ± 0.1	14.0 ± 0.3	66.1 ± 3.5	560 ± 10	2258 ± 10	2329 ± 5
GBFS	1.6 ± 0.1	16.0 ± 0.1	1465 ± 15	497 ± 17	993 ± 72	2885 ± 5

Table 3.2. Composition of raw materials determined by XRF oxide analysis (precision ± 0.1 wt. %)

Compound (wt. %)	**MgO**	**FA**	**GBFS**
Na_2O	<0.1	1.1	0.4
MgO	88.9	1.7	7.9
Al_2O_3	1.7	25.2	12.0
SiO_2	4.3	50.2	36.6
P_2O_5	<0.1	0.3	<0.1
K_2O	0.1	3.6	0.7
CaO	2.1	2.4	40.2
Fe_2O_3	1.5	9.3	0.4
Total	98.8	93.8	98.3

3.2 Mix design

For compressive strength, X-ray diffraction and thermal analysis investigation, the precursors (MgO, KH_2PO_4, H_2O, SCM (referring to either FA or GBFS) and H_3BO_3) were mixed initially for 10 minutes in a Kenwood mixer at speed 1. Afterwards, the paste was transferred to a high shear Silverson mixer operating at 4000 rpm for 10 minutes to ensure a homogenous paste was achieved. The cement paste was cast into steel cube moulds or centrifuge tubes (and then sealed) and cured in an environmental chamber at 20 °C and 95 % relative humidity until testing. For miniature-slump and calorimetry analysis, small cement batches (<100 g) were prepared by hand, each paste was mixed for 5 minutes (mini-slump) or 2 minutes (calorimetry) prior to analysis. The formulations used throughout this study involve the addition of boric acid as a setting retarder to ensure that a workable paste is formed. The addition of dead-burnt MgO (low reactivity) and supplementary cementitious materials (FA or GBFS, which act as diluents) have also been reported to further extend the setting time of the acid-base reaction [18, 41].

3.2.1 Formulation calculations

The formulations used to produce the blended MKPC pastes are shown in Table 3.3. These formulations were derived from a previous study that investigated FA/MKPC binders (0.26 and 0.28 water-to-solids (w/s) ratio) for ILW waste encapsulation of reactive metal (uranium) [14]. In the present work, it was decided to expand the w/s ratio study with the aim of further reducing the water content. In addition to varying w/s ratio, the inclusion of GBFS was explored as it is frequently used with the UK nuclear industry, however is not commonly studied within MKPC binders.

The molar ratio of magnesium to phosphorous (Mg/P) was calculated to be 1.7: 1 ratio (based on previous research [18]) with the addition of 50 wt. % SCM and 2 wt. % H_3BO_3 (the wt. % calculations are based on the sum of MgO, KH_2PO_4 and H_2O). It was found that at SCM additions other than 50 wt. % (i.e. 40 and 60 wt. %), severe cracking occurs during the first three days of curing (Appendix C). The water-to-solid (w/s) ratio is calculated by H_2O (g) divided by the sum of MgO (g), KH_2PO_4 (g) and SCM (g), which relates to w/s = H_2O / (MgO + KH_2PO_4 + SCM).

Table 3.3. FA/MKPC and GBFS/MKPC formulations based on three water-to-solids (w/s) ratios: 0.22, 0.24 and 0.26 w/s to ± 0.1 g precision

w/s	MgO (g)	KH_2PO_4 (g)	H_2O (g)	SCM (g)	H_2BO_3 (g)
0.22	160	318	180	329	13
0.24	156	309	192	329	13
0.26	149	303	206	329	13

Table 3.4. Formulation of MKPC pastes based on a 0.24 water/solids ratio, using a 500 g batch size to ± 0.1 g precision

Blend	MgO (g)	KH_2PO_4 (g)	H_2O (g)	SCM (g)	H_3BO_3 (g)
MKPC	132.3	262.8	96.0	-	9.8
FA/MKPC	77.8	154.6	96.0	165.0	6.5
GBFS/MKPC	77.8	154.6	96.0	165.0	6.5

3.3 Analytical methods

3.3.1 Compressive strength

Samples for compressive strength (CS) were prepared in triplicate using 50 x 50 x 50 mm (± 0.5 mm) stainless steel moulds, each mould was individually coated in a plastic film (cling film) in order to prevent the MKPC binder bonding to steel [65] as shown in Fig. 3.1. As soon as the samples were cast, they were repeatedly tapped on a hard surface to remove any entrained air bubbles. The cast mould was placed inside a plastic sample bag and cured in an environment chamber at 20 °C and 95 % relative humidity. After two days, the MKPC cubes were demoulded and returned to the chamber. Compressive strength was determined at 3, 7 and 28 days curing ages, using a Controls Automax 5.0 testing machine at a load rate of 0.25 MPa/s. The values reported correspond to an average of three measurements, the calculated error bars are equivalent to ± 1 standard deviation. The compressive strength method was based to the British/European Standard (BS EN 12390-3:2009). The compressive strength method involved placing the cube specimens on clean, dry platens loaded perpendicular to the casting face [66]. The load rate chosen throughout these experiments was lower than the recommended load rate 0.6 ± 0.2 MPa/s. After compression, the failure mode was assessed to determine if the specimen passed or failed. To pass, the cube specimen should exhibit shearing of all four sides, the reader is referred to BS EN 12390-3:2009 [62] for depictions of failed compression modes.

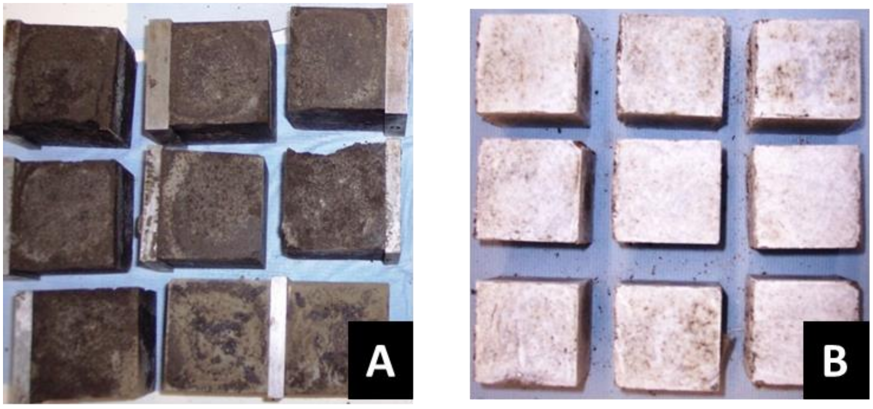

Fig. 3.1. FA/MKPC cubes at day 2 curing from: (A) stainless steel moulds and (B) plastic lined stainless steel moulds

3.3.2 Fourier-transform infrared spectroscopy

Fourier-transform infrared spectroscopy is a useful analytical technique used to identify the structure of a compound, as no compound will have exactly the same FT-IR spectrum [67]. IR radiation (mid-IR between 4000 – 500 cm^{-1} [68]) creates a vibrational response (above the natural bond vibration) in a molecule when the IR radiation is at the correct frequency and can be absorbed, it results in the stretching or bending of covalent bonds [67]. A molecule will only absorb a particular frequency, which means that FT-IR spectroscopy can detect similar bonds in a wide range of compounds, for example C = O bonds absorb the IR radiation in the range of 1800 – 1650 cm^{-1} [67]. However, only bonds that are IR active (i.e. have a dipole moment that varies with the vibration) can be detected [69].

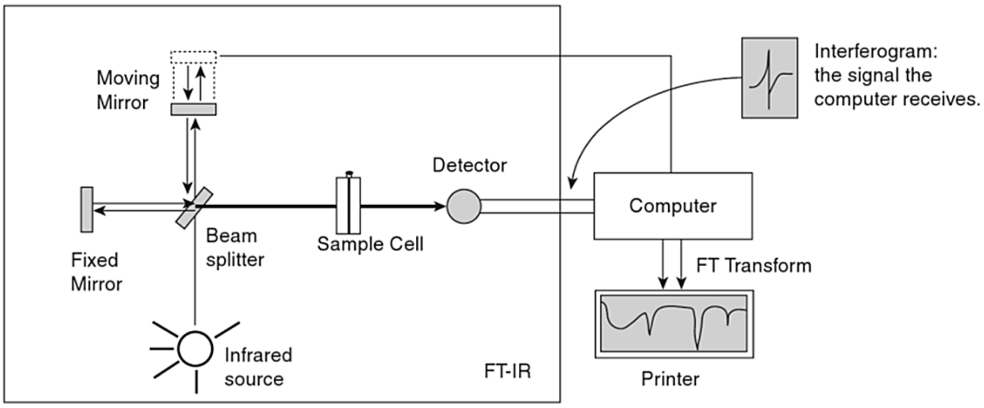

Fig. 3.2. Schematic of a Michelson interferometer extracted from [67]

The principle of FT-IR spectroscopy (Fig. 3.2) involves an IR source being passed through a beam splitter, which is a mirror angled at 45° to the IR source. The beam splitter creates two perpendicular beams (i.e. at 90° to each other) [70]. The deflected beam is sent to a fixed mirror, where it is returned to the beam splitter. The undeflected beam continues to the moving mirror and is also returned to the beam splitter, however the moving mirror creates different wavelengths within the undeflected beam [67]. As the two beams return to the beam splitter they recombine to a form single beam that contains both constructive and deconstructive interferences as a result of the moving mirror [70]. This beam is referred to as the interferogram and contains all of the incident IR radiation but with a wide range of wavelengths. The interferogram then passes through the sample, which immediately absorbs wavelengths corresponding to the frequencies within the sample [67]. As the transmitted interferogram reaches the detector it contains the information of the absorbed frequencies from within the sample, the signal is processed and absorbed frequencies extracted using Fourier-transform, which creates an FT-IR spectrum. Prior to sample collection, a background sample is collected in order to detect the presence of CO_2 and water vapour, which can then be automatically extracted from the FT-IR spectrum of the sample [67]. The units of the spectrum are recorded in wavenumbers (number of cycles per centimetre) and the % transmittance, which is the measure of IR radiation transmitted by the sample [68].

3.3.2.1 Experimental parameters

In Chapter 8, Fourier-transform infrared spectroscopy (FT-IR) was carried out using a Perkin Elmer 2000 FTIR spectrometer recording % transmittance against the wavenumber (cm^{-1}) between 4000 - 500 cm^{-1}. Samples were prepared according to the KBr pellet method [68, 70], at 1 wt. % loading where 2 mg of a sample is ground into 200 mg KBr.

3.3.3 Isothermal calorimetry

The principle of isothermal calorimetry (IC) is to measure the heat of a reaction in a non-invasive and non-destructive environment at a constant temperature (i.e. in a heat sink) [71]. It is compared to a reference sample, so that any external heat can be subtracted and records power (watts) against time by a direct measurement of the temperature changes. The data can be used to determine the kinetic and thermodynamic behaviour of a reaction [71].

Chapter 4: IC was performed on the MKPC-only and blended MKPC binders using an isothermal calorimeter (TAM Air, TA Instruments) at 20 °C. Each sample (≈ 15 g) was externally mixed for two minutes, weighed into a plastic ampoule and placed into the instrument for 7 days, using a H_2O reference calculated to match the total H_2O content of each formulation.

3.3.4 Miniature slump

The miniature-slump (or mini-slump) technique is based on the work of Kantro [72] and is ideal for small sample sizes. It requires a sheet of poly(methyl methacrylate) marked with 2x2 cm grid squares and a poly(tetrafluoroethylene) cone based on a scaled-down Abrams cone: (h = 57 mm, ø (top) = 19 mm and ø (bottom) = 38 mm)

[72]. After mixing the samples by hand for 5 minutes, the sample was poured into the cone (in the centre of the calibration grid). The cone was quickly lifted in a smooth motion and the paste was left for 30 seconds to equilibrate. A photograph was taken of the final mini-slump from directly above the sample, the slump area was then calculated using ImageJ software [73] calibrated to the grid squares (Fig. 3.2). The flow areas reported in Chapter 4 are based on the average of nine measurements, the calculated error bars are equivalent to ± 1 standard deviation.

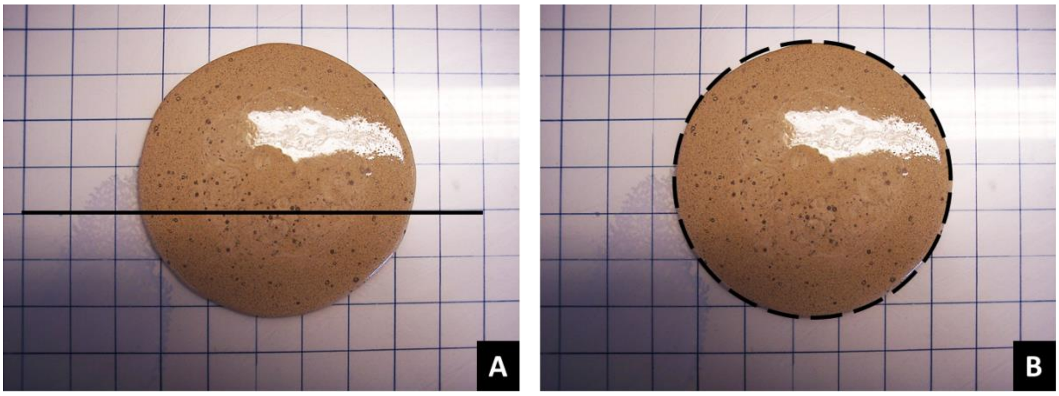

Fig. 3.3. Mini-slump calculation using ImageJ software [73]: calibrate using the 2x2 cm grid (A) and then measure the flow area (B)

3.3.5 Mössbauer spectroscopy

Mössbauer spectroscopy uses gamma radiation (from the decay of Co-57) to determine the oxidation state and co-ordination number of compounds commonly containing iron or tin as the gamma ray will only be absorbed if the sample contains a similar atom [69]. The sample is located in a fixed position and the gamma ray is moved at a constant velocity either towards the sample or away from the sample stage. This process creates an energy spectrum of gamma rays that can be absorbed by the sample [69]. In quadrupolar samples, the absorbed peak of the Mössbauer spectrum splits (quadrupole splitting), which is sensitive to the local structure and oxidation state, whilst in paramagnetic samples hyperfine Zeeman splitting occurs that results in six peaks (sextet) [69].

3.3.5.1 Experimental parameters

Chapter 7: Mössbauer spectroscopy was performed on the high temperature FA/MKPC samples to determine the Fe oxidation states using a Wissel spectrometer (50 Ci ^{57}Co(Rh) source) using 512 channels. Fe oxidation sites were assigned by fitting Lorentzian doublets and sextets using the Recoil software [74].

3.3.6 Scanning electron microscopy

To study the microstructure and composition of blended MKPC binders scanning electron microscopy (SEM) was used. In this technique, electrons generated from an electron gun (usually a tungsten filament) are accelerated between 1 - 30 keV in an electron beam onto the sample surface [75]. During the interaction between the incident beam and the sample, several signals are produced: secondary electrons, backscattered electrons and X-rays (Fig. 3.4). The volume of sample that the incident beam has contact with is referred to as the interaction volume [75].

Secondary electrons (SE) are emitted from the K-shell of the sample atoms by inelastic scattering interactions with the incident beam and have a low energy (10 to 50 eV) and consequently can only be detected in a few nanometres of the sample. Secondary electrons have the smallest sampling volume, which leads to a higher spatial resolution [75]. The secondary electrons are detected using a scintillator-photomultiplier system, the electrons are accelerated through a charged metal grid (at 10 keV), which improves the efficiency of detection as it attracts the secondary electrons. After passing through the metal grid, the electrons interact with the scintillator, which emits light. The light is transferred though a light pipe (or guide) to the scintillator where the photons are converted into pulses of electrons that can be amplified [75]. Backscattered electrons (BSE) are associated with elastic scattering (> 90°) of the incident beam and have a high energy (50 to 90 % of the incident beam) [76]. These electrons are used for imaging, diffraction and chemical identification.

The latter can be obtained through an atomic number contrast, where the high diffraction of the electrons is directly proportional to the atomic number squared [76]. Thus, heavy elements (i.e. Fe) appear much brighter than lighter elements. Backscattered electrons can be detected using the scintillator if a negative charge is applied to repel the secondary electrons. The signal can be weak because only the X-rays on a direct path can be detected [76] so longer collection times are required.

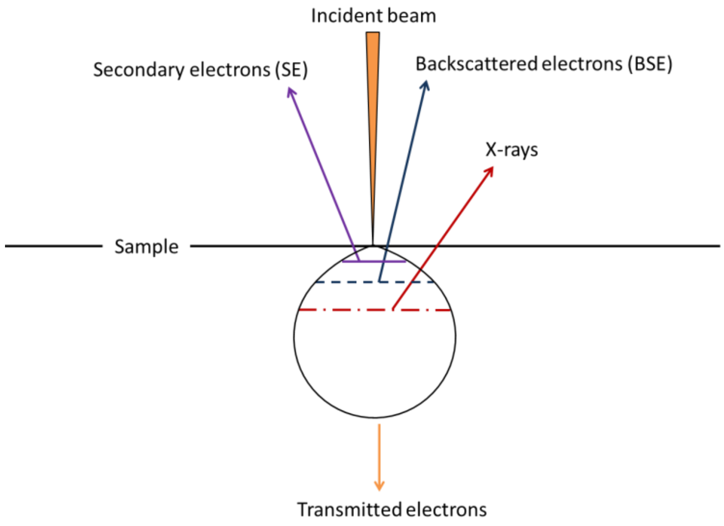

Fig. 3.4. The interaction volume of an incident beam and the regions where the signals: secondary electron, backscattered electron, and X-rays originate

3.3.6.1 Energy dispersive X-ray spectroscopy

Energy dispersive X-ray spectroscopy (EDX) is used in conjunction with the BSE mode, to provide detailed elemental analysis of the sample, the resulting spectra can be obtained as: elemental maps, EDX point or linescans. The incident electron beam ionises an electron from the inner electron shell, which is promptly replaced by a higher energy electron to fill the electron vacancy [77]. This leads to the emission of an X-ray with a characteristic energy that is detected by the energy dispersive spectrometer and can be associated with the element that is was produced from [75]. For this analytical technique the volume of material contributing to X-rays (i.e. sampling volume) is the same order of the interaction volume [76].

3.3.6.2 Experimental parameters

Samples were sectioned using an Isomet saw, encapsulated in resin and left to harden for 24 hours. The resin was then ground using grit paper ascending through grit sizes 240, 600, 800 and 1200 until the cement surface had been exposed. The sample was then polished using Isopropyl alcohol (IPA) and diamond pastes decreasing from 6, 3, 1 and 0.25 µm. Once the sample was polished, it was carbon coated and the sides coated with conductive paint to reduce the charge build-up on the sample.

Chapter 6: Micrographs were collected using a Jeol JSM 6400 SEM at a 20 kV accelerating voltage and a working distance of 15 mm. Elemental maps were collected using a Link ISIS EDX (energy dispersive X-ray spectrometer) detector and analysed using INCA software.

Chapters 4, 7 and 8: Micrographs were collected using a low vacuum Hitachi TM3030 analytical benchtop SEM with an integrated Bruker EDX system (Quantax 70) at 15 kV and a 7.0 mm working distance.

3.3.7 Solid-state nuclear magnetic resonance (NMR) spectroscopy

3.3.7.1 Principle

Solid-state nuclear magnetic resonance (NMR) spectroscopy is a technique that can provide detailed structural information about the atomic environments present within both crystalline and disordered phases [78]. The principle of NMR spectroscopy is to utilise the magnetic moment of nuclei with a quantum spin number greater than zero. When a nucleus is exposed to a strong magnetic field, the ground energy state is split into various energy levels that are either parallel or against the applied magnetic field (Zeeman splitting) [78]. When exposed to a pulse of plane-polarised radiofrequency radiation, the lower energy states (those parallel) absorb energy and become excited to the higher energy state but when the radiofrequency pulse is removed, the excited energy states return to the lower energy states (i.e. relaxation) and in the process emit radiofrequency radiation [79]. This induces a voltage in the spectrometer coil and is recorded as a function of time, referred to as the free induction decay (FID). The resonance frequency can then be extracted by Fourier-transform calculations [78].

The frequency of the detected resonance is dependent upon the local chemical environment and the nearest-neighbours of a nucleus. Small differences in the detected resonance frequency are related to the electron shielding of the local environment. This variation in the frequency is referred to as the chemical shift, which is reported in NMR spectra relative to an external standard reference nucleus [78, 79]. This makes NMR highly sensitive to the local environment making it useful for studying poorly crystalline materials.

3.3.7.2 Magic angle spinning (MAS)

Magic angle spinning (MAS) is a technique frequently used within solid-state NMR experiments. In the solid-state, nuclei experience resonance broadening due to: dipole-dipole interactions, chemical shift anisotropy and quadrupolar interactions [78, 79]. These interactions can be reduced or eliminated by spinning the sample rapidly (10-15 kHz) at an angle of 54.74° to the applied magnetic field [78]. Nuclei that have spins greater than ½ experience quadrupole moments as a result of the non-spherical charge distribution interacting with the electric field gradient [80]. This quadrupolar interaction typically affects the line broadening of the NMR spectra through first and second-order interactions. MAS NMR experiments can remove the first-order interactions but not those of the second-order interactions [78, 80]. The resulting spectrum is resolved into single resonances with numerous spinning side bands, the latter a side-effect of sample spinning, which complicates spectra analysis. To improve the second-order interactions spinning at multiple angles, either simultaneously in double rotation spinning or sequentially in double angle spinning [78]. Another way to improve the resolution of half-integer quadrupolar nuclei (by averaging out quadrupole effects) is to employ multiple-quantum magic angle spinning (MQMAS), which is a simple method that uses the probe to generate a 2D spectrum [80]. The requirements for this experiment are: firstly, rotating the sample around the magic angle (54.74° [78]), which removes dipolar interactions and the chemical shift anisotropy. Secondly, to correlate the multiple quantum transitions to the central transition (I = 1/2, -1/2) in order to remove the second-order interactions. [80].

3.3.7.3 Cross polarisation (CP)

Cross polarisation (CP) involves the transfer of the magnetisation from one nucleus (usually abundant ^{1}H) to another nucleus, which usually has a spin ½ and a lower abundancy (e.g. ^{31}P) [78]. One advantage of the CP experiment is that the signal to noise ratio of the spectra can be enhanced as ^{1}H nuclei have a short relaxation time, which means that a more rapid radiofrequency pulse can be used [78]. This means that more scans can be achieved in a given time compared to the direct excitement (standard) method, which improves to the signal to noise ratio [79]. The ^{1}H nucleus magnetisation is transferred to local ^{31}P environments, which means that only structures associated with hydrogen (i.e. hydrated phosphates), can be detected during CP NMR experiments. This could lead to more detailed information about the materials structure.

3.3.7.4 Experimental parameters

All ^{27}Al (spin, I = 5/2), ^{29}Si (I = 1/2) and ^{31}P (I = 1/2) MAS NMR spectra were collected at the EPSRC National Solid-state NMR Service on a Varian VNMRS 400 (9.4 T) spectrometer using o.d. zirconia rotors with either a 4 mm probe (^{27}Al, ^{31}P) or 6 mm probe for (^{29}Si). The chemical shifts of the ^{27}Al, ^{29}Si and ^{31}P spectra were referenced to external samples of 1.0 M aqueous $Al(NO_3)_3$, tetramethylsilane (TMS), and 85 % H_3PO_4, respectively.

Chapters 5, 6 and 8: ^{27}Al MAS NMR spectra were collected at 104.198 MHz and a spinning speed of 14 kHz, employing a pulse width of 1 µs (25 °), a relaxation delay of 0.2 s, and with a minimum of 7000 scans. ^{29}Si MAS NMR spectra were collected at 79.435 MHz at a spinning speed of 6.8 kHz and employed a pulse duration of 4.7 µs (90 °) and a relaxation delay of 1.0-5.0 s, with a minimum of 1200 scans. ^{31}P MAS NMR spectra were collected at 161.874 MHz at a spinning speed of 10.0 kHz with a pulse duration of 4.4 µs (90 °) and relaxation times of 10 and 300 s, with a minimum of 110 and 4 scans, respectively. ^{31}P[^{1}H] CP/MAS NMR spectra were collected at 161.874 MHz at a spinning speed of 10 kHz with a pulse duration of 4.4 µs, acquisition time of 30.0 ms at a recycle time of 1.0 s, and a minimum of 120 scans.

Chapter 7: ^{27}Al MAS NMR spectra were collected at 104.198 MHz and a spinning speed of 14 kHz, employing a pulse width of 1 µs (25 °), a relaxation delay of 0.2 s, with 1500 - 7000 scans. The ^{29}Si MAS NMR spectra were collected at 79.435 MHz at a spinning speed of 6.8 kHz, and employed a pulse duration of 6.2 µs (90 °) and a relaxation delay of 1.0 - 5.0 s, with 1660 - 54160 scans.

High field solid-state MAS NMR spectra for ^{25}Mg ($I = 5/2$) and ^{39}K ($I = 3/2$) nuclei were collected at The UK 850 MHz solid-state NMR Facility, The University of Warwick. These experiments were carried out using magnesium and potassium sources of natural abundance, where the NMR active isotopes, ^{25}Mg and ^{39}K, were present at 10.1 % [81] and 93.1 % [78], respectively.

Chapters 5 and 6: Solid-state NMR spectra for ^{25}Mg and ^{39}K nuclei were collected on a Bruker Advance III 850 (19.96 T) spectrometer using 4 mm o.d. zirconia rotors. ^{25}Mg MAS NMR spectra were collected at 52.05 MHz at a spinning speed of 10.0 kHz with a pulse duration of 5.0 µs (90 °) and recycle time of 2.0 s for 5800 scans. ^{25}Mg MAS NMR chemical shifts were referenced to an external sample of MgO; the chemical shift of MgO (26 ppm) is defined with respect to the hydrated Mg^{2+} ion at $\delta = 0$ ppm as a primary reference [78]. ^{39}K MAS NMR spectra were collected using an echo sequence at 39.7 MHz, spectra were collected at a spinning speed of 15.0 kHz, a pulse duration of 15.0 µs (90 °) and a recycle time of 2.0 s for 29900 scans. ^{39}K MAS NMR chemical shifts were referenced to solid KBr, which has a chemical shift of 0 ppm with respect to the hydrated K^{+} ion [82]. ^{25}Mg and ^{39}K simulations were performed using

Bruker TopSpin 3.2 software [83] considering the second-order quadrupolar interaction for the central transition only.

3.3.8 Thermal analysis

Several thermal analysis techniques were used to determine the thermal dehydration/contraction behaviour of MKPC binders and the polymorphic events associated with the dehydration of struvite-K, which were: thermogravimetric analysis, differential thermogravimetric analysis, differential thermal analysis and dilatometry (also referred to as thermomechanical analysis) [69].

Thermogravimetric analysis (TGA) is an analytical technique used to measure the mass loss of a sample as a function of a controlled heating programme under a controlled atmosphere (usually N_2). Only thermal events associated will mass loss are detected i.e. dehydration, which are usually observed over a distinct temperature range [84]. Differential thermogravimetric analysis (DTG) is the derivative of the TGA, where extra information can be extracted from the TGA data in order to further distinguish the thermal events, e.g. the separation of overlapping thermal events [84]. Differential thermal analysis (DTA) is a technique that measures the thermal response from a sample compared to that of an inert reference during a controlled heating or cooling programme [85]. The sample temperature will be equal to the inert reference until the occurrence of a thermal event (exothermic or endothermic), whereupon the temperature difference is recorded [69]. One advantage of using the DTA technique is the additional detection of thermal events with no associated mass loss, e.g. polymorphic transitions [69].

Dilatometry is a technique that measures linear changes in a sample during a controlled heating/cooling temperature programme that can detect contraction and expansion (i.e. volume changes) [69]. The linear changes of a sample is calibrated to an internal micrometer, whilst the temperature is calibrated to a standard material that was exposed to the same experimental conditions [86].

3.3.8.1 Experimental parameters

Chapters 4 and 7: Thermal analysis data were collected using Pyris 1 TGA in alumina crucibles under a N_2 atmosphere at 10 °C/min, up to 1000 °C. In Chapter 7, dilatometry data was collected using a NETZSCH DIL 402 C dilatometer between 20 - 1200 °C at 10 °C/min under a constant 50 mN load in air, using cylindrical specimens of $ø = 8.5 \pm 0.1$ mm and $l = 5.7 \pm 0.2$ mm.

Chapter 5: Thermal analysis data of pure struvite-K were collected using Pyris 1 TGA and Perkin Elmer DTA 7 instruments, in alumina crucibles under a N_2 atmosphere at 10 °C/min, up to 1000 °C.

Chapter 8: Thermal analysis data were collected using a Perkin Elmer TGA 4000 instrument in alumina crucibles under a N_2 atmosphere at 10 °C/min, up to 500 °C. Prior to the experiment run, the samples were held at 30 °C for 30 minutes to remove any free water.

3.3.9 Vicat

A Mastrad E040 automatic vicat apparatus was used to determine the initial and final set of each cement batch. At time = 0 hrs, the wet cement slurry was poured into a 70 mm diameter mould placed on a Perspex plate. A 1.13 mm diameter needle set in free fall mode was used for penetrating the cement every 15 minutes over a total of 41 penetrations. The depth of penetration was automatically recorded onto paper.

3.3.10 X-ray diffraction

X-ray diffraction (XRD) is an analytical technique that provides structural information allowing identification of the component crystalline phases of a material. X-rays (referred to as monochromatic X-rays) are generated via contact between an electron beam and a metal target (e.g. Cu or Mo). In the Cu target, the incident electron beam excites an inner shell electron (1s), immediately afterwards an electron from higher atomic shell (2p) is demoted to the inner shell. The energy difference is balanced by the emission of characteristic X-rays, which for Cu is a combination of Kα_1 and Kα_2, producing an average wavelength of 1.5418 Å [69]. The Kα_2 contributions can be removed from the diffraction pattern by utilising a monochromator (e.g. Ge(111)), which produces a pure Kα_1 X-ray of 1.5406 Å. When a sample is exposed to X-rays, the incident X-ray interacts with atoms of a crystal structure in lattice planes (described by Miller indices, *hkl*) that act as a semi-transparent mirror. The interplanar difference between the lattice planes is referred to as the d spacing [69]. When an incident X-ray is diffracted off a lattice plane, the angle of the diffracted X-ray is equal to the incident X-ray (θ). In order to satisfy Bragg's Law ($n\lambda = 2d \sin\theta$, Fig. 3.5), diffracted X-rays are only in phase and interfere constructively when the distance between two incident X-rays (on different lattice planes) is a whole integer (n) [65]. A diffraction pattern is generated by detecting the intense diffracted X-ray, which is plotted against the diffraction angle (2θ).

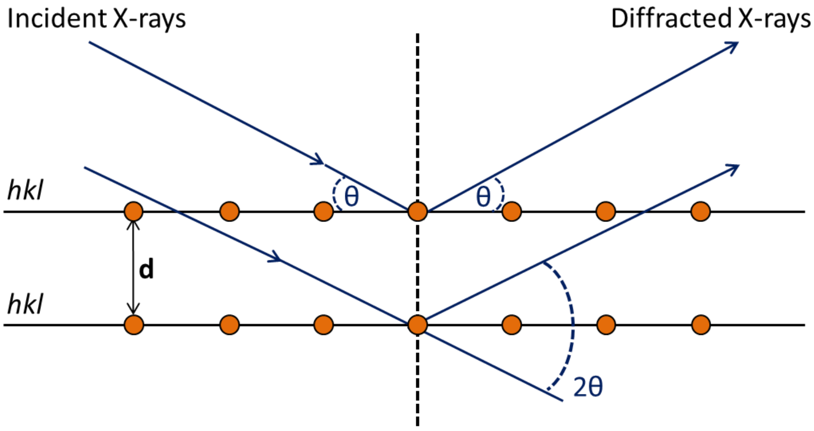

Fig. 3.5. Derivation of Bragg's Law, $n\lambda = 2d \sin\theta$

3.3.10.1 Experimental parameters

3.3.10.1.1 Powder X-ray diffraction (XRD)

Hardened paste samples cured for 28 days were crushed and subsequently ground using an agate mortar and passed through a 63 µm brass sieve prior to powder XRD analysis. All diffraction patterns were analysed using the STOE WinXPOW 2.1 software using the PDF2 database from the International Centre for Diffraction Data (ICDD) [87].

Chapters 4, 6 and 8: Powder X-ray diffraction (XRD) patterns were collected between 10° < 2θ < 50° using a STOE STADI P diffractometer with an image plate detector in transmission mode. The diffractometer uses a Ge(111) monochromator (and produces a high purity Cu $K_{\alpha 1}$ (1.5406 Å) source.

Chapter 7: Powder X-ray diffraction patterns were collected between 10° < 2θ < 50° using a Bruker D2 PHASER diffractometer with a LYNXEYE detector and a Cu $K_{\alpha(1+2)}$ (1.5418 Å) source using a step size of 0.02° 2θ and a count time of 1 s per step, the Cu $K_{\alpha 2}$ reflections were stripped using Bruker software, DIFFRAC.EVA.

3.3.10.1.2 High temperature XRD (HTXRD)

Chapter 5: In situ high temperature X-ray diffraction (HTXRD) patterns were collected of pure struvite-K between 10° < 2θ < 50° in reflection mode using a Siemens D5000 diffractometer with no primary monochromator to strip the Cu contributions, as such the X-ray source was an average Cu $K_{\alpha(1+2)}$ wavelength of 1.5418 Å. source The diffraction pattern was collected at a step size of 0.02° 2θ, and a count time of 3 s per step, with the Cu $K_{\alpha 2}$ reflections removed by DIFFRAC Plus software. The sample was mounted onto a platinum platform. HTXRD data were collected at temperatures: 20, 400, 800, 1000 and 1200 °C, the sample was held at the desired temperature during analysis and then ramped at 10 °C/min until the next analysis temperature was reached.

3.3.10.1.3 Synchrotron X-ray diffraction (SXRD)

Synchrotron X-ray diffraction (SXRD) operates on the same principle of powder XRD but provides high resolution diffraction patterns using synchrotron radiation, which is very intense. The electrons are generated in an electron gun and accelerated up to high speeds by the linear accelerator (known as the linac) and the booster synchrotron into the large storage ring, where the path of the electrons are directed by the straight and bending magnets [88]. Synchrotron radiation is produced when the path of the electrons in the storage ring is changed and the electrons lose energy, similar to bremsstrahlung radiation in an X-ray tube, which is channelled into beamlines. The straight sections contain insertion devices that have alternating magnetic fields, this causes the electrons to oscillate and produces more synchrotron radiation (through braking radiation). Two important insertion devices are the undulators and wigglers, whose magnetic field is in the vertical, which deflects the high energy electrons horizontally creating synchrotron radiation that is linearly polarised [88].

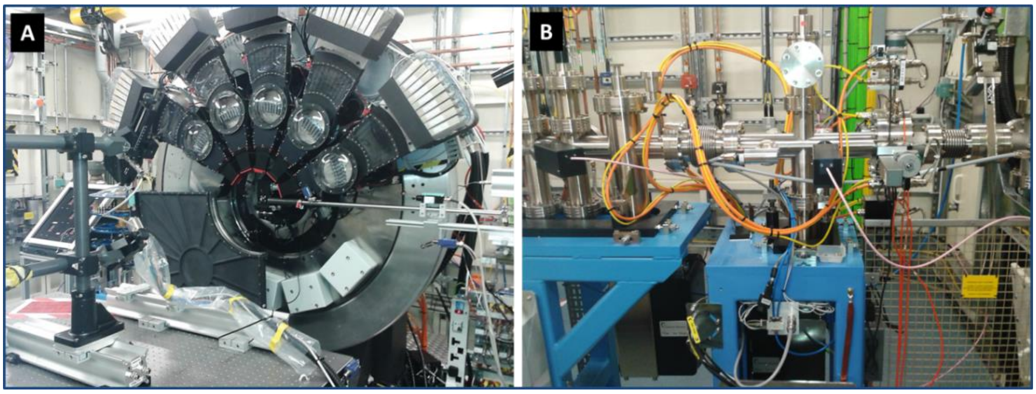

Fig. 3.6. Synchrotron X-ray diffraction, Beam I11 at Diamond Light Source, UK: (A) XRD instrument and (B) the X-ray beam

Chapter 4: Time-resolved SXRD (λ = 0.825700 Å) was conducted on beamline I11 at the Diamond Light Source (DLS) using the position sensitive detector on fresh FA/MKPC and GBFS/MKPC pastes (w/s = 0.24), each scan time was typically ≈ 2 min. In a disposable container, H_3BO_3 was added to H_2O and stirred for 1 min after which, the dry precursors (MgO, KH_2PO_4 and FA/GBFS) were added and mixed for an additional 2 minutes. Using capillary action, the cement paste was drawn into Kapton® polyimide tubes (ø = 0.8 µm) and was flamed sealed in a borosilicate capillary tube (ø = 1 mm

4 Formulation optimisation of blended MKPC binders

4.1 Introduction

In the UK, Portland cement (PC) blended with either fly ash (FA, up to 35 wt. %) or ground granulated blast furnace slag (GBFS, up to 90 wt. %) are used for the encapsulation of intermediate level waste streams [4, 5]. However, the high pH of PC based encapsulants (≈ pH 13) can promote the corrosion of Al, whilst Mg and U can corrode in the high free water environment of PCs [13, 19, 89]. Corrosion of these reactive metals leads to the formation of expansive corrosion products and hydrogen gas, which increases the internal stress of the conditioned wasteform and ultimately can affect the long term stability of the waste package. The near-neutral pH, low water demand and high early strength properties [21] of magnesium potassium phosphate cement (MKPC) binders have established them as possible alternative encapsulant in the UK for niche waste streams, e.g. for reactive metals (Al, Mg and U) with the potential to reduce corrosion within the conditioned wasteforms [15, 17-19].

Initial studies have optimised the FA/MKPC system in order to identify a workable formulation envelope for UK requirements and to accommodate for scale-up and provide the optimal plant operation allowances [18, 19]. It is reported that the micro-structure and mechanical properties of MKPC binders are sensitive to the water-to-solids (w/s) ratio. In low w/s binders, residual KH_2PO_4 can react by the formation of amorphous magnesium phosphate phase with a lower bound water content [90]. This phase is reported to seal pores, forming a continuous and uninterrupted cementitious matrix [91]. Whilst in high w/s ratio binders, a highly crystalline matrix is formed with an excess of unreacted water that gradually evaporates during aging. This can result in a porous structure that has a detrimental effect on the mechanical properties of the cement [90, 92]. The theoretical paste saturation was calculated by Covill *et al.* to be a 0.26 w/s ratio [18], which allows the acid-base reaction to proceed until completion. This formulation produced compressive strength values (≈ 25 MPa at day 28 curing) that exceed the recommended minimum for a typical nuclear waste package (>4 MPa) based on a 500 L stainless steel drum [93]. This FA/MKPC formulation was described as mechanically and chemically stable as no differences were observed in XRD or TGA data after curing for 360 days, which indicated that this formulation would be suitable for waste encapsulation applications. However, no detailed analysis was provided by Covill [14] stating the effect of a varying water content on the acid-base reaction of FA/MKPC binders during the initial and early reaction periods (i.e. less than 72 hours).

As such in this chapter, the effect of water content on the physical properties and the exothermic behaviour of FA/MKPC binders was investigated to understand the reaction chemistry of the MKPC system. In conjunction with this study, MKPC binders were also blended with ground granulated blast furnace slag (GBFS) to determine if alternative supplementary cementitious materials could be utilised within the MKPC system without negative impact upon the reaction chemistry and physical properties of the hardened binders. The subsequent optimised formation will undergo long-term uranium corrosion trials (2 years) to determine their feasibility as an encapsulant within the UK nuclear industry. Results and Discussion

4.2 Results and Discussion

4.2.1 Miniature-slump

The mini-slump measurements were conducted on all of formulations tested to assess the workability of the blended MKPC binder, as it is important from an industrial deployment perspective that the encapsulant grout has sufficient workability for two reasons, firstly to ensure that the grout is pourable and remains fluid to allow for complete waste encapsulation and secondly, to allow time for plant hold-ups. The benchmark is to not set within 4 hours but to have final set within 24 hours [94]. The mini-slump results shown in Fig. 4.1 indicated that as the water to solids (w/s) ratio, increased the mini-slump flow area of the pastes also increased in both the FA/MKPC and GBFS/MKPC binders. It was observed that the GBFS/MKPC binders had a higher flow area than the FA/MKPC binders, which was unexpected. It was envisioned that the inclusion of FA in MKPC binders would enhance the workability (i.e. fluidity) more than the angular GBFS particles as a result of the “ball-bearing effect” of the spherical FA particles [18, 54, 95, 96]. The characteristics of the raw materials in part explain the differences observed in mini-slump measurements of the FA/MKPC and GBFS/MKPC binders. The FA used in this study has a finer particle size (resulting in a higher powder surface area) compared to the GBFS (as shown in Table 3.1), which is a special coarse material preferred for nuclear applications in the UK. Consequently, the FA absorbed more water than the GBFS, which reduced the overall fluidity of the FA/MKPC paste.

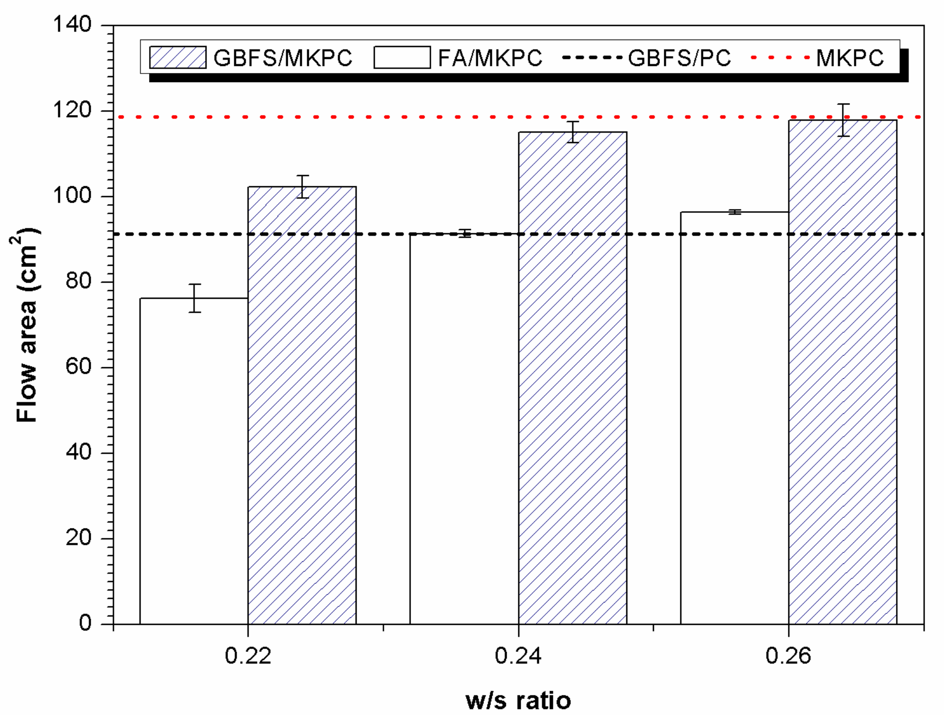

Fig. 4.1. Mini-slump flow areas of fresh FA/MKPC and GBFS/MKPC pastes at 0.22, 0.24 and 0.26 w/s ratios compared to a BFS/PC grout (0.35 w/s) represented by the dashed line

Only minor differences were observed in the flow areas of the 0.24 and 0.26 w/s ratios in both the FA/MKPC and GBFS/MKPC binders, at 5 cm^2 and 3 cm^2, respectively. This indicated that utilising the 0.24 w/s ratio would generate an 8 % reduction in the water content without having a negative impact upon the workability and therefore deployment of the cement in industrial applications. Additionally, any reduction in the water content of the cement encapsulant is expected to reduce the rates of reactive metal corrosion, due to less water being available to take part in the corrosion reactions [19]. For reference, an MKPC-only system (for a 0.24 w/s [97], represented by the dotted red line) was found to achieve a flow area of 118.7 ± 7.4 cm^2. This implies that the inclusion of SCMs into MKPC binders resulted in an increased water demand, and consequently reduced the fluidity, however, more suitable working times were achieved (Table 4.1). The final setting time of MKPC-only binders was found to occur at 1.25 hours and the sample was hot to the touch, whereas in blended binders the initial set is delayed up to 5 hours and the final set extended to 7.5 hours (Table 4.1). The FA/MKPC and GBFS/MKPC mini-slump results were also compared to a standard Portland cement (PC) composite grout (3:1 GBFS/PC, 0.35 w/s) that is typically used in the UK nuclear industry. This PC based encapsulant achieved a mini-slump flow area of 91.3 ± 1.7 cm^2, depicted by the dashed black line in Fig. 4.1. The MKPC formulations achieved an equivalent (or greater) flow area that the industry standard grout with the exception of the 0.22 w/s FA/MKPC formulation, and as such it can be concluded that the workability of these binders would be suitable for industrial applications.

Table 4.1. Setting time of FA/MKPC and GBFS/MKPC determined using vicat measurements

Sample	w/s	pH (0 hrs.)	pH (4 hrs.)	Initial set (hrs.) ± 0.3	Final set (hrs.) ± 0.3
FA/MKPC	0.22	5.2	6.2	2.0	6.0
FA/MKPC	0.24	5.2	6.2	4.5	7.0
FA/MKPC	0.26	5.5	6.3	5.0	7.5
GBFS/MKPC	0.22	5.5	6.2	1.0	4.5
GBFS/MKPC	0.24	5.4	6.2	2.0	6.0
GBFS/MKPC	0.26	5.4	6.1	3.5	7.0

4.2.2 Powder X-ray diffraction

The X-ray diffraction patterns of the hardened FA/MKPC and GBFS/MKPC binders are shown in Fig. 4.2 and Fig. 4.3. Diffuse scattering was identified in the FA/MKPC binder between 15° $< 2\theta <$25° and in the GBFS/MKPC binder between 25° $< 2\theta <$ 35°, which is associated with the glassy fractions present in the FA (aluminosilicate) and the GBFS (calcium aluminosilicate) precursors. Struvite-K ($MgKPO_4{\cdot}6H_2O$, powder diffraction file (PDF) #75-1076) was observed to be the main crystalline phase, with traces of periclase (MgO, PDF #45-0946) identified in all formulations investigated. Unreacted MgO was observed in the diffraction patterns for FA/MKPC and GBFS/MKPC due to the MgO being added in excess into the cement binders. This was for two reasons, firstly, to ensure that the phosphate source (KH_2PO_4) was fully consumed in the acid-base reaction and secondly, to provide nucleation sites (around unreacted MgO particles) for the formation of struvite-K [37-39].

In the FA/MKPC w/s ratio binders, quartz (SiO_2, PDF #11-0252), mullite ($3Al_2O_3.2SiO_2$, PDF #15-0776) and hematite (Fe_2O_3, PDF #87-1164) were identified, whilst åkermanite ($Ca_2MgSi_2O_7$, PDF #76-0841) reflections were observed in the GBFS/MKPC w/s ratio binders, which are typical crystalline phases present in these materials. The phase assemblage in the FA/MKPC and GBFS/MKPC binders in Fig. 4.2-4.3 did not appear to change with a varying w/s ratio, however the relative intensity of the struvite-K reflections increased with an increasing water content when compared to the relative intensity of the main periclase reflection at 42.9° = 2θ. Hall *et al.* [90] describes this observation to be the result of increased formation of the cementitious phase, struvite-K. The inclusion of FA and GBFS did not affect the crystalline properties of blended MKPC binders, as no additional crystalline phases were detected nor the crystallisation of struvite-K affected. The results presented suggest that blended MKPC binders are chemically stable to small alterations in the water content and the SCMs used, which concurs with previous work performed by Covill *et al.* [18].

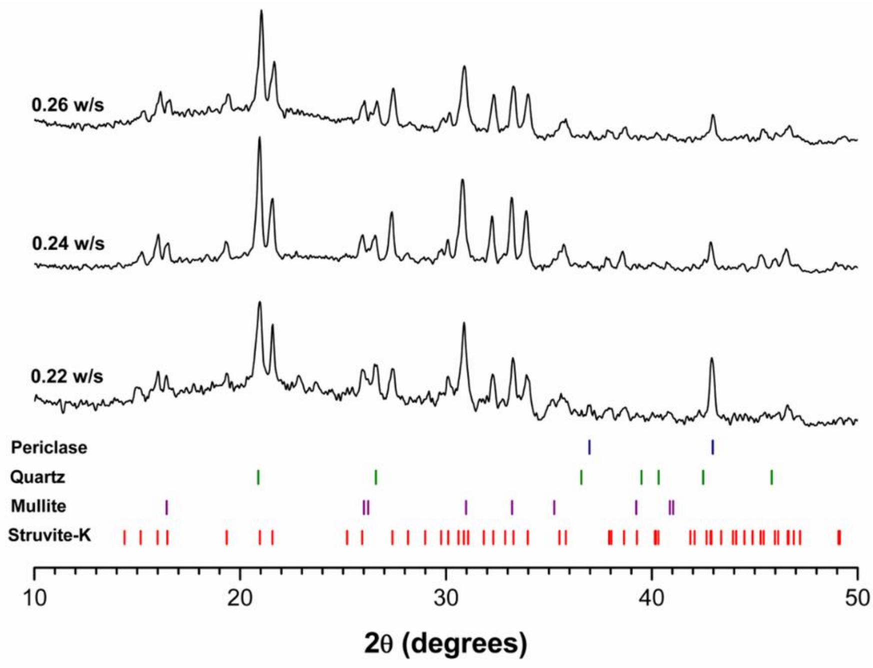

Fig. 4.2. X-ray diffraction patterns of FA/MKPC pastes at various w/s ratio after 7 days curing

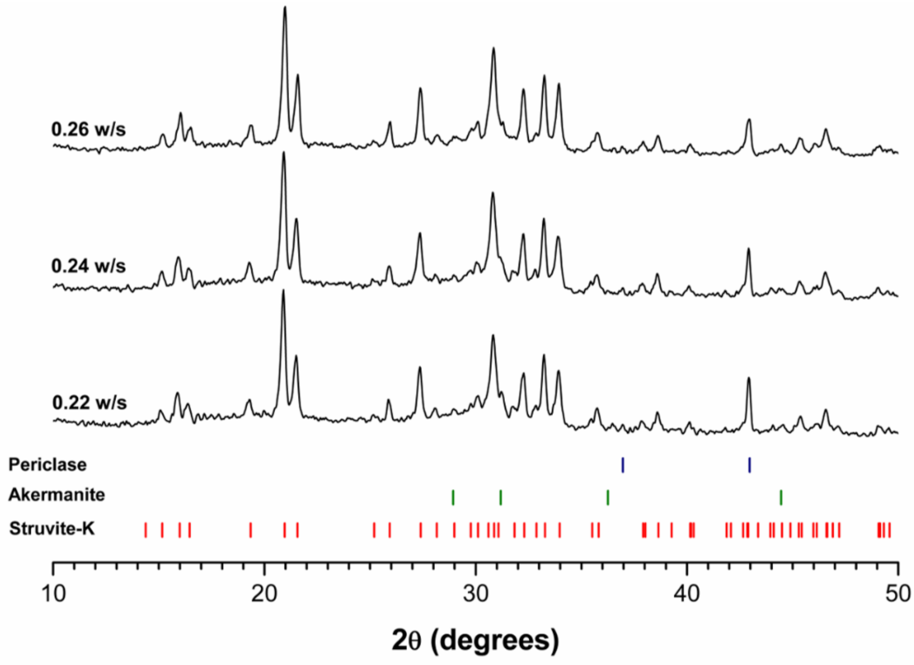

Fig. 4.3. X-ray diffractogram of GBFS/MKPC pastes at various w/s ratio after 7 days curing

4.2.3 Thermal analysis

The dehydration behaviour of the FA/MKPC and GBFS/MKPC binders, shown in Fig. 4.4- Fig. 4.5, was found to be comparable to pure struvite-K systems [98]. A large mass loss occurred between 50 and 150 °C, which was associated with the one-step dehydration of $MgKPO_4{\cdot}6H_2O$ to $MgKPO_4$ (Eq. 8). The TGA data highlighted that no secondary mass loss events occurred in the two binders. The effect of varying the water content on the TGA of the hardened FA/MKPC and GBFS/MKPC binders was found to result in minor changes in the total mass loss from the dehydration of struvite-K, which is in agreement with the XRD data, as the w/s ratio increased in the blended MKPC binders so does the struvite-K formation.

$$MgKPO_4{\cdot}6H_2O_{(s)} \rightarrow MgKPO_{4\,(s)} + 6H_2O_{(g)} \qquad \text{Eq. 5}$$

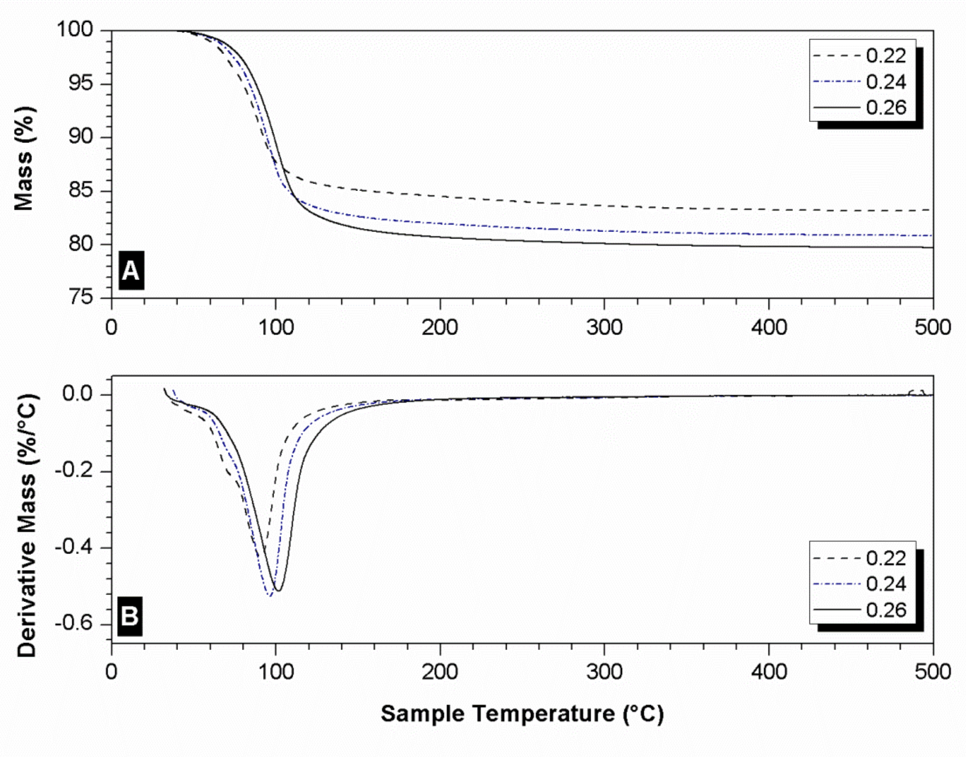

Fig. 4.4. TGA (A) and DTG (B) traces of hardened FA/MKPC pastes after 28 days curing, at various w/s ratios

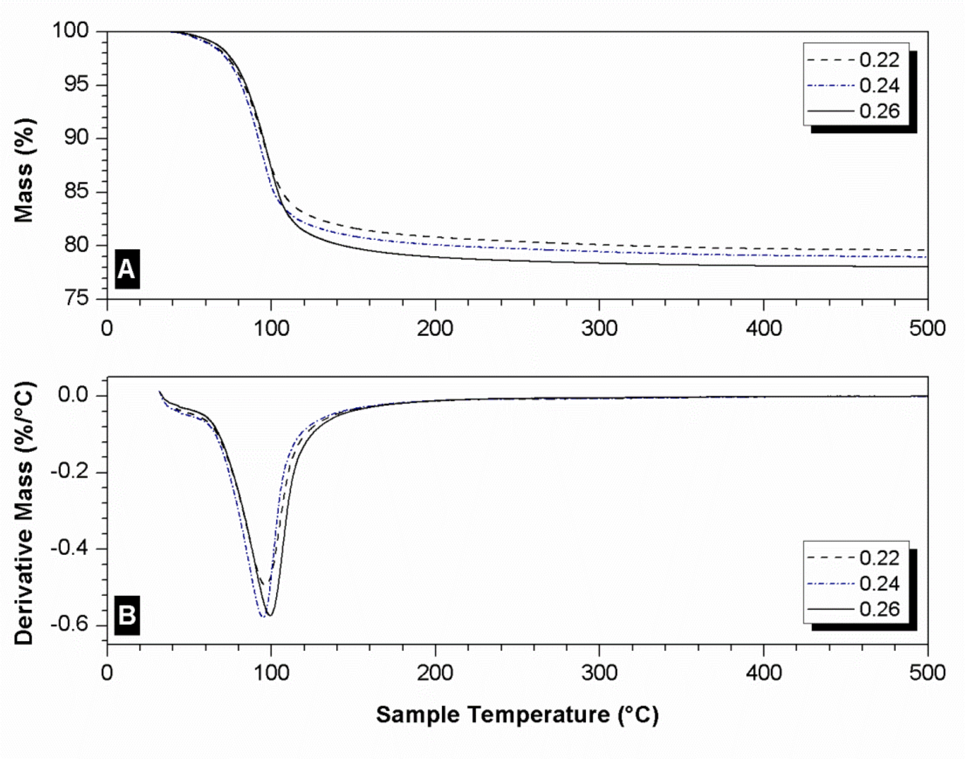

Fig. 4.5. TGA (A) and DTG (B) traces of hardened GBFS/MKPC pastes after 28 days curing, at various w/s ratios

The differential thermogravimetry (DTG) data for the formulations, shown in Fig. 4.4-Fig. 4.5, highlight that the maximum mass loss due to dehydration of struvite-K occurred at ≈ 100 °C. The DTG plots suggest that the temperature for maximum mass loss slightly increases with the increasing w/s ratio. This could result from longer dehydration times due to the presence of more water. The maximum mass loss was greatest for the 0.24 w/s ratio in both FA/MKPC and GBFS/MKPC binders, however, the 0.26 w/s and 0.24 w/s ratios are likely to be within statistical error. This suggests that in these w/s ratios a similar quantity of struvite-K was formed. However, there was large a difference between the former w/s ratios and the 0.22 w/s sample for both the FA/MKPC and GBFS/MKPC systems. The varied DTG dehydration behaviour of the FA/MKPC binders below 80 °C is due to the presence of free water in the samples. To eliminate free water TGA samples should be held at room temperature for 30 minutes under a N_2 gas flow.

4.2.4 Compressive strength

The compressive strength (CS) of blended MKPC binders was found to vary as a function of both the supplementary cementitious material used and the water content, as shown in Fig. 4.6. The CS values for FA/MKPC binders reached between 20 to 25 MPa (for all w/s ratios studied at day 28 curing), which is comparable to literature based on similar systems [18, 89]. However, the GBFS/MKPC binders were observed to have superior mechanical properties compared to the FA/MKPC binders with the CS values ranged between 25 to 36 MPa for the w/s ratios at day 28 curing. The most noteworthy difference between the two blended systems occurred in the 0.22 w/s formulation (at day 28 curing), where the FA/MKPC binder achieved a CS value of 16.4 MPa ± 0.3 MPa and the GBFS/MKPC binder achieved a CS value of 35.6 MPa ± 1.4 MPa. It is postulated that the difference in mechanical properties can be explained by the powder properties of FA and GBFS, as reported in Table 3.1. Firstly, the FA has a much narrower particle size distribution and larger surface area (2258 m^2/kg) than the GBFS (993 m^2/kg). This results in FA having a greater water demand, which could be detriment to struvite-K formation in the FA/MKPC binder. Secondly, the difference could be due to the particle packing capabilities of FA (spherical particles) and GBFS (angular particle), where the latter has a better physical interlocking in the MKPC binder than FA [99]. However, these properties cannot be solely attributed to the mechanical performance differences observed between the FA/MKPC and GBFS/MKPC binders in the 0.22 w/s (≈ 15 MPa) and 0.24 w/s (≈ 10 MPa) formulations.

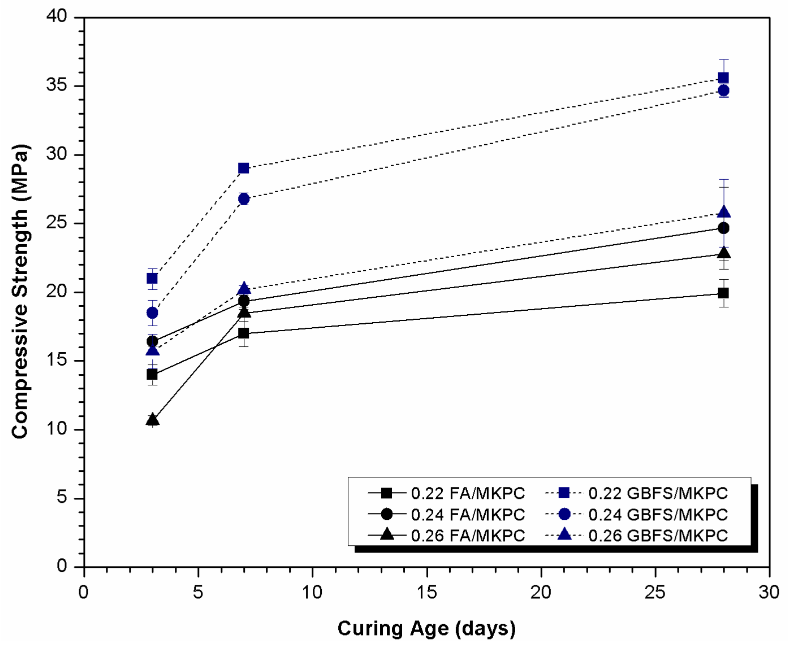

Fig. 4.6. Compressive strength of FA/MKPC and GBFS/MKPC hardened pastes cured for up to 28 days, as a function of the w/s ratio

Despite the differences in CS values, all of the FA/MKPC and GBFS/MKPC w/s formulations exceeded the minimum required compressive strength for a typical UK nuclear waste package of >4 MPa (based on a 500 L stainless steel drum) [93]. The effect of varying the w/s ratio in the MKPC binders appeared to be variable depending upon the supplementary cementitious material. For the FA/MKPC binders, the 0.24 and 0.26 w/s formulations achieved similar CS results, with the lowest strength attributed to the water deficient 0.22 w/s sample, which could be the result of a high FA water demand. Whilst in the GBFS/MKPC samples, the highest strength was achieved by the 0.22 and 0.24 w/s formulations. This was consistent with the literature [63, 65] that high water content samples have lower mechanical properties due to an increased porosity. The findings of this study indicate that the 0.24 w/s formulation would form a suitable encapsulant and should undergo further investigations, as it is not practical to study all six formulations. As such, the remainder of this work will focus on FA/MPKC and GBFS/MKPC binder at a 0.24 w/s ratio.

4.2.5 Early age hydration behaviour

To determine the effect of water content on the hydration characteristics of fresh FA/MKPC and GBFS/MKPC pastes, isothermal calorimetry (IC) was conducted on the 0.22, 0.24 and 0.26 w/s formulations. Whilst time-resolved synchrotron XRD was undertaken on the preferred w/s formulation (0.24 w/s) in order to elucidate the role of SCMs (i.e. inert filler or chemical participants) independent of the water content within the MKPC system. This was performed in conjunction with the IC of an MKPC-only (0.24 w/s) binder, which was used as a reference.

4.2.5.1 MKPC-only

In the calorimetric traces (heat flow and cumulative) of the MKPC-only binder (Fig. 4.7), a rapid exothermic peak was observed where the maximum heat flow achieved around ≈ 1 hr, a second exothermic event occurred between 10 to 50 hrs Fig. 4.7, which was associated with a low heat flow. The shape of the calorimetric trace of the MKPC-only sample is similar to those reported in the literature for magnesium phosphate cements (with no SCMs) [43, 100, 101]. The first exothermic peak is reported by Qiao *et al.* [101] to be associated with the acid-base reaction of the magnesium phosphate cement, i.e. dissolution of MgO and KH_2PO_4 leading to formation of struvite-K (Eq. 5-7), whilst the second exothermic peak relates to setting of the MKPC binder [101] through the formation of a continuous network [102].

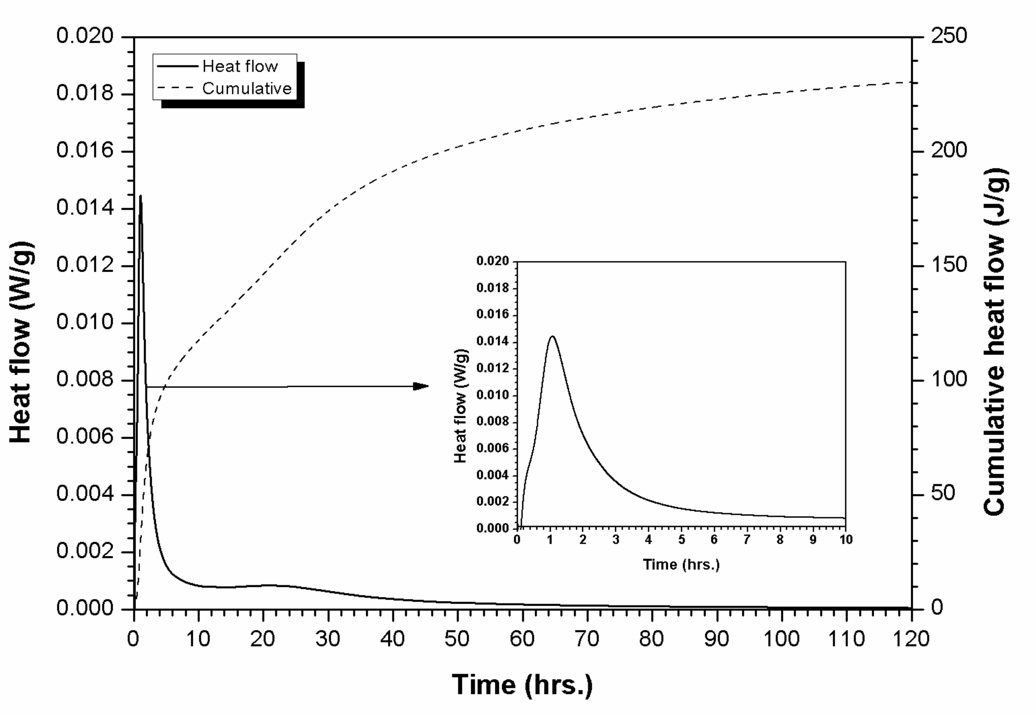

Fig. 4.7. Normalised calorimetric traces for MKPC-only at 0.24 w/s

A disparity exists between the calorimeter data presented for the MKPC-only binder (Fig. 4.7) and that in the literature, with respect to the duration of the acid-base reaction. In the literature, the cumulative heat evolution of the MKPC-only binder (and thus, acid-base reaction) was concluded after <6 hours [101], which is considerably shorter than the 50 hours cumulative heat evolution exhibited in Fig. 4.7. One possible explanation for the extension of the heat evolution could be the inclusion of 2 wt. % boric acid in the MKPC-only binder as a set retarder. This theory is supported by MAP cements (with no SCMs), where an extension of the setting time by 20 minutes was successfully achieved with the addition of 20 % borax ($Na_2B_4O_7 \cdot 10H_2O$, by phosphate weight) [44], whilst Hall *et al.* [43] further delayed the setting time of similar systems up to 80 minutes with the addition of 12.5 g of boric acid (based on a 1.5 kg batch).

4.2.5.2 FA/MKPC

4.2.5.2.1 Isothermal calorimetry

The calorimetric traces for FA/MKPC binders at w/s ratios: 0.22, 0.24 and 0.26 are presented in Fig. 4.8. The hydration behaviour of the FA/MKPC binders appeared to be comparable to the MKPC-only binder (Fig. 4.7), with two exothermic peaks detected, the first (sharp and short) corresponded to the dissolution-precipitation of struvite-K, whilst the second (broad and long) related to the extended hydration through the formation of an interconnected cement paste [100]. This signifies that the inclusion of FA did not affect the typical two-step hydration behaviour of MKPCs as observed in this study and reported in the literature [100, 101].

Differences were observed between the heat flow/duration of MKPC-only and the FA/MKPC binders, which were further amplified as the water content was increased. One fundamental explanation for this is quite simply that the FA/MKPC binders are diluted with 50 wt. % FA, meaning there are fewer reactants per gram of the IC sample compared to the MKPC-only binder and thus, resulted in a lower exothermic output. This dilution effect was further extended between the three w/s ratios, where the reactants were more diluted in the higher water content FA/MKPC sample, resulting in a lower maximum heat flow and longer reaction duration (Fig. 4.8). The maximum heat flow associated with the dissolution-precipitation of struvite-K (Fig. 4.8) around ≈ 2 hrs appeared to substantially decrease in the FA/MKPC binders with higher w/s ratios. This indicated that the 0.22 w/s FA/MKPC binder was initially the most reactive with the reaction reaching completion by 65 hours whilst the 0.26 w/s FA/MKPC binder was the least reactive and did not reach completion until 80 hours. These results indicate that there is an optimum reaction period to allow for sufficient strength forming to occur as shown in Fig. 4.6, where the lowest compressive strength (19.9 MPa at day 28) was associated with the 0.22 w/s binder, which also had the shortest cumulative heat evolution period (Fig. 4.8) of 65 hours. Using strength-forming and cumulative reaction time as an indicator for the ideal w/s formulation, the optimum FA/MKPC binders would be the 0.24 w/s ratio.

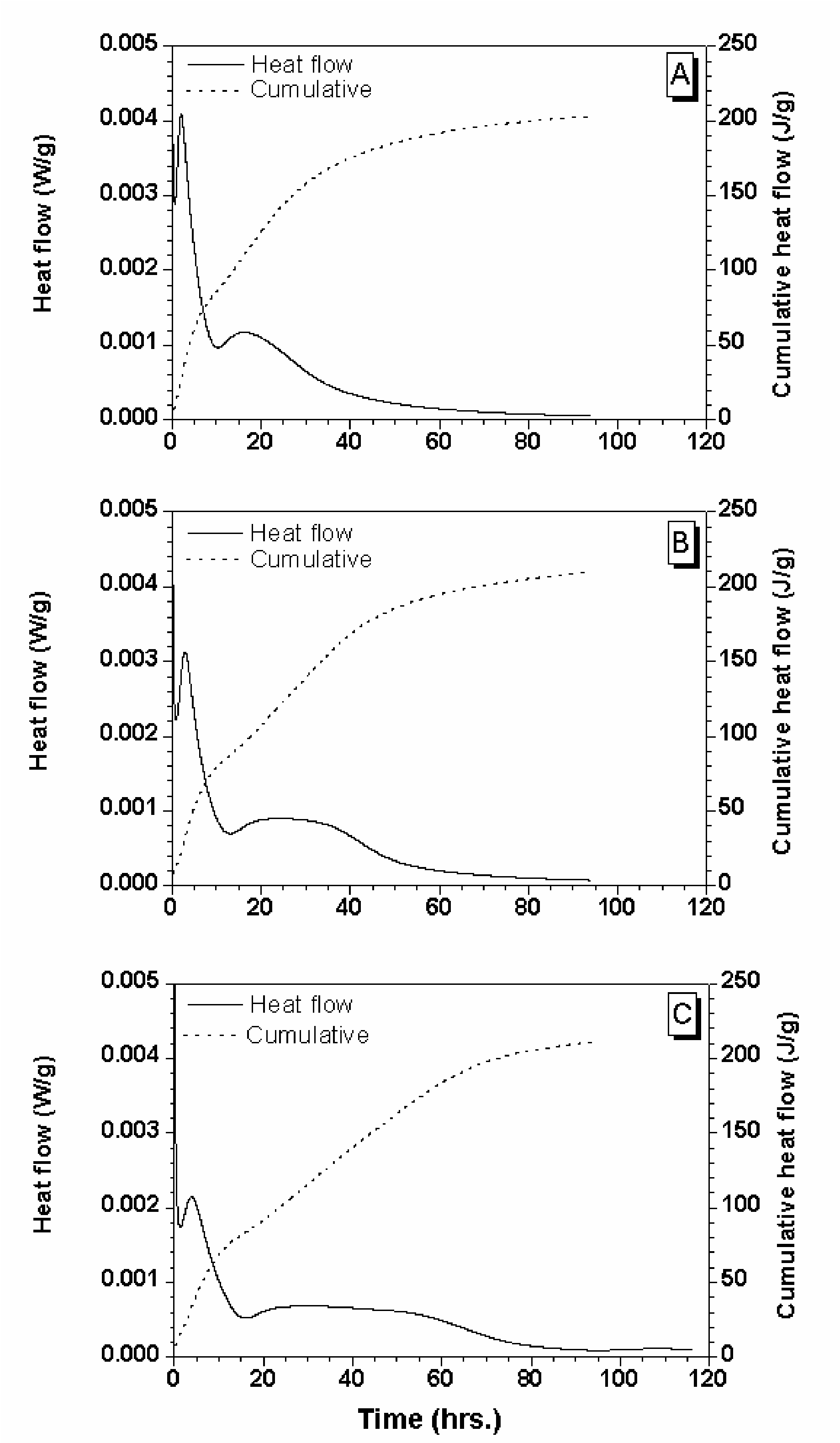

Fig. 4.8. Normalised calorimetric traces for fresh FA/MKPC pastes at (A) 0.22 w/s, (B) 0.24 w/s and (C) 0.26 w/s

4.2.5.2.1 Synchrotron X-ray diffraction (SXRD)

The hydration behaviour of the FA/MKPC binder (0.24 w/s) was observed from 0.5 to ≈ 60 hours using synchrotron X-ray diffraction (SXRD, Fig. 4.9). In the initial diffraction patterns (0.5 – 1.5 hours), only reflections associated with unreacted periclase (MgO, PDF #45-0946, [103]) and the crystalline phases present in the FA, mullite (PDF #15-0776, [104]), quartz (SiO_2, PDF #11-0252, [105]) and hematite (Fe_2O_3, PDF #87-1164, [106]) were observed. The crystalline FA phases were still evident at the latest time point (58.8 hrs), which indicated that the FA did not react within in this system/timescale. The emergence of struvite-K ($MgKPO_4 \cdot 6H_2O$, PDF #75-1076, [22]) reflections was observed at 2 hours, after which the relative intensity of struvite-K reflections increased with time (up to ≈ 60 hours), commensurate with periclase consumption.

Prior to the crystallisation of struvite-K at 2 hours, neither the phosphate reagent (KDP) nor intermediate phosphate phases were identified in the FA/MKPC diffraction patterns. To highlight this, the KDP (potassium dihydrogen phosphate, KH_2PO_4) powder diffraction file (#35-0807, [107]) was included in Fig. 4.9. This indicated that the complete dissolution of KDP occurred between the sample preparation and prior to the first diffraction pattern collected at 30 minutes. Due to the narrow Kapton tubes (ø = 0.8 mm) used, the KDP was ground slightly using a pestle and mortar to reduce the particle size, which may have increased the reactivity of the KDP compared to the calorimetry FA/MKPC sample. Although the early hydration behaviour of the FA/MKPC binder is similar to magnesium ammonium phosphate (MAP) binders, where the phosphate reagent ($NH_4H_2PO_4$) completely dissolved within 20 minutes of mixing and distinctive struvite reflections appeared after 1 hour [108]. Neiman [39] further proposes the formation of a poorly crystalline magnesium phosphate gel occurs prior to the crystallisation of struvite [39, 109], which is associated with the through-solution precipitation mechanism.

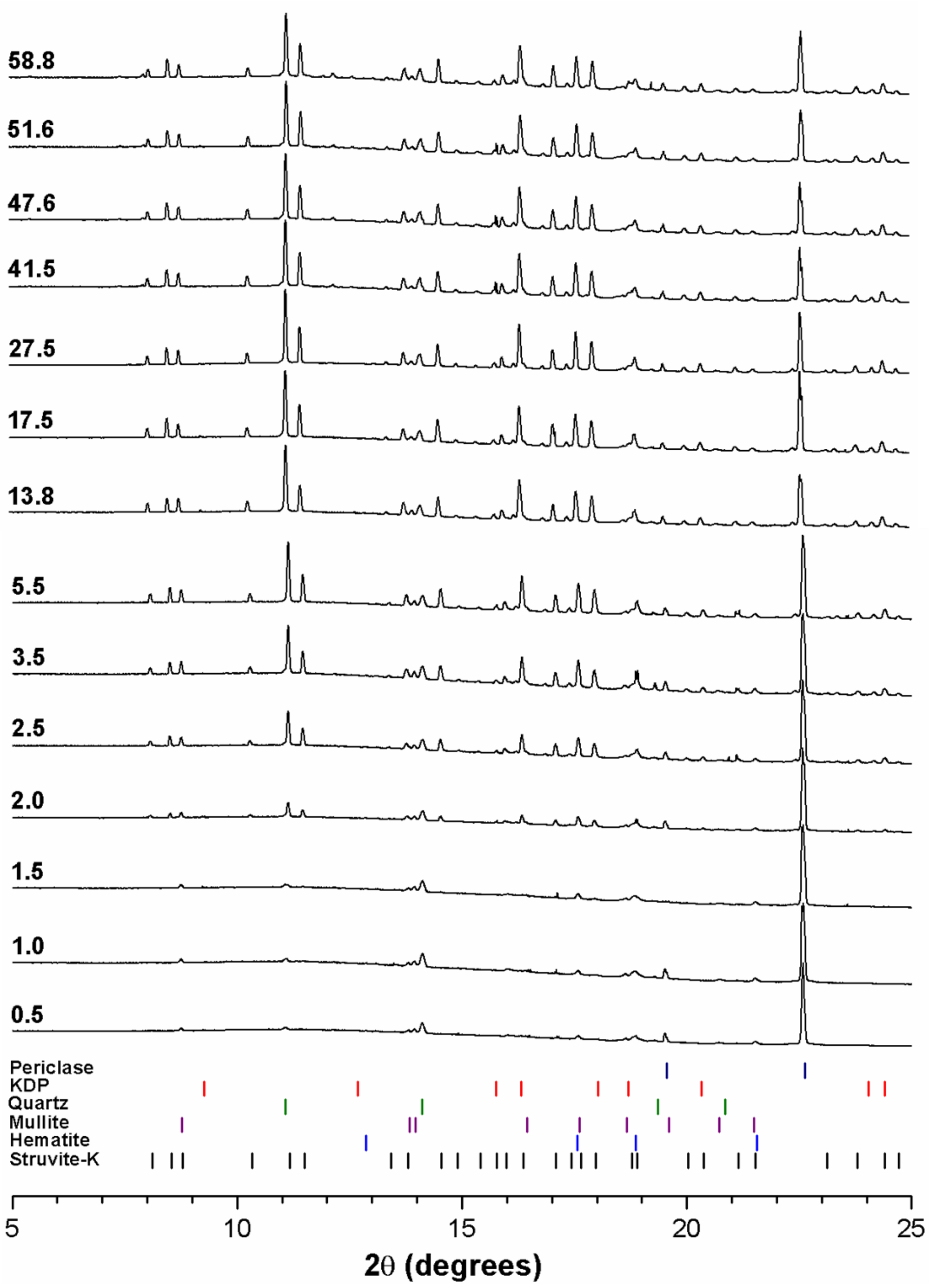

Fig. 4.9. Time resolved synchrotron X-ray diffraction of 0.24 w/s FA/MKPC binder, diffraction labels indicate the time (hrs) lapsed between sample preparation and data collection

The SXRD data (Fig. 4.9) supports the precipitation of struvite-K during the first exothermic peak in the calorimetry trace for the FA/MKPC (0.24 w/s) binder (Fig. 4.8). The relative intensity of the struvite-K reflections increased up to 13 hours, which was indicative of a continuing crystallisation process. During this time, the final set of the FA/MKPC binder was observed in the vicat measurements (Table 4.1). The second exothermic peak in Fig 4.8 occurred between 12 to ≈ 60 hours, as such this event could be attributed to the formation of an interconnected struvite-K network as part of the strength forming phase of the MKPC binder.

4.2.5.3 GBFS/MKPC

4.2.5.3.1 Isothermal calorimetry

The calorimetric traces of the GBFS/MKPC binders at 0.22, 0.24 and 0.26 w/s ratios (Fig. 4.10) clearly demonstrate a considerable difference in the hydration behaviour compared to the MKPC-only and FA/MKPC binders, where a sharp heat flow it observed for the first ≈ 6 hours followed by a slower rate of reaction. The addition of GBFS changed the reaction kinetics of the MKPC systems, although the pH of the GBFS/MKPC binders is comparable to FA/MKPC binders (Table 3.1). All GBFS/MKPC binders exhibited a substantial increase in the duration of the induction period compared to the equivalent FA/MKPC binders. Varying the water content in the GBFS/MKPC resulted in reaction delay, with time taken for the reaction to reach completion being 67, 83 and 100 hours for 0.22, 0.24 and 0.26 w/s ratios respectively. This suggests that one effect of increasing the water content in GBFS/MKPC binders is slower reaction kinetics. The compressive strength data presented in Fig. 4.6 follows a similar pattern to the calorimetry data of the GBFS/MKPC binders. The highest compressive strength (36.6 MPa at day 28) was attained for the 0.22 w/s binder, which also had the shortest reaction period. This indicates that for GBFS/MKPC binders, the optimum w/s ratio would be the 0.22 w/s formulation however, the fluidity of this binder (102.3 ± 2.6 cm^2) was significantly below that of the 0.24 w/s binder (115.1 ± 2.4 cm^2) as shown in Fig. 4.1. As such, the optimum GBFS/MKPC binder was concluded to be the 0.24 w/s formulation, which provided a balance between compressive strength, reaction duration and fluidity (i.e. the workability).

Varying the water content produced notable changes in the heat flow of MKPCs blended with GBFS, whereas those blended with FA showed subtler changes. In both systems, the rate of heat evolution was most rapid at lower w/s ratios. The heat evolution of the FA/MKPC binders was similar to the MKPC-only system and ammonium-based phosphate cements (MAP cements). The duration of the heat evolution (i.e. cumulative flow) for MAP cements with borax additions was typically only extended up to 80 hours [43], whereas the cumulative heat evolution for all of the FA/MKPC and GBFS/MKPC formulations extended passed 95 hours. This is postulated to be the effect of retarding the system with 2 wt. % boric acid and diluting the reactants (MgO, KH_2PO_4, and H_2O) with 50 wt. % addition of supplementary cementitious materials (FA and GBFS).

The calorimetric traces in Fig. 4.10 appear to have three distinct exothermic events, which could be associated with the dissolution/precipitation processes and the development of the set cementitious binder. It is postulated that GBFS is acting as a chemical participant rather than being inert filler, which could lead to the formation of secondary reaction products highly intermixed within the MKPC binder. There is no calorimetry data on GBFS/MKPC formulations available in the open literature to support these results, but the distinct calorimetric response of GBFS/MKPC binders was reproducible at all w/s ratios investigated (Appendix C). The SXRD is important to understand the crystalline behaviour of these binders, as only the 0.24 w/s was studied the hydration behaviour of the 0.22 and 0.26 w/s binders will be inferred.

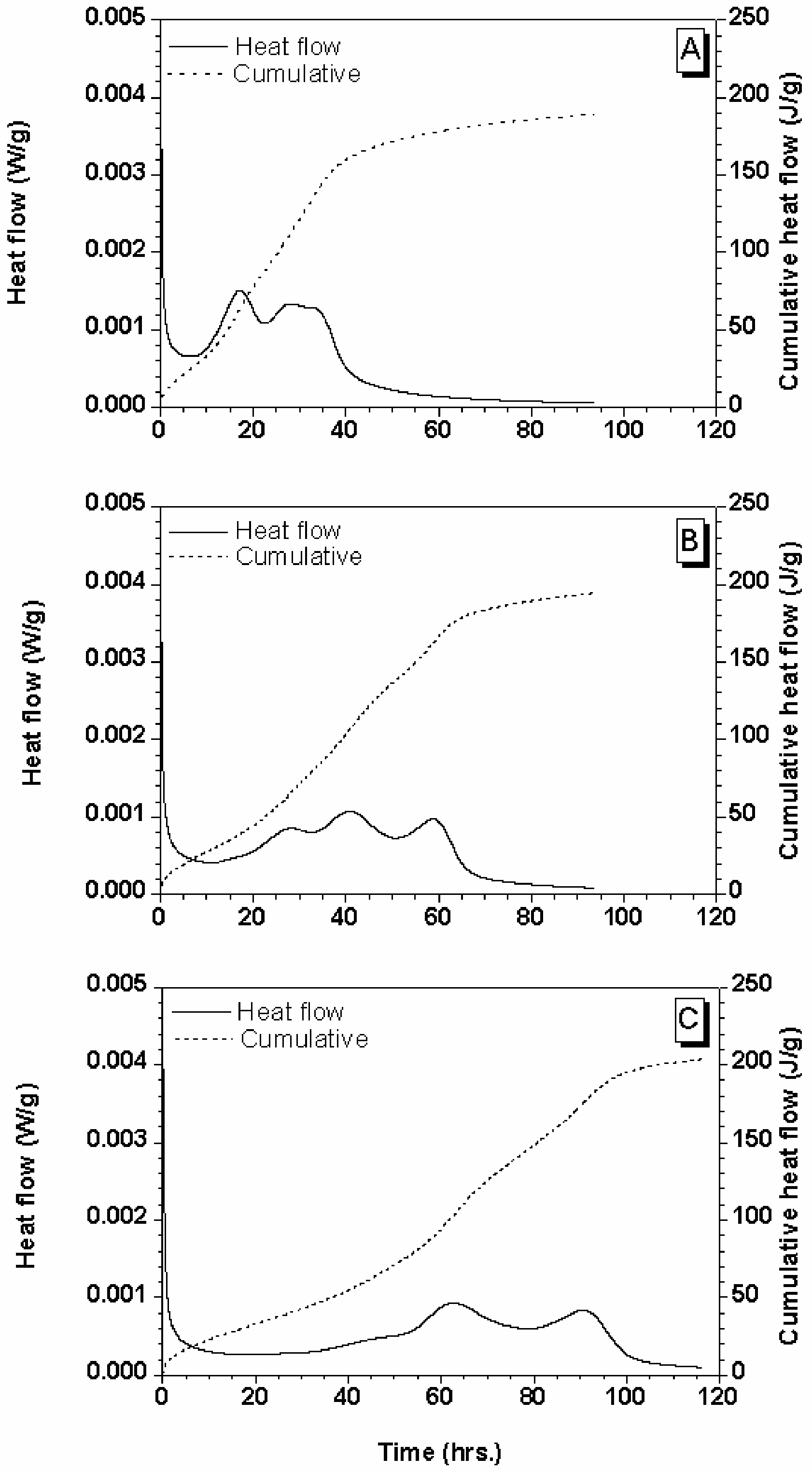

Fig. 4.10. Normalised calorimetric traces for fresh GBFS/MKPC pastes at (A) 0.22 w/s, (B) 0.24 w/s and (C) 0.26 w/s

4.2.5.3.2 Synchrotron X-ray diffraction (SXRD)

The time-resolved SXRD patterns of the GBFS/MKPC binder supported the occurrence of a delayed reaction mechanism, in-line with the calorimetry data Fig. 4.10. In the first two hours, reflections associated with MgO and KDP were detected in contrast to the FA/MKPC binder at a similar time point, this indicated that the KDP did not undergo dissolution and as such, no poorly crystalline struvite-K could have formed in this system. Reflections associated with a minor contamination were found in Fig. 4.12, identified as Portland cement (alite, PDF #85-1378, [110]) and calcite ($CaCO_3$, PDF #05-0586, [111]). The reflections were evident at the latest time point (57.7 hours), which suggests that the PC did not react to C-S-H or interfere with the acid-base reaction of this binder. However, it is possible that these contaminants may have increased the pH of the GBFS/MKPC binder to higher than normal (Table 4.1).

The dissolution of KDP was observed in Fig. 4.12 to commence at 13.9 hours, noted by the decreasing relative intensity of the KDP reflection, whilst reflections associated with struvite-K began to emerge with the relative intensity increasing until all of the KDP was consumed in the diffraction pattern at 57.7 hours. Over the first few hours, the relative intensity of the periclase reflection was observed to decrease suggesting that dissolution of this phase had begun. The calorimetric trace of the GBFS/MKPC (0.24 w/s) binder highlighted three exothermic events centred at 28 hrs, 40 hrs and 59 hours. It appears that all of these events were associated with the dissolution of the reactants and the precipitation of crystalline struvite-K.

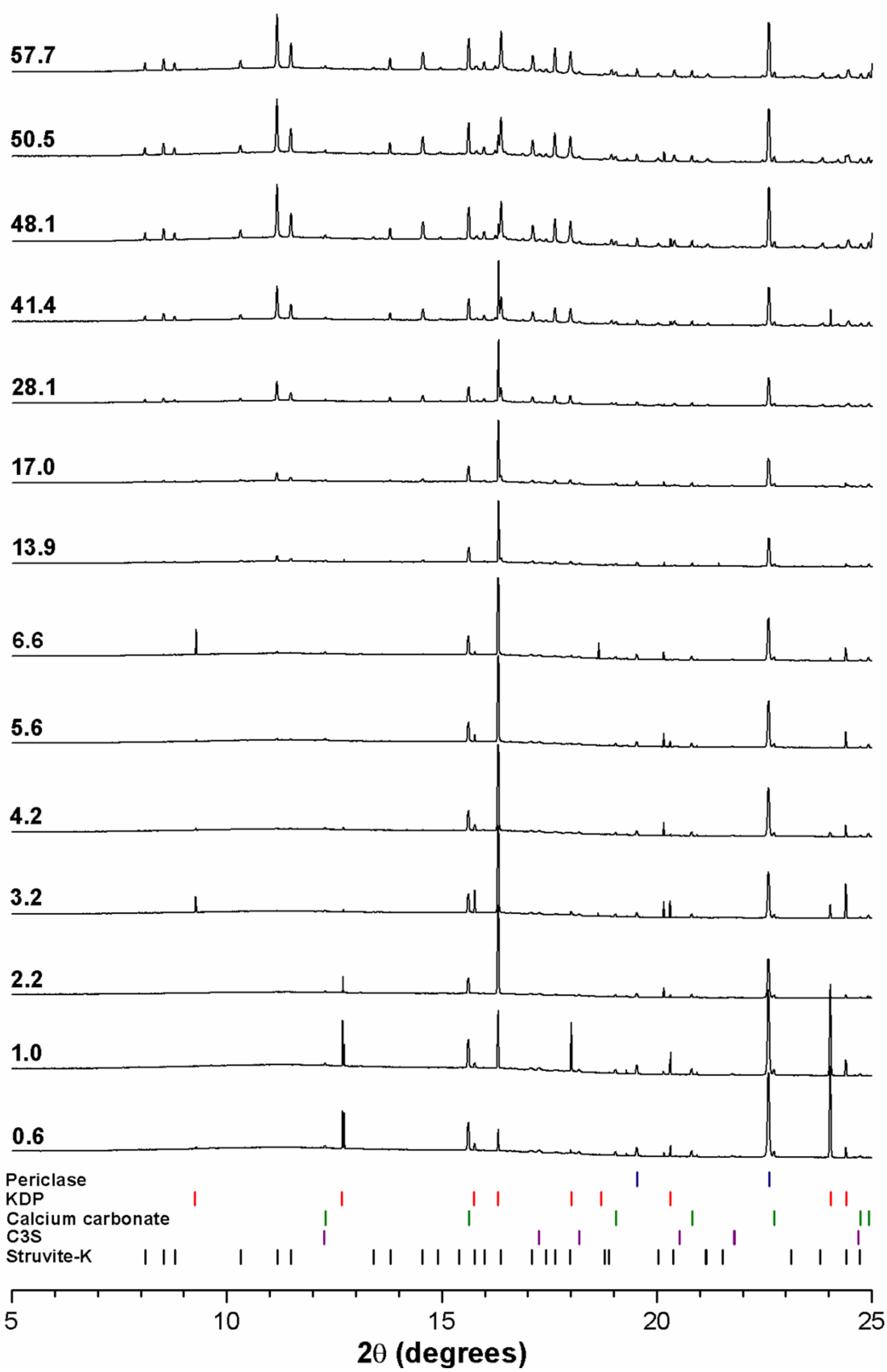

Fig. 4.11. Time resolved synchrotron X-ray diffraction of 0.24 w/s GBFS/MKPC binder, diffraction labels indicate the time (hrs) lapsed between sample preparation and data collection

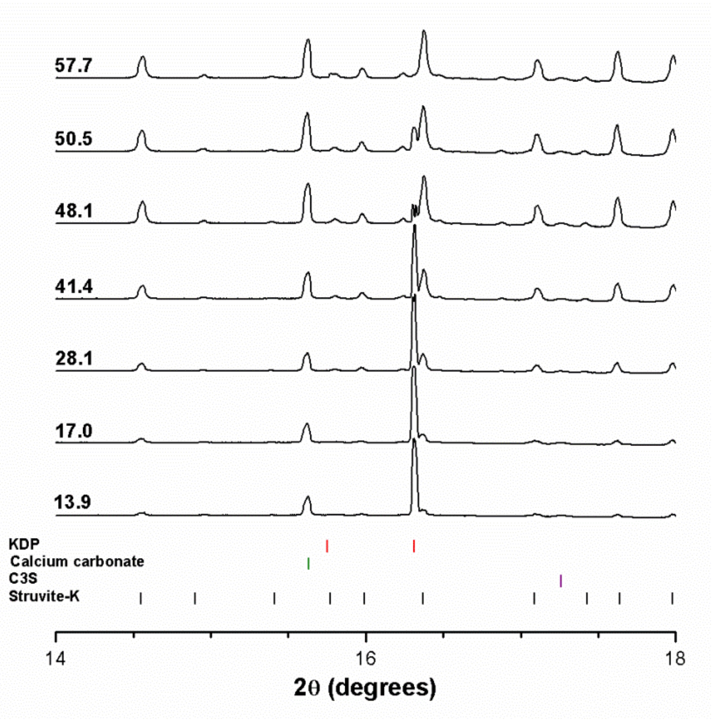

Fig. 4.12. Key time resolved synchrotron X-ray diffraction of GBFS/MKPC binder extracted from Fig. 4.11

4.2.6 Uranium encapsulation in blended MKPC binders

4.2.6.1 Experiment set-up

To validate the optimised blended MKPC described earlier in this Chapter, long-term (700 days) corrosion studies were conducted using natural uranium foil in small scale trials based on measuring water displacement. Natural uranium foil (Goodfellows, 0.178 mm) was cut into strips (*w* = 10 mm, *l* = 29 mm) using a scalpel (Table 4.2), the surface areas were calculated in triplicate using ImageJ software [73]. Each U foil strip was cleaned using a 50:50 solution of nitric acid/water to remove the oxide layer (UO_2). The black oxide layer is evident on all but one of the U foil samples in Fig. 4.14, where the latter had already been cleaned.

To remove any trace of the oxide layer and nitric acid, the foil strips were then washed several times using deionised water. The cement pastes were mixed according to Table 4.3; each paste was mixed by hand for 5 minutes after which it was poured to fill a 15 mL centrifuge tube that contained the U foil strip. The samples were lightly tapped on the laboratory bench to remove any entrained air bubbles from the mixing process. Within 10 minutes of mixing the samples, the experiment was set-up to the according to the schematic and photographs shown in Figs. 4.13-14.

Table 4.2. Sample data for natural uranium foil samples

Sample	Binder	Mass (mg) ± 0.1	Surface area (mm^2) ± 1.0
1	FA/MKPC	673.2	557.62
2	FA/MKPC	692.9	565.96
3	FA/MKPC	697.3	570.56
4	GBFS/MKPC	744.3	630.70
5	GBFS/MKPC	725.0	611.20
6	GBFS/MKPC	721.4	608.09
7	GBFS/PC	702.2	598.36
8	GBFS/PC	737.8	619.24

Table 4.3. Cement formulations for uranium corrosion trials to ± 0.1 g precision

Blend	MgO (g)	KH_2PO_4 (g)	H_2O (g)	SCM (g)	H_3BO_3 (g)	w/s
FA/MKPC	77.8	154.6	96.0	165.0	6.5	0.24
GBFS/MKPC	77.8	154.6	96.0	165.0	6.5	0.24
Blend	**PC (g)**	**GBFS (g)**	**H_2O (g)**	-	-	**w/s**
GBFS/PC	55.6	166.7	77.8	-	-	0.35

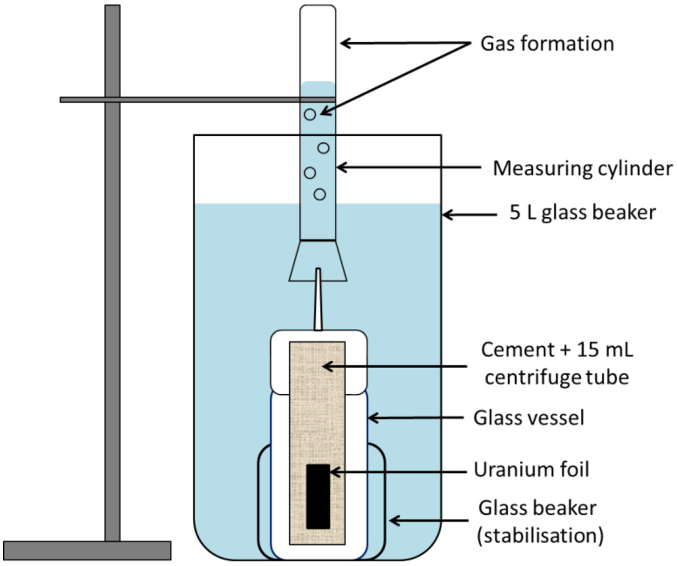

Fig. 4.13. Schematic of the water displacement experiment

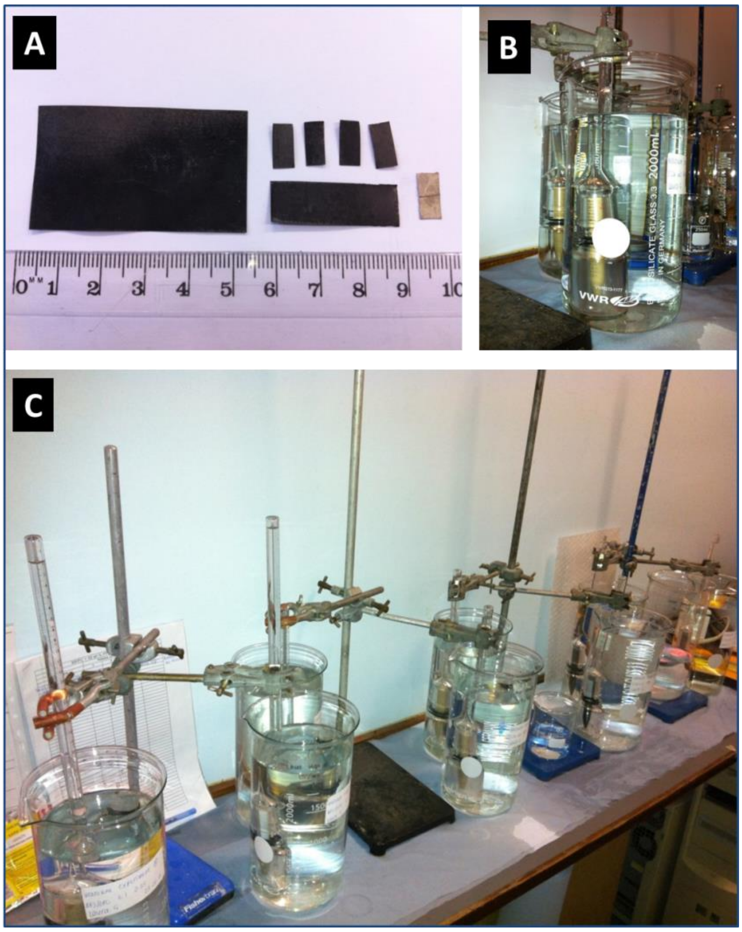

Fig. 4.14. Uranium corrosion experiments, (A) uranium foil, (B) a single completed set-up and (C) the full set-up

Gas volume measurements were taken every hour for the first 8 hours, and then once a day for the first month. After which measurements were taken every 2-3 days up to 6 months period, between 6-24 months measurements were taken weekly. The measuring cylinders were refilled as and when the gas volume was nearing capacity, which was 15 mL for the blended MKPC binders and 30 mL for the GBFS/PC samples. Biannually the water was treated with virkon S, which is a disinfectant. The water was completely replaced once a year. For analysis purposes the gas volume data was binned into 50-day collection periods, in which the volume observed includes the preceding 49 days of measurements. The temperature of the laboratory (which had a low foot fall, no windows and air conditioning) was recorded for the duration of the experiments at 1 hour intervals (Fig. 4.15) using an Omega-63 data logger. The temperature range was frequently between 20 to 25 °C but did experience occasions where it decreased to 15 °C or was extended up 30 °C. Figs. 15B-15C highlights the variance in a one month and one-week period (Feb to March 2013).

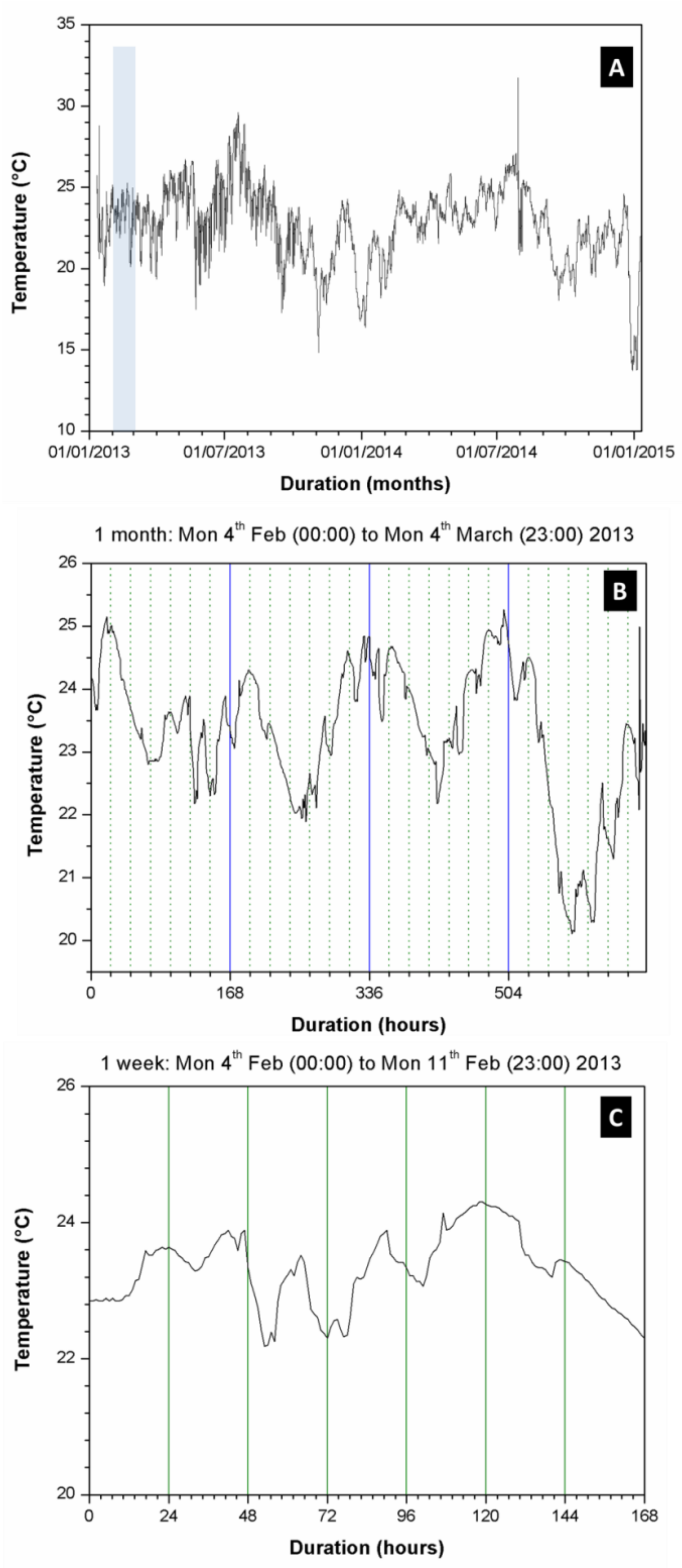

Fig. 4.15. The temperature data for the uranium corrosion trials: (A) Jan 2013 – Jan 2015, where data was extracted from the highlighted (blue) region to show the temperature variance in (B) 1 month and (C) 1 week

4.2.6.2 Corrosion results

The cumulative gas volume for the FA/MKPC, GBFS/MKPC and GBFS/PC binders are presented in Fig. 4.16. The total gas volume generated for the FA/MKPC, GBFS/MKPC and GBFS/PC samples were recorded to be: 64.7, 70.4 and 143.5 mL, respectively after 700 days (Tables 4.4-4.6), which is a significantly longer corrosion study than usually undertaken. The results indicated that the employment of blended MKPC binders in the encapsulation of uranium could reduce reactive metal corrosion by half compared to the UK nuclear industry standard grout, GBFS/PC.

After 100 days of uranium/grout interactions, Fig. 4.16 indicates that 10.8 ± 2.8 mL (FA/MKPC) and 13.0 ± 2.8 mL (GBFS/MKPC) of gas was evolved. These results appear comparable to a corrosion trial undertaken using FA/MKPC binders at 0.26 and 0.28 w/s ratios, where an average gas evolution of 11.2 ± 0.1 mL (0.26 w/s) and 13.7 ± 7.5 mL (0.28 w/s) was observed after 90 days [14]. However, this similarity can be discarded when taking into account the gas evolution to surface area ratio. The current study utilised natural uranium foil sections (l = ≈ 29 mm, w = ≈ 10 mm, d = 0.178 mm), whilst Covill [14] used natural uranium cylinders, referred to as pucks, (ø = 28 mm, h = ≈ 8.5 mm) sectioned from a Magnox fuel rod [14]. The average gas evolution to surface area ratios are:

- FA/MKPC (0.26 w/s) binder was 0.56 mL/cm^2, calculated from [14]
- FA/MKPC (0.24 w/s) binder was 1.93 mL/cm^2
- GBFS/MKPC (0.24 w/s) binder was 1.49 mL/cm^2

The calculated gas evolution to surface area ratios suggest that the blended MKPC binders used in this study performed worse than expected. One possible explanation for this difference could be associated with the uranium preparation. As discussed in section 4.2.6.1, the uranium foil was cleaned with nitric acid to remove the protective passivation layer (UO_2), whilst the uranium pucks were only cleaned with cyclohexane [14]. This indicates that careful consideration should be taken with regards to the uranium preparation, specimen size and data collection for corrosion trials.

The gas volume generation of the blended MKPC binders appeared to peak at 200 days with a steady decrease in the volume generated over time (Fig. 4.17). The GBFS/PC appeared to follow a similar pattern to the blended MKPC binders, albeit at a greater rate. Fig. 4.16 highlights the importance of conducting long-term corrosion studies as above 100 days the difference between the binders significantly increased. Small scale corrosion studies using BFS/PC and FA/PC grouts (at varying replacement ratios) were found to have high early corrosion rates that was attributed the free water in the PC grouts reacting with Magnox swarf, however, as the PC hydrated to form C-S-H products, the corrosion rate decreased [11]. A similar trend was observed in Fig. 4.17, where the gas volume generated substantially decreased as curing age increased.

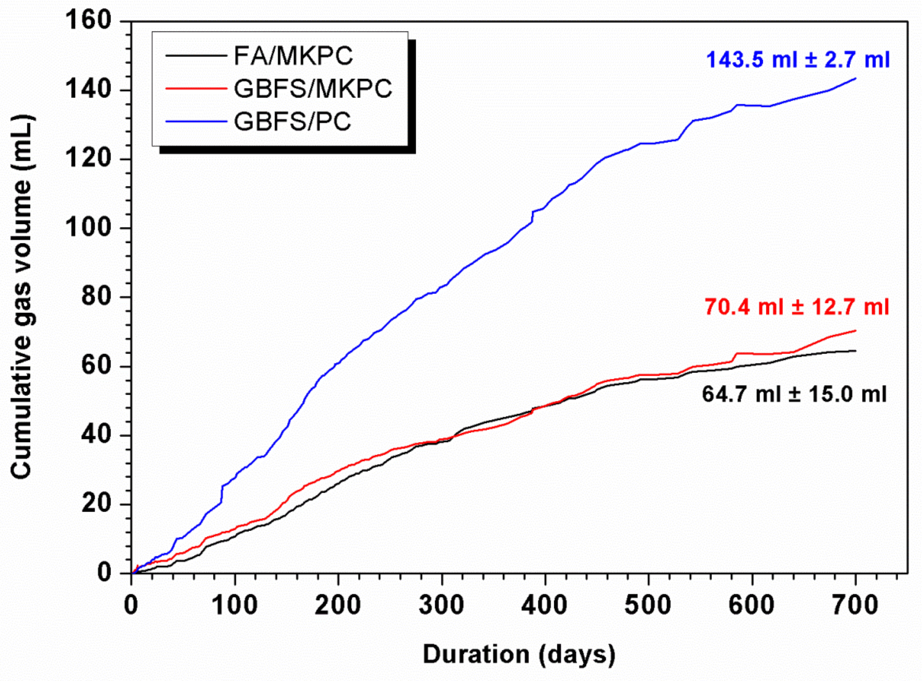

Fig. 4.16. Uranium corrosion trial of FA/MKPC, GBFS/MKPC and GBFS/PC pastes up to 700 days

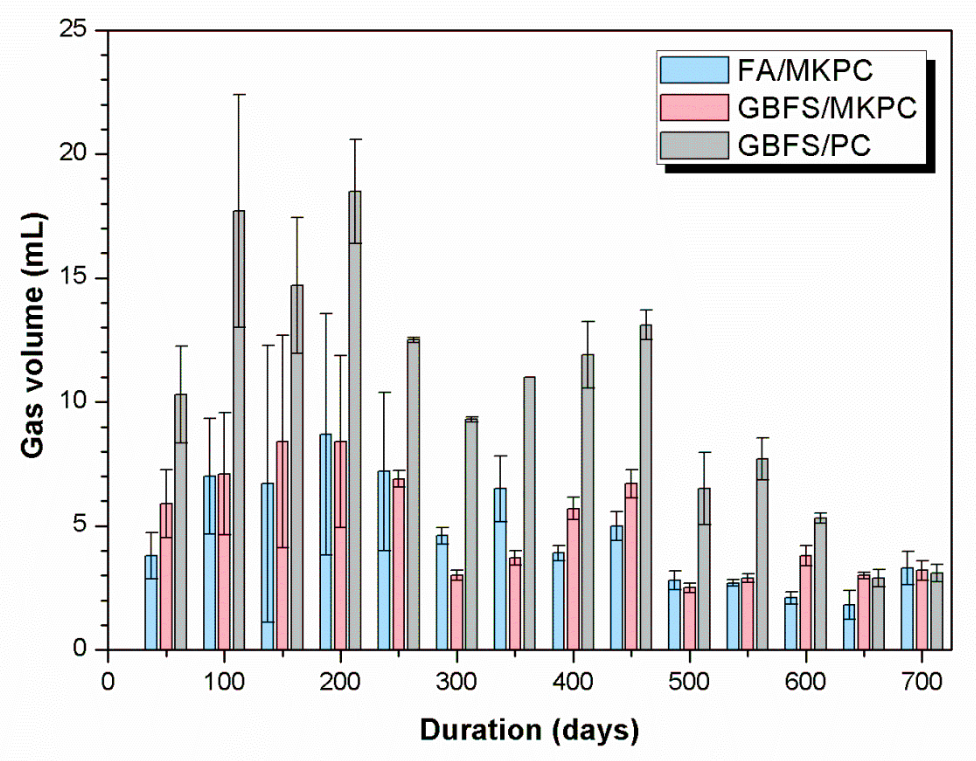

Fig. 4.17. Comparison of the observed gas volumes of FA/MKPC, GBFS/MKPC and GBFS/PC binders up to day 700¸ the error bars are equivalent to ± 1 standard deviation

Table 4.4. Gas volume generation of FA/MKPC (0.24 w/s) containing natural uranium up to 700 days

Duration (days)	Gas volume (mL) ± 0.1 mL								
	Sample 1		**Sample 2**		**Sample 3**		**Average**		
	Obs.	*Total*	*Obs.*	*Total*	*Obs.*	*Total*	*Obs.*	*Total*	*S.D*
50	3.0	3.0	5.1	5.1	3.3	3.3	3.8	3.8	0.9
100	3.9	6.9	7.6	12.7	9.5	12.8	7.0	10.8	2.8
150	1.9	8.8	3.6	16.3	14.5	27.3	6.7	17.5	7.6
200	4.0	12.8	6.7	23.0	15.4	42.7	8.7	26.2	12.4
250	6.1	18.9	13.9	30.2	9.5	52.2	7.2	33.4	13.8
300	3.9	22.8	4.7	34.9	4.3	56.5	4.6	38.0	13.9
350	5.0	27.8	8.2	43.1	6.1	62.6	6.5	44.5	14.2
400	4.1	31.9	3.4	46.5	4.0	66.7	3.9	48.4	14.3
450	5.8	37.7	4.9	51.4	4.4	71.1	5.0	53.4	13.7
500	3.2	40.9	2.3	53.7	3.0	74.1	2.8	56.2	13.7
550	2.8	43.7	2.5	56.2	2.6	76.7	2.7	58.9	13.6
600	1.9	45.6	2.1	58.3	2.5	79.2	2.2	61.1	13.9
650	1.0	46.6	2.0	60.3	2.4	81.6	1.8	62.9	14.4
700	0.9	47.5	2.0	62.3	2.5	84.1	1.8	**64.7**	**15.0**

Table 4.5. Gas volume generation of GBFS/MKPC (0.24 w/s) containing natural uranium up to 700 days

	Gas volume (mL) ± 0.1 mL								
Duration (days)	**Sample 1**		**Sample 2**		**Sample 3**		**Average**		
	Obs.	*Total*	*Obs.*	*Total*	*Obs.*	*Total*	*Obs.*	*Total*	*S.D*
50	5.1	5.1	7.8	7.8	4.7	4.7	5.9	5.9	1.4
100	5.7	10.8	10.6	18.4	5.1	9.8	7.1	13.0	2.8
150	7.5	18.3	14.1	32.5	3.7	13.5	8.4	21.4	7.6
200	7.1	25.4	13.1	45.6	4.9	18.4	8.4	29.8	11.5
250	5.8	31.2	6.6	52.2	6.0	24.4	6.9	35.9	11.8
300	3.2	34.4	3.0	55.2	2.7	27.1	3.0	38.9	11.9
350	3.8	38.2	3.3	58.5	4.0	31.1	3.7	42.6	11.6
400	6.1	44.3	6.0	64.5	5.1	36.2	5.7	48.3	11.9
450	6.2	50.5	7.5	72.0	6.4	42.6	6.7	55.0	12.4
500	2.2	52.7	2.6	74.6	2.6	45.2	2.5	57.5	12.5
550	3.0	55.7	3.1	77.7	2.7	47.9	2.9	60.4	12.6
600	3.0	59.6	3.5	81.2	4.0	51.9	3.8	64.2	12.4
650	3.0	62.6	3.1	84.3	2.8	54.7	3.0	67.2	12.5
700	2.8	65.1	3.7	88.0	3.5	58.2	3.2	**70.4**	**12.7**

Table 4.6. Gas volume generation of GBFS/PC (0.35 w/s) containing natural uranium up to 700 days

Gas volume (mL) ± 0.1 mL							
Duration (days)	**Sample 1**		**Sample 2**		**Average**		
	Obs.	*Total*	*Obs.*	*Total*	*Obs.*	*Total*	*S.D*
50	8.3	8.3	12.2	12.2	10.3	10.3	2.0
100	13.0	21.3	22.4	34.6	17.7	28.0	6.7
150	17.4	38.7	11.9	46.5	14.7	42.6	3.9
200	20.6	59.3	16.4	62.9	18.5	61.1	1.8
250	12.4	71.7	12.6	75.5	12.5	73.6	1.9
300	9.4	81.1	9.2	84.7	9.3	82.9	1.8
350	11.0	92.1	11.0	95.7	11.0	93.9	1.8
400	10.5	102.6	13.2	108.9	11.9	105.8	3.2
450	12.5	115.1	13.7	122.6	13.1	118.9	3.8
500	7.1	122.2	4.2	126.8	6.5	124.5	2.3
550	6.8	129.0	8.5	135.3	7.7	132.2	3.2
600	5.1	134.1	5.5	140.8	5.3	137.5	3.4
650	3.3	137.4	2.6	143.4	2.9	140.4	3.0
700	3.4	140.8	2.7	146.1	3.1	**143.5**	**2.7**

4.2.6.3 Scanning electron microscopy

The backscattered electron images of the FA/MKPC and GBFS/MKPC binders encapsulated with uranium foil were typical for these systems (albeit without uranium). The GBFS/PC was unable to be analysed due to the sample breaking during sectioning. In the FA/MKPC binder (Fig. 4.18), large struvite-K crystallites, unreacted periclase and the spherical particles associated with fly ash were clearly evident. A good adhesion with the uranium foil is observed at 18 months with no evidence that the uranium has corroded. The elemental maps suggest that K and Ca (Fig. 4.18: K and Ca) were associated with the uranium foil, however this is due to an overlapping of the characteristic X-rays detected by EDX analysis. For K, the Kα1 X-ray (3.314) coincided with the Mβ X-ray of U at 3.336 keV, whilst the Ca Kα1 and Kα2 X-rays (3.692 and 3.689 keV, respectively) slightly overlaid the M2N1 X-ray of U at 3.724 keV. The SEM/EDX analysis in this study indicated that the FA/MKPC (0.24 w/s) is a suitable for the encapsulation of corrosion with no detrimental effect on the typical microstructure. It is reported that uranium pucks encapsulated within FA/MKPC binders will undergo oxidation (observed as a black surface using optical microscopy) when in direct contact with the MKPC binder [14] however, no evidence for this uniform oxidation later was found in Figs. 4.18-4.19. The summary of uranium corrosion trials conducted by Covill revealed that even after 360 days, no uranyl phosphate compounds or other corrosion products were identified up to 360 days [14], which supports the SEM/EDX of the FA/MKPC binder aged for 18 months in Fig. 4.18.

In the GBFS/MKPC binder (Fig. 4.19), a continuous struvite-K matrix was observed with embedded angular GBFS particles. The condition of the encapsulated uranium foil was substantially different compared to the FA/MKPC binder. A corrosion layer can be distinguished from the pristine uranium foil, which is evident all around the boundary of the U foil. In between the corrosion layer and the U foil, an interstitial space was created devoid of the elements displayed in Fig. 4.19. This indicated that no corrosion products, other than UO_2, were formed. The interstitial space was created by the expansion of the UO_2 corrosion layer into the GBFS/MKPC binder. The densities of U metal and UO_2 can be used to explain why this mechanism occurs. In order to have the same U content, UO_2 (being less dense at 10.97 g/cm^3) will need to occupy a larger volume than the denser U metal (18.95 g/cm^3) and as such, the delaminated corrosion layer is formed *via* expansion. A slight chemical difference was observed in the bottom section of the U foil (labelled in Fig. 4.19), where a Si-rich region (Fig. 4.19: Si) was present in the interstitial space. It is postulated that this could be associated with sample preparation for example, if the U foil was not perfectly perpendicular to the resin, the sample would not be fully exposed during grinding/polishing. Additional sample preparation and SEM/EDX analysis at higher magnifications could determine (or deny) the existence of the Si-rich region within the GBFS/MKPC binder.

The GBFS/MKPC corrosion microstructure is similar to that of an GBFS/PC sample encapsulated with aluminium, in which a transition zone consisting of a porous layer between the grout and metal [13]. This feature was described to be formed by hydrogen generated during the initial corrosion of aluminium [13]. The similar overall gas volume generation of the FA/MKPC and GBFS/MKPC binders at 64.7 and 70.4 mL, respectively cannot justify the difference observed in the microstructure, as such it is postulated that the two binders undergo different corrosion mechanisms. This could be associated with the redox potential of GBFS, which is slightly reducing due to the sulphate content [30], further work is needed to understand this in detail.

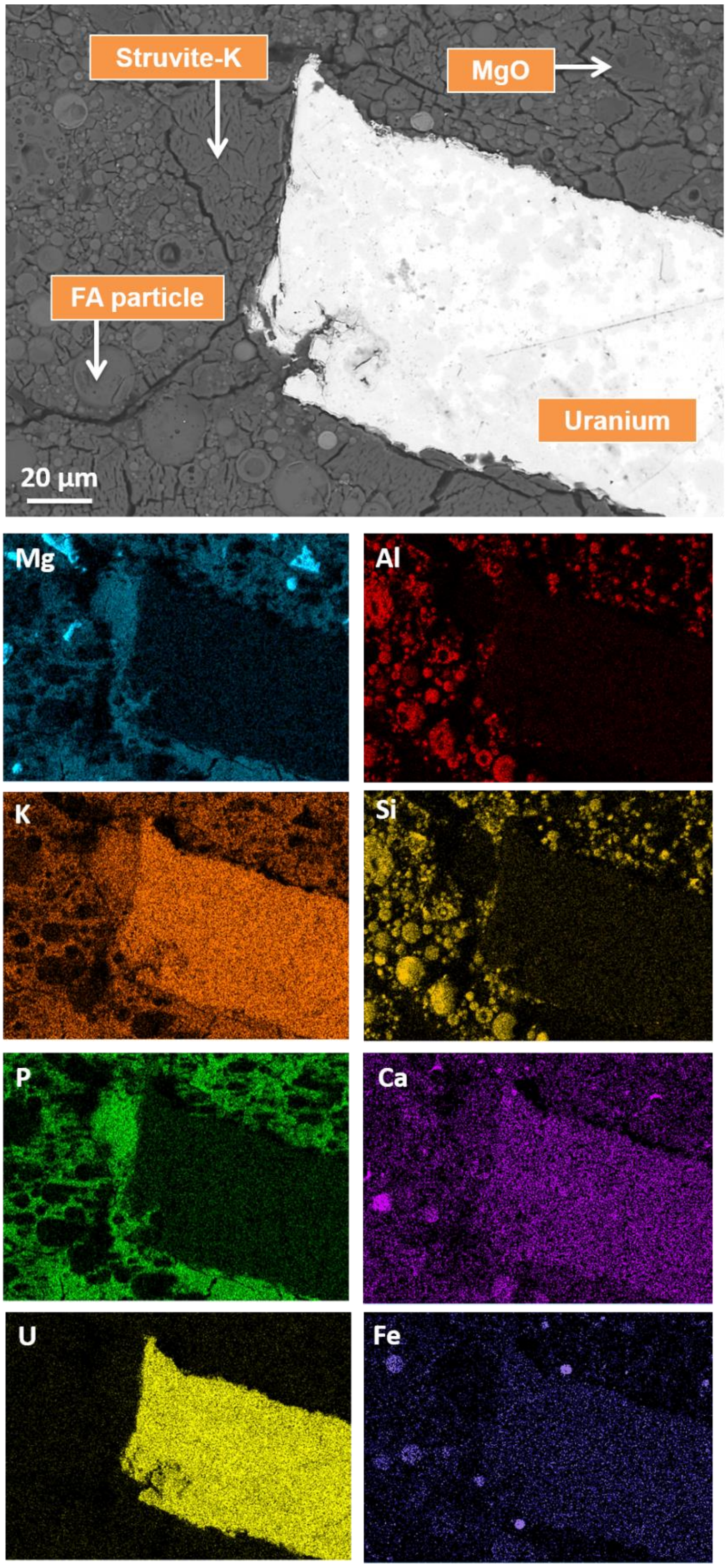

Fig. 4.18. FA/MKPC (0.24 w/s) with encapsulated uranium foil at 18 months

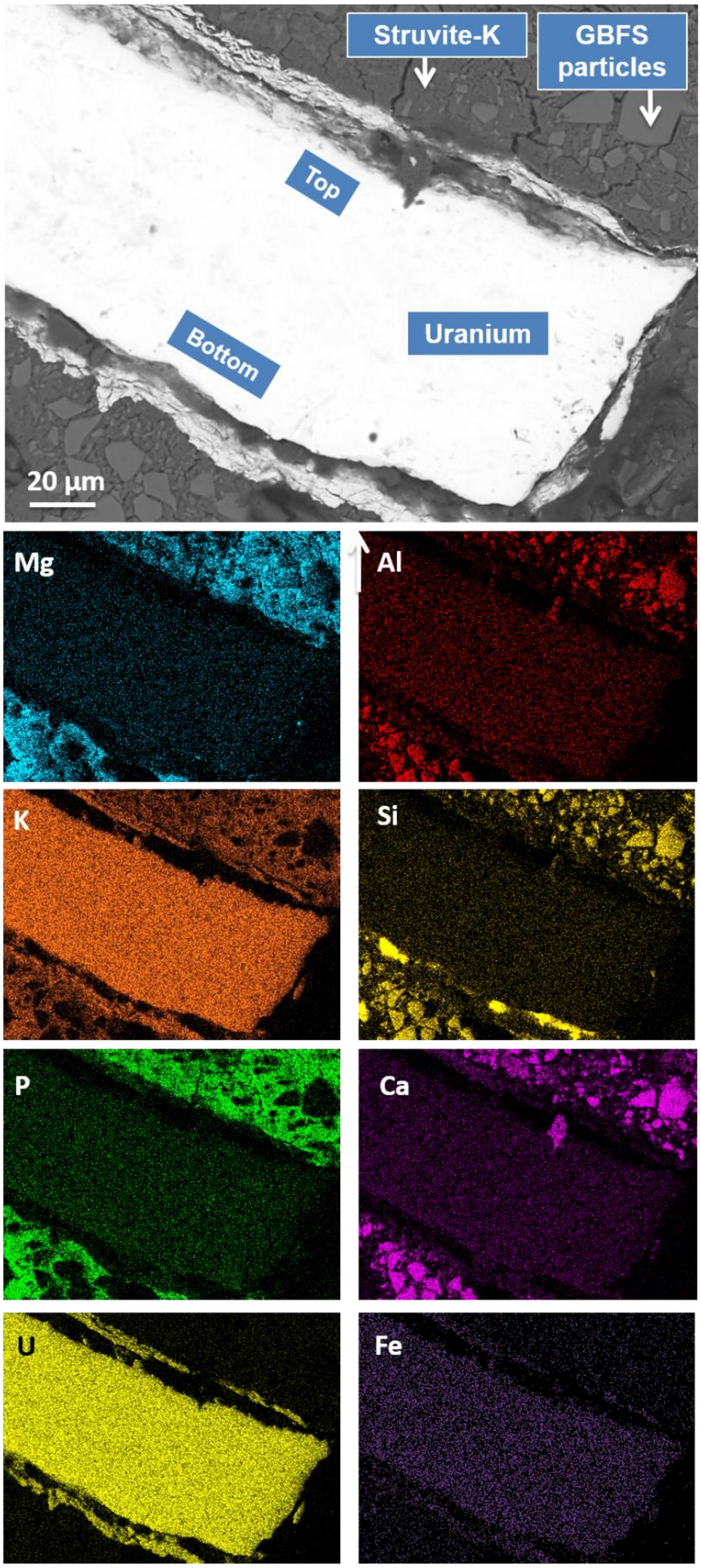

Fig. 4.19. GBFS/MKPC (0.24 w/s) with encapsulated uranium foil at 18 months

4.3 Conclusions and Future work

Investigation of various w/s ratios have reduced the water content successfully by 8 % (based on the 0.24 w/s ratio) from previous literature formulations [18] whilst still retaining mechanical and chemical integrity of the hardened blended MKPC monoliths. The reduction in water content could reduce the amount of water available to support corrosion of encapsulated ILW reactive metals. There appeared to be no differences in the XRD phase assemblage or thermal analysis between the two binders studied: FA/MKPC and GBFS/MKPC. The compressive strength of the GBFS/MKPC system was notably higher than that of the FA/MKPC system.

Calorimetry data for the GBFS/MKPC binders made at different water-to-solids ratios suggests that although there is little difference identified in XRD/TGA analysis, the heat of reaction behaviour and heat flow varied considerably compared to the FA/MKPC formulations. This characteristic is advantageous for industrial applications as the output and setting time can be controlled by modifying the SCM included in the MKPC binder. The calorimetry and compressive strength data both suggest there is potential for secondary reaction products to form within the GBFS/MKPC binders, which would be expected fill any pores. The optimised blended MKPC binders were found to reduce the corrosion of uranium by half compared to the industry standard and as such, could be an alternative encapsulant for the legacy ILW reactive metal inventory. However, significant differences were observed in the microstructural properties of these binders at 18 months, which needs further investigation.

Note: From this point onwards, all of the MKPC, FA/MKPC and GBFS/MKPC formulations are all based on the 0.24 water to solids ratio.

Further work should be undertaken in the following areas:

- In-depth analysis of the encapsulated uranium samples to elucidate the corrosion products (if any) for each binder including: X-ray absorption spectroscopy (for phosphorous) and analysis of µ-X-ray computed tomography data collected at Central Laboratory, National Nuclear Laboratory.
- Large scale corrosion trials using uranium and Magnox swarf simulant of the blended MKPC binders to determine the reproducibility of the small scale trials in this study, including direct hydrogen measurements.

5 Synthesis and characterisation of pure struvite-K, $MgKPO_4·6H_2O$

This short chapter was included to introduce the basic characterisation of pure struvite-K prior to:

- *Chapter 6 - where it was used as a reference for the solid-state ^{25}Mg and ^{39}K MAS NMR experiments*
- *Chapter 7 - where it was the baseline for the high temperature stability experiments*
- *Chapter 8 - where it was used during scoping gamma (Cs-137) irradiation experiments*

5.1 Introduction

The mineral struvite ($MgNH_4PO_4·6H_2O$) was first identified in 1845 within the grounds of St. Nicholas church, Hamburg by Ulex [112], who postulated that struvite was formed over many years as a result of urine filtration through soil laden with putrefied vegetation. A number of years later (in 1887), struvite was also discovered in moist bat guano under investigation from the Skipton caves in Victoria, Australia, amongst other newly discovered magnesium phosphate minerals (hannayite and newberyite) [113, 114]. Several studies have since detailed the structure of struvite (orthorhombic, space group $Pmn2_1$) and its common analogues, $MgMPO_4·6H_2O$, where M^+ is one of Rb^+, Cs^+, Tl^+ or K^+ [22, 35, 115]. These cation substitutions within the struvite structure have shown not to distort the orthorhombic symmetry with the exception of Cs^+, which formed a hexagonal structure (space group $P6_3mc$) due to its larger ionic radius [22, 35, 115]. The work discussed here will focus only the properties of struvite-K, $MgKPO_4·6H_2O$. Mathew and Schroeder [22] reported that only minor structural differences were observed in the struvite-K crystal structure when compared to that of struvite. This was due to the weak interactions between NH_4 or K and the oxygen atoms in the water molecules within the crystal structure.

As such, the unit cell parameters of struvite and struvite-K are reported to be: *a* = 6.941 ± 0.002, *b* = 6.137 ± 0.002, *c* = 11.199 ± 0.004 Å [115] and a = 6.873 ± 0.002, b = 6.160 ± 0.002, c = 11.087 ± 0.003 Å [22], respectively. Struvite-K has long been reported to be isostructural with the naturally cementitious struvite, however, it was only classified as a natural mineral in 2003 by the Commission of New Mineral and Mineral Names, International Mineralogical Association after it was discovered in two locations: Binntal in Switzerland and the Styria region of Austria [116].

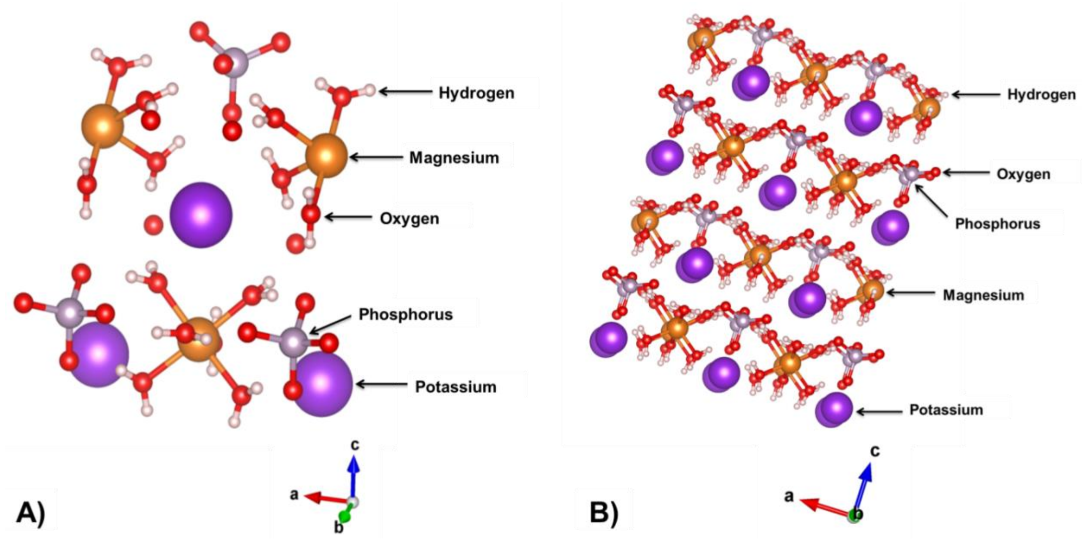

Fig. 5.1. The (A) unit cell and (B) crystal structure of struvite-K based on data obtained from Mathew and Schroeder [22] produced using VESTA [117]

The utilisation of struvite as the main binding phase in inorganic magnesium phosphate cements (acid-base cements, Eq. 9) has received considerable attention since the 1970s due to their quick setting time and high early strength properties [21]. The application of these alternative magnesium phosphate cements became prevalent in niche rapid infrastructure repairs (e.g. roads, bridges [21] and runways [118]) in place of traditional Portland cement binders.

Eq. 6 $MgO_{(s)} + NH_4H_2PO_{4\,(s)} + 5H_2O_{(l)} \rightarrow MgNH_4PO_4{\cdot}6H_2O_{(s)}$

However, it was found that ammonia was liberated from these struvite-based cements during both the mixing and setting processes [39]. This resulted in a move towards utilising struvite-K based cements (Eq. 4), which are referred to as magnesium potassium phosphates cements (MKPCs) and are currently favoured in waste management applications, in particular for nuclear waste immobilisation/encapsulation [18, 61, 119]. Due to the increased interest in struvite-K based cements at present, it is important to investigate and characterise the chemical environments present in this mineral.

5.2 Materials and Methods

The struvite-K precursors were: KH_2PO_4 (>99 % purity, Prayon), available as Food Grade E340 MKP, $MgCl_2$ (anhydrous, ≥98 % purity, Sigma Aldrich), KOH solution (45 wt. % in H_2O, Sigma Aldrich) and deionised H_2O.

A solution with 25 g KH_2PO_4, 5 g $MgCl_2$ and 100 mL of deionised H_2O was prepared in a conical flask, which was transferred to a clamp stand and positioned in an angled position. After this, KOH (20 mL) was added dropwise to the solution until a pH of 7.5 was achieved as determined using a digital pH meter. A 3-point calibration (at pH = 4, 7 and 10) was undertaken prior to the pH measurements using pH buffer solutions. The solution was held static for 7 days at room temperature, the resulting white precipitate was suction filtered and washed multiple times with deionised H_2O followed by a final acetone wash. Following this, the product was transferred to a vacuum desiccator to dry for 2 days prior to characterisation (Appendix D).

5.3 Results and Discussion

5.3.1 In situ high temperature X-ray diffraction (HTXRD)

The diffraction pattern of struvite-K (Fig. 5.2, 20 °C) synthesised in this study revealed that only reflections corresponding to struvite-K ($MgKPO_4·6H_2O$, PDF #75-1076), were identified, which indicated a pure sample was prepared using the Mathew and Schroeder method [22]. In situ HTXRD of struvite-K was conducted to determine the high temperature behaviour as a baseline for Chapter 7.

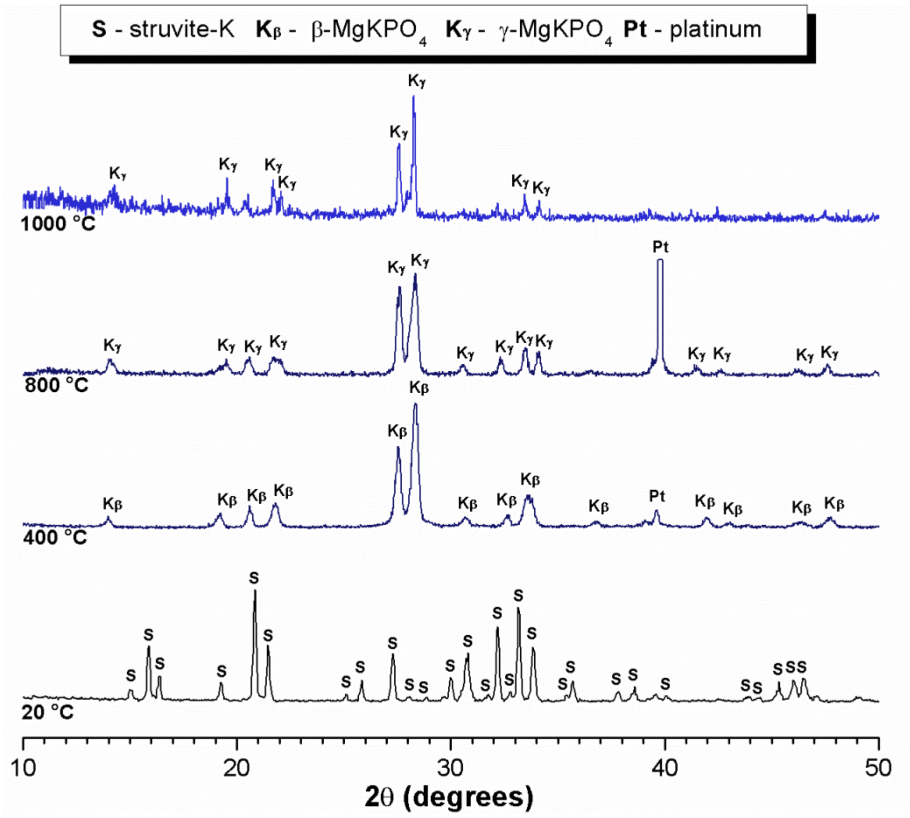

Fig. 5.2. HTXRD patterns of struvite-K powder up to 1000 °C

After exposure to 400 °C, it was found that the struvite-K reflections disappeared following dehydration between 50 – 150 °C (Fig. 5.3) The dehydration product was described by Wallez *et al.* [120] to exist as either the α, β or γ-$MgKPO_4$ phase, each can be identified by distinctive X-ray diffraction patterns. The reflections at 400 °C, were characteristic of the β-$MgKPO_4$ phase (PDF #50-0149, *Pna2₁*) whilst before 800 °C, a β to γ phase transition occurred resulting in the γ-$MgKPO_4$ phase (PDF #50-0151, *Pnma*) to be present at 800 °C. These assignments are in agreement with Wallez *et al.* [120], who reported two endothermic transitions, α to β and β to γ at 362 °C and 422 °C, respectively. The β-$MgKPO_4$ and γ-$MgKPO_4$ phase transitions resulted in the formation of a stabilised stuffed tridymite structure ($A^{I}B^{II}PO_4$), where the Mg atoms are all tetrahedrally coordinated [120]. However, the structure of the α-$MgKPO_4$ phase is reported to be comprised of two Mg co-ordination sites (tetrahedral and pentahedral), this causes a distortion of the typical stuffed tridymite framework [120], which can be observed by the reported lattice parameters in Table 5.1. As a consequence of the α to β-$MgKPO_4$ phase transition taking place at 362 °C, below the temperature of the first in situ HTXRD scan, the α-$MgKPO_4$ phase (*$P2_1/c$*) was not detected in the pure struvite-K. Platinum (PDF #04-0802) reflections were also detected in both the 400 and 800 °C diffraction patterns, which is an artefact from the sample holder.

Table 5.1. Reported lattice parameters for heated $MgKPO_4$ [120]

		Lattice Parameters			
Compound	**Space group**	***a* (Å)**	***b* (Å)**	***c* (Å)**	**β (deg)**
α-$MgKPO_4$	$P2_1/c$	8.549	5.078	18.996	91.68
β-$MgKPO_4$	$Pna2_1$	8.586	9.254	5.296	
γ-$MgKPO_4$	Pnma	8.645	5.279	9.335	

In isostructural struvite ($NH_4MgPO_4{\cdot}6H_2O$) systems [22, 116] poorly crystalline phases (e.g. $MgHPO_4$) were observed between 200 - 700 °C [39, 121-123] whilst above 700 °C, only magnesium phosphate phases were identified, which was attributed to ammonia liberation [121, 123]. In contrast, it was found that struvite-K retained both its crystalline nature and the K^+ ion after high temperature exposure, as evidenced by the continued presence of γ-$MgKPO_4$ reflections at 1000 °C. This indicates that struvite-K is more withstanding of exposure to high temperatures than struvite.

5.3.2 Thermal analysis

Thermal analysis of synthetic struvite-K (Fig. 5.3) revealed a single, yet notable, mass loss (40 %) between 40 - 200 °C. This event corresponds to the one-step dehydration of struvite-K (Eq. 8) reported in the literature for both synthetic struvite-K [98] and MKPCs [119]. The differential thermal analysis (DTA) supported the occurrence of the endothermic dehydration of struvite-K, which was observed around 130 °C in Fig. 5.4. Additionally, the DTA thermograph revealed the presence of an exothermic event (with no mass loss) between 390 - 445 °C (with the maximum at 405 °C), which is postulated to be associated with both the α to β-$MgKPO_4$ and β to γ-$MgKPO_4$ phase transitions. These transitions were observed by DSC measurements to occur at 362 °C and 422 °C, respectively [120]. It may be possible that the two transitions overlap in this study due to the relatively high heating rate (10 °C/min) of the DTA experiment. Another possible explanation for this could the different starting materials. Wallez *et al.* [120] synthesised pure α-$MgKPO_4$ (with an XRD pattern reported for this phase at 20 °C) whilst in this study, $MgKPO_4$ was only formed during the dehydration of struvite-K. This process occurs between 50 - 200 °C and initially results in the formation of a poorly crystalline material (Fig. 5.3). The long-range order of the struvite-K dehydration product ($MgKPO_4$) was only re-established at 400 °C, which is above the reported (and observed) α to β to γ -$MgKPO_4$ phase transition temperature [120] and consequently, the α-$MgKPO_4$ phase was not observed in the struvite-K system.

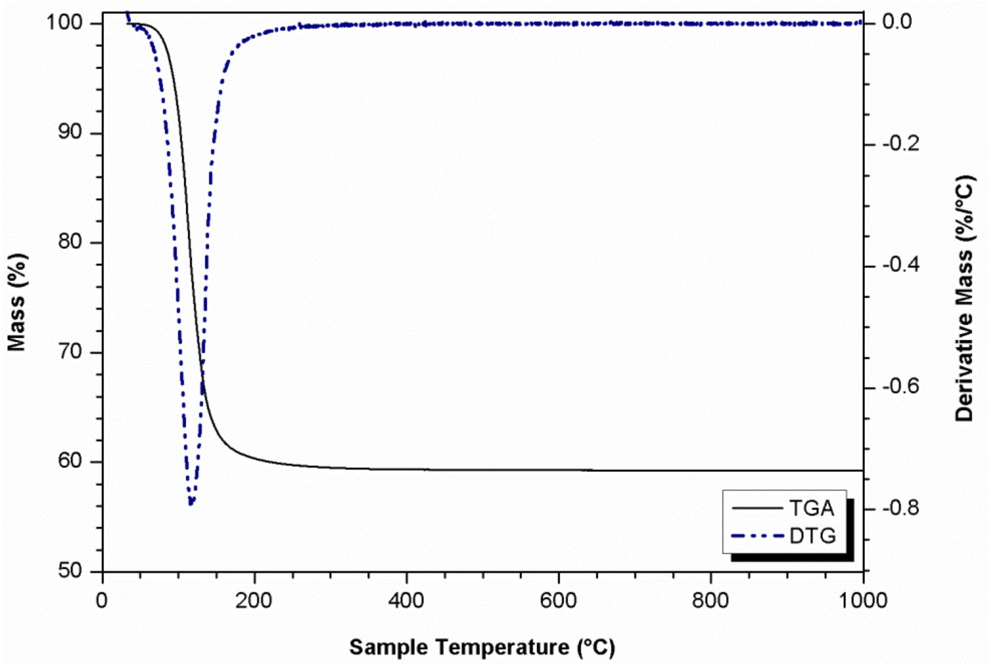

Fig. 5.3. Thermogravimetric analysis of synthetic struvite-K

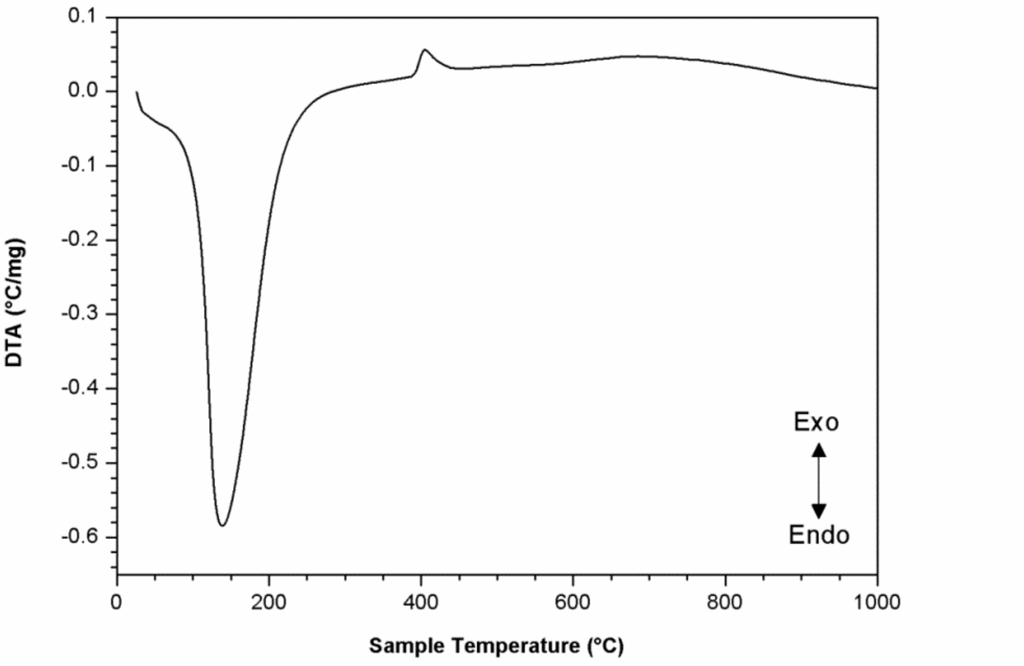

Fig. 5.4. Differential thermal analysis of synthetic struvite-K

5.3.3 Nuclear magnetic resonance spectroscopy

The local chemical environments present within pure struvite-K were determined using ^{31}P, ^{25}Mg and ^{39}K MAS NMR spectroscopy (Figs. 5.5-5.7) at room temperature. The ^{31}P MAS NMR spectrum (Fig. 5.5) exhibited a single sharp resonance centred at 6.2 ppm in the orthophosphate region, which was associated with crystalline struvite-K and was in agreement with published ^{31}P MAS NMR data for isostructural struvite, where a single resonance was observed at 6.1 ppm [124-126]. Alongside the ^{31}P MAS NMR data, cross-polarisation (CP) NMR was used to examine the ^{31}P-^{1}H nuclei interactions. Typically, CP/MAS experiments are performed to observe hydrated phases within a system. In this study, cross polarisation was utilised to study the hydrated phosphate phases present in synthetic struvite-K. In Fig. 5.5, the CP/MAS spectrum clearly shows a single resonance (at 6.2 ppm), which indicated that all of the P-H interactions within this specimen were associated with the struvite-K phase.

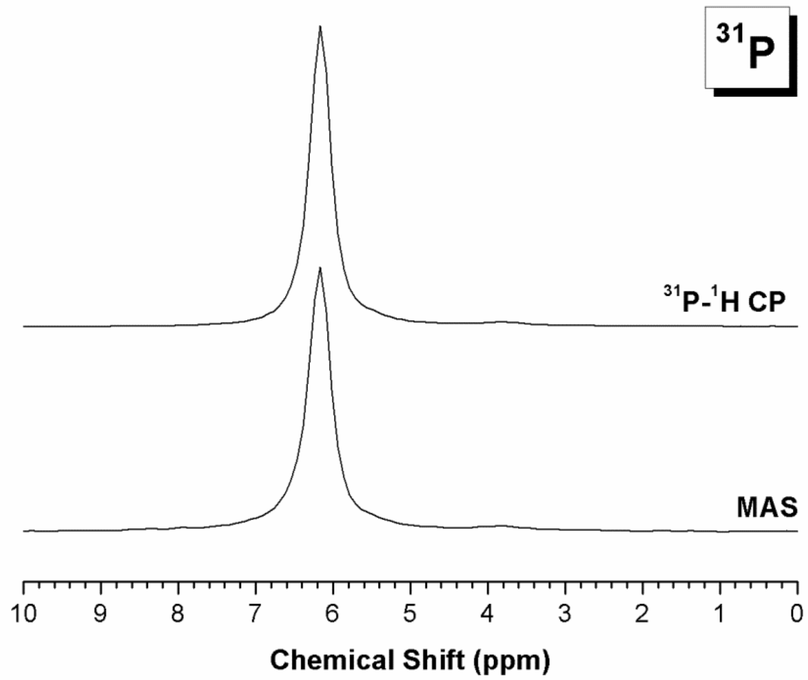

Fig. 5.5. ^{31}P MAS and ^{31}P-^{1}H CP/MAS NMR spectra (9.4 T, 10 kHz) for struvite-K at relaxation times 10 s and 1 s, respectively

The ^{25}Mg and ^{39}K MAS NMR nuclei have quadrupole moments as a result of the non-spherical charge distribution (spins 5/2 and 3/2, respectively) interacting with the electric field gradient [80]. This quadrupolar interaction typically affects the NMR spectra by: resonance broadening, chemical shift anisotropy and dipolar coupling, all but the resonance broadening can be removed by using MAS experiments [80]. These nuclei are also often difficult to observe due the low natural abundancy of ^{25}Mg and the low sensitivity of ^{39}K nuclei [82]. In order to off-set these effects and enhance sensitivity, high-field (19.96 T) solid state MAS NMR spectra of struvite-K were collected. However, the distinct resonance shapes observed in Figs. 5.6-5.7 clearly indicated that the ^{25}Mg and ^{39}K environments in struvite-K underwent broadening due to the second-order quadrupolar interactions [81]. An empirical fitting method was used in Topspin 3.2 [83] to simulate the experimental spectrum for the observed nuclei and to determine the quadrupolar parameters (Table 5.2): isotropic chemical shift (δ_{iso}), quadrupolar coupling constant (C_Q) and asymmetry (η_Q). The calculated ^{25}Mg quadrupolar parameters of struvite-K were found to be comparable to those for struvite and are reported to be 1.0 ppm (δ_{iso}), 3.56 MHz (C_Q) and 0.34 (η_Q) [81]. It is therefore assumed that the quadrupolar parameters calculated for ^{39}K MAS NMR (Table 5.2, Fig. 5.7) are likely to be representative of struvite-K.

Table 5.2. NMR quadrupolar parameters for sites calculated in synthetic struvite-K using high-field ^{25}Mg and ^{39}K MAS NMR nuclei experiments

	Experimental NMR		
Site	**δ_{iso} (ppm) (± 0.1)**	**C_Q (MHz) (± 0.1)**	**η_Q (± 0.02)**
Mg	-1.0	3.8	0.33
K	-73.1	2.2	0.14

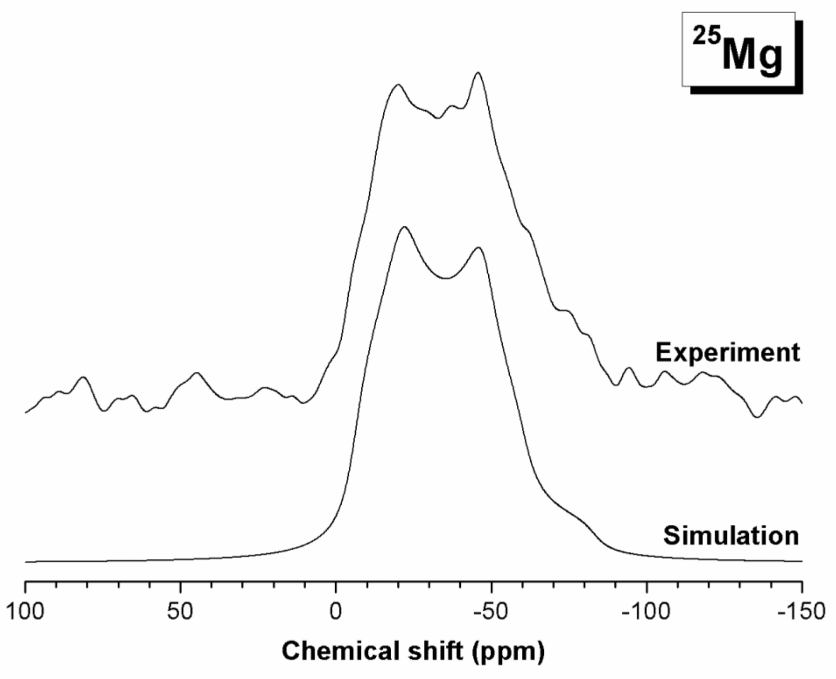

Fig. 5.6. ^{25}Mg MAS NMR spectrum (19.96 T, 10.0 kHz) of struvite-K, simulation was performed considering the second-order quadrupolar interaction for the central transition only

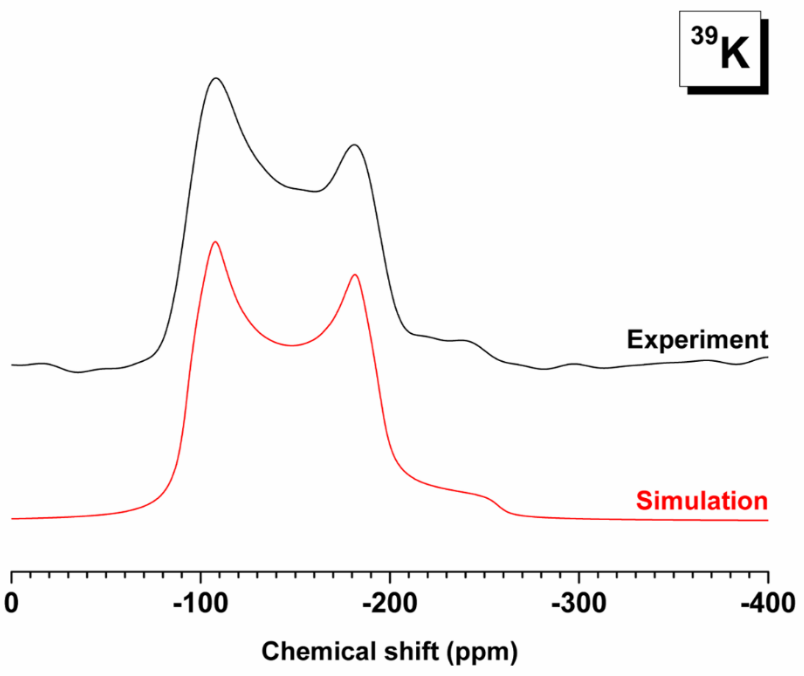

Fig. 5.7. ^{39}K MAS NMR spectra (19.96 T, 15.0 kHz) of struvite-K, simulation was performed considering the second-order quadrupolar interaction for the central transition only

The ^{25}Mg MAS NMR spectrum of pure struvite-K (Fig. 5.6) identified a single resonance, which was centred at δ_{iso} = -1.0 ppm, and associated with struvite-K where Mg is observed to octahedrally coordinated as $Mg(H_2O)_6^{2+}$ species in the crystal structure (Fig. 5.1). Similarly, the ^{39}K MAS NMR spectrum (Fig. 5.7) also exhibited a single resonance, which was centred at δ_{iso} = -73.1 ppm and was assigned to struvite-K. The K^+ ion was bonded five O atoms, one from a PO_4^{3-} unit and the remaining to H_2O molecules [22] as displayed in Fig. 5.1. In conjunction with the experimental data, the simulations for both ^{25}Mg and ^{39}K nuclei supported the existence of a single Mg and K environment present in the struvite-K crystal structure.

5.4 Conclusions and Future work

In this study, it was found that pure struvite-K undergoes a single step dehydration <120 °C leading to formation of the dehydration product, $MgKPO_4$, which is poorly crystalline up to 400 °C where it undergoes a phase transition to the β-$MgKPO_4$ phase and then secondly, to theγ-$MgKPO_4$ phase upon further heating. This was dissimilar to the dehydration behaviour of struvite, were the simultaneous loss of ammonia and water is observed, resulting in the formation of a poorly crystalline $MgHPO_4$ phase [123]. High field solid state ^{25}Mg and ^{39}K MAS NMR spectra and their corresponding quadrupolar parameters were presented for synthetic struvite-K for the first time. It has been shown experimentally and theoretically that both the Mg and K environments exist as single sites, which is in agreement with the reported crystal structure and existing ^{25}Mg MAS NMR data for isostructural struvite.

Further work should be undertaken in the following areas:

- Rietveld refinement of the XRD data to confirm the lattice parameters and crystal structure of pure struvite-K.
- High field (19.96 T) ^{39}K MAS NMR of struvite ($MgNH_4PO_4{\cdot}6H_2O$) and its analogues to support the NMR data presented for struvite-K, including calculation of the NMR parameters using TopSpin 3.0 [83] (based on experimental data) and QuadFit [127] from the refined crystal structures.
- XRD and DTA experiments to collect both heating and cooling data to further investigate the phase transitions associated with the struvite-K dehydration product, α-$MgKPO_4$. Including using a slower heating/cooling rate (2 °C/min) to separate the phase transitions into distinct regions.

6 Characterisation of blended MKPC binders

This chapter is based on the following published manuscript:

Gardner et al. Characterisation of magnesium potassium phosphate cements blended with fly ash and blast furnace slag, Cement and Concrete Research, ***2015****, vol. 74, pp. 78-87.*

6.1 Introduction

Magnesium potassium phosphate cement is a clinker-free acid-base cement, in which the development of, and therefore mechanical strength, is a direct result of the rapid formation of cementitious hydrogel type products [102]. The chemical reaction resulting in the formation of MKPCs (Eq. 4) is based on the dissolution of MgO and KH_2PO_4 reacting in solution to form struvite-K ($MgKPO_4{\cdot}6H_2O$). When compared to conventional Portland cements, MKPCs have different properties including near-neutral pH, low water demand, low drying shrinkage and high early compressive strength [36]. These properties make MKPCs remarkably versatile, and this cementing system has been used for rapid repair of damaged roads, bridges and runways [21], in conditioning various nuclear waste streams containing reactive metals [18, 61] and in dental castings with antibacterial properties [128].

In practical application, MKPC binders are frequently blended (up to 50 wt. % replacement) with fly ash (FA) to reduce water demand of the paste, and lower the exothermic output of the acid-base reaction, which avoids cracking of the hardened paste. The inclusion of FA in MKPC enhances the workability of the binder via the "ball-bearing effect" of the spherical particles [18, 54, 95, 96]. Several studies [18, 39, 129] based on FA/MKPC blended binders have suggested that FA simply acts as a diluent or inert filler, that modifies the aesthetics of MKPC to be compatible to traditional Portland cement, which has been deemed important for rapid-repair applications [54]. Conversely, others hypothesise that FA replacement promotes high mechanical strength in FA/MKPC binders, as a consequence of the formation of a secondary amorphous phase containing silicon-phosphate bonds [129, 130]. This is commensurate with the work of Wilson and Nicholson [102], who suggested that aluminosilicate glass can react with phosphoric acid to form a strong phosphate bonded cement. It is conceivable that the glassy aluminosilicate fraction of the FA reacts in the initially acidic environment of the MKPC, forming a secondary phase intermixed with struvite-K. If this occurs, it could result in a matrix of higher density that would be more impermeable to water, have a higher mechanical strength [131, 132] and provide additional sites for sorption of radionuclides, which would be of importance for application in the encapsulation of radioactive wastes. However, previous studies have not identified additional crystalline or amorphous reaction products, for example by powder X-ray diffraction or Fourier transform infrared spectroscopy, although the compressive strength and setting characteristics were altered in MKPC with the inclusion of FA [133].

Ground granulated blast furnace slag (GBFS) is a FA alternative that could be used as a diluent within MKPC binders. GBFS/MKPC blended binders are novel and little open literature is available concerning their properties. However, it should be noted that crystalline and amorphous blast furnace slags have been previously employed as filter/sorbent materials to remove phosphates from wastewater systems such as constructed wetlands and soil infiltration systems [134-136]. As such, it is conceivable that slag-phosphate interactions could occur within this system and potentially lead to the formation secondary reaction products.

The reaction of supplementary cementitious materials (SCMs), FA and GBFS, at the pH and chemical speciation conditions reached within MKPC binders, are largely unclear, detailed chemical or microstructural characterisation of secondary cementitious phases forming in FA/MKPC or GBFS/MKPC binders has not yet been reported, and there is a lack of evidence regarding whether or not the dissolution of FA or GBFS particles occurs (and to what extent) within MKPC-based binders. It is therefore imperative to develop an in-depth mechanistic understanding of the role of FA and GBFS within the phase assemblage of MKPC binders.

In this chapter, FA/MKPC and GBFS/MKPC binders were investigated via mechanical testing (compressive strength), XRD, SEM, ^{25}Mg MAS NMR, ^{27}Al MAS NMR, ^{29}Si MAS NMR, ^{31}P MAS NMR, ^{31}P[^{1}H] CP/MAS NMR and ^{39}K MAS NMR spectroscopy techniques, with the aim of providing the detailed characterisation of these systems.

6.2 Results and Discussion

6.2.1 Compressive strength

The compressive strength of blended MKPC binders (0.24 w/s) varied depending on the supplementary cementitious material added, as shown in Fig. 6.1. The compressive strength values of the FA/MKPC binder were comparable with data available for similar systems [18, 89]. The GBFS/MKPC was observed to have superior mechanical properties compared to the FA/MKPC binder at all curing ages investigated. At day 28, there was a notable (10 MPa) difference between the FA/MKPC (24 MPa) and GBFS/MKPC (34 MPa) binders. This difference can in part be explained by the powder properties (Table 3.1) of the raw FA and GBFS. Firstly, the particle size distribution (d_{90} = 66.1 and 1465.0 µm, respectively) and the BET surface area (2258 and 993 m^2/kg, respectively) indicate that the FA has a much narrower and larger surface area that the GBFS. This results in the FA having a greater water demand and can reduce the formation of struvite-K, which is the strength-forming phase within these blended MKPC binders. Secondly, the shape of the FA/GBFS particles can affect the compressive strength values due to particle packing effects described by Provis *et al.* [99], where the angular GBFS particles can interlock much better than the spherical FA particles and would result in a fewer voids voidage within the GBFS/MKPC binder. However, these differences in the powder properties is unlikely to be the sole cause of a 10 MPa variation in the mechanical performance.

The FA/MKPC binder achieved comparable compressive strength values to the MKPC-only binder (Fig. 6.1) whereas the GBFS/MKPC binder was notably stronger. During testing, it was observed that the failure mode of the MKPC-only was via viscoelastic deformation, rather than brittle fracture as in the FA/MKPC and GBFS/MKPC binders. This suggested a possible chemical interaction between GBFS, FA and MKPC influenced the cementitious properties of the binder.

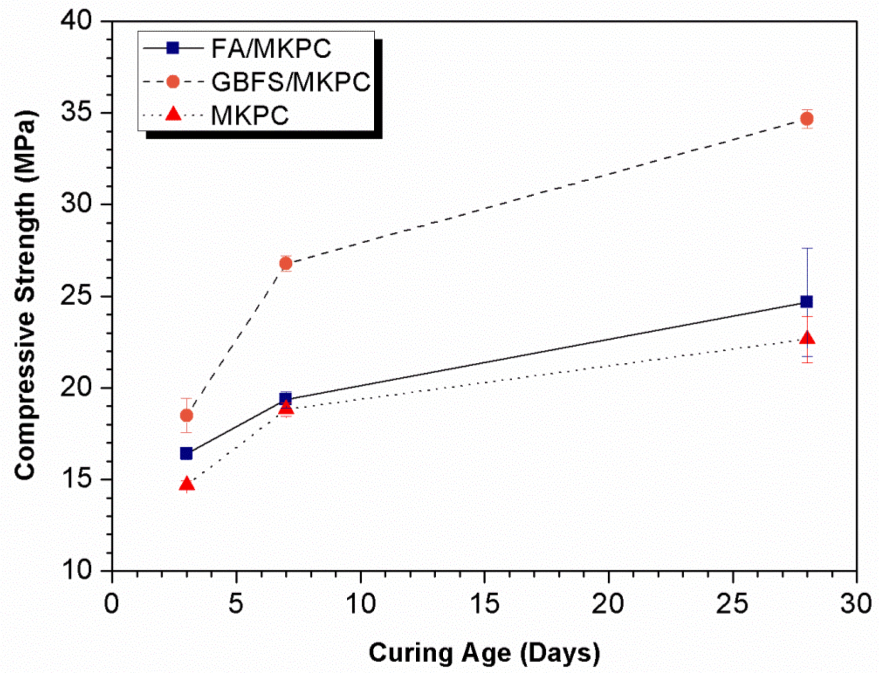

Fig. 6.1. Compressive strength of MKPC, GBFS/MKPC and FA/MKPC, as a function of curing time, the error bars are equivalent to ± 1 standard deviation

6.2.2 X-ray diffraction

The diffraction patterns of the anhydrous GBFS and FA, along with the hardened GBFS/MKPC and FA/MKPC binders cured for 28 days, are shown in Fig. 6.2. In the anhydrous GBFS, traces of åkermanite ($Ca_2MgSi_2O_7$, PDF #76-841) were observed, while in unreacted FA, quartz (SiO_2, PDF #11-0252) and mullite ($3Al_2O_3.2SiO_2$, PDF #15-0776) were identified. Diffuse scattering was identified, in FA between $15° < 2\theta < 25°$, and in GBFS between $25° < 2\theta < 35°$, which is associated with the X-ray amorphous aluminosilicate (FA) and calcium aluminosilicate (GBFS) glassy fractions that constitute the bulk material. Struvite-K ($MgKPO_4{\cdot}6H_2O$, PDF #75-1076) was found to be the main crystalline product forming in MKPC binders.

Traces of periclase (MgO, PDF #45-0946) were also identified in the MKPC binders, as MgO was added in excess (1.7:1 Mg/P molar ratio) of the stoichiometric proportions to ensure the conversion of all phosphate to struvite-K. In the MKPC-only system, the use of a stoichiometric ratio of MgO to KH_2PO_4 has been found to give complete reaction with no residual MgO visible in XRD [98, 137]. Crystalline secondary products were not observable in the MKPC blended either with FA or GBFS, and the degree of crystallinity of the struvite-K was found to be high.

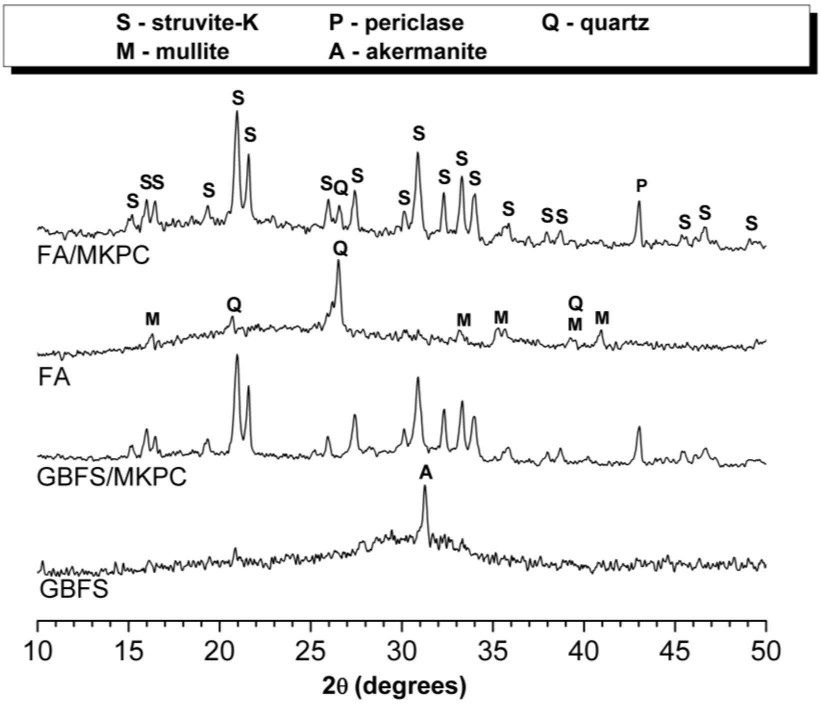

Fig. 6.2. X-ray diffraction patterns of GBFS/MKPC and FA/MKPC pastes after 28 days of curing

6.2.3 Scanning electron microscopy

Backscattered electron images of FA/MKPC and GBFS/MKPC binders are shown in Fig. 6.3, where the formation of a continuous struvite-K phase embedded with large struvite-K crystallites can be seen in both systems. The embedded particles of struvite-K, with a laminar habit, appeared to be highly cracked in polished sections, probably due to dehydration under vacuum for analysis. Angular light grey particles correspond to unreacted GBFS (Fig. 6.3A), while spherical particles of varying size (Fig. 6.3B) are FA particles. A similar microstructure has previously been reported for FA/MKPC [18], however, there are no reports of the microstructure of GBFS/MKPC binders in the open literature. The large struvite-K crystals are known mainly to occur in systems prepared using boric acid to retard the setting reaction [43], which therefore allows time for the large ordered crystalline structure to form within the adhesive binder [102].

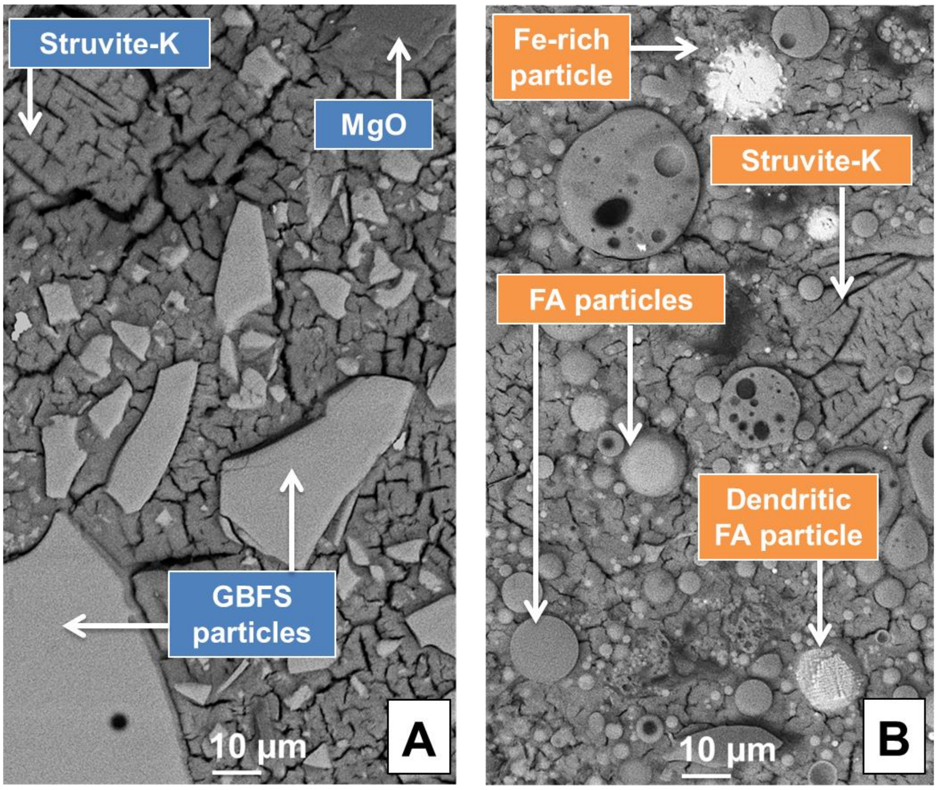

Fig. 6.3. Backscattered electron micrographs of (A) GBFS/MKPC and (B) FA/MKPC hardened pastes after 28 days of curing

6.2.3.1 Elemental mapping - GBFS/MKPC

In the GBFS/MKPC binder, a homogeneous distribution of Mg and P throughout the sample was observed in EDX maps (Fig. 6.4), consistent with the formation of crystalline struvite-K as the main binding phase of the system. Embedded unreacted

MgO (Fig. 6.4: Mg) particles were identified, consistent with XRD data in Fig. 6.2. Angular particles of various sizes rich in Ca, Al and Si (Fig. 6.4) correspond to the unreacted calcium aluminosilicate glassy fraction present in GBFS particles. The Al and Si EDX maps (Fig. 6.4: Al and Si) show incorporation of these elements in the binding matrix, indicating that dissolution of GBFS had occurred. GBFS dissolution and subsequent reaction to form a secondary phase would explain the enhanced strength development of the binder [96] as a result of filling pores in the matrix. The "area of interest" in Fig. 6.5 shows an embedded GBFS particle immediately neighbouring a region rich in Al, Si and P, which may be a secondary reaction product.

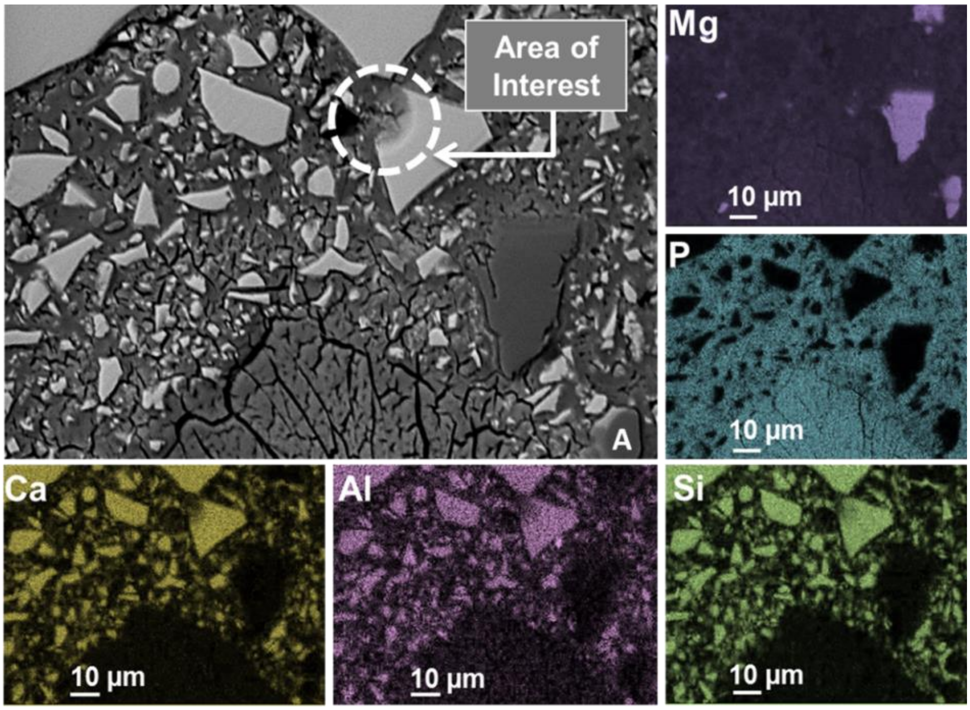

Fig. 6.4. Backscattered electron image and elemental maps of hardened GBFS/MKPC paste after 28 days of curing

Slags have previously been utilised as sorbents for phosphate removal from wastewater systems, and the mechanism for this process is controlled by the pH: at pH ≤ 6, the mechanism is phosphate adsorption onto the surface of the slag particles [135] whereas at pH ≥ 8, the phosphate precipitates as calcium phosphates [136]. In the GBFS/MKPC binder, the majority of the Ca (Fig. 6.4: Ca) appeared to be retained within the unreacted GBFS particles with no evidence presented for the formation of calcium phosphates. The feature labelled as “A” in Fig. 6.4 has been highlighted to demonstrate the impurities found in the MgO used in this study, feature “A” indicates that the MgO particles are ingrained with calcium silicate phase impurities present at 2.1 (Ca) and 4.3 (Si) wt. %, as determined by bulk XRF analysis (Table 3.2).

6.2.3.2 Elemental mapping - FA/MKPC

In the production of FA there is a negligible exchange of mass between particles, due to the nature of the coal combustion process. Therefore, FA particles have a wide variance in local composition, mineralogy and particle size, and this leads to a variable rate of reaction between particles [138]. The separation of Fe-rich and Al-Si-rich phases within fly ash particles can resulting in the formation of insoluble Fe-rich dendritic particles [139], such particles were observed in Fig. 6.3, labelled as “dendritic particle”. The backscattered micrograph of a FA particle (Fig. 6.5) highlights the variability within a FA particle, which is observed to be a plerosphere (contains smaller FA particles) with dendritic regions (Fe rich) [138]. In this particle, the dendritic phase must have formed during the cooling of the raw FA due to the perfect alignment of the dendritic phase with the circumference of the particle rather than through the separation of Fe-rich and Al-Si-rich phases within FA particles. Phase separation is reported to occur as a result in different glass dissolution rates under alkaline conditions leading to etching of the Al-Si rich matrix to form insoluble Fe-rich dendritic particles [139].

In addition to these FA characteristics, it was observed that the complete dissolution of the particle wall was observed in the FA particle (feature labelled “A” in Fig. 6.5). It is postulated that this dissolution occurred during the acid-base reaction of the FA/MKPC binder because the struvite-K matrix was observed within the particle wall opening. As a result of dissolution there is potential for the formation of secondary reaction products, which could be based on an Al and/or Si phase. Whilst the identification of the Fe-rich phases present in FA particles (e.g. hematite) [140] suggest they do not take part in any secondary reactions.

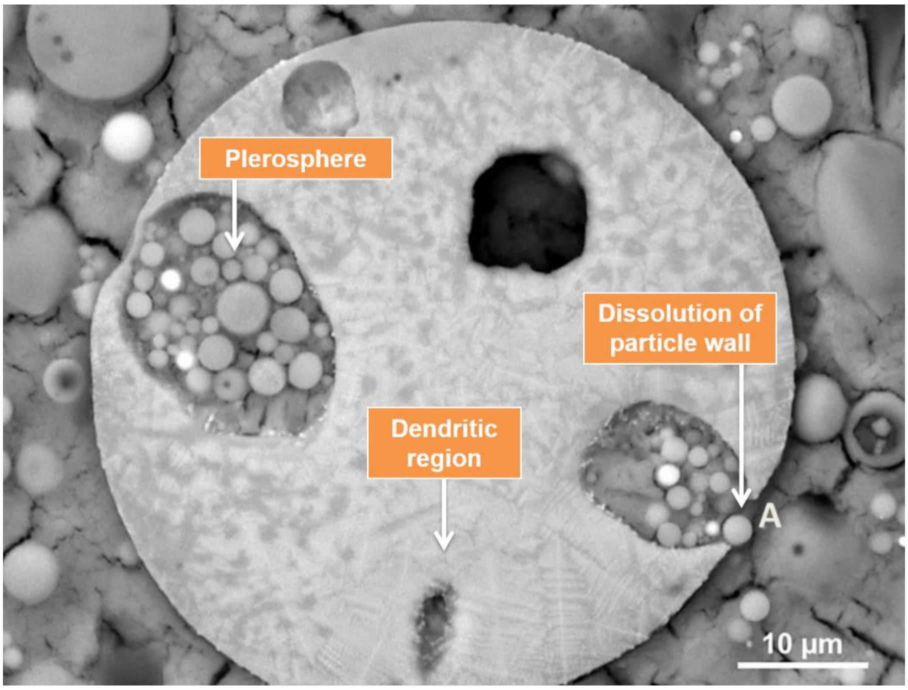

Fig. 6.5. Backscattered electron micrograph of a single FA particle showing prominent Al and Si dissolution resulting in phase separation leaving dendritic Fe-rich phases

A highly dense microstructure was identified in FA/MKPC binders (Fig. 6.6), large struvite-K crystals were found to be surrounded by FA cenospheres. Similarly, to GBFS/MKPC, unreacted MgO grains were evident throughout the matrix, the distinct radial growth pattern of the large struvite-K crystallite in Fig. 6.6 appeared to be centred around a Mg-rich region (Fig. 6.6: Mg). This indicated that the MgO particle acted as nucleation site for struvite-K formation within this sample. A transition zone between the large struvite-K crystallite and the matrix was also observed, where small FA cenospheres agglomerated in the boundary of the struvite-K. The Ca present in the FA/MKPC matrix (Fig. 6.6.Ca) appeared to be associated with Ca impurities within unreacted MgO grains (2.1 wt. % by XRF analysis of MgO, Table 3.2) rather than from the siliceous fly ash, which has a Ca content of 2.4 wt. % by XRF analysis of FA, Table 3.2. The unreacted MgO grains were also found to be associated with silicon impurities (4.3 wt. % by XRF analysis of MgO, Table 3.2), potentially a calcium silicate impurity. The main binding matrix was observed to be notably enriched in Al and Si (Fig. 6.6),resulting from the dissolution of the aluminosilicate FA particles within this system, leading to the formation of a secondary product, further examination using NMR analysis was conducted on these system to elucidate; (1) if there was a secondary reaction product and (2) the chemical formula of the additional phase.

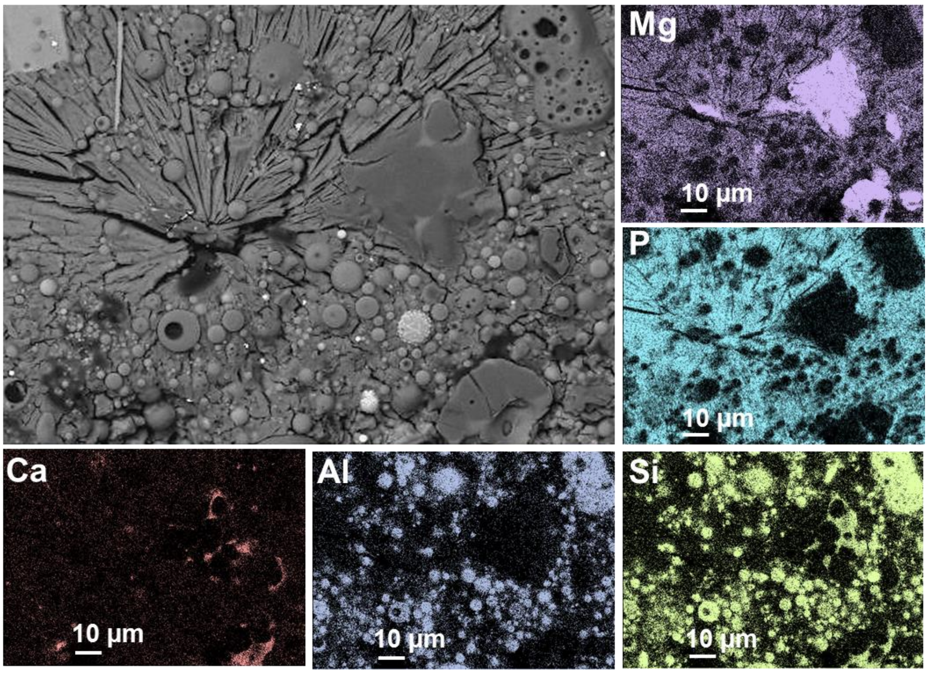

Fig. 6.6. Backscattered electron micrograph and elemental maps of hardened FA/MKPC paste after 28 days of curing

6.2.4 Nuclear magnetic resonance spectroscopy

6.2.4.1 ^{27}Al MAS NMR

^{27}Al MAS NMR spectra are known to clearly show three distinct Al coordination environments (Al^{IV}, Al^{V} and Al^{VI}), which for cements are located at chemical shifts between 52 to 80 ppm, 30 to 40 ppm and -10 to 15 ppm, respectively [78]. Two Al environments were identified in the ^{27}Al MAS NMR spectrum of unreacted GBFS, as shown in Fig. 6.7A. The first, and dominant site represents a broad Al^{IV} environment centred at 56 ppm, assigned to the aluminosilicate glassy fraction of the slag [141].

The second Al environment can be assigned to a minor band in the Al^{VI} region centred at 11 ppm, which may be attributed to a minor octahedral Al environment in the slag glass. In comparison, the GBFS/MKPC binder (Fig. 6.7A) has a narrower and slightly more deshielded Al^{IV} region than the unreacted slag, with a resonance centred at 54 ppm. The minor Al^{VI} environment in the GBFS/MKPC binder appeared to be more prominent than the unreacted GBFS. This may simply be because of a reduction in the intensity of the underlying resonance in this region during reaction.

The change in the Al^{IV} region in the GBFS/MKPC binder can be assigned to the remaining unreacted slag, which can undergo selective dissolution at the pH conditions reached in these binders (and thus display an apparent shift in its resonance position as one or more of the multiple Al environments present are selectively removed). The potential formation of a highly cross-linked secondary phase, more likely an aluminosilicate type product, can also be indicated by such a shift, where the Al selectively leached from the slag remains in tetrahedral coordination but shows a more ordered nature than in the unreacted slag glass. In blended Portland cement and alkali-activated slag systems, the Al^{IV} region usually sharpens upon reaction due to the formation of an Al-substituted calcium silicate hydrate (C-(A)-S-H) [142] type gel. In non-cross-linked C-A-S-H type phases, the chemical shift of tetrahedrally coordinated Al occurred at 74 ppm [143-146], when ^{27}Al MAS NMR spectra were collected at the magnetic field used in the present study. The fact that the reaction product peak here is located far from 74 ppm indicated that formation of a C-A-S-H product did not occur in the GBFS/MKPC binder.

In the Al^{VI} region (-10 to 15 ppm), the most obvious difference between the GBFS/MKPC and GBFS ^{27}Al MAS NMR spectra was the presence of a high intensity band centred at -9.5 ppm in the reacted material that was not present in the unreacted GBFS. This resonance can be assigned to the secondary reaction product forming in the GBFS/MKPC binder, which must be present at a very substantial concentration to display such a clear NMR signal. The resonance is more shielded (more negative chemical shift) than the resonances which have been assigned to Al^{VI} in the literature for condensed and intermediate alumina, aluminium hydroxide polymorphs and aluminosilicates [141, 147, 148], and Al-rich hydrous reaction products forming in GBFS-blended Portland cement [149], which are all usually identified between 0-13 ppm. An aluminium phosphate phase may potentially be formed as a result of chemical interactions between the GBFS and MKPC components. Aluminium-phosphate bonds are typically observed in ^{27}Al NMR spectra between 45 ppm and – 25 ppm, with three main phosphate environments: $Al(OP)_4$ centred at ~40 ppm, $Al(OP)_5$ centred at ~10 ppm, and $Al(OP)_6$ centred at ~ -20 ppm [78]. Accordingly, the additional signal at -9.5 ppm in the GBFS/MKPC binder could possibly be attributed to an $Al(OP)_6$-containing phase, however, the ^{31}P NMR spectra in Fig. 6.7A call such an interpretation into question, as will be discussed in the following section.

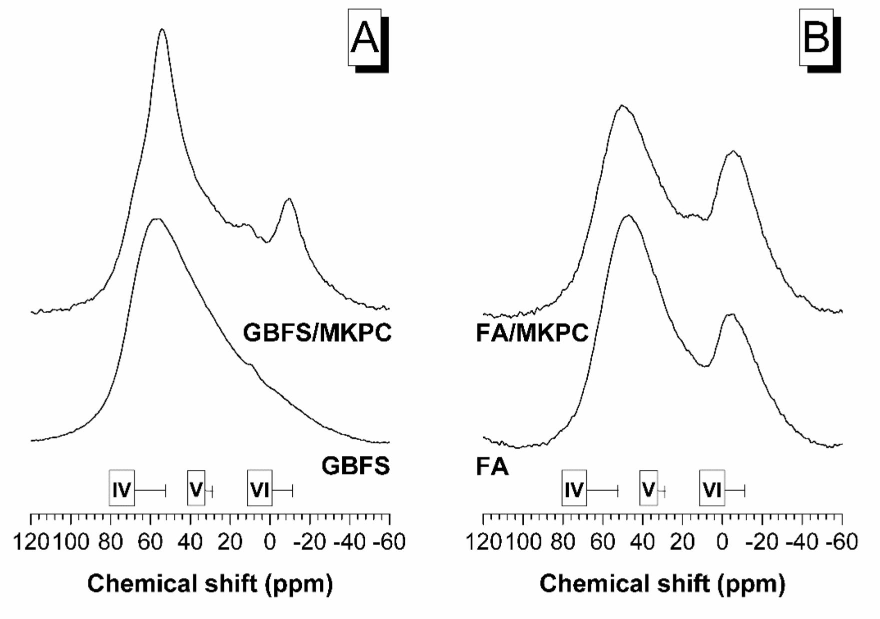

Fig. 6.7. ^{27}Al MAS NMR spectra (9.4 T, 14 kHz) for (A) unreacted GBFS and GBFS/MKPC hardened paste, and (B) unreacted FA and FA/MKPC hardened paste

Fig. 6.7B shows the ^{27}Al MAS NMR spectra for the unreacted FA and the FA/MKPC binder. The unreacted FA was found to have two main Al environments, Al^{IV} and Al^{VI}, centred at 47 ppm and -5 ppm, respectively. The band at -5 ppm can be assigned to mullite [150, 151], as identified by XRD (Fig. 6.2), while the broad band centred at 47 ppm can be assigned to the tetrahedral resonance of mullite (reported to be at 46 ppm [151]) and mullite-like glassy phases present in the FA [143]. In the FA/MKPC binders, the Al^{IV} band is slightly deshielded compared to the unreacted FA, with a chemical shift centred at 50 ppm.

In alkali-activated fly ash systems, the Al^{IV} region has been observed to sharpen due to the formation of a sodium aluminosilicate hydrate (N-A-S-H) type gel [143] but major differences were not observed in the lineshape of the spectrum in this region (Fig. 6.7B) suggesting that in the current study, the formation of typical alkali-activated fly ash phases did not occur. Formation of a new, low intensity band in the Al^{VI} region (centred at 14 ppm), and a slight increase in the intensity of the main Al^{VI}, centred at -5 ppm, are observed. These changes may be assigned to the secondary reaction product forming in the FA/MKPC binder, however, the paramagnetic relaxation of the NMR signal associated with the high Fe content of the fly ash limits the resolution achievable. Similarly to the GBFS/MKPC binder (Fig. Fig. 6.7B), the chemical shift changes do not correspond to the formation of aluminium hydroxide polymorphs and aluminosilicates [148], as they have not been identified in these binders, neither through XRD (Fig. 6.2) nor through thermogravimetry (Fig. 4.4Fig. 4.5). The ^{27}Al MAS NMR spectra (Fig. 6.7) have conclusively identified that minor chemical changes occurred in the octahedral and tetrahedral aluminium environments present within raw FA and GBFS, resulting from a direct interaction with the MKPC binder. It is likely that secondary reaction products were formed however, more in-depth analysis is required to determine the composition of the additional phase.

6.2.4.2 ^{31}P MAS NMR

Cross-polarisation (CP) NMR can be applied to examine the ^{31}P[^{1}H] interactions within a sample, in conjunction with information from ^{31}P MAS spectra. For GBFS/MKPC the CP/MAS NMR (Fig. 6.8A) shows a sharp resonance at 6.2 ppm in the orthophosphate region, which is associated with struvite-K. The low intensity broad signal centred at 3.6 ppm corresponds to KH_2PO_4 (spectrum not shown), in agreement with previously reported values [152]. KH_2PO_4 was used as a precursor to produce MKPC, and its presence in residual form indicates that the reaction did not proceed to completion, however no reflections for the excess KH_2PO_4 were observed in the X-ray diffraction patterns of the GBFS/MKPC and FA/MKPC binders (Fig. 6.2). Struvite-K is an isostructural analogue of struvite, and the ^{31}P chemical shift of struvite-K from the blended MKPC binders correlates well with that of struvite-K reported in Chapter 5 and with struvite at 6.1 ppm [124].

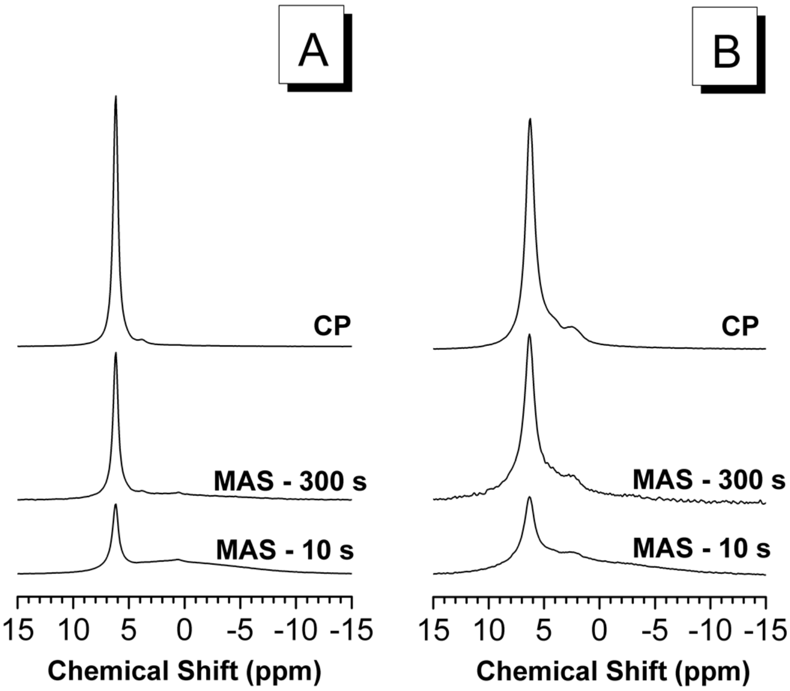

Fig. 6.8. ^{31}P MAS and CP/MAS NMR spectra (9.4 T, 10 kHz) for: (A) GBFS/MKPC and (B) FA/MKPC at MAS at relaxation times of 10 and 300 s, and ^{31}P CP/MAS at a relaxation time of 1 s

The $^{31}P[^1H]$ CP/MAS NMR spectrum of FA/MKPC (Fig. 6.8) was very similar to that of the GBFS/MKPC binder. However, there appeared to be an additional low intensity $^{31}P[^1H]$ signal located as a shoulder on the crystalline struvite-K peak, centred at 4 ppm, which may be related to an amorphous and/or partially substituted struvite-K phase, the identification of this peak is not yet entirely clear.

^{31}P MAS NMR experiments conducted at different relaxation times (10 and 300 s) enabled identification of low intensity phosphorus environments that have no ^{31}P[^{1}H] interactions, and thus do not appear in the CP/MAS spectra. In Fig. 6.8, the appearance of a broad signal between 4 to -4 ppm was observed for both the GBFS/MKPC and FA/MKPC binders. This is indicative of an amorphous phosphorus environment within these systems, and the feature appeared to be slightly more intense in the FA/MKPC binder than the GBFS/MKPC binder. The fact that this does not appear in the ^{31}P[^{1}H] CP spectra indicates that it is related to a phosphorus environment that has no intimate interaction with hydrogen, and therefore cannot be attributed to struvite-K.

Based on the chemistry of the binder, it is a logical progression to postulate that the changes observed in the ^{31}P spectra correspond with the additional octahedral Al signal observed in the ^{27}Al spectra (Fig. 6.7). However, the ^{31}P MAS NMR spectra (Fig. 6.8) for both the FA/MKPC and GBFS/MKPC binders, do not exhibit resonances necessary to satisfy a Al-P relationship within these systems, which would be in the range of -15 to -35 ppm [78]. Furthermore, multinuclear experiments intended to analyse Al-P interactions in these systems did not show any identifiable signals. It is therefore only possible to state that an amorphous orthophosphate environment exists in both binders without measurable aluminium interactions.

6.2.4.3 ^{29}Si MAS NMR

In the ^{29}Si MAS NMR spectrum of the unreacted GBFS shown in Fig. 6.9A, a broad resonance centred at -75 ppm was observed, consistent with the glassy fraction and the minor åkermanite present in the slag [141]. The spectrum of the GBFS/MKPC binder (Fig. 6.9A) has a similar lineshape to that of the unreacted slag, however, the formation of an additional broad band between -90 to -112 ppm was observed. Chemical shifts in this range of values are known to correspond to highly cross-linked Q^4 type sites [153] . This secondary band indicates that during the partial dissolution of GBFS, the Si reacted to form a highly cross-linked Si-rich type phase due to the presence of the observed [Q^4] chemical shift in the ^{29}Si MAS NMR spectrum for the GBFS/MKPC binder.

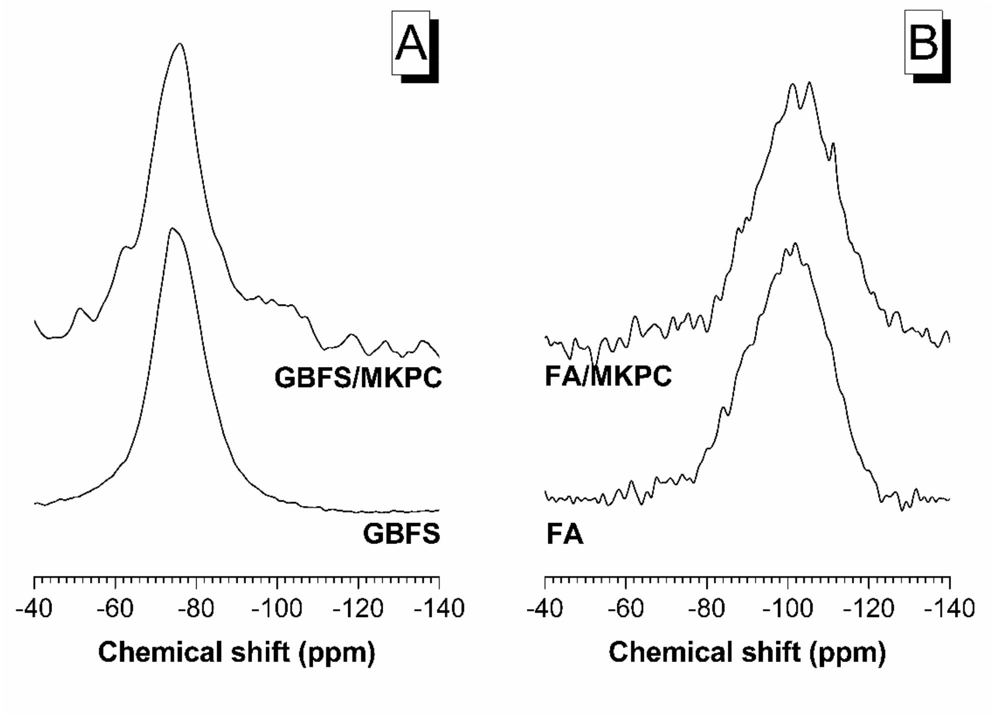

Fig. 6.9. ^{29}Si MAS NMR spectra (9.4 T, 6.8 kHz) of (A) unreacted GBFS and GBFS/MKPC hardened paste, and (B) unreacted FA and FA/MKPC hardened paste

The broad asymmetric ^{29}Si resonance observed between -76 and -122 ppm, centred at -102 ppm, for the FA sample (Fig. 6.9B) is consistent with the wide variety of Si environments present in the amorphous and crystalline phases in FA: a combination of quartz (~ -107 ppm) [154], mullite (~ -86 ppm) [151], and the vitreous fraction [155]. The FA/MKPC sample also displayed a broad resonance, between -80 and -124 ppm, centred at -103 ppm, unlike the GBFS/MKPC binder no sizeable ^{29}Si MAS NNR resonances were observed outside of the main broad resonance associated with unreacted FA. However, the presence of a defined peak (at -111 ppm) within the broad resonance could indicate the occurrence of a minor change in the Si environments within the FA/MKPC binder. There are two possible explanations for this: (1) variation in the NMR experiment conditions resulted in a more defined spectrum for the FA/MKPC binder, which was measured for 4900 repetitions, compared to 3600 repetitions for the unreacted FA or (2) due to the formation of secondary reaction products.

6.2.4.4 ^{25}Mg MAS NMR

High-field MAS NMR experiments for ^{25}Mg and ^{39}K nuclei were conducted on the GBFS/MKPC binder to explore any transformation in the chemical environments of these elements and are shown in Fig. 6.10 and Fig. 6.11, respectively. Unfortunately, it was not possible to study these nuclei in the FA/MKPC binder due to the relatively high iron content of the fly ash (9.34 % by XRF oxide analysis, Table 3.2). Table 6.1 defines the quadrupolar parameters: isotropic chemical shift (δ_{iso}), quadrupolar coupling constant (C_Q) and asymmetry (η_Q) used to simulate the spectra for the GBFS/MKPC binder as shown in Fig. 6.10-6.11) identifies two ^{25}Mg MAS NMR environments within the GBFS/MKPC, which are related to struvite-K (M2) and excess MgO (M1) respectively. The isotropic chemical shift, δ_{iso}, of MgO was calculated to be 26.4 ppm, which is consistent with data reported in the literature [156]. MgO is octahedrally coordinated and highly symmetrical, and therefore does not experience strong quadrupolar effects. The GBFS/MKPC binder showed a similar ^{25}Mg MAS NMR spectrum to pure synthetic struvite-K, $MgKPO_4 \cdot 6H_2O$ (reported in Chapter 5), where the Mg was represented by a single resonance. Using the empirical fitting method in TopSpin 3.2 [83] and the experimental data for pure struvite-K, the isotropic chemical shift for the Mg present in the GBFS/MKPC binder was calculated to be δ_{iso} = -1.0 ppm. The Mg is octahedrally coordinated within the crystal structure, as $Mg(OH_2)_6$ [22]. The quadrupolar parameters determined for struvite-K are comparable to those reported for struvite in the literature [81] but currently there is no published ^{25}Mg MAS NMR data to support the spectrum observed for struvite-K

Åkermanite ($Ca_2MgSi_2O_7$), identified as the only identifiable crystalline phase in GBFS (Fig. 6.2) should have a single resonance at a chemical shift of 47 ppm [156], however, this region overlaps with the much stronger signal of struvite-K. Due to the low content of åkermanite in the binder it was not possible to distinguish this resonance in Fig. 6.10. The ^{25}Mg MAS NMR resonances observed in the GBFS/MKPC spectrum can be fully assigned to a combination of MgO and struvite-K, at δ_{iso} = 26.4 and -1.0 ppm, respectively. This indicates that the magnesium present in the system does not form any secondary reaction products within the GBFS/MKPC binder.

Table 6.1. NMR quadrupolar parameters for sites calculated using high-field ^{25}Mg and ^{39}K MAS NMR nuclei experiments

		Experimental NMR		
Compound	**Nuclei site****	**δ_{iso} (ppm) (± 0.1)**	**C_Q (MHz) (± 0.1)**	**η_Q (± 0.02)**
MgO	^{25}Mg1	26.4	0.0 [156]	N/A
Struvite-K*	^{25}Mg2	-1.0	3.8	0.33
GBFS/MKPC	^{25}Mg1	26.4	0.0	N/A
GBFS/MKPC	^{25}Mg2	-1.0	3.8	0.33
Struvite-K*	^{39}K1	-73.1	2.2	0.14
GBFS/MKPC	^{39}K1	-73.1	2.2	0.14
GBFS/MKPC	^{39}K2	-107.7	0.1	0.10

*Struvite-K data also reported in Table 5.2, **The nuclei site number denoted for each nucleus (e.g. ^{25}Mg1) represents an arbitrarily assigned number for identification purposes, not the atomic position in the crystal structure.

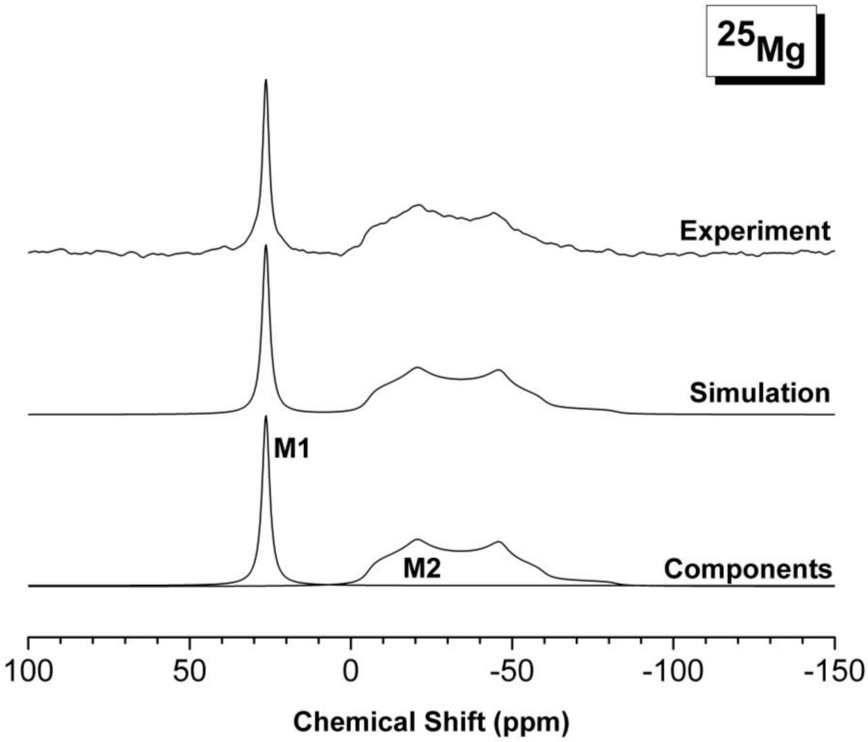

Fig. 6.10. 25Mg NMR spectrum (19.96 T, 10.0 kHz) of GBFS/MKPC, simulations were performed considering the second-order quadrupolar interaction for the central transition only

6.2.4.5 ^{39}K MAS NMR

The ^{39}K MAS NMR spectrum of the GBFS/MKPC binder (Fig. 6.11) was found to exhibit a dominant resonance assigned to struvite-K, where the potassium environment undergoes a quadrupolar distortion in the peak shape, similar to that of the ^{25}Mg/^{39}K MAS NMR resonance shape of pure struvite-K (Figs. 5.6 and 5.7). Using Topspin 3.2 [83] via an empirical fitting method the quadrupolar parameters (isotropic shift, asymmetry and line broadening) for the ^{39}K MAS NMR spectrum of GBFS/MKPC can be determined. Whilst the experimental data from the pure struvite-K sample (Table 5.1) was used a reference standard for the GBFS/MKPC binder as there is no published ^{39}K NMR data for struvite-K or struvite. Using this method, the simulated spectrum indicated that there are two ^{39}K sites present in the GBFS/MKPC binder. The first and most dominant (K1) is the resonance associated with struvite-K, which has an isotropic chemical shift of δ_{iso} = -73 ppm (K1) and was comparable to that reported for struvite-K system (Chapter 5).

The simulation in Fig. 6.11, suggests the presence of a secondary K environment (K2) downfield of the main struvite-K resonance. The K2 phase has been estimated to have an isotropic chemical shift of δ_{iso} = -107.7 ppm (Fig. 6.11), it is possible to confidently conclude that the K2 phase was not associated with free hydrated K^+ ions, which would have a resonance at 0 ppm [82]. Attempts to fit the lineshape with dispersions in quadrupole coupling parameters, consistent solely with a disordered K environment, were unsuccessful. Also, a direct comparison between the ^{39}K MAS NMR spectra of GBFS/MKPC and pure struvite-K (Fig. 6.12) clearly demonstrates the presence of the low intensity resonance, which is labelled as K2. This resonance cannot be replicated using the struvite-K quadrupolar parameters, even when extensively varied. Therefore, it is suggested that the K2 environment must be incorporated within a secondary phase in the GBFS/MKPC binder. Certain potassium feldspars ($KAlSi_3O_8$) exhibit ^{39}K MAS NMR resonances within the region of the K2 environment [157-159], whilst their ^{27}Al and ^{29}Si signals at 50 to 65 ppm and -86 to -107 ppm respectively, are consistent with the spectra reported here. Given the aluminosilicate-rich nature of the SCMs and the large quantity of potassium added to these systems as KH_2PO_4, there could be the potential for poorly crystalline assemblages of this nature. Further work is thus required to fully understand the formation of K-Al-Si secondary phases in these blended MKPC binders.

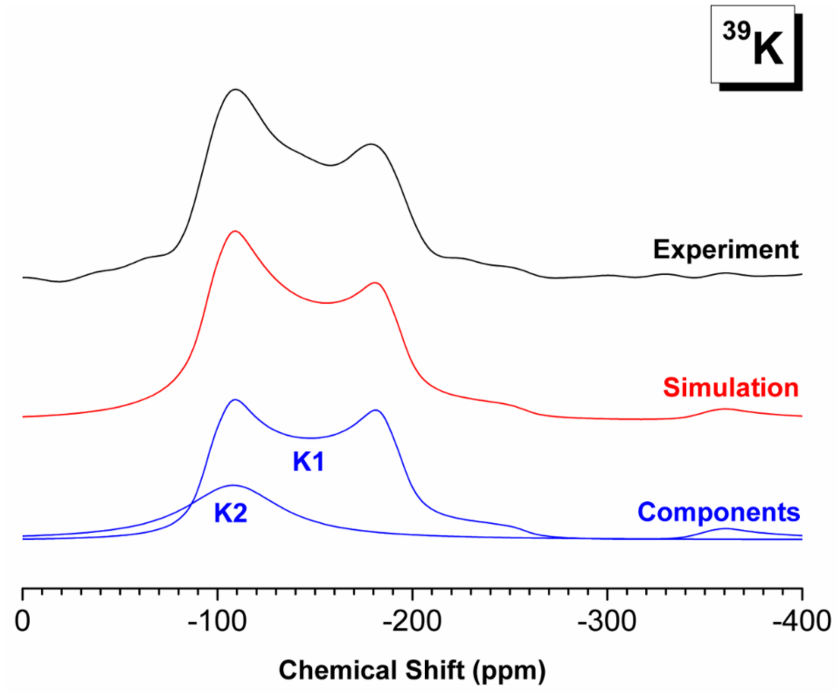

Fig. 6.11. ^{39}K NMR spectra (19.96 T, 15.0 kHz) of GBFS/MKPC, simulations were performed considering the second-order quadrupolar interaction for the central transition only

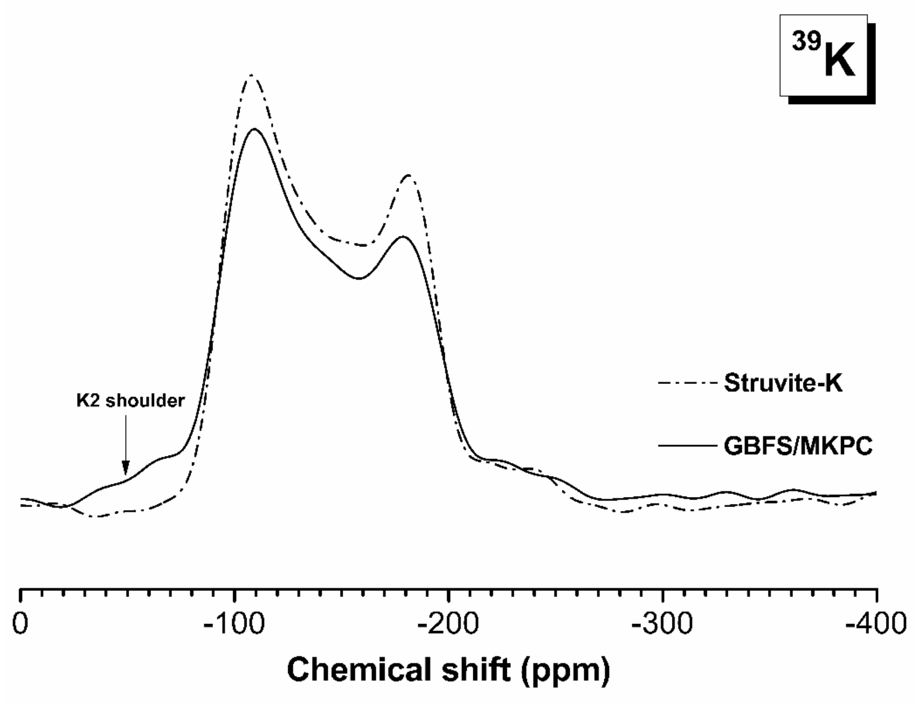

Fig. 6.12. ^{39}K NMR spectra (19.96 T, 15.0 kHz) of GBFS/MKPC and pure struvite-K

6.3 Conclusions and Future work

The principal role of FA and GBFS in blended MKPC binders is as a filler and diluent. However, microstructural characterisation and multinuclear NMR spectra indicated dissolution of the aluminosilicate glassy fractions of both FA and GBFS under the near-neutral pH conditions prevailing within MKPC binders. This has been unambiguously demonstrated for the first time in this contribution. The ^{27}Al and ^{29}Si MAS NMR do not show the formation of C-(A)-S-H gels, as reported in the literature, which is a clear difference between the behaviour of these SCMs under near-neutral pH conditions compared to the reaction products formed through their hydration at high pH. This suggests that the latent hydraulic nature of the slag and pozzolanic nature of the fly ash are not being activated within the near-neutral pH conditions of MKPC binders. Therefore, the chemical changes identified through SEM and NMR investigations are the result of dissolution of the Al and Si from the GBFS and FA particles, induced by the phosphate species present in the MKPC formulations. The secondary products forming in MKPC blended with FA and GBFS are highly enriched in Al and Si, which could potentially lead to the formation of a potassium aluminosilicate phase. The additional phases formed through these interactions may enhance overall densification and potentially increase the durability of MKPC binders. NMR spectra were provided for the first time to reporting the true isotropic chemical shift and quadrupolar parameters for the ^{25}Mg and ^{39}K nuclei present in GBFS/MKPC binders.

Further work should be undertaken in the following areas:

- Clarification of the existence of both the potassium aluminosilicate phase and an amorphous orthophosphate phase, as proposed from the NMR spectra reported in this chapter, ^{27}Al MQMAS NMR experiments will be used to elucidate the K-Al-Si relationships within the GFBS/MKPC binder.

7 High temperature stability of MKPC binders

This chapter is partially based on the following published manuscript:

*Gardner et al. Evolution of phase assemblage of blended magnesium potassium phosphate cements binders at 200 and 1000 °C, Advances in Applied Ceramics, **2015**, vol. 114, pp. 386-392.*

7.1 Introduction

Cementitious binders based on the magnesium potassium phosphate (MKPC) bonding are in general, near-neutral pH systems formed from the acid-base reaction of KH_2PO_4 and dead burnt MgO [160]. These properties have led to their consideration as encapsulants for certain nuclear wastes (especially reactive metals, such as Al, Mg and U) that may otherwise corrode in the high pH conditions or with the high availability of free water within conventional Portland cement (PC) based encapsulants [15, 17-19].

The acceptance of a conditioned wasteform/waste package is contingent on meeting strict safety requirements, laid out in waste package specifications and acceptance criteria. In the UK, these conditions pertain to the mechanical, thermal and immersion properties of the wasteforms and waste packages [28, 161]. The thermal properties of waste packages are especially important for understanding and assessing the potential impact of accident scenarios, such as fires, which might occur during transportation, or after emplacement of a waste package into an engineered repository (either for temporary, or final storage). It is imperative that waste packages minimise the release of radioactive material under such fire conditions, which may burn hotter, and for longer due to limited access, especially if deep underground in a geological repository [161]. This is especially pertinent in light of the recent fires and subsequent radionuclide release at the Waste Isolation Pilot Plant (WIPP) in the USA [162], which highlight the importance of understanding how waste packages might evolve and behave at elevated temperatures.

Cementitious materials typically undergo dehydration and breakdown of the principal binding phases upon heating, which leads to the evaporation of water and the build-up of pressure within the pores [163, 164]. As a consequence of the internal stresses generated by differential thermal expansion and shrinkage, in addition to the water evaporation, severe loss of mechanical performance is typically experienced, for example a GBFS/PC (1:1) mortar exposed to 900 °C for 4 hours lost ≈ 84 % of its initial strength of 30 MPa at 20 °C [163]. Thus, external fires may have a deleterious effect upon the performance of conventional Portland cement based wasteforms, which might ultimately result in the release of radionuclides to the immediate or wider environment, depending upon the scale and location of a fire.

Magnesium phosphate compounds have historically found uses as refractory materials for furnaces [31, 165-167], therefore it is anticipated that MKPCs may be capable of withstanding a wide range of temperature conditions. Most of the literature regarding the thermal properties of magnesium phosphate cements describes magnesium ammonium phosphate cements ($MgNH_4PO_4 \cdot 6H_2O$, struvite) rather than MKPC binders. In ammonium-containing systems, various phase transitions were noted upon heating, resulting in intermediate poorly crystalline phosphate assemblages [39, 168] and ultimately sintering of the phosphate materials to form a ceramic-like phase at 1300 °C [168].

In practical cementitious applications, MKPC binders are often blended (up to 50 wt. % replacement) with supplementary cementitious materials (SCMs) to minimise cracking due to the exothermic output of the acid-base reaction, to reduce material costs and to ensure sufficient workability. A recent study on MKPCs blended with up to 40 wt. % fly ash [169] reported the conversion of struvite-K ($MgKPO_4 \cdot 6H_2O$) to $MgKPO_4$ via a dehydration process, when exposed to 1000 °C for 3 hours, with retention of around ≈ 25 % of the original compressive strength, but without the presentation of detailed characterisation data. Preliminary studies of MKPC binders blended with 50 wt. % fly ash (FA/MKPC) and ground granulated blast furnace slag (GBFS/MKPC) showed that a disordered $MgKPO_4$ phase was formed upon heating to 200 °C, followed by crystallisation at temperatures below 1000 °C.

In this study, FA/MKPC and GBFS/MKPC cements were exposed to temperatures between 20 to 1200 °C, and the resulting products characterised using dilatometry, X-ray diffraction (XRD), scanning electron microscopy (SEM), solid state magic angle spinning (MAS) nuclear magnetic resonance (NMR) techniques (^{27}Al and ^{29}Si) and Mössbauer spectroscopy. We discuss the microstructural stability of these MKPC materials under exposure to high temperatures to elucidate the possible failure mechanisms in potential fire scenarios related to storage in a geological disposal facility.

7.1.1 Thermal test procedure

Blended MKPC samples (0.24 w/s) were cut into cylinders (*h* 10 ± 0.1 mm, ϕ 14 ± 0.5 mm) *using* a Buehler Isomet low speed saw. Using a zirconia tile, the samples were placed into a pre-heated furnace (Elite, model 15/5) at 200, 400, 800, 1000 and 1200 °C ± 10 °C, respectively. After allowing time for the furnace to stabilise (<5 minutes) and a 30 minute thermal exposure, the samples were removed and quenched to room temperature, as illustrated in Fig. 7.1. Sample dimensions were measured using digital callipers and weighed before and after high temperature exposure to allow changes in physical properties to be determined.

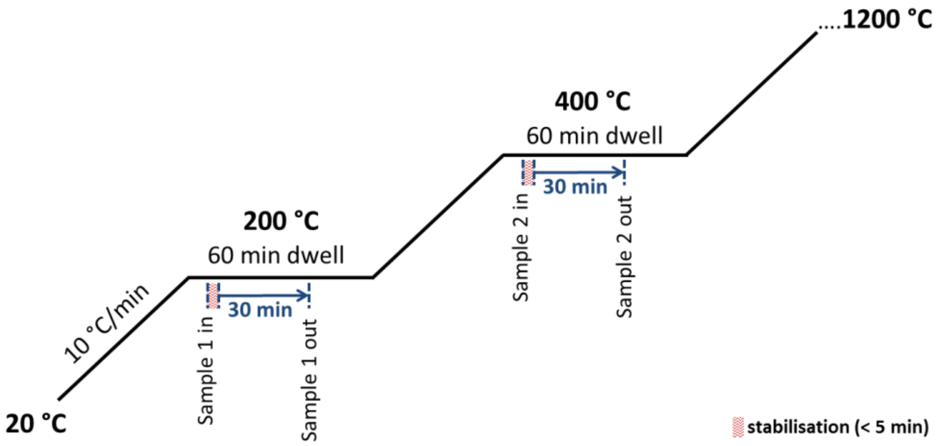

Fig. 7.1. Fire performance thermal treatment programme

The thermal test methodology used in this study was complementary to both the IAEA transport regulations [170] and the Radioactive Waste Management Limited (RWM) requirements for a geological disposal facility (GDF) in the UK [161]. The former requires samples to be fully engulfed at an average temperature of 800 °C for a 30 minute period [170], whereas the RWM parameters increased both the average temperature and exposure time to 1000 °C and 1 hour, respectively [161]. The enhanced RWM parameters are intended to take into account the higher potential risk factor associated with fire incidents in a geological disposal because (1) any below-ground fire may reach higher temperatures due to heat reflected off tunnel features, and (2) the restricted access (compared to an above-ground fire) would increase the response time and therefore there is potential for the fire to burn for longer [161]. For blended MKPC formulations to be used in waste encapsulation and long-term storage in a GDF, it is essential that the waste packages can withstand higher temperatures whilst retaining their structural integrity and minimising radiological release. As a compromise to the two set of regulations described above, the samples in this study were exposed for 30 minutes to temperatures of 1200 °C, which surpasses the current IAEA transport regulations. The duration required for the enhanced RWM parameters (1 hour) was based on full-scale waste packages but as relatively small sample sizes were used in this study, an exposure time of 30 minutes was deemed acceptable.

7.2 Results and Discussion

7.2.1 Physical properties

In FA/MKPC and GBFS/MKPC binders, the principal mass loss event occurred below 200 °C, which resulted in a mass change of ≈ -20.7 % at 200 °C (Table 7.1) for both binders, consistent with the dehydration of struvite-K (to be discussed further in section 7.2.2). The mass decrease from 20 °C was associated volumetric contractions of 6.1 % for FA/MKPC and 8.8 % for GBFS/MKPC, respectively. For each measurement, the volumetric and mass differences were calculated relative to a specimen not exposed to heat (i.e. kept at room temperature) and measured ex-situ therefore, the changes do not represent incremental volume/mass changes from in-situ heating. Similar volumetric and mass changes were observed in the samples exposed to 400 and 800 °C. However, at 1000 °C, the relative volumetric change (%) for both the FA/MKPC and GBFS/MKPC samples (compared to the 20 °C specimen) appeared to decrease, as shown in Table 7.1. This is postulated to be associated with phase assemblage changes in the blended MKPC binders resulting from the FA or GBFS reacting with the dehydration product, $MgKPO_4$.

Table 7.1. The volumetric (± 0.4 %) and mass changes (± 0.3 %) of FA/MKPC and GBFS/MKPC binders exposed to high temperatures*

Temperature (°C)	% change after heating (compared to a 20 °C sample)			
	FA/MKPC		GBFS/MKPC	
	Volume	Mass	Volume	Mass
200	-6.1	-20.7	-8.8	-20.8
400	-6.3	-23.2	-8.6	-23.5
800	-8.4	-26.3	-8.7	-24.0
1000	-4.2	-26.4	-3.4	-23.7
1200	-1.2	-29.2	-8.9	-28.2

*The quoted errors are derived from calculated standard deviations from the 800 °C experiment, which was performed in triplicate.

At 1200 °C, the volume change of the GBFS/MKPC binder appeared to significantly increase to - 8.9 % of the original volume (at 20 °C), whereas the FA/MKPC continued to reduce in volume compared to the 20 °C specimen. In Fig. 7.2, the photographs of the FA/MKPC and GBFS/MKPC binders indicate that no macroscopically visible spalling or cracking occurred as a result of physical changes caused by exposure to high temperatures. In the FA/MKPC binder (Fig. 7.2A), a progressive colour change (from dark grey via reddish brown to a final dark brown) was observed between the 20 °C and 1200 °C samples, which is postulated to be associated with iron oxidation in the fly ash. In the GBFS/MKPC binder (Fig. 7.2B), a more subtle colour change (from grey to light grey) was observed, and the greenish tinge observed at low temperature exposure (200 °C) was attributed to polysulfide species released by the GBFS [26] faded with increasing temperature to be indistinguishable at 1200 °C.

(A) FA/MKPC

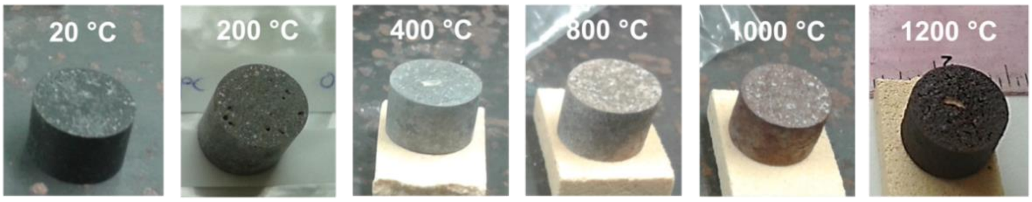

(B) GBFS/MKPC

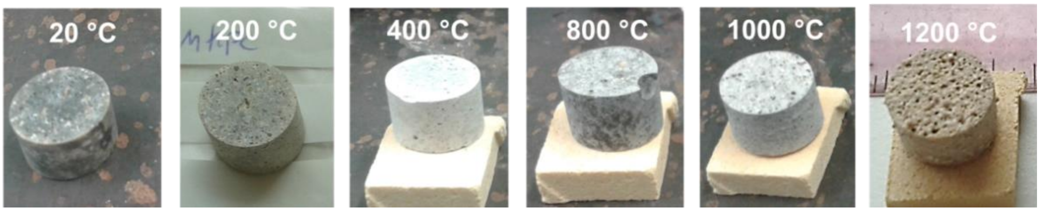

Fig. 7.2. Photographs of (A) FA/MKPC and (B) GBFS/MKPC hardened pastes exposed to temperatures between 20 and 1200 °C. The samples are 14 mm diameter (± 0.6 mm) and 10 mm height (± 0.5 mm)

The dilatometric traces of the FA/MKPC and GBFS/MKPC binders are presented in Fig. 7.3. Both samples experienced a shrinkage event between 30 - 200 °C, which was associated with the dehydration of struvite-K and was followed by a second shrinkage event between 500 - 700 °C. The dilatometry data closely matches the measurements reported in Table 7.1 (up to 800 °C) even though the latter were taken using digital micrometer after each sample was quenched in air to room temperature (rather than in situ at high temperature as for the dilatometry samples).

However, a thermal expansion was noted in the dilatometric samples of both binders from 700 to 1200 °C (Fig.7.3), which was dissimilar to the volumetric changes reported in Table 7.1 for the GBFS/MKPC binder exposed to 1200 °C. This dissimilarity is postulated to be associated with the formation of additional crystalline phases *via* the reaction of the supplementary cementitious materials (FA, GBFS) and the dehydrated struvite-K product ($MgKPO_4$). To support this theory, evidence for new crystalline phases were identified in the XRD analysis for both blended binders at >800 °C (to be discussed in section 7.2.3). The dilatometric samples experienced a total shrinkage of ≈ 4 %, the impact of this shrinkage on the physical properties did not result in cracking on spalling, which was encouraging from a fire performance aspect as both the FA/MKPC and GBFS/MKPC binders can physically withstand exposure to high temperatures.

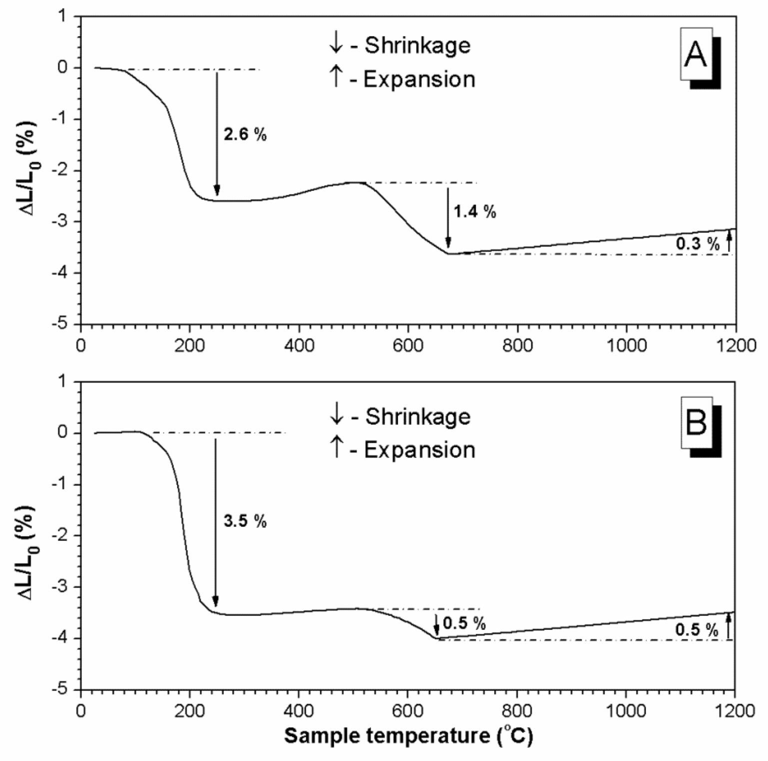

Fig. 7.3. Dilatometric traces of the (A) FA/MKPC and (B) GBFS/MKPC up to 1200 °C

7.2.2 Thermal analysis

The dehydration behaviour of FA/MKPC and GBFS/MKPC binders as measured using TGA and differential thermogravimetric (DTG) analysis, shown in Fig. 7.4, was found to be comparable to that of pure struvite-K systems [98]. A large mass change occurred between 50 °C and 150 °C, which were calculated to be -18 % and -20 % for the two blends respectively. This was assigned to the single-step dehydration of $MgKPO_4 \cdot 6H_2O$, leading to the formation of the dehydration product, $MgKPO_4$ (Eq. 8).

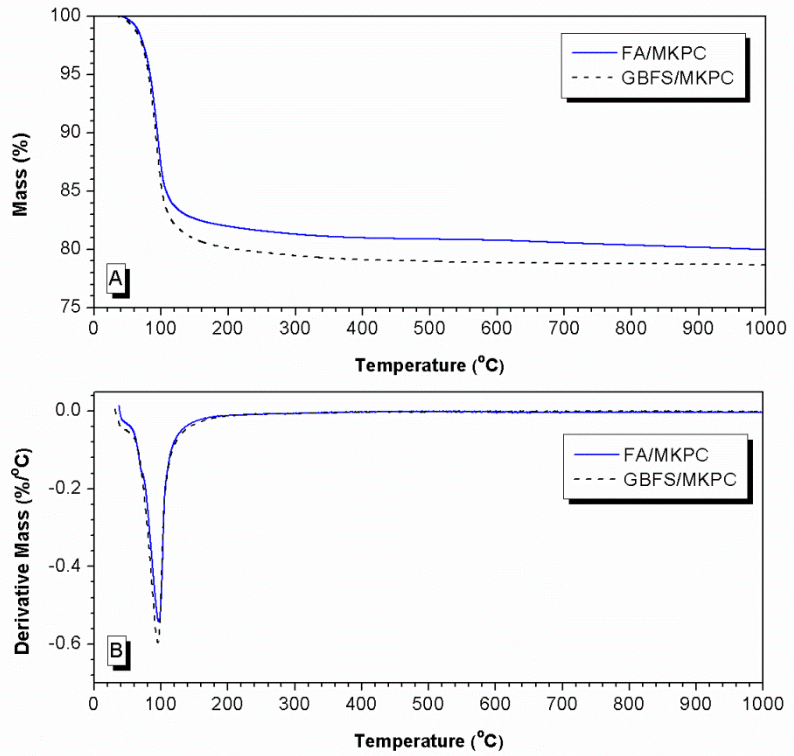

Fig. 7.4. TGA/DTG of (A) FA/MKPC and (B) GBFS/MKPC pastes after 7 days curing

There was a 2 % point difference in TG data between FA/MKPC and GBFS/MKPC, which indicated that in a 20 mg TGA sample that there is more of the cementitious struvite-K phase was present in the GBFS/MKPC sample. This could potentially be explained by the surface area values reported for FA and GBFS, where the BET values (Table 3.1) are reported to be: 2258 m^2/g and 993 m^2/g, respectively. The FA has a significantly larger surface area than the GBFS and therefore a higher water demand, which would result in less water being available for the formation of struvite-K in the

FA/MKPC binder. The DTG analysis shown in Fig. 7.4B further emphasises that only one mass loss event occurred, suggesting that the inclusion of FA and GBFS within MKPC binders does not have an effect on the dehydration behaviour.

7.2.3 Powder X-ray diffraction

7.2.3.1 FA/MKPC

At 20 °C struvite-K was identified as the main crystalline product formed in the FA/MKPC binder (Fig. 7.5). Traces of unreacted periclase (MgO, PDF #45-0946) from the excess dead burnt magnesia, along with crystalline quartz (SiO_2, PDF #78-2315) and mullite ($3Al_2O_3.2SiO_2$, PDF #15-0776) from the unreacted FA were also identified. After exposing the FA/MKPC binder to 200 °C, the reflections for periclase, quartz and mullite remained unchanged, whereas the struvite-K reflections disappeared due to dehydration. No reflections associated with newly formed magnesium phosphate phases were observed, which suggests that the struvite-K collapsed to a non-crystalline phase upon exposure to 200 °C. This is in agreement with the thermal investigations of struvite ($NH_4MgPO_4.6H_2O$), it was established that no reflections for the equivalent dehydration product were identified between 200 – 700 °C for the struvite system [39, 121, 122]. Neiman and Sarma [39] postulated that this was due to the formation of a non-crystalline polymeric phase, whereas Sarkar [121] suggested that $MgHPO_4$ was formed due to liberation of both the crystal-bound H_2O and NH_4, that occurred because struvite is unstable above 50 °C

The long-range order partially returned at 400 °C, evidenced by the appearance of α-$MgKPO_4$ (PDF #50-0146, *P2₁/c*) reflections amongst the reflections assigned to the FA crystalline phases (quartz and mullite) and excess periclase. The identification of the α-$MgKPO_4$ phase at 400 °C was contradictory to the in situ HTXTD observations for pure struvite-K (Fig. 5.2), where the β-$MgKPO_4$ phase was detected at 400 °C. The likely explanation for this difference is associated with the experimental conditions (i.e. in situ for struvite-K vs. ex situ for the blended MKPC binders). We postulate that the β-$MgKPO_4$ phase in the FA/MKPC binder underwent a reverse phase transition upon quenching to the α-$MgKPO_4$ phase prior to data collection. In accordance with the ex situ behaviour of the FA/MKPC binder, any reference to the dehydration product herein will refer to the α-$MgKPO_4$ phase.

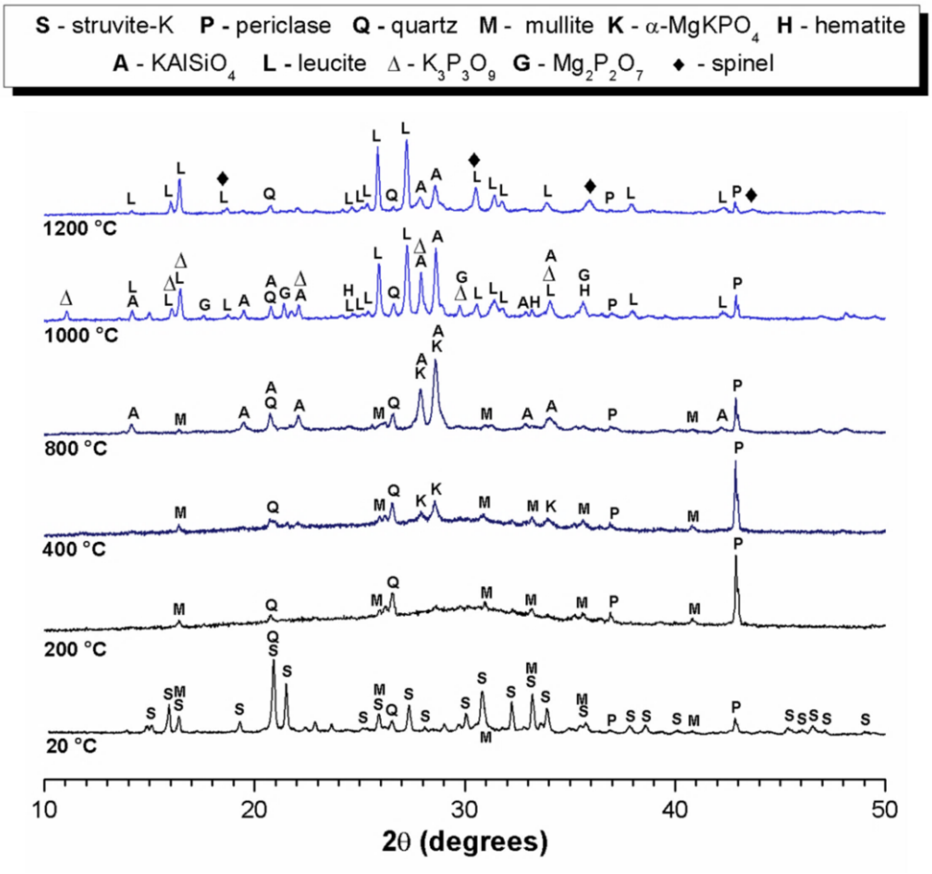

Fig. 7.5. Ex situ X-ray diffractogram of hardened FA/MKPC binders heated up to 1200 °C

After exposure at 800 °C, new crystalline reflections emerged in the FA/MKPC specimen, which were associated with a potassium aluminosilicate phase ($KAlSiO_4$, PDF #31-0965). The main reflections at 27.9° and 28.6° 2θ overlap those previously assigned to the α-$MgKPO_4$ phase at 400 °C. It is postulated that at 800 °C, both phases are present due to the irregular shape of the main reflections and through the existence of several reflections associated with the $KAlSiO_4$ phase. Rietveld refinement conducted on this diffraction pattern would assist in elucidated the correct phase assemblage (to be included in future work). The emergence of $KAlSiO_4$

could be attributed to the crystallisation of amorphous potassium aluminosilicate previously identified within FA/MKPC binders at room temperature (discussed in Chapter 6). Alternatively, it could be the result of a reaction between potassium being extracted from the main Mg-P rich phase to interact and with the FA particles, which are rich in Al and Si, to form phases such as $KAlSiO_4$ observed at 800 °C, and leucite ($KAlSi_2O_6$, PDF #38-1423) observed above 1000 °C. Further phase assemblage changes occurred as a result of FA and $MgKPO_4$ reactions in the FA/MKPC binder at 1000 °C (Fig. 7.5), this was represented by the increased number of reflections associated with leucite, $K_3P_3O_9$ (PDF #70-0048), $Mg_2P_2O_7$ (PDF #32-0626) and hematite (Fe_2O_3, PDF #33-0664). The phase assemblage transformation of the FA/MKPC binder, struvite-K to leucite ($KAlSi_2O_6$) at 1200 °C combined with the physical properties observed (no specimens displayed macro-cracks) suggests that the changes are stable and don't result in negative impacts on the materials.

A similar transition was observed in FA-derived geopolymers, where leucite was identified as the main crystalline product formed in a K-aluminosilicate binder upon exposure to 1200 °C [171]. Comparatively, in a potassium geopolymer (derived from kaolinite, Si/Al ratio = 1), it was found that both $KAlSiO_4$ and leucite phases were stable between 1000 - 1400 °C [157]. In the current study, the Si/Al ratio in the FA/MKPC binder was approximately 2 (Table 3.2), which resulted in the presence of both $KAlSiO_4$ and leucite at 1000 °C leading to the preference for leucite at 1200 °C. It is postulated that the interaction between FA and potassium in the FA/MKPC binder was similar to geopolymer systems [157], although taking place under much less alkaline conditions

The $Mg_2P_2O_7$ phase identified in Fig. 7.5 was also found in struvite-based ($NH_4MgPO_4 \cdot 6H_2O$) dental investments heated between 750 – 1100 °C, which implies that the two systems behaved comparably when exposed to high temperatures [39, 168]. After exposure at 1200 °C, the relative intensities of the $KAlSiO_4$ and SiO_2 reflections appeared to decrease whilst the relative intensities of leucite reflections increased. This indicated that further reactions were taking place at 1200 °C, which was reinforced by the formation of an iron-magnesium aluminate spinel phase similar to $Mg_1Al_{0.8}Fe_{1.2}O_4$ (PDF #71-1235) and loss of Mg or P-containing phases (e.g.

$K_3P_3O_9$ and $Mg_2P_2O_7$). The observed phase assemblage alludes to a chemical reorganisation at 1200 °C, leading to Mg and P incorporation into non-crystalline phases (i.e. glass fractions).

7.2.3.2 GBFS/MKPC

At 20 °C, the diffraction pattern of the GBFS/MKPC binder (Fig. 7.6) was similar to previous results where struvite-K was identified as the main crystalline phase, in addition to the reflections associated with unreacted periclase and åkermanite (Ca_2MgSiO_7, PDF #76-0841) from the raw GBFS. After exposure at 200 °C, the long-range order of the dehydration product disintegrated in a similar fashion to the FA/MKPC binder (as discussed above) and thus, to struvite systems. The phase assemblage at 200 °C was mainly represented by diffuse scattering was observed between $25° < 2\theta < 35°$ assigned to the GBFS glassy fraction and the poorly crystalline dehydration product. The glassy phase could not be clearly identified at 20 °C due to the struvite-K reflections, which are very crystalline. The diffuse scattering presented in Chapter 6 (Fig. 6.2) for raw GBFS is similar to that observed in the GBFS/MKPC binder at 200 °C (Fig. 7.6). It was also observed that quartz (SiO_2, PDF #78-2315) contamination from the cleaning media (sand) was present in the 200 °C diffraction pattern.

At 400 °C, low intensity reflections associated with α-$MgKPO_4$ (PDF #50-0146) emerged, signifying that the long-range order of this phase increased at 400 °C in the GBFS/MKPC binder. Similarly to the FA/MKPC binder, it is postulated that the $MgKPO_4$ α to β phase transition reversed upon cooling, as the diffraction pattern was comparable to the α-$MgKPO_4$ phase reported by Wallez *et al.* [120]. After exposure at 800 °C, additional reflections corresponding to α-$MgKPO_4$ emerged alongside a calcium magnesium potassium phosphate phase ($Ca_9MgK(PO_4)_7$, PDF #88-0798). In the 1000 °C diffraction pattern (Fig. 7.6) reflections due to forsterite (Mg_2SiO_4, PDF #34-0189) reflections emerged, whilst the relative intensity of the $Ca_9MgK(PO_4)_7$ reflections increased suggesting more of this phase had formed than at 800 °C.

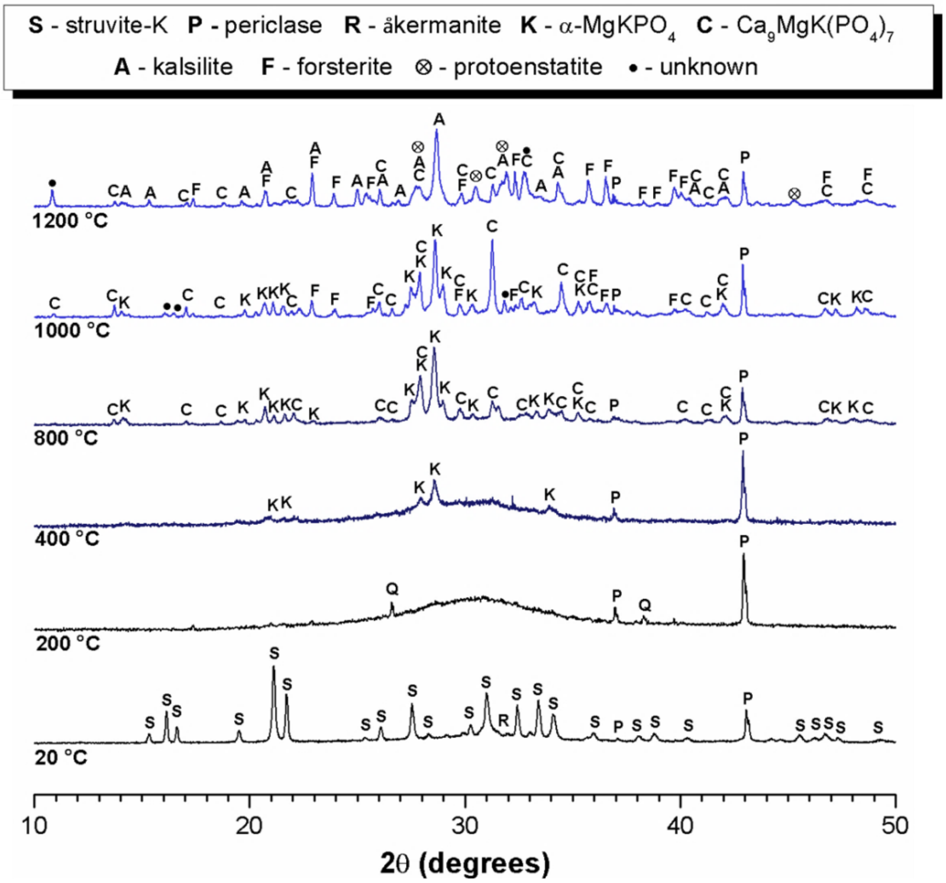

Fig. 7.6. Ex situ X-ray diffractogram of hardened GBFS/MKPC binders heated up to 1200 °C

A phase reorganisation was observed in the 1200 °C diffraction pattern (Fig. 7.6) with the emergence of prominent phases: forsterite, kalsilite ($KAlSiO_4$, PDF #33-0989) and protoenstatite ($MgSiO_3$, PDF #75-1334). Additionally, the relative intensity of the forsterite reflections appeared more intense than in the 1000 °C diffraction pattern. These combined changes signified that the GBFS had begun a solid state reaction with the dehydration product within the GBFS/MKPC binder. It is also expected that in the GBFS/MKPC binder a poorly crystalline $CaO\text{-}MgO\text{-}SiO_2\text{-}P_2O_5$ glass component was formed after exposure to high temperatures, in similar behaviour to bioactive glasses ($CaO\text{-}MgO\text{-}SiO_2\text{-}P_2O_5$), which are formed after calcination at 700 °C in air for 3 hrs [172]. This explanation could account for the lack of Ca or P rich phases observed in the XRD data at 1200 °C.

7.2.4 Nuclear magnetic resonance spectroscopy

7.2.4.1 ^{27}Al MAS NMR

The ^{27}Al MAS NMR spectra for the FA/MKPC and GBFS/MKPC binders exposed to temperatures between 20 and 1200 °C are shown in Fig. 7.7. The unreacted FA (Fig. 7.7A) has two main Al environments, Al^{IV} and Al^{VI} centred at 50 ppm and -6 ppm, respectively. The resonance at -6 ppm corresponds to the Al^{VI} sites in mullite [150, 151] whilst the broad resonance centred at 50 ppm was associated with a combination of the highly cross-linked aluminosilicate glassy fraction present in FA and the tetrahedral mullite resonance reported to occur at 46 ppm [151]. Compared to the raw FA spectrum, the intensity of the Al^{IV} resonance at 50 ppm appeared to increase in the FA/MKPC binder at 20 °C, whilst the Al^{VI} resonance at -6 ppm intensity was reduced. There were no major changes in the aluminium environments within the FA/MKPC binder exposed to 400 °C, concurrent with the XRD data Fig. 7.5. However, the resonance at -6 ppm associated with Al^{VI} mullite environments [24, 25] disappeared in the sample exposed 800 °C, whilst the intensity of the Al^{IV} resonance (centred at 50 ppm) increased. These spectral differences indicated that a FA reaction contributed to the altered phase assemblage observed at 800 °C (Fig. 7.5). This is because the Al^{IV} environment associated with the glassy FA fraction sharpened (i.e. had a higher crystallinity) whilst the mullite contributions appeared diminished.

Upon exposure to 1000 °C, the Al^{VI} resonance was almost entirely eliminated, and the Al^{IV} resonance presented an asymmetric shape, comprised of three distinct, but overlapping Al^{IV} environments positioned at 68, 59, and 46 ppm, respectively. The latter is associated with a remnant FA environment and demonstrates that the FA had not fully transformed at this temperature. The resonances centred at 68 and 59 ppm are indicative of leucite formation [173, 174] and are consistent with the XRD phase assignments (Fig. 7.5). In the sample exposed to 1200 °C, the leucite resonance sharpened whilst a decreased contribution from the remnant FA was observed, indicative of a continuing FA reaction.

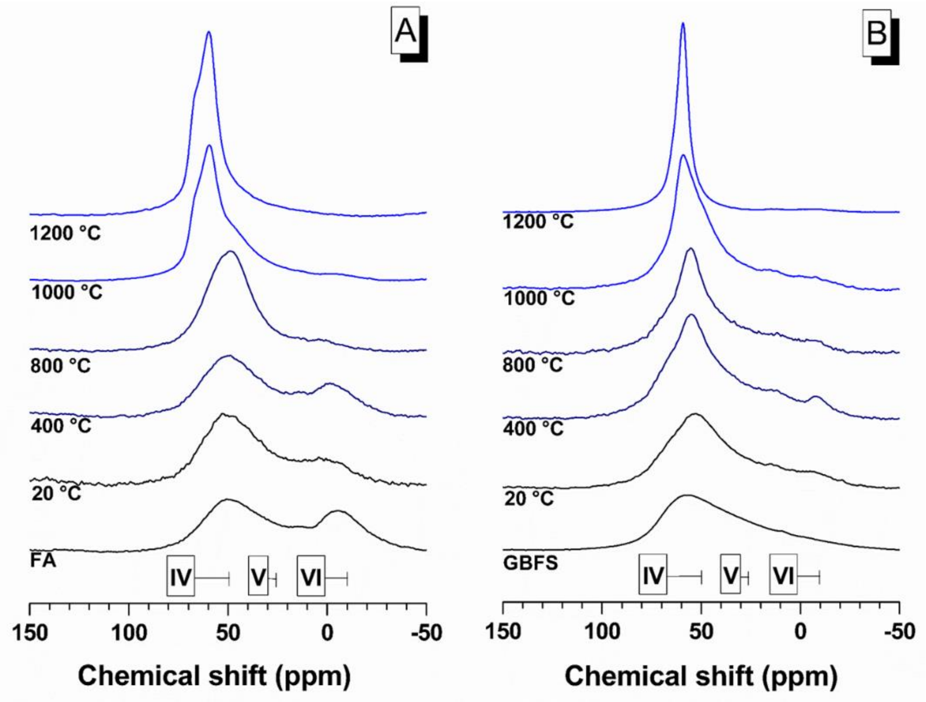

Fig. 7.7. Normalised ^{27}Al MAS NMR spectra of hardened (A) FA/MKPC and (B) GBFS/MKPC pastes heated between 20 - 1200 °C

In Fig. 7.7B two Al environments were observed in the ^{27}Al MAS NMR spectrum of unreacted GBFS. The dominant site was represented by a broad Al^{IV} environment centred at 56 ppm assigned to the calcium aluminosilicate glass, which constitutes the majority of the slag [141]. The second Al site was a small resonance in the Al^{VI} region centred at 9 ppm, associated with a minor octahedral Al environment present in the unreacted slag glass. In the GBFS/MKPC binder at 20 °C, the main Al^{IV} resonance was narrower, slightly more intense and shifted upfield (to be centred at 53 ppm) compared to raw GBFS. This is associated with the secondary reaction product discussed in Chapter 6, which is likely to be a potassium aluminosilicate phase, however the exact composition of this phase is not currently know. Between the samples exposed ay 400 and 1000 °C, a gradual downfield shift in the broad Al^{IV} resonance from 55 ppm to 59 ppm was observed, along with increased asymmetry in the resonance shape, which was most notable after exposure to 1000 °C. In samples treated at 1200 °C, a sharp resonance associated with the [Q^4(4Si)] units of an ordered kalsilite structure was observed at 59.1 ppm in ^{27}Al MAS NMR (Fig. 7.7B)

[175, 176], which validated the presence of a single Al-containing phase within the XRD analysis (Fig. 7.6) and signalled that a solid state reaction with the dehydration product had taken place within the GBFS/MKPC binder.

7.2.4.2 ^{29}Si MAS NMR

The ^{29}Si MAS NMR spectra of the FA/MKPC and GBFS/MKPC binders exposed to temperatures between 20 °C and 1200 °C are shown Fig. 7.8. The unreacted FA had a broad resonance between -76 and -122 ppm, which was centred at -102 ppm (Fig. 7.8A). This was assigned to the crystalline and glassy aluminosilicate phases present within FA, which are a combination of quartz (≈ -107 ppm) [154], mullite (≈ -86 ppm) [151], and the vitreous fraction [155]. In the FA/MKPC specimen at 20 °C, the chemical shift range of this broad resonance was observed with a slight upfield shift, centred at -105 ppm. After exposure at 400 °C, the resonance lineshape was similar to the FA/MKPC spectrum at 20 °C whereas in the sample exposed to 1000 °C, the resonance shapes and chemical shifts of the partially resolved component peaks varied considerably. These component peaks were identified in the sample exposed to 1000 °C at -86, -92 and -96 ppm with additional resonances at -82 and -106 ppm for the sample exposed to 1200 °C, which are consistent with the presence of a fraction of the Si in the samples as leucite ($KAlSi_2O_6$) [177], as identified by XRD (Fig. 7.5). Although $KAlSiO_4$ was identified in the XRD analysis it was difficult to distinguish this phase within the ^{29}Si MAS NMR spectra, for the samples exposed to 1000 and 1200 °C, as the typical $KAlSiO_4$ resonances are located at –89 ppm [175] and as such, were overlapped by the distinctive leucite environments.

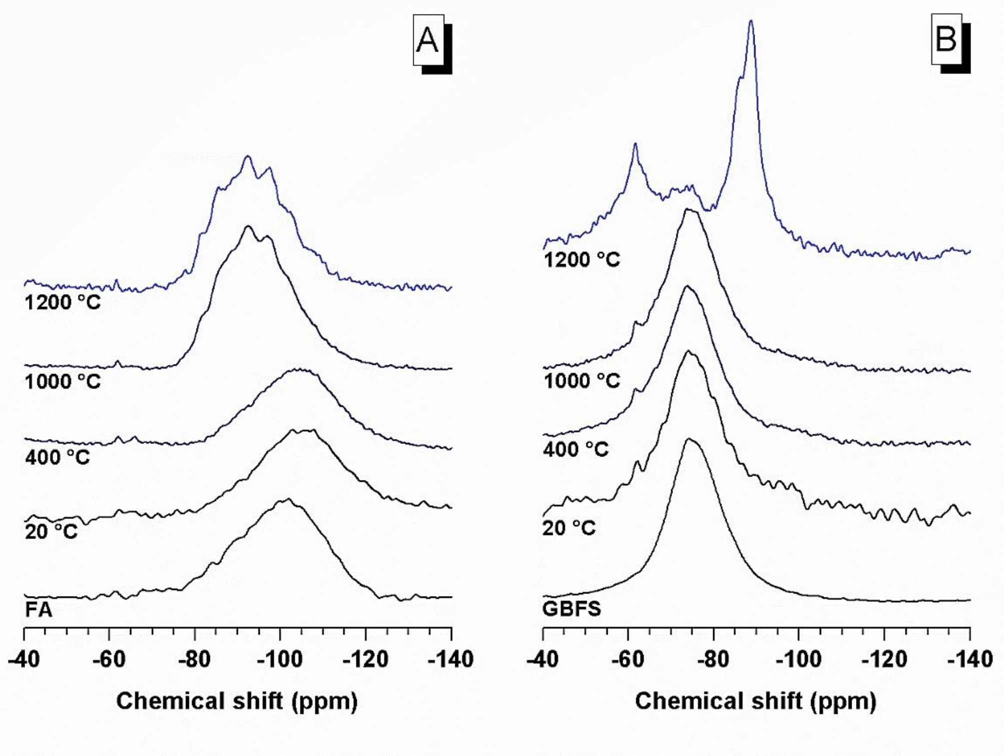

Fig. 7.8. Normalised ^{29}Si MAS NMR spectra of hardened (A) FA/MKPC and (B) GBFS/MKPC pastes heated between 20 - 1200 °C

In Fig. 7.8B, the unreacted GBFS exhibited a broad resonance centred at -74 ppm, consistent with the glassy fraction and the minor åkermanite present in the slag [178]. The GBFS/MKPC binders exposed to 20 °C, 400 °C and 1000 °C all had a similar resonance centred at -75 ppm with a minor resonance at -62 ppm. In the ^{29}Si MAS NMR spectrum (Fig. 7.8B), no differences were observed in the Si environments when compared to the 20 °C specimen, which concurred with the XRD analysis. However, in the GBFS/MKPC binder exposed to 1200 °C, the intensity of the unreacted GBFS resonance at -73 ppm decreased in concurrence with the emergence of additional, sharp and intense resonances centred at -61.6, -86.2 and -88.8 ppm. Several new Si environments were identified in the XRD analysis (forsterite, kalsilite and protoenstatite), the spectral changes observed in the ^{29}Si MAS NMR spectra for the GBFS/MKPC binder (Fig. 7.8B) reinforce the likelihood of a GBFS – α-$MgKPO_4$ reaction. However, the low intensity resonance centred at -73 ppm (associated with residual GBFS glass fraction) indicated that the reaction was incomplete after exposure to 1200 °C, even though no GBFS particles were identified in the microstructure Fig. 7.12C.

The resonance reported at -61.6 ppm corresponded to forsterite (Mg_2SiO_4) [179, 180], whilst the resonance at -88.8 ppm was associated with an ordered kalsilite structure [175, 176]. It is postulated that the resonance at -86.2 ppm could also be associated with kalsilite, the difference being that it has undergone a transformation to its orthorhombic structure at 897 °C. Once quenched to room temperature this phase is denoted as O1-$KAlSiO_4$ [181, 182]. The reported spectrum for this phase has two partially overlapping resonances at -85.5 and -88.5 ppm and is similar in resonance shape to that observed in the 1200 °C ^{29}Si MAS NMR spectrum [181]. As such, we hypothesise that a combination of the ordered kalsilite and O1-$KAlSiO_4$ could be present after exposure to 1200 °C. Protoenstatite, identified at high temperature in the current study (Fig. 7.6), is the orthorhombic polymorph of enstatite and is reported to be the stable form of $MgSiO_3$ present between 1000 and 1300 °C [183]. The contribution of protoenstatite in the ^{29}Si MAS NMR spectrum (Fig. 7.8B) is expected to appear as a single resonance positioned at -84.2 ppm related to the Si Q^2 environment [184, 185], however, it could not be confidently assigned in this study as this region was overwhelmed by the kalsilite resonance at -88 ppm.

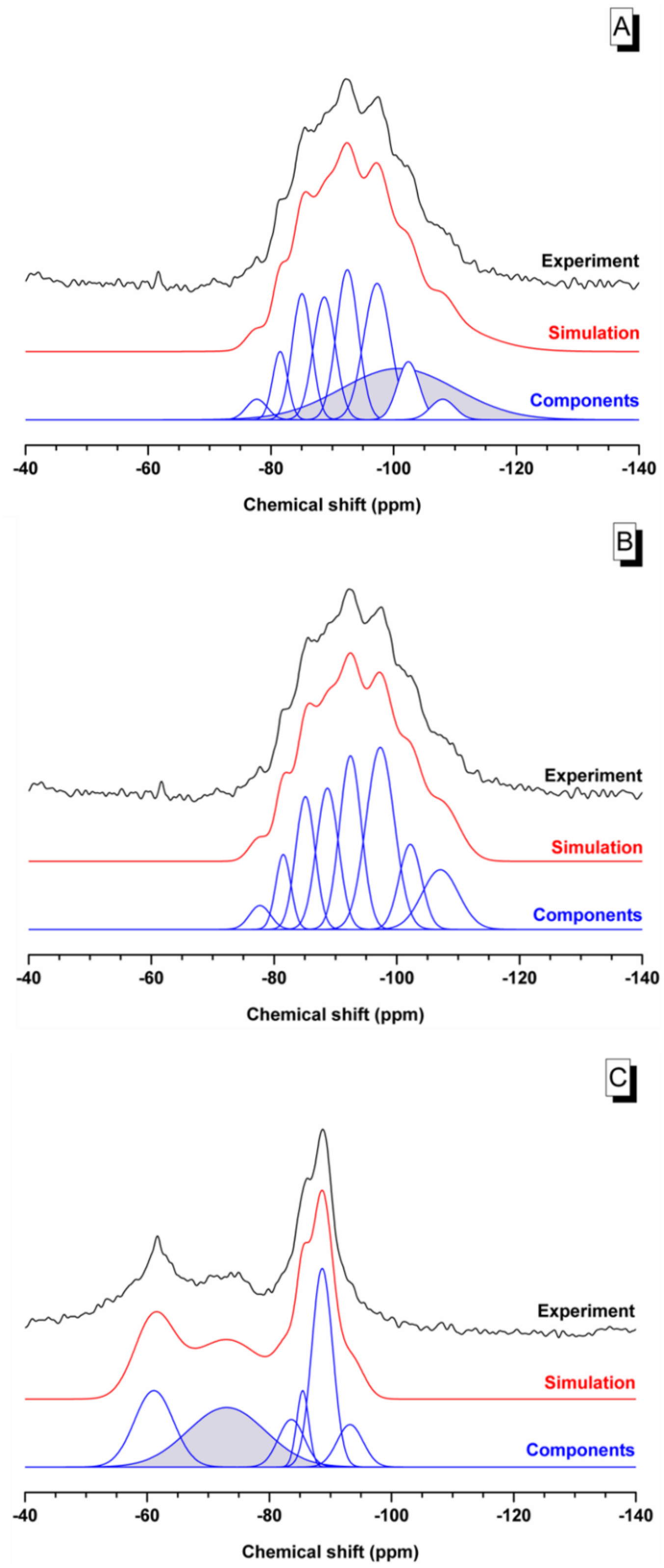

Fig. 7.9. Deconvoluted ^{29}Si MAS NMR spectra at 1200 °C (A) FA/MKPC with remnant fly ash (B) FA/MKPC fully reacted and (C) GBFS/MKPC with remnant slag

In order to resolve the ^{29}Si MAS NMR spectra, deconvolutions were performed in Microsoft Excel using the minimum combination of Gaussian lines (using a similar methodology to Bernal *et al.* [143]) to accurately describe the spectra for the FA/MKPC and GBFS/MKPC binders exposed to 1200 °C (Fig. 7.9). The numerical values for the deconvolutions are shown in Tables. 7.2-7.4**.**

Brown *et al.* [177] reported that the ^{29}Si MAS NMR spectra for natural and synthetic leucite is represented by a broad resonance comprised of several Si environments, centred at: -81, -85.5, -88, -92, -97 and -101 ppm. These chemical shift values were used to constrain the deconvolutions (± 1 ppm) for the FA/MKPC spectra shown in Fig. 7.9A and 7.9B. In the leucite structure, there are only three tetrahedral sites (Si^{IV}) however, there are 15 possible assignments because each Si^{IV} site can be associated with up to four coordinated Al atoms [177]. As such, it was not possible to assign the specific [Q] species for each environment described in Tables 4.2 and 4.3. The reason for including two deconvolutions of the ^{29}Si MAS NMR spectrum for FA/MKPC at 1200 °C was to determine if there could be any contributions associated with remnant fly ash (centred at –100.8 ppm) within the broad leucite resonance. The postulated remnant FA contribution is represented by the light grey Gaussian peak in Fig, 7.9A however, the deconvolution shown in Fig. 7.9B demonstrates that the FA/MKPC spectrum (at 1200 °C) can accurately be fitted without a FA contribution. Further investigations by SEM/EDX analysis and Mössbauer spectroscopy revealed that the FA in the FA/MKPC binder fully reacted by 1200 °C (to be discussed in sections 7.2.5 and 7.2.6) consequently, the deconvolution presented in Fig. 7.9B is likely to be correct.

For the ^{29}Si MAS NMR spectrum of the GBFS/MKPC binder, only one deconvolution was performed because it was clear from the distinctive remnant GBFS resonance centred at -73 ppm (highlighted in grey shading within Fig. 7.9C) that the GBFS was still present at 1200 °C. This chemical shift value concurs with the reported value for glassy silicate structures often found in blast furnace slag [186]. The remainder of the deconvolution was simulated using known chemical shifts of kalsilite and forsterite constrained to ± 1 ppm of the literature values. Forsterite is reported to have a single resonance at -61.9 ppm, which is related to a [Q^0] Si species [180] whilst, kalsilite has several possible resonances centred at: -84.9, -88.5 and -93.9 ppm, which are likely to be assigned to [Q^4(4Al)] and [Q^4(3Al)] species [181].

Using these assignments for GBFS, forsterite and kalsilite, it was not possible to perfectly simulate the ^{29}Si MAS NMR spectrum for the GBFS/MKPC binder at 1200 °C. However, the addition of a Gaussian peak (centred at -83.6 ppm) enabled the deconvolution to be accurately described. It is possible that the phase assignment could be associated with protoenstatite, which is reported to have single resonance at -84 ppm [185] and was previously identified in the XRD analysis (Fig. 7.6: 1200 °C). From these deconvolutions, it is clear that remnant GBFS was still present in the GBFS/MKPC binder at 1200 °C, however it is likely that the FA within the FA/MKPC binder had fully reacted.

Table 7.2. ^{29}Si MAS NMR chemical shifts calculated by deconvolution of the FA/MKPC spectrum (Fig. 7.9A)

	Position (ppm)	FHWM (ppm)
Leucite (1)	-77.7	4.0
Leucite (2)	-81.5	2.0
Leucite (3)	-85.1	3.7
Leucite (4)	-88.7	4.2
Leucite (5)	-92.5	4.2
Leucite (6)	-97.3	5.1
Leucite (7)	-102.4	4.2
Leucite (8)	-108.0	4.7
FA (9)	-100.8	22.0

Table 7.3. ^{29}Si MAS NMR chemical shifts calculated by deconvolution of the FA/MKPC spectrum (Fig. 7.9B)

	Position (ppm)	FHWM (ppm)
Leucite (1)	-77.7	4.0
Leucite (2)	-81.5	2.9
Leucite (3)	-85.1	3.7
Leucite (4)	-88.7	4.2
Leucite (5)	-92.5	4.2
Leucite (6)	-97.3	5.4
Leucite (7)	-102.4	4.3
Leucite (8)	-107.1	7.0

Table 7.4. ^{29}Si MAS NMR chemical shifts calculated by deconvolution of the GBFS/MKPC spectrum (Fig. 7.9C)

	Position (ppm)	FHWM (ppm)
Forsterite	-61.3	7.5
Protoenstatite	-83.6	5.0
GBFS	-73.0	15.0
Kalsilite (1)	-83.6	5.0
Kalsilite (2)	-85.5	2.3
Kalsilite (3)	-93.2	5.0

7.2.5 Scanning electron microscopy

Backscattered electron micrographs and elemental maps of FA/MKPC and GBFS/MKPC binders not subjected to thermal treatment are shown in Figs. 7.10-7.11, respectively. The formation of a continuous struvite-K binder was observed, with larger struvite-K crystallites of this phase embedded in the continuous (and apparently microcrystalline) binder in both systems. Spherical particles of varying sizes and with high-contrast Fe-rich inclusions correspond to unreacted FA particles, whilst angular light grey particles correspond to unreacted GBFS. The dark grey angular particles present in both Figs. 7.10-7.11 correspond to unreacted MgO. The following section describes the morphology and chemical distribution of phases in each MKPC binder after exposure at 1000 and 1200 °C.

7.2.5.1 Elemental mapping - FA/MKPC

The FA/MKPC binder underwent transformation at 1000 °C to a smooth, but porous microstructure rather than being comprised of the distinct struvite-K and FA features (Fig. 7.10A). However, the shape of the remnant FA particles in the Al and Si EDX maps (Fig. 7.10B: Al and Si) were still clearly visible at 1000 °C. It is postulated that the FA could continue to react at longer durations and/or exposure to higher temperatures, which is supported by the microstructure of the FA/MKPC binder exposed to 1200 °C (discussed below). It is important to note, that the aim of this study was to observe the fire performance of the FA/MKPC binder (with respect to IAEA and RWM fire performance parameters), not to fully react the FA. The microstructure of the FA/MKPC binder at 1000 °C indicated that this system can withstand fire conditions, resulting in the formation of a “ceramic-like” microstructure.

A homogenous distribution of Mg, P and K was observed in the elemental maps, however, Bragg reflections indicative of the dehydrated α-$MgKPO_4$ phase were absent from the XRD data at 1000 °C. As the melting point of $MgKPO_4$ (1404 °C) [120] was not exceeded in this study, a poorly crystalline α-$MgKPO_4$ phase must be present. The distinct correlations observed in the FA/MKPC microstructure between the Mg, K and P elements (Fig. 7.10C: Mg, K and P) suggest that this may be the case. The Fe EDX map in Fig. 7.10B indicated that this element was distributed into rims around the excess MgO particles and as discrete particles within the voids of the cement, which are postulated to be associated with hematite. This is further highlighted in Fig. 7.11, where the BSE/EDX micrograph has been enhanced to show the behaviour of the Fe at 1000 °C in the FA/MKPC binder.

After exposure to 1200 °C, the FA/MKPC binder appeared to have a smooth microstructure with very little porosity, albeit with the exception of Fe-rich phase that indicated that the FA particles had fully reacted. The microstructure can be described as three compositions (according to the elemental maps): the light grey phase correspond to $KAlSiO_4$ and $KAlSi_2O_6$ (Fig. 7.10C: Al, Si and K) indicating that K migrated from the dehydration product into the $KAlSiO_4$ and $KAlSi_2O_6$ structures at 1200 °C (this concurs with the XRD analysis in Fig. 7.5), the medium grey phase is likely related to a poorly crystalline Mg-P-K phase rather than the dehydration product, α-$MgKPO_4$ (Fig. 7.10C: Mg, P and K) as no crystalline reflections could be assigned to this phase at 1200 °C. The Fe (Fig. 7.10C) appears to be highly localised in the light angular particles, which correspond to the spinel phase ($MgAl_{0.8}Fe_{1.2}O_4$, Fig. 7.10C: Fe) identified in the XRD analysis (Fig. 7.5). The actual composition of the spinel in the GBFS/MKPC binder at 1200 °C was calculated using SEM/EDX point analysis (based on 10 points) to have Al/Mg and Fe/Mg ratios of 0.71 ± 0.06 and 1.12 ± 0.35 (atomic %), respectively, which appears to be closely related to the XRD matched phase, $MgAl_{0.8}Fe_{1.2}O_4$.

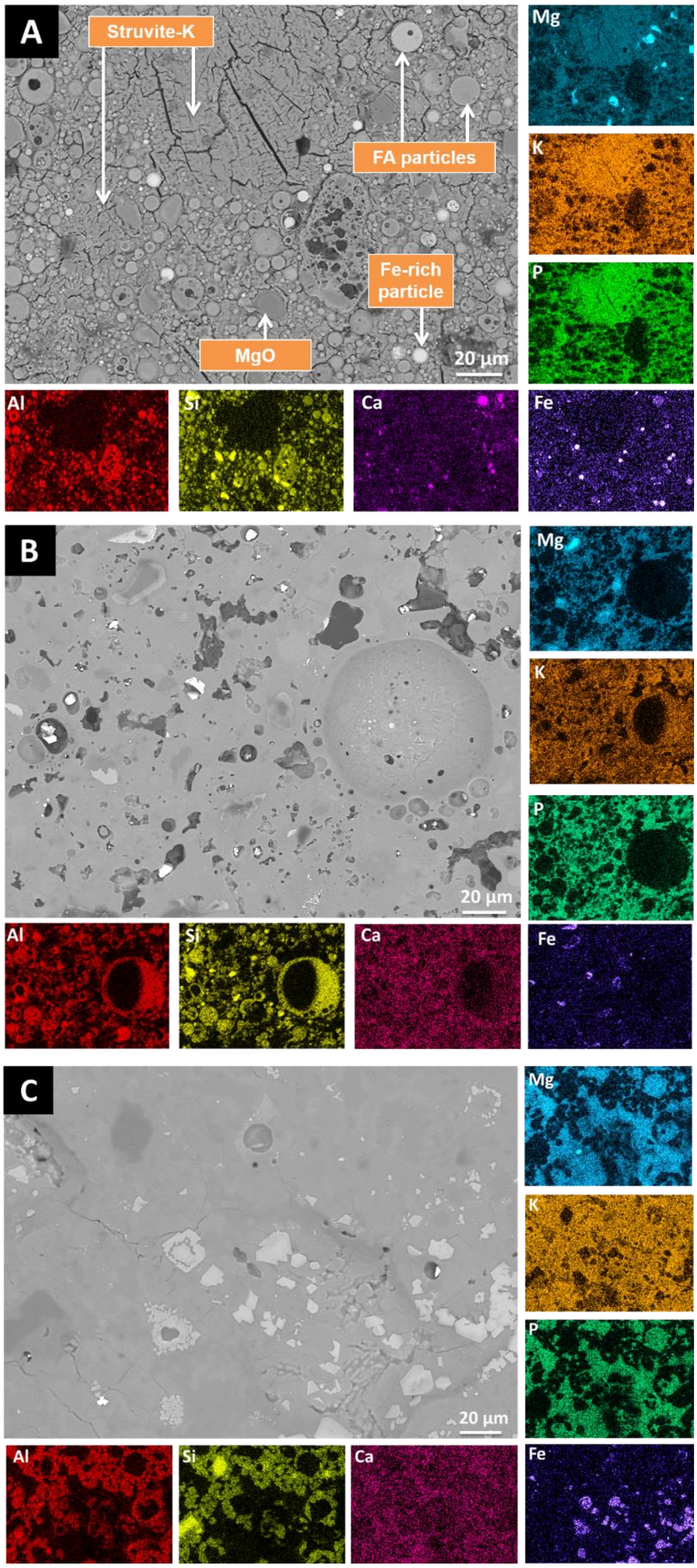

Fig. 7.10. Backscattered electron micrographs and elemental maps of FA/MKPC after exposure to temperatures of (A) 20 °C, (B) 1000 °C and (C) 1200 °C

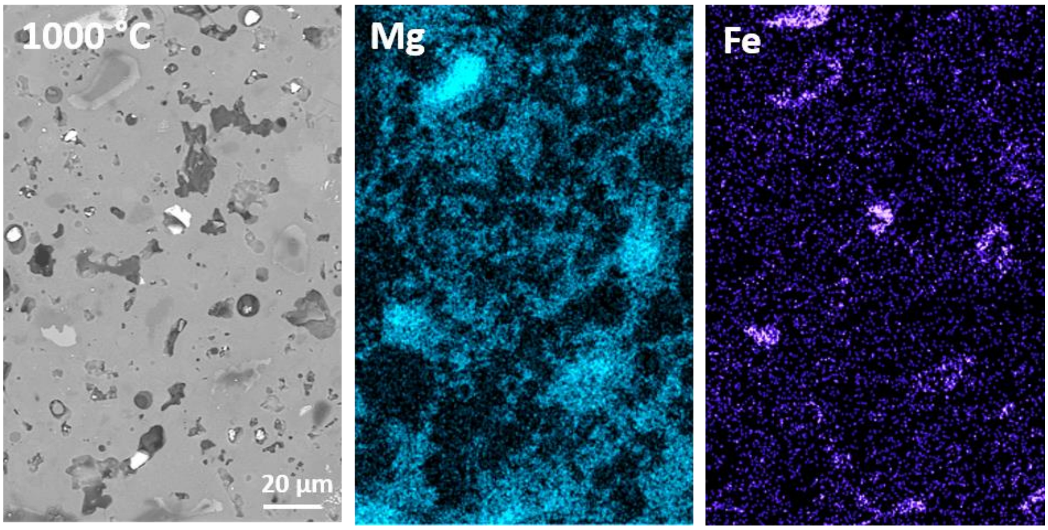

Fig. 7.11. Backscattered electron micrograph, Mg and Fe EDX map for FA/MKPC binder exposed to 1000 °C, extracted from Fig. 7.10B

7.2.5.2 Elemental mapping - GBFS/MKPC

Differences in the microstructure were observed in the GBFS/MKPC binder exposed to 1000 °C (Fig. 7.12B) when compared to 20 °C sample. A continuous phase with a chemical composition consistent with the dehydration product, α-$MgKPO_4$, was identified in the SEM/EDX (Fig. 7.12B: Mg, K and P) interspersed with unreacted MgO, GBFS particles and large areas of porosity (Fig. 7.12B). This was dissimilar to the FA/MKPC binder, where evidence of K migration into the $KAlSiO_4$ and $KAlSi_2O_6$ structures was observed, this highlights that the SCMs behave differently at 1000 °C. Consequently, the Al, Si and the majority of the Ca present in the GBFS/MKPC binder (Fig. 7.12B) remained associated with the remnant GBFS particles. A rim rich in Ca, Mg, K and P (Fig. 7.12B) was found on the larger GBFS particles, which is hypothesised to be associated with the $Ca_9MgK(PO_4)_7$ phase identified in the phase assemblage (Fig. 7.6). Upon exposure to 1200 °C (Fig. 7.12C) a smooth and continuous morphology, with very little porosity was evident in the GBFS/MKPC microstructure. This supports the occurrence of a GBFS – α-$MgKPO_4$ reaction as no remnant GBFS particles were detected in the microstructure (Fig. 7.12C), unlike at 1000 °C. A strong relationship was evident between Ca, K, and P (Fig. 7.12C) indicative of a calcium potassium phosphate phase. It is possible to conclude that this calcium potassium phosphate phase must be poorly crystalline because no reflection were identified in the XRD analysis (Fig. 7.6), in fact there were very few P-containing phases identified, suggesting that the formation of “glass-like” phases occurred in the GBFS/MKPC binder at 1200 °C. Interestingly, Mg was no longer associated with P in the GBFS/MKPC specimen, but rather with forsterite and protoenstatite, which was indicative of Ca/Mg competition at this temperature. As a result of these changes, the microstructure can be described to contain two compositions (based on the elemental maps), where the light grey phase is rich in Ca, K, and P (Fig. 7.12C) and likely to be associated with a calcium potassium phosphate phase of unknown composition. The dark grey phase is rich in Al, Si and Mg (Fig. 7.12) represents a combination of kalsilite, forsterite and protoenstatite.

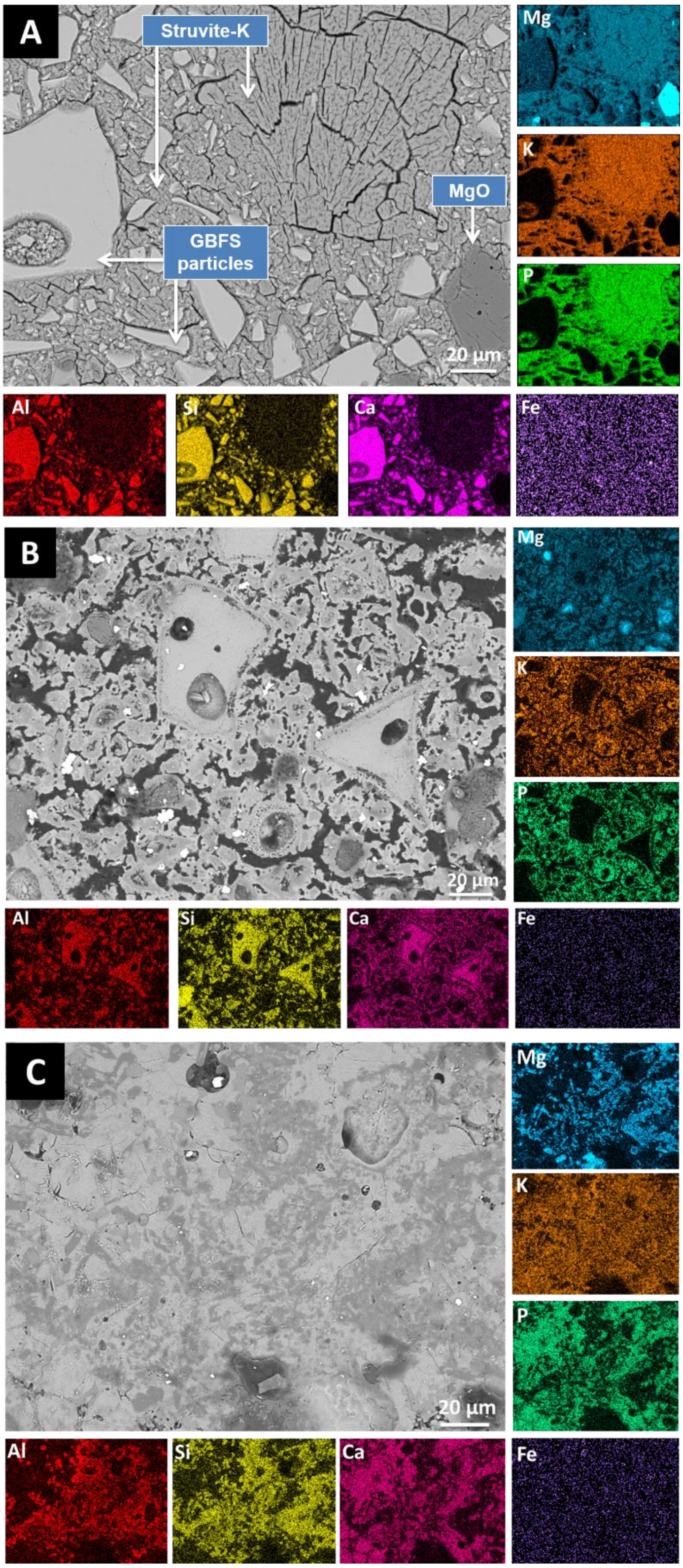

Fig. 7.12. Backscattered electron micrographs and elemental maps of GBFS/MKPC binders after exposure to temperatures of (A) 20 °C, (B) 1000 °C and (C) 1200 °C

7.2.6 Mössbauer spectroscopy

Mössbauer spectroscopy was utilised to investigate Fe speciation in FA/MKPC binders exposed to high temperatures, data are shown for raw FA and FA/MKPC binders treated at 20, 800, 1000 and 1200 °C in Fig. 7.13. Analysis of raw FA (Fig. 7.13A) indicated that both magnetic and non-magnetic fractions, in the form of hematite, magnetite and mullite (described as $3Al_2O_3.2SiO_2$ but with Fe substitution for some of the Al when present in fly ash [187]) were observed. Two doublets with isotropic shifts centred at 0.39 ± 0.02 and 0.78 ± 0.06 mm/s were associated with mullite, whilst the three sextets were associated with magnetic Fe species identified as hematite and magnetite. With increasing temperature (up to 1000 °C) preferential Fe oxidation, from Fe^{2+} to Fe^{3+}, was observed, as indicated by increased hematite and reduced mullite contributions. This was consistent with the observed colour change (grey to red/brown) observed at 1000 °C (Fig. 7.2A). At 1200 °C, notable changes in the Mössbauer spectrum where a single signal was observed rather than the sextuplets previously discussed to be associated with magnetite and hematite, (Fig. 7.13E) confirmed the presence of a spinel phase, similar to $MgAl_{0.8}Fe_{1.2}O_4$ identified by XRD and SEM/EDX analysis.

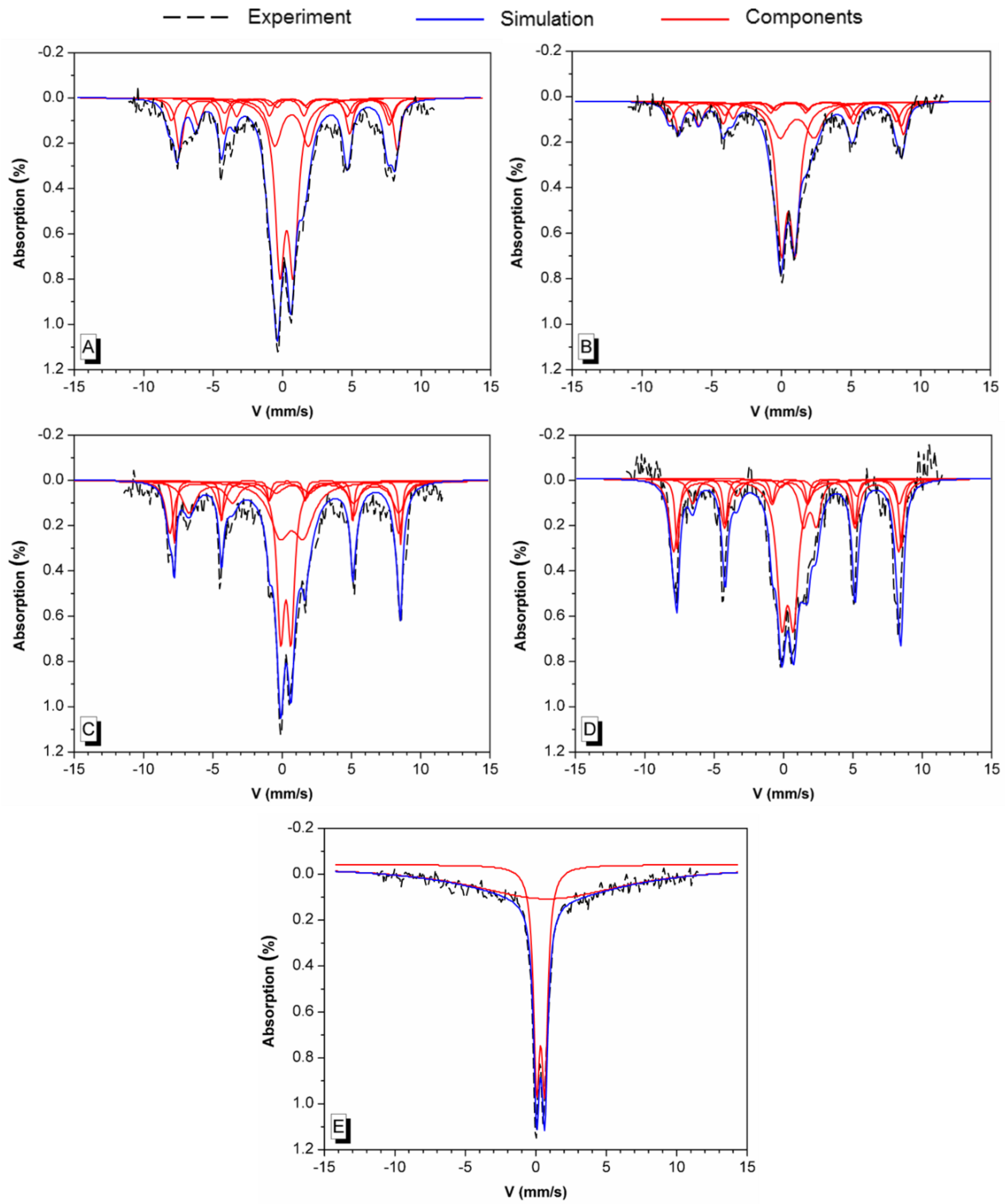

Fig. 7.13. Mössbauer spectroscopy of (A) raw FA, FA/MKPC at (B) 20 °C, (C) 800 °C, (D) 1000 °C and (E) 1200 °C. The data are represented by the black dashed lines, while the simulations are represented by the solid (blue and red) lines

7.3 Conclusions and Future work

The exposure of FA/MKPC and GBFS/MKPC binders to 200 °C resulted in the dehydration of $MgKPO_4 \cdot 6H_2O$ and consequent formation of the dehydration product, α-$MgKPO_4$, which had no long-range order between under 400 °C. At and above 800 °C, the formation of additional phases indicated that a reaction between the dehydration product and the FA or GBFS (above 1000 °C) had taken place. This resulted in the formation of leucite (FA/MKPC) and kalsilite (GBFS/MKPC) amongst other crystalline phases (for example: hematite, spinel, forsterite, protoenstatite). As a result of this phase assemblage restructure, considerable changes were observed in the microstructures of FA/MKPC and GBFS/MKPC binders compared to the blended binders at 20 °C. Although the FA/MKPC and GBFS/MKPC binders were considerably altered at high temperatures, they formed well-understood stable products whilst retaining dimensional stability. This suggests that these systems could be expected to meet the fire performance requirements for UK ILW associated with transport (withstanding exposure to a hydrocarbon fire at 800 °C for 30 minutes) [170] and geological disposal (withstanding exposure to a fire at 1000 °C for 60 minutes) [161] of specified types of nuclear waste.

Further work should be undertaken in the following areas:

- The high temperature stability criteria should be implemented over a range of specimen sizes (up to and including full inactive wasteforms) to determine the reproducibility of the results reported in this chapter, and to provide confidence in the performance of blended MKPC binders under accident conditions for nuclear waste applications.

- Synthesis of α-$MgKPO_4$ using the solid state procedure described by Wallez *et al.* [120] followed by in situ HTXRD and TGA/DSC to determine the transition behaviour of $MgKPO_4$ up to 1200 °C, which would directly support the current study.

- In situ HTXRD data of the FA/MKPC and GBFS/MKPC binders to support the occurrence of α to β to γ $MgKPO_4$ transitions in these systems. This investigation should include collection of HTXRD and TGA/DSC cooling data, to confirm the β-$MgKPO_4$ phase transition reversed upon quenching.

- Ex situ thermal treatment of the pure struvite-K (up to 1200 °C) with subsequent ^{31}P MAS NMR analysis to understand the migration of P from crystalline to poorly crystalline phases, in order to confidently interpret the ^{31}P MAS NMR spectra of the blended MKPC binders (Appendix E).

- Rietveld refinements of the ex situ high temperature diffraction patterns to enable confident phase assignments.

8 Radiation stability of blended MKPC binders

8.1 Introduction

For employment in nuclear waste encapsulation applications, cementitious grouts are required to have suitable properties, as discussed on Chapter 7. Encapsulants should have a satisfactory accident performance (i.e. thermal incident) during storage or final disposal scenarios and they should also provide radiation shielding of the waste, as such they should be tolerant to substantial levels of radiation. The most penetrating form of radiation is gamma radiation, which can affect a conditioned wasteform from the encapsulated waste and from neighbouring packages [10]. As the conditioned wasteform needs to contain the radioactive waste in a safe manner and prevent release, it is necessary that the encapsulant grout and 500 L stainless steel container are tolerant to gamma irradiation. The Nuclear Decommissioning Authority report that for ILW conditioned waste packages, which equates to an absorbed gamma dose of 0.56 Gy/hr and is predicted to decrease to 1.9×10^{-3} Gy/hr after 300 years [188]. Accordingly, the maximum life-time (300 years) gamma dose of an ILW 500 L drum waste package is estimated to be 10 MGy [188]. The significant contribution to the radiogenic heat in ILW mainly arises from radionuclides: Co-60, Sr-90, Cs-137, Pu-239 and Am-241 [189], with gamma irradiation largely from the decay of Co-60, Cs-137 and Am-241 [190]. In the reactive metal waste streams discussed in Chapter 2, these radionuclides are present in the following quantities (reported as TBq/m^3):

- 2D22 - 1.92×10^{-1} (Co-60), 1.93×10^{1} (Sr-90), 2.79×10^{1} (Cs-137), 5.53×10^{1} (Pu-239) and 1.48 (Am-241) [7]
- 2D24 – 2.12×10^{-1} (Co-60), 2.48×10^{1} (Sr-90), 4.10×10^{1} (Cs-137), 7.14 x 10-^{1} (Pu-239) and 1.93 (Am-241) [8]

8.1.1 Generation of gamma radiation

Gamma radiation is the product of radioactive decay, where an unstable nuclide transforms to a stable nuclide by the emission of electromagnetic radiation (i.e. a photon). In gamma decay, there is no change in the number of protons or neutrons, it is only associated with the release of energy [191], as gamma rays photons with energy in the keV to tens of MeV range, but typically around 1 MeV [77]. The energy emitted equates to the energy difference between the initial and final states involved, as demonstrated for the decay chains of Cs-137 and Co-60 in Figs. 8.1 and 8.2.

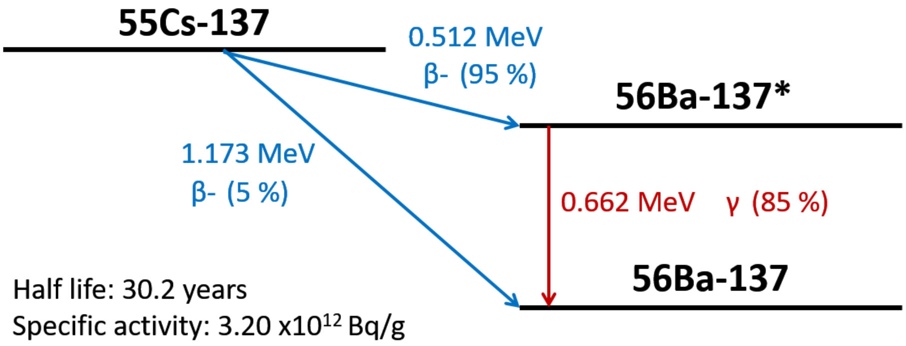

Fig. 8.1. Cs-137 decay chain, the data was extracted from [190]

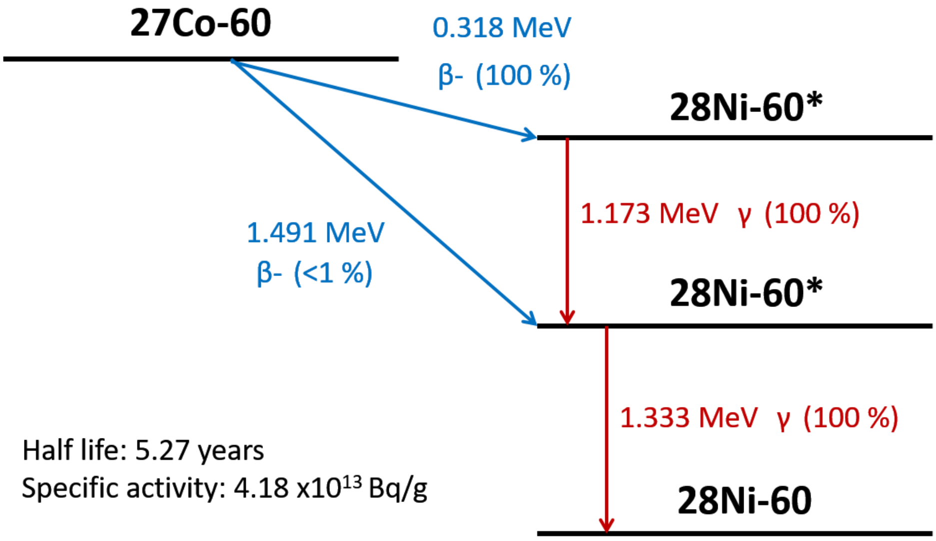

Fig. 8.2. Co-60 decay chain, the data was extracted from [190]

8.1.2 Interaction of gamma radiation with materials

Gamma radiation can interact with materials in three ways: Compton scattering, pair production, and the photoelectric effect (Fig. 8.3). The photoelectric effect is associated with the complete conversion of the gamma energy via the expulsion of an electron from the inner shell of an atom. The excited atom has two options for de-excitation: (1) release an electron, known as an Auger electron; or (2) transfer an electron from a higher atomic shell to the inner shell, which results in the emission of an X-ray that has a characteristic energy and it is the basis of X-ray fluorescence spectroscopy [77]. Compton scattering occurs when the incident gamma ray interacts with a loosely bound electron resulting in a scattered electron (i.e. recoil) and gamma ray of a lower energy (i.e. minus the energy absorbed by the electron). This interaction is dominant when the energy of the gamma ray exceeds the binding energy of inner electrons (Fig. 8.4) [191]. Pair production only occurs when the energy of the incident gamma ray exceeds 1.022 MeV, which is the rest mass of two electrons [77]. Unlike Compton scattering, all of the energy is converted into an electron-positron pair. The positron will capture an electron as it loses energy (i.e. it slows down) and undergo annihilation, resulting the formation of two gamma rays that move in opposite directions to conserve [77].

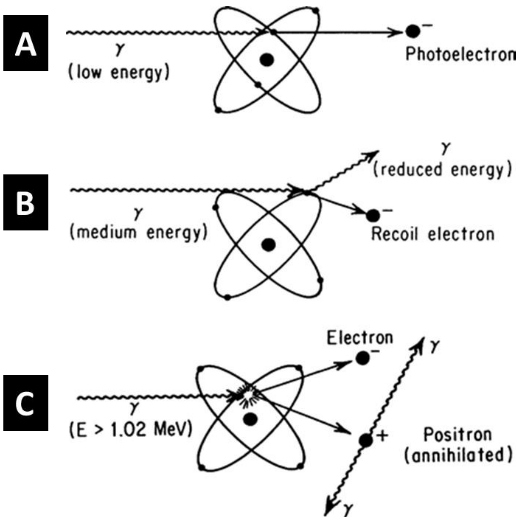

Fig. 8.3. Schematic of gamma ray interactions with matter: (A) photoelectric, (B) Compton scattering and (C) pair production extracted from [191]

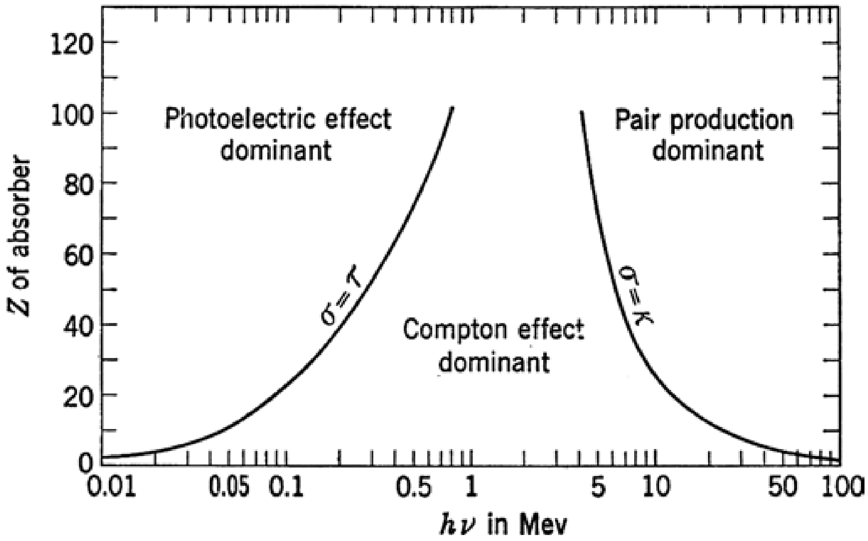

Fig. 8.4. Schematic of the dominant mechanism for gamma ray interactions with matter, extracted from [191]

As demonstrated in Figs. 8.1-8.2, the emitted gamma ray energy from nuclear decay was 0.662 MeV for Cs-137, and 1.173 plus 1.333 MeV for Co-60. According to Fig. 8.4, the dominant effect in matter (i.e. MKPCs) using gamma radiation sources will be the Compton scattering (or effect), whilst, secondary interactions with matter occur via the photoelectric effect [191]. The dominant interaction with matter is described by the curves in Fig. 8.4, which represent the intersect for the atomic number (Z)/photon energy plane where Compton scattering (σ) is equal to the photoelectric effect (τ, left curve) and pair production (κ, right curve) [191].

8.1.3 Interaction of gamma irradiation with ILW encapsulant grouts

The majority of the cement irradiation studies have chiefly focussed on gamma irradiation of Portland cements blended with FA or GBFS. Kontani *et al.* [192] described gamma irradiation of PC pastes to result in the decomposition of the hydrated PC phases (e.g. C-S-H, portlandite, ettringite [24]) via radiolysis. This leads to the formation of hydrogen and hydrogen peroxide species that further degrade into water and oxygen [169]. Radiolysis can also cause internal overpressure resulting in stress-induced cracking of the wasteforms and the accumulation of explosive hydrogen gas [193], which is undesirable during storage or within in a geological repository. The typical effects of radiolysis occuring in PC grouts include: reduced compressive and tensile strength, amorphisation of crystalline cement hydrated phases, and/or densification and decomposition of hydrated phases [194, 195]. These effects could potentially be detrimental to the continued ability of the cement to encapsulate the radioactive waste. Another impact of gamma radiation on PC pastes is the dehydration of the hydrated PC phases through radiogenic heating [169].

The mechanical properties of irradiated PC concretes were investigated by Soo and Milan [195], who reported that the compressive strength of PC concretes was dependent upon the irradiation exposure time rather than the total accumulated dose. For example, at low a gamma dose rate (0.031 kGy/hr) a drop in compressive strength was observed at just 0.1 MGy, whilst at a high gamma dose rate (380 kGy/hr), the compressive strength was found to decrease after the absorption of 10 MGy [195]. The mechanism for strength loss in these samples was attributed to radiolysis of hydrated cement phases (e.g. C-S-H, portlandite, ettringite 17]).

However, in PC composite grouts irradiated in a Harwell spent fuel pond at a dose rate of 10 kGy/hr, no differences were observed in the mechanical properties of GBFS/PC and FA/PC grouts as a results of exposure to radiation doses of 9-12 MGy [196], albeit occasional cracking of the samples was detected associated with hydrogen generation from the radiolysis of water within the sample [196]. In a GBFS/PC sample, exposed to a total of 87 MGy, no obvious changes were identified in the microstructural properties of this grout apart from the formation of additional ettringite, which was thought to be the result of accelerated oxidation of the sulphur species present in GBFS [5]. The literature of PC based encapsulants indicated that they have a significant radiation tolerance to gamma irradiation, and as such are suited to application in intermediate level encapsulation [4, 5].

At present there is very little scientific data available regarding the radiation stability of blended MKPC binders, as such more technical information is required to ensure that they have a high degree of radiation tolerance prior to deployment as an encapsulant of ILWs in the UK. In this chapter, initial scoping investigations were conducted using Cs-137 gamma radiation at low dose rates/total doses. Whilst Co-60 gamma irradiation experiments to determine the effect of the absorbed dose (kGy) and the applied dose rate (kGy/hr) using XRD, FTIR, TGA/DTG, SEM/EDX and solid-state NMR techniques. This work aims to define the radiation tolerance boundaries for these materials, supporting their potential use as nuclear waste encapsulants.

8.2 Scoping irradiation trial using Cesium-137

8.2.1 Experimental set-up

Blended MKPC binders (FA/MKPC and GBFS/MKPC at 0.24 w/s) were produced in accordance with the formulations reported in Table 3.4 and cured for 28 days in an environment chamber at 20 °C and 95 % relative humidity. After which, the hardened samples were ground in a pestle and mortar prior to being sieved to 63 µm. Samples were weighed (1-2 g) into 5 mL screw-cap centrifuge tubes and organised into total dose batches (in 50 mL centrifuge tubes). The sealed samples were placed inside the 3.8 L canister (Fig. 8.5B) and irradiated using a CIS 437 C irradiator (Fig. 8.5A) with a Cs-137 source (0.662 MeV) at a dose rate of 0.15 kGy/hr to achieve total doses of: 2, 6, 15 and 24 kGy (Table 8.1). The gamma radiation behaviour of pure struvite-K synthesised in Chapter 5 was used as a reference for the blended MKPC binders.

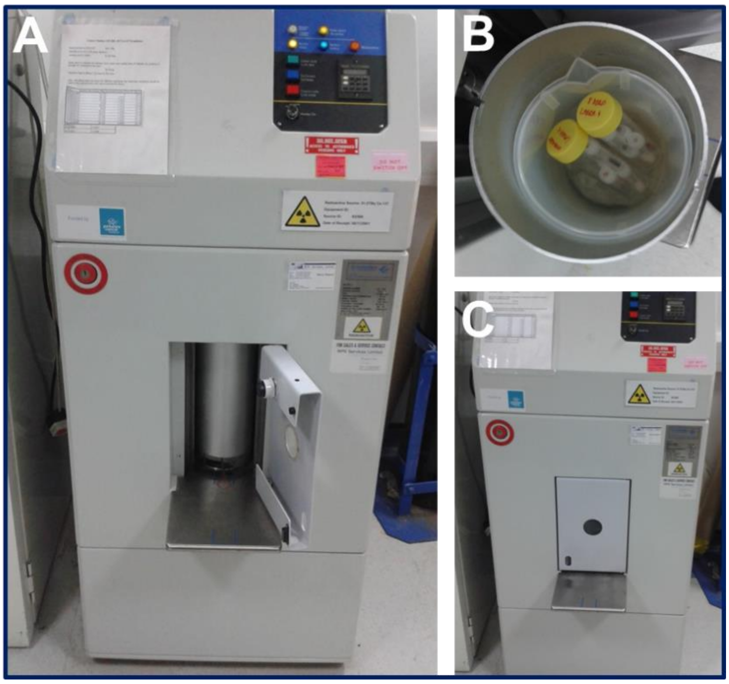

Fig. 8.5. Photographs of (A) the opened Cs-137 irradiator, (B) the sample containment and (C) the closed irradiator

Table 8.1. Scoping trial information for the Cs-137 irradiated specimens

Sample No.	Sample	Time (hr)	Dose Rate (kGy/hr)	Dose (kGy)
1	Struvite-K	0.0	0.00	0.0
2	Struvite-K	2.0	0.15	0.3
3	Struvite-K	6.0	0.15	0.9
4	Struvite-K	15.0	0.15	2.3
5	Struvite-K	24.0	0.15	3.6
7	FA/MKPC	0.0	0.0	0.0
8	FA/MKPC	2.0	0.15	0.3
9	FA/MKPC	6.0	0.15	0.9
10	FA/MKPC	15.0	0.15	2.3
11	FA/MKPC	24.0	0.15	3.6
12	GBFS/MKPC	0.0	0.0	0.0
13	GBFS/MKPC	2.0	0.15	0.3
14	GBFS/MKPC	6.0	0.15	0.9
15	GBFS/MKPC	15.0	0.15	2.3
16	GBFS/MKPC	24.0	0.15	3.6

8.2.2 Results and discussion

8.2.2.1 X-ray diffraction

The X-ray diffraction patterns of irradiated pure struvite-K ($MgKPO_4 \cdot 6H_2O$, PDF #75-1076) in Fig. 8.6 concur with XRD data presented in Chapter 5, in which only reflections associated with struvite-K were identified. After exposure to gamma radiation up to 3.6 kGy, there were no apparent changes in the phase assemblage or the relative intensities of the reflections. This indicated that struvite-K can withstand low levels of radiation without undergoing dehydration (via radiolysis). It was expected that dehydration due to radiogenic heating would result in the formation of the dehydration product, α-$MgKPO_4$, which was previously identified in struvite-K (Chapter 5) and the blended MKPC binders (Chapter 7). The XRD analysis indicates that during irradiation in the Cs-137 irradiator, the samples were not exposed to temperatures greater than 50 °C, which is the temperature at which struvite-K begins to dehydrate as observed in Fig. 5.2.

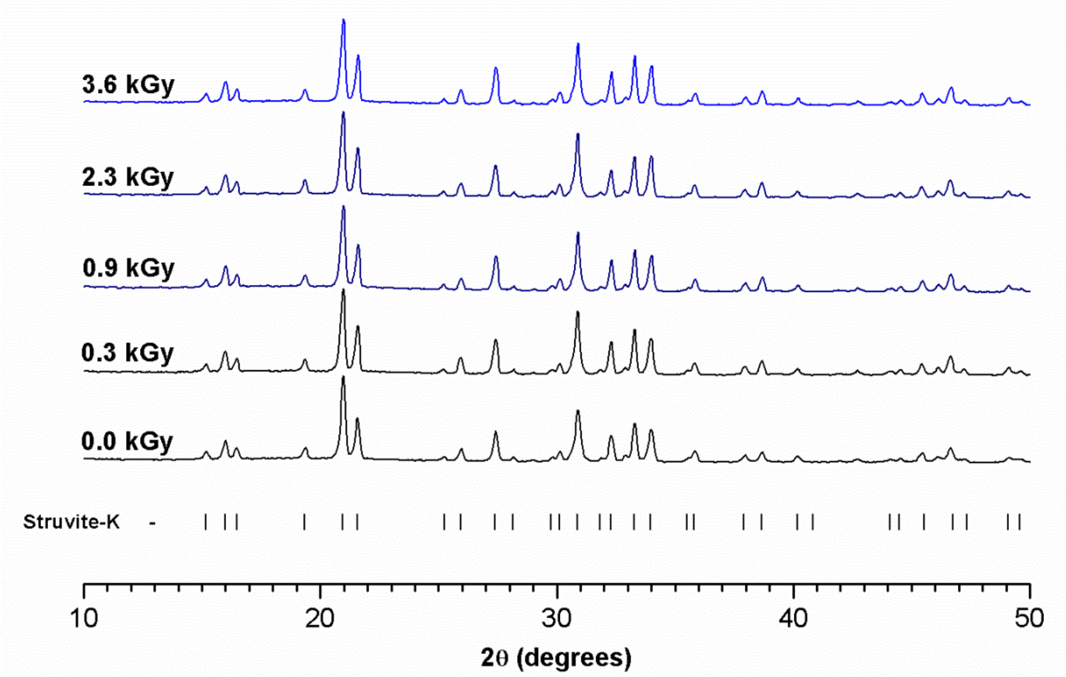

Fig. 8.6. Diffraction patterns of struvite-K at 28 days curing irradiated between 0 - 3.6 kGy

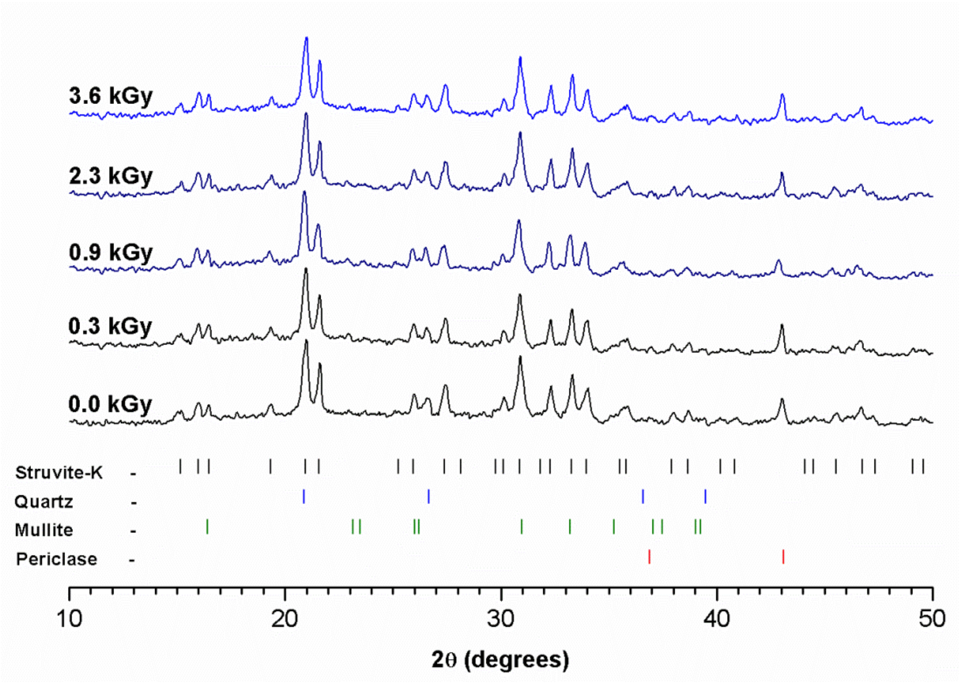

Fig. 8.7. Diffraction patterns of hardened FA/MKPC specimens at 28 days curing irradiated between 0 - 3.6 kGy

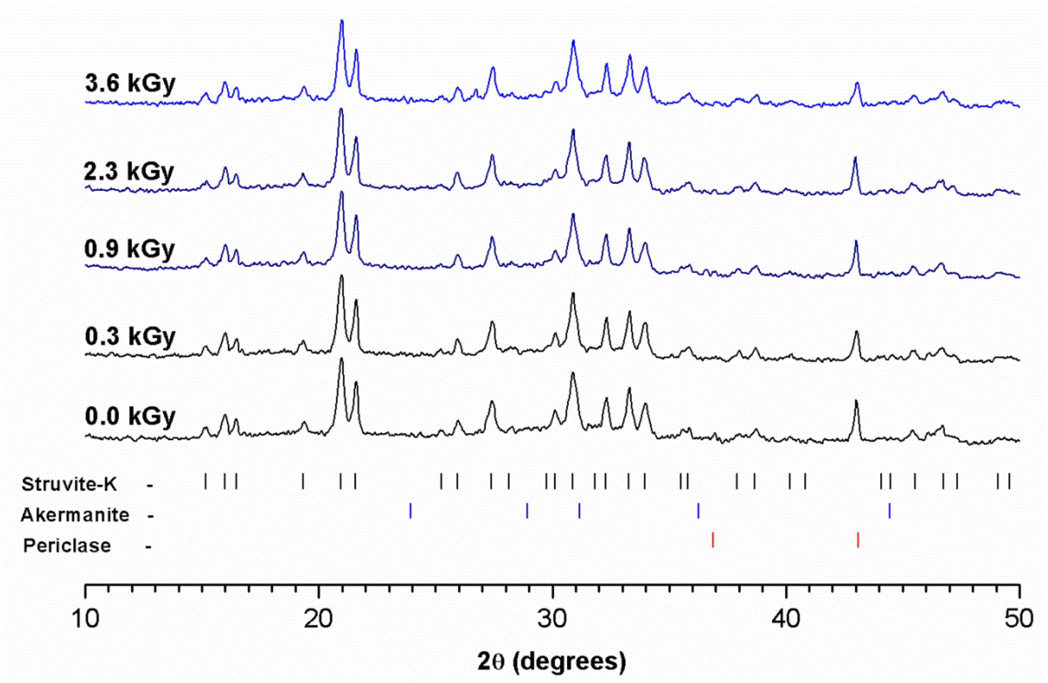

Fig. 8.8. Diffraction patterns of hardened GBFS/MKPC specimens at 28 days curing irradiated between 0 - 3.6 kGy

In the FA/MKPC binder (Fig. 8.7) and the GBFS/MKPC binder (Fig. 8.8) reflections associated with struvite-K constituted the majority of reflections observed. Additional crystalline phases identified include: unreacted periclase (MgO, PDF #45-0946); quartz (SiO_2, PDF #11-0252) and mullite ($3Al_2O_3.2SiO_2$, PDF #15-0776) in the FA/MKPC samples; and åkermanite in the GBFS/MKPC samples, where the main reflection was at 2θ = 31°. After exposure up to 3.6 kGy (equivalent to 24-hour irradiation at dose rate 0.15 kGy/hr), no differences were observed in the phase assemblage of the blended MKPC binders, which was concurrent with the XRD analysis of pure struvite-K in Fig. 8.6. It has been shown that low absorbed radiation doses have no impact upon the crystalline nature of blended MKPC binders and its cementitious phase, struvite-K.

8.2.2.2 Fourier-transform infra-red spectroscopy

The FTIR spectra shown in Fig. 8.9 are typical of those described in the literature for pure struvite-K systems [35, 98, 137]. The broad, asymmetric band between ≈ 3600 - 2500 cm^{-1} is associated with overlapping bands relating to H-O-H stretching vibrations of crystalline water, more specifically with the v_1 (symmetric) and v_3 (asymmetric) vibrations [35]. The weak band located at 2360 cm^{-1} was assigned to P-O-H vibrations, whilst the double split band at 1678 and 1616 cm^{-1} is associated with H-O-H v_2 (asymmetric) bending vibrations of crystalline water, the band at 798 cm^{-1} is associated with H_2O – H_2O hydrogen bond vibrations [35, 137]. There are four vibration modes of the PO_4^{3-} unit, of these: only v_3 (asymmetric stretching) and v_4 (asymmetric bending) are IR active [197], which were observed as strong bands at 1018 cm^{-1} and 573cm^{-1}, respectively [197].The band at 744 cm^{-1} is assigned to vibrations of the Mg – O bond [98].

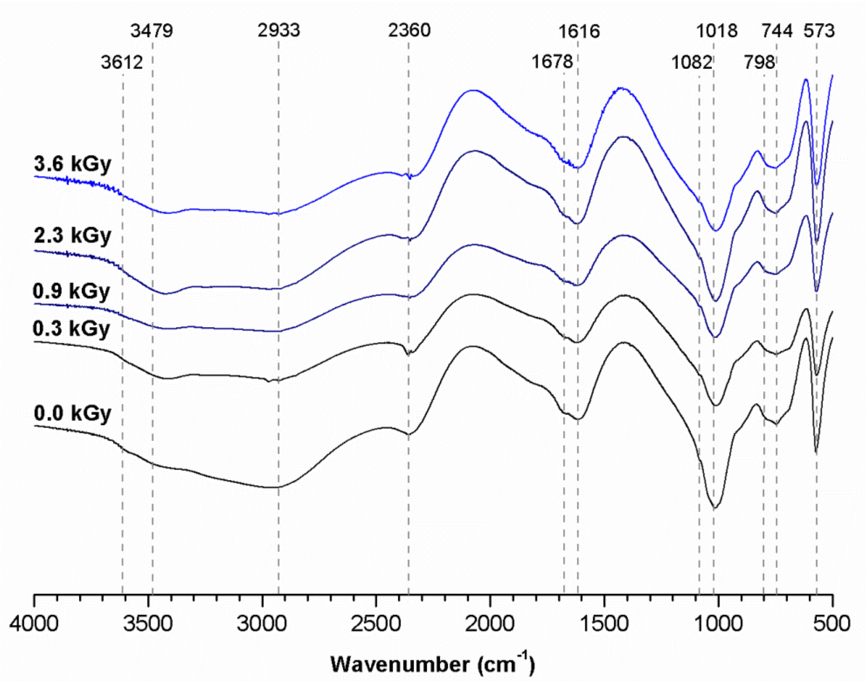

Fig. 8.9. FTIR spectra of struvite-K at 28 days curing irradiated between 0 - 3.6 kGy

The intensity of the broad band between 3600 - 2500 cm^{-1} and the double split band at ≈ 1670 cm^{-1} (associated with the crystalline H_2O stretching and bending vibrations) was observed to decrease between the control (0.0 kGy) the struvite-K sample irradiated to 0.3 kGy (Fig. 8.9). At the higher total irradiation doses, no additional changes associated with these regions were observed. It is postulated that the apparent reduction in the H_2O content between 0.0 and 0.3 MGy could be associated with the loss of free water/pore water from within the sample. However, due to clear differences in the intensity of the PO_4^{3-} unit vibrations and the Mg-O bond, is it also possible that the observed differences could be the result of sample preparation, e.g. enforced errors whilst preparing/pressing the 2 wt. % specimen in KBr.

The FTIR spectra for blended MKPC binders, FA/MKPC (Fig. 8.10) and GBFS/MKPC (Fig. 8.11) were observed to exhibit a similar sample preparation artefact. An additional shoulder was observed in the FA/MKPC binder at 1114 cm^{-1}, which is associated Si-O stretching vibration of quartz present in the raw FA [198]. No additional bands were observed in the unirradiated GBFS/MKPC sample or in the irradiated samples indicative of radiation stability.

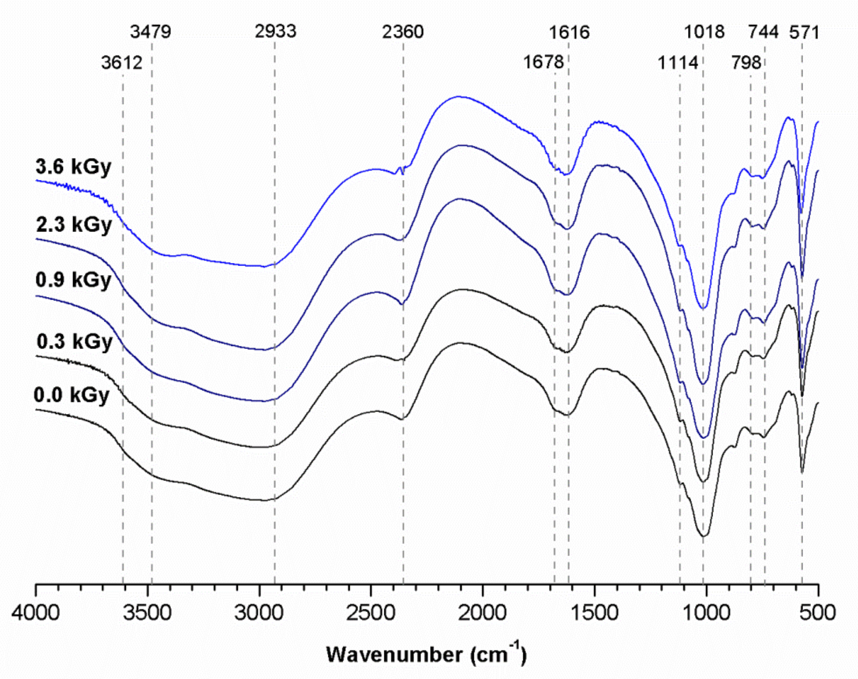

Fig. 8.10. FTIR spectra of hardened FA/MKPC specimens at 28 days curing irradiated between 0 - 3.6 kGy

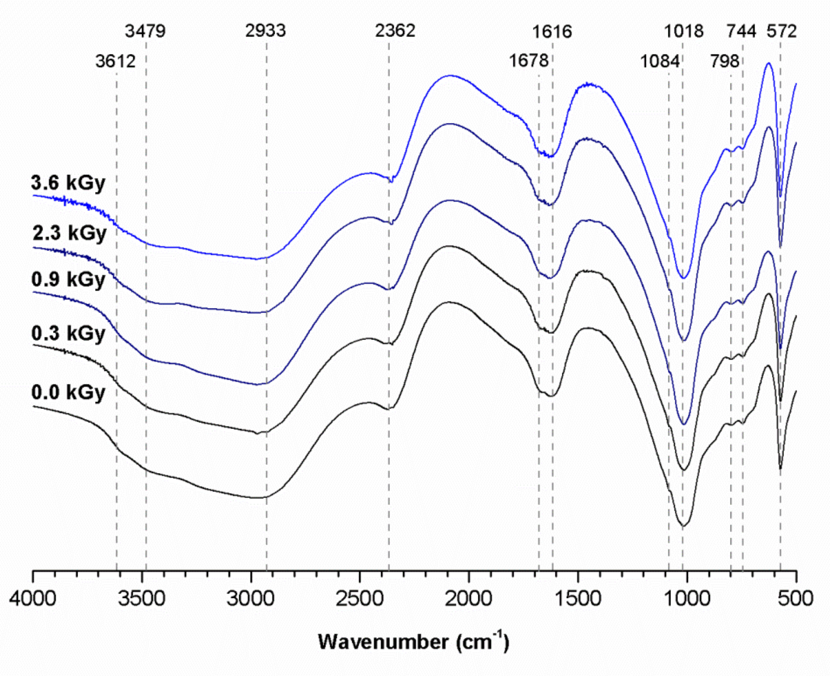

Fig. 8.11. FTIR spectra of hardened GBFS/MKPC specimens at 28 days curing irradiated between 0 - 3.6 kGy

In magnesium phosphate cements (with no filler), it is reported that symmetry or asymmetry of the band at 1018 cm^{-1} can be used as a proxy to indicate the hydration product formed [108]. For example, the hexahydrate phase (i.e. struvite or struvite-K) exhibits a symmetric band, whilst an asymmetric band (or a shoulder) is indicative of more than one hydration product (i.e. hexahydrate and monohydrate phases) [108]. In this study, the FTIR spectra for struvite-K, FA/MKPC and GBFS/MKPC indicate that only the hexahydrate product was formed, as identified by the symmetric band at 1018 cm^{-1} in Figs. 8.9-8.1 consistent with the XRD analysis (Figs. 8.6-8.8).

8.2.2.3 Thermal analysis

In Fig. 8.12, a one-step dehydration of struvite-K to $MgKPO_4$ (Eq. 8) occurs between 40 - 200 °C, as discussed in Chapter 5 and concurs with Zhang *et al.* [98]. After exposing the pure struvite-K samples to gamma irradiation up to 3.6 kGy, no distinct differences in the dehydration behaviour can be ascertained. The sample irradiated to 0.9 kGy was found to dehydrate at a slower rate compared to the other struvite-K samples (unirradiated and irradiated), this was further emphasised in the DTG plot (Fig. 8.12B). However, no differences were observed in the overall mass loss (around ≈ 40 wt. %) for each sample, which concurs with the dehydration of struvite-K in Chapter 5 and supports the FTIR analysis. This indicates that the highlighted difference in the 0.9 kGy struvite-K sample was within the expected range for the dehydration behaviour of struvite-K rather than an effect from exposure to gamma irradiation.

The thermal behaviour of the FA/MKPC (Fig. 8.13) and GBFS/MKPC (Fig. 8.14) binders exposed to gamma irradiation were very similar to that of struvite-K, as a single dehydration event was identified between 50 - 150 °C. The mass loss was found to be around 18 and 20 wt. %, respectively concurrent with the thermal analysis results in Chapter 7. The DTG plots (Fig. 8.13B and Fig. 8.14B) highlight that the dehydration of struvite-K in MKPC binder reaches a maximum at 100 °C, in agreement with [18] and [98]. There appeared to be no significant effect of Cs-137 radiation on the FA/MKPC and GBFS/MKPC binders under low dose rate conditions.

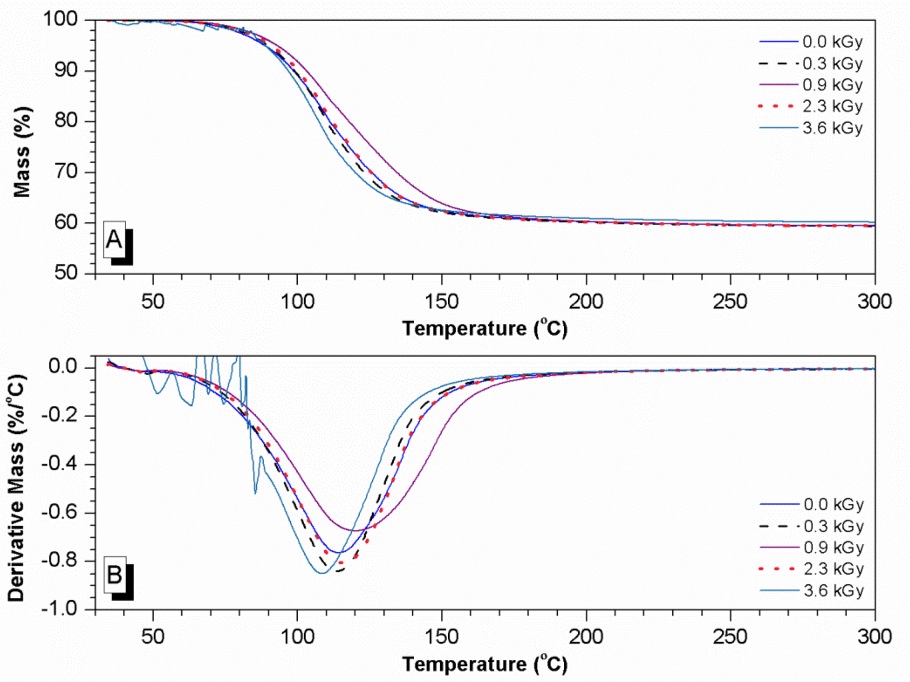

Fig. 8.12. TGA (A) and DTG (B) traces of struvite-K irradiated between 0 - 3.6 kGy

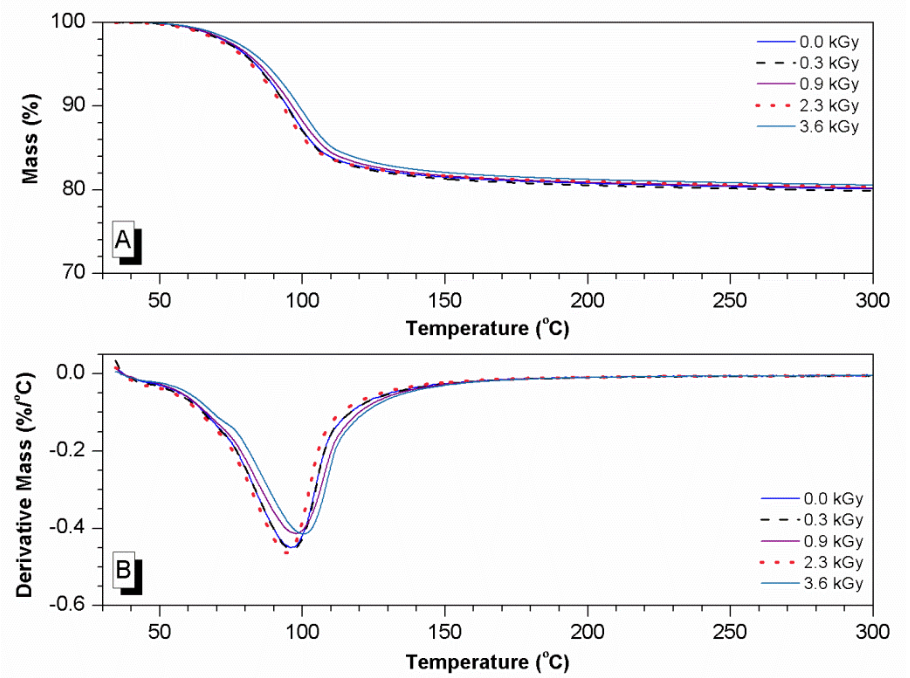

Fig. 8.13. TGA (A) and DTG (B) traces of hardened FA/MKPC specimens at 28 days curing irradiated between 0 - 3.6 kGy

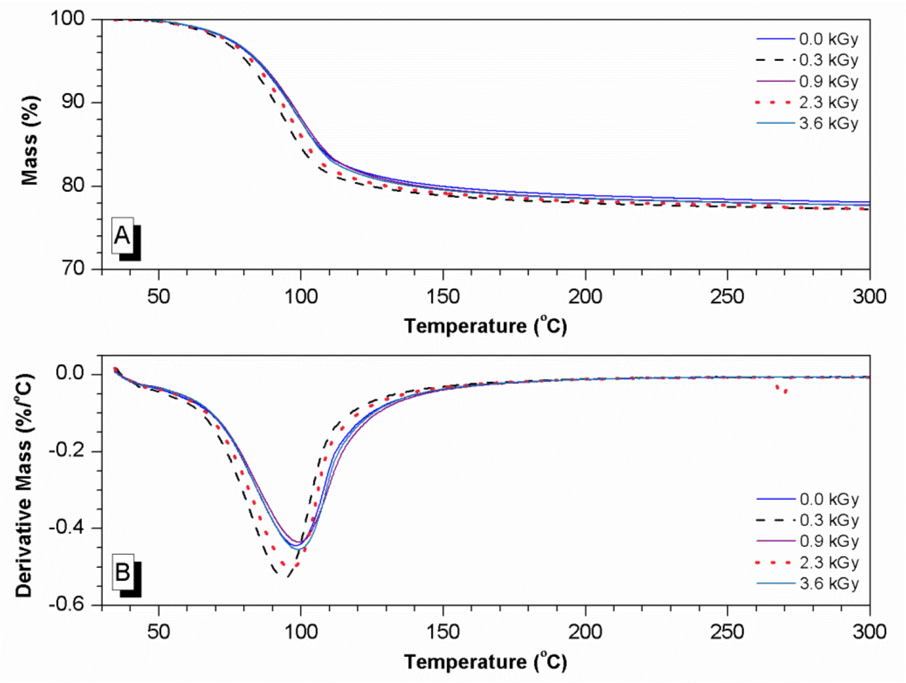

Fig. 8.14. TGA (A) and DTG (B) traces hardened GBFS/MKPC specimens at 28 days curing irradiated between 0 - 3.6 kGy

8.2.3 Summary

At the radiation doses investigated in the scoping study (0 - 3.6 kGy) the results indicated that there was no alteration of the typical phase assemblage of pure struvite-K and the blended MKPC binders or the dehydration behaviour. It is postulated that the blended MKPC binders and pure struvite-K exhibit a degree of radiation tolerance but further work is needed to determine the extent of this tolerance. As such, the results in this scoping study validate the continuation of gamma irradiation studies on blended MKPC binders. The effect of high gamma dose rate/total dose on the chemical and microstructural properties of MKPC binders will be discussed in the following section.

8.3 The effect of Cobalt-60 irradiation on blended MKPC binders

8.3.1 Experimental set-up

Blended MKPC binders (FA/MKPC and GBFS/MKPC) were produced in accordance with the formulations reported in Table 3.4. To prepare the samples for the irradiation experiments, the samples were cured for an initial 28 days in an environmental chamber at 20 °C and 95 % relative humidity. After this curing period, the FA/MKPC and GBFS/MKPC specimens) were then ground in a ball-mill and sieved to 63 µm using a brass sieve. For SEM analysis, the blended MKPC samples were sectioned into pucks (ø = 14 mm, *h* = 2-3 mm) and then split into two equal segments using an Isomet slow saw. The powdered samples were weighed (5 g) into 20 mL glass vials and the SEM section added. A rubber stopper was placed into the glass vial prior to an aluminium-lid being crimp sealed onto the vial under an argon atmosphere (using a glove bag) in order to achieve a tight seal. The sealed samples were transferred to the Dalton Cumbrian Facility (DCF) at the University of Manchester for irradiation in the self-shielded Co-60 irradiator (Fig. 8.15), the specification of which is listed below:

Specification of the Co-60 gamma irradiator [199]:

- Model 812 self-contained irradiation facility (Foss Therapy Services, Inc.)
- Sample chamber: *w* = 20.3, *d* = 25.4 and *h* = 30.5 cm
- Sample chamber volume: > 9.0 L
- Dual rod assembly assemblies (total of 6 sources)
- Activity: 535.4 TBq

The average dose rates and total doses of the FA/MKPC and GBFS/MKPC samples are detailed in Tables 8.2-8.3, for brevity the FTIR, XRD, TGA and SEM/EDX results for the radiation dose rates ≈5.0 kGy/hr and ≈3.0 kGy/hr are located in Appendix F, where the actual dose rates for all of the samples in this study are also located. The actual dose rate varied depending on when the sample was irradiated due to the decay of the Co-60 source. To ensure that the FA/MKPC and GBFS/MKPC binders were exposed to similar dose rates, the positions of the samples where fixed to the left (FA/MKPC) and right side (GBFS/MKPC) of the sample holder (Fig. 8.16). Due to the number of hours required to achieve the total doses required (Tables. 8.2-8.3), a stop/start method was adopted. The blended MKPC samples were irradiated during the evening sessions (i.e. after 6 pm) and removed from the irradiator in the morning. This process was continued until the desired final total dose for each sample was attained. During a continuous operation, the temperature within the irradiator stabilised around 45 °C at 6 hours (Fig. 8.17) but due to the stop/start nature of these experiments, the control samples were only stored at room temperature.

The duration of the irradiation experiments varied depending upon the final dose, position and availability in the Co-60 irradiator (as discussed above) however, this resulted in different final curing ages for the FA/MKPC and GBFS/MKPC samples at the point of XRD, FTIR, TGA and SEM analysis. The last samples to be analysed in this study were aged for one year, albeit they had been stored in glass vials (under argon) after the initial 28-day curing period in a controlled environment. Covill [18] studied similar FA/MKPC binders up to 360 days and observed no differences in the phase assemblage as a result of curing age. Thus, it was decided that all samples should be batched from one FA/MKPC and one GBFS/MPKC mix, in order to eliminate any batch to batch variations that could occur.

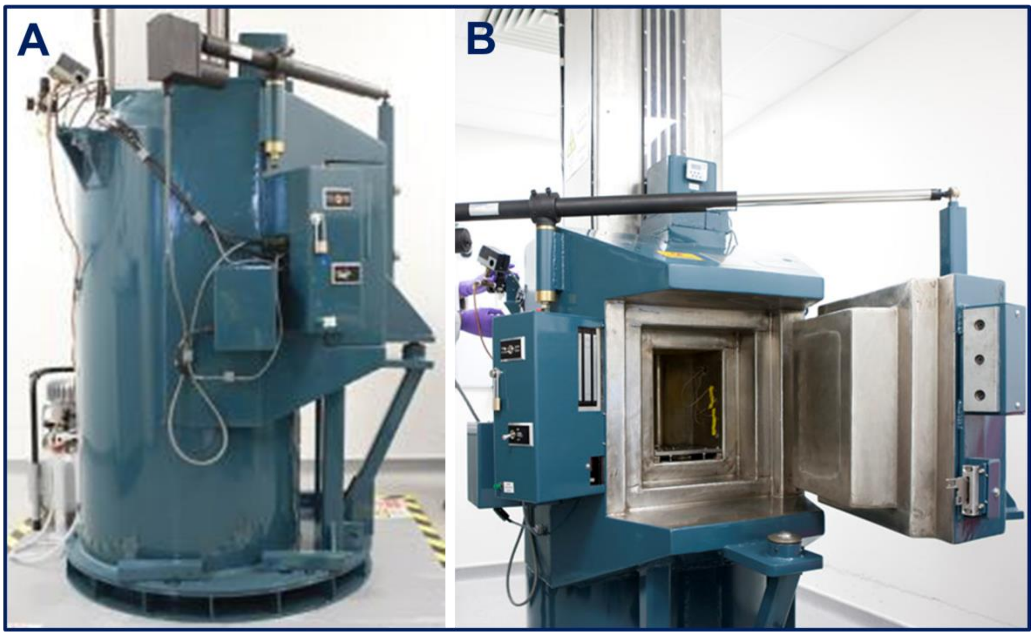

Fig. 8.15. Photographs of the a) closed Co-60 irradiator and b) the opened Co-60 irradiator [199]

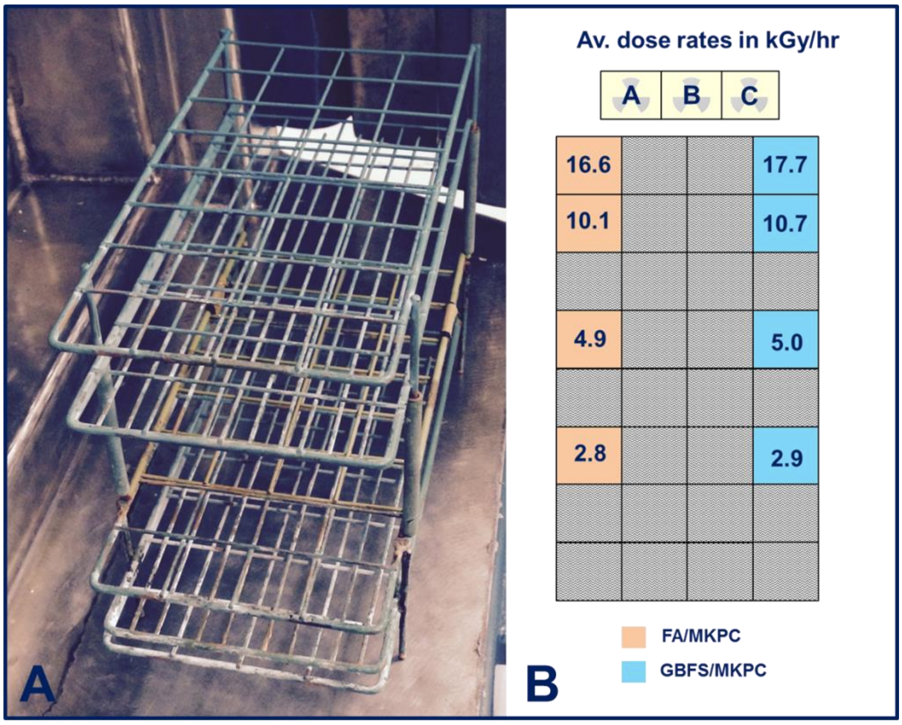

Fig. 8.16. Schematic of the (A) specimen tray and (B) the irradiation positions, Co-60 rods are labelled A-C

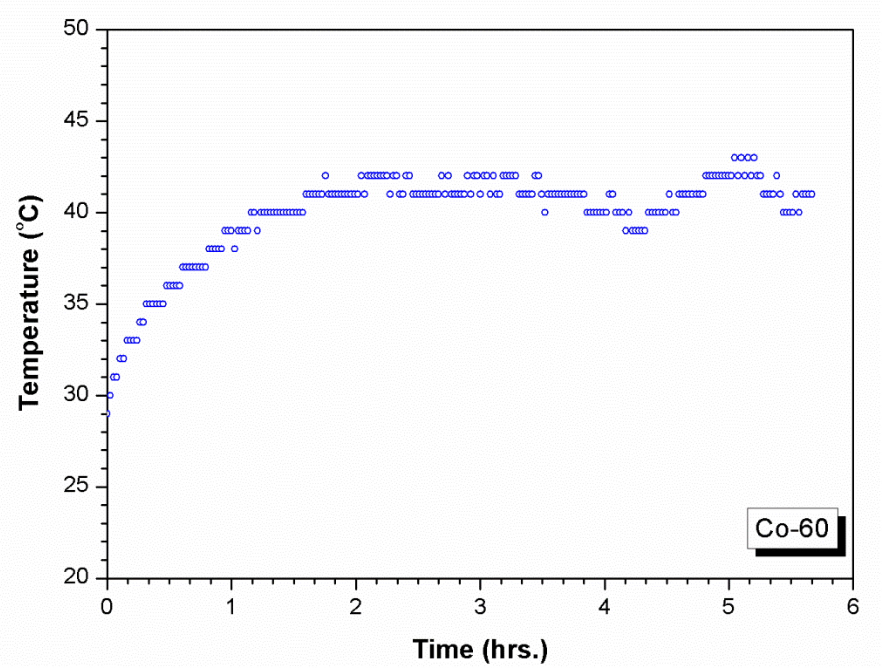

Fig. 8.17. Temperature variance during irradiation up to 6 hours continuous operation, data provided by R. Edge at the Dalton Cumbrian Facility, University of Manchester

Table 8.2. Average dose summary of the Co-60 irradiated FA/MKPC binders

Sample No.	Av. Dose Rate (kGy/hr)	Dose (MGy)
1	0.0	0.0
2	16.6 ± 0.7	1.0
3		2.4
4		4.7
5		7.0
6		9.6
7	10.1 ± 0.3	1.0
8		2.3
9		4.9
10		7.9
11		9.4
12	4.9 ± 0.3	0.5
13		1.0
14		1.5
15		2.4
16		4.8
17	2.8 ± 0.1	0.5
18		1.0
19		1.5
20		2.5

Table 8.3. Average dose summary of the Co-60 irradiated GBFS/MKPC binders

Sample No.	Av. Dose Rate (kGy/hr)	Dose (MGy)
1	0.0	0.0
2	17.7 ± 0.4	1.1
3		2.6
4		5.1
5		7.6
6		10.0
7	10.7 ± 0.5	1.1
8		2.5
9		5.0
10		8.0
11		10.3
12	5.0 ± 0.3	0.5
13		1.0
14		1.5
15		2.5
16		5.0
17	2.9 ± 0.1	0.5
18		1.0
19		1.5
20		2.6

8.3.2 Results and discussion

8.3.2.1 Powder X-ray diffraction

The phase assemblage of the FA/MKPC binders was previously discussed within section 8.2.2.1. The main crystalline phases identified in Figs. 8.18-8.19 were: struvite-K, unreacted periclase, quartz and mullite from the unreacted FA. This was in agreement with all of the FA/MKPC XRD data reported in this body of work. FA/MKPC samples irradiated in the Co-60 irradiator are shown in Fig. 8.18, up to a total dose of 9.6 MGy, the samples were irradiated at an average dose rate of 16.6 kGy/hr.

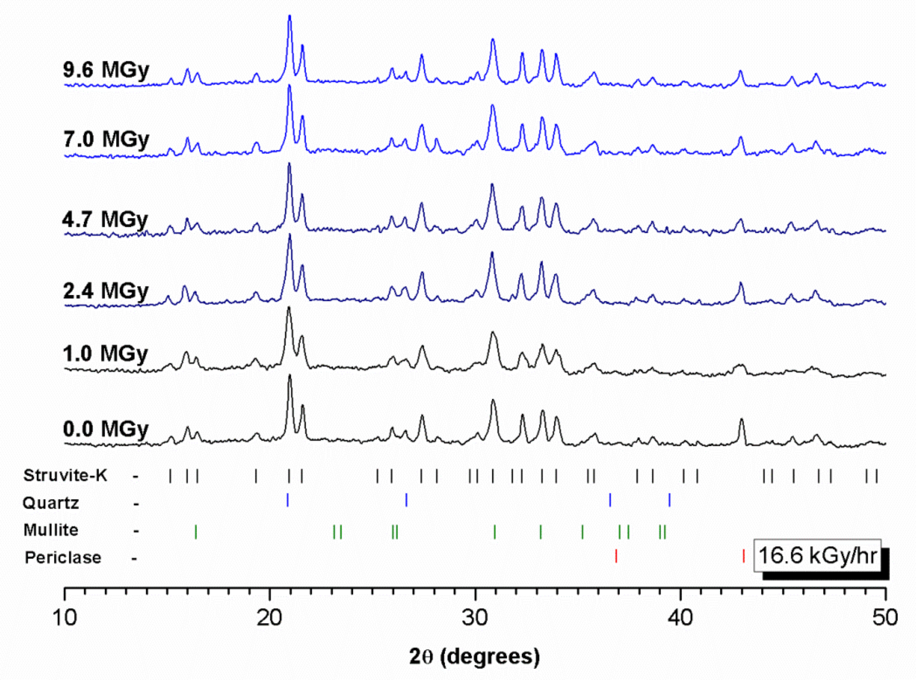

Fig. 8.18. Diffraction patterns of FA/MKPC exposed to: 0.0, 1.0, 2.4, 4.7, 7.0 and 9.6 MGy at 16.6 kGy/hr

In Fig. 8.18 it was found that the dominant crystalline reflections remained associated with struvite-K, the main binding phase within FA/MKPC binders. This indicated that these binders are stable to high levels of gamma radiation, up to approximately 10 MGy. The relative intensities of struvite-K, periclase and quartz reflections appeared to remain constant, which suggested that there was no change in the composition or distribution of these phases via radiolysis or dehydration due to radiogenic heat. At the dose rate, av. 10.1 kGy/hr, the results were comparable to the diffraction patterns of the av. dose rate 16.6 kGy/hr obtained up to total dose of 9.4 MGy (Fig. 8.19).

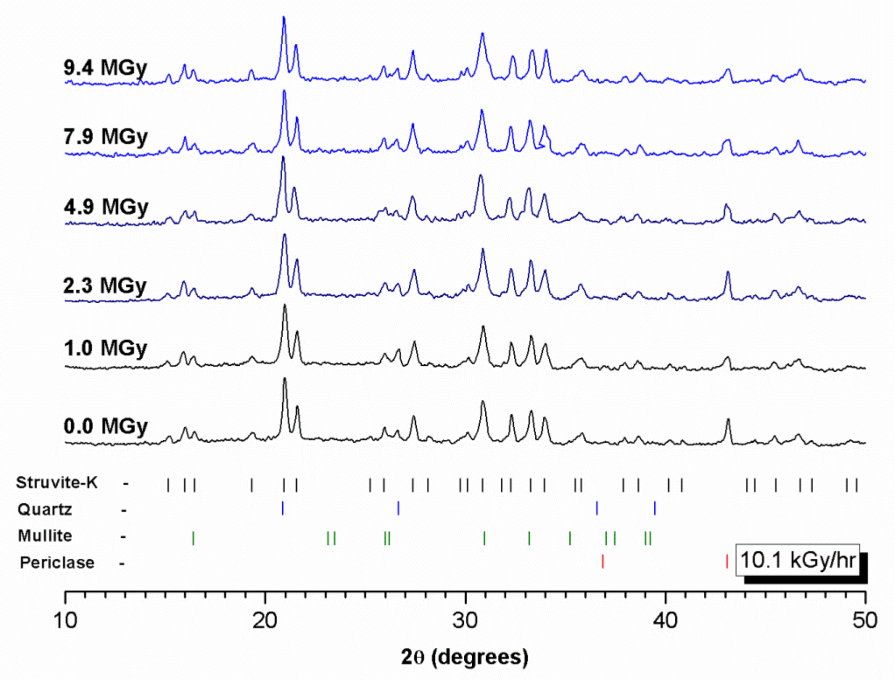

Fig. 8.19. Diffraction patterns of FA/MKPC exposed to: 0.0, 1.0, 2.3, 4.9, 7.9 and 9.4 MGy at 10.1 kGy/hr

The phase assemblage of the GBFS/MKPC binders was previously discussed within section 8.2.2.1. After irradiation with a Co-60 source, it was found that the main crystalline phases in Figs. 8.20-8.21 were: struvite-K, unreacted periclase, and åkermanite from the unreacted concurrent with previous data. The unirradiated and irradiated GBFS/MKPC binders are shown in Fig. 8.20. The irradiated samples were obtained at an average dose rate of 17.7 kGy/hr in the Co-60 irradiator up to a total dose of approximately 10.0 MGy. No differences in the relative intensities of the crystalline reflections were identified or the formation of additional phases was observed. Concurrent behaviour was exhibited in the GBFS/MKPC binders irradiated at the av. dose rate of 10.7 kGy/hr (Fig. 8.21). The diffraction patterns for blended MKPC binders indicate the existence of a high level of radiation tolerance up to approximately 10 MGy, which is significant for waste encapsulation applications as the gamma irradiation dose (from internal waste and neighbouring waste packages) to the conditioned wasteform is predicted to be 10 MGy after 300 years emplacement in a geological repository [188].

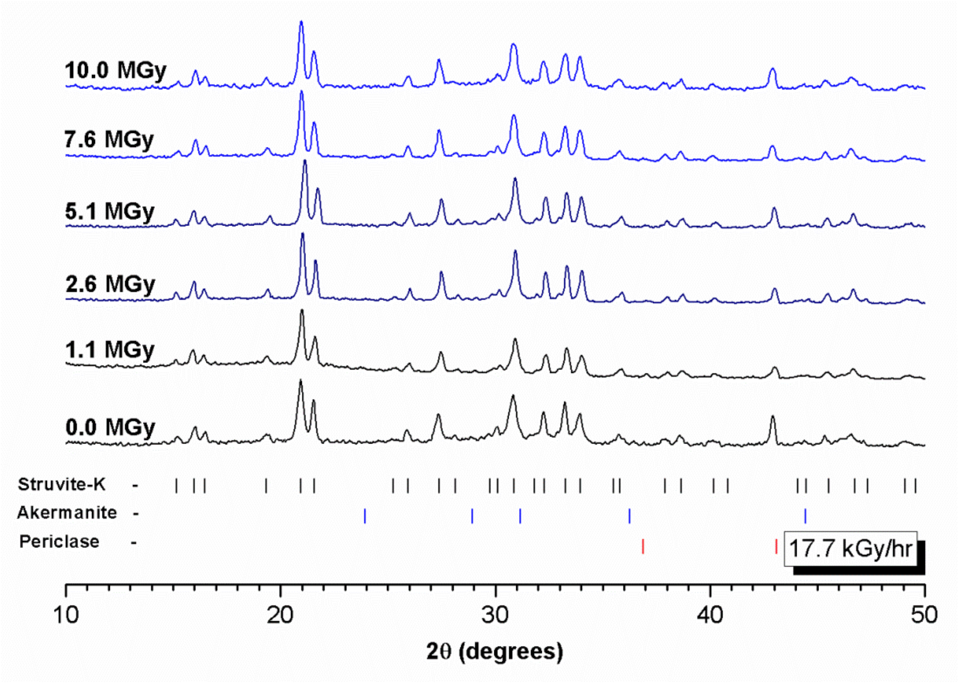

Fig. 8.20. Diffraction patterns of GBFS/MKPC exposed to: 0.0, 1.1, 2.6, 5.1, 7.6 and 10.0 MGy at 17.7 kGy/hr

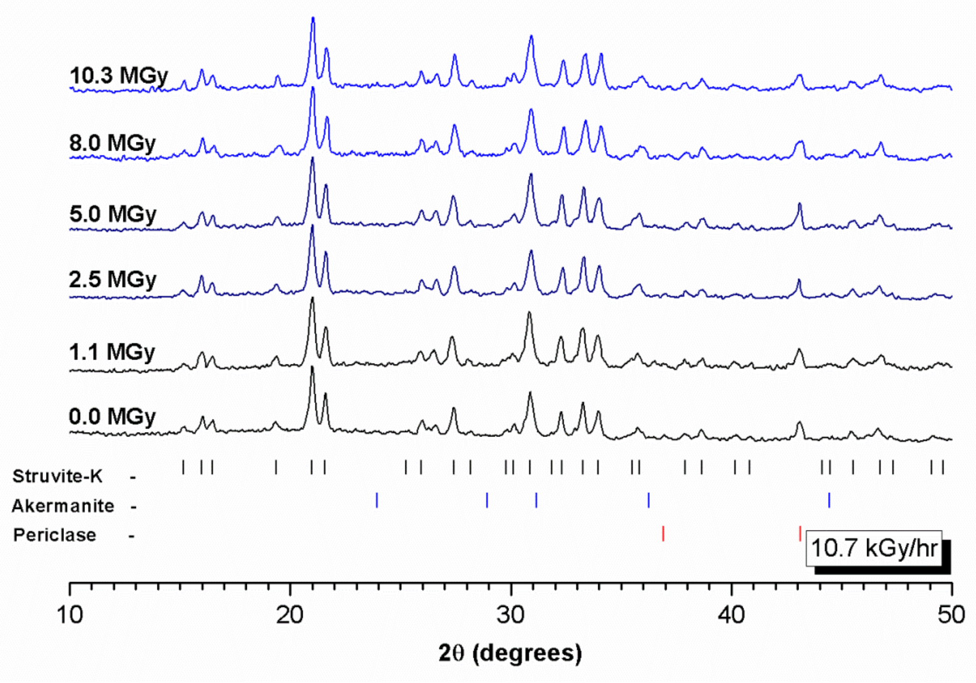

Fig. 8.21. Diffraction patterns of GBFS/MKPC exposed to: 0.0, 1.1, 2.5, 5.0, 8.0 and 10.3 MGy at 10.7 kGy/hr

8.3.2.2 Fourier-transform infra-red

The FTIR spectra for the FA/MKPC and GBFS/MKPC binders are shown in Figs. 8.22-8.25. It is immediately apparent that there was no change in the characteristic vibration bands for these samples. The FA/MKPC samples displayed in Fig. 8.22 were irradiated at the highest dose rate (av. 16.6 kGy/hr) up to 9.6 MGy, however, in the FTIR spectra, the intensity of the H-O-H stretching and bending vibrations associated with crystalline water between 3600-2500 cm^{-1} (comprised of multiple overlapping bands) and between 1678-1616 cm^{-1} [35, 137] did not change compared to the unirradiated sample (0.0 MGy). Along with the observations that no intensity changes of the PO_4^{3-} unit at 1018 cm^{-1} and 573cm^{-1} [197] and the Mg-O band at 744 cm^{-1} [98] indicated that the hydrated cement product (struvite-K) was still the dominant phase in this system. Comparable FTIR spectra were obtained for the FA/MKPC binders irradiated at the av. dose rate of 10.7 kGy/hr (Fig. 8.23). This supports the continued presence of crystalline water and indicated that the radiolysis is not a dominant radiation effect within these systems.

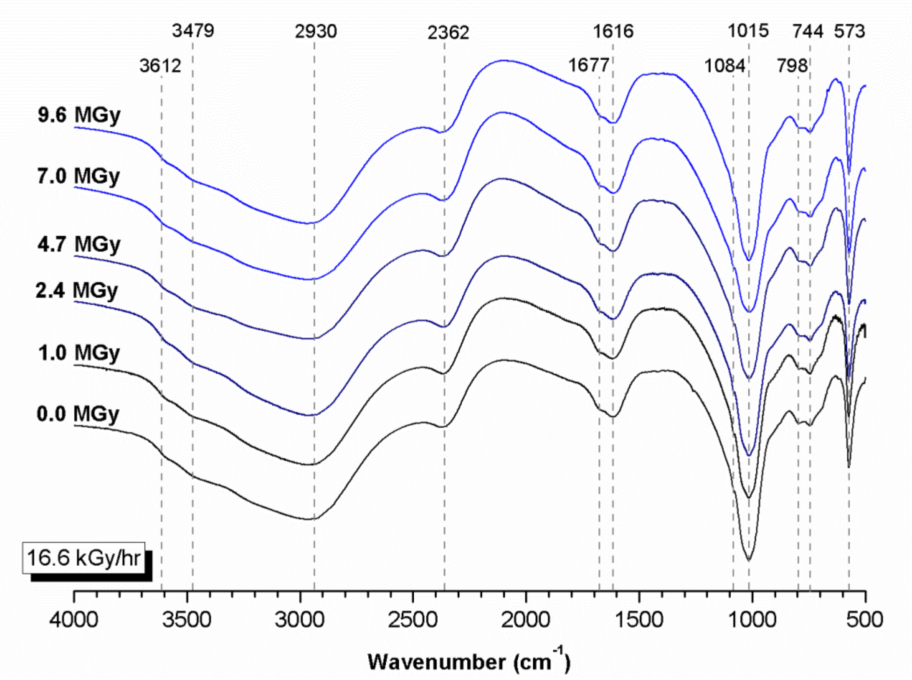

Fig. 8.22. Spectra of FA/MKPC specimens exposed to: 1.0, 2.4, 4.7, 7.0 and 9.6 MGy at 16.6 kGy/hr

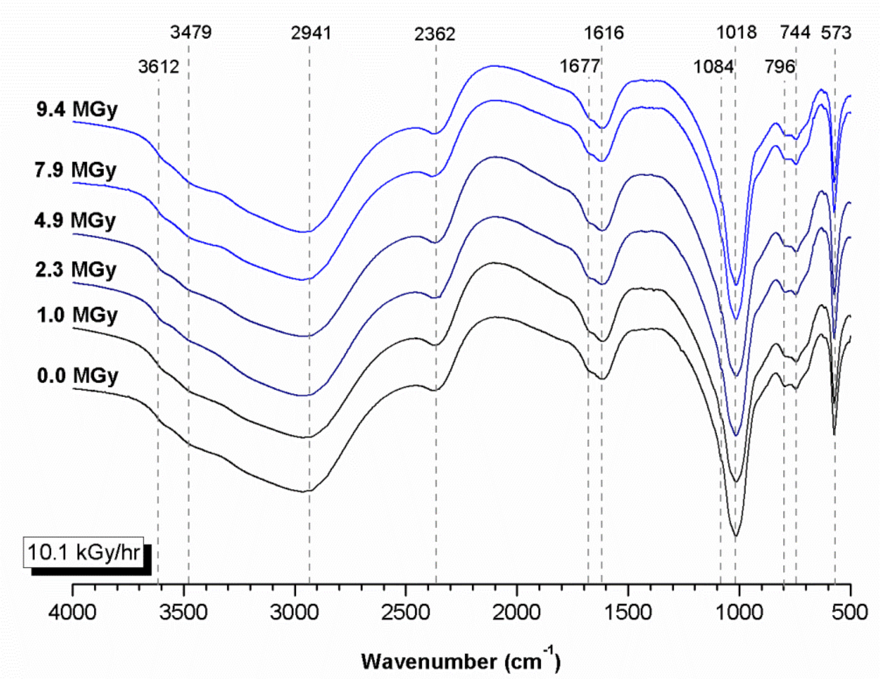

Fig. 8.23. Spectra of FA/MKPC specimens exposed to: 1.0, 2.3, 4.9, 7.9 and 9.4 MGy at 10.1 kGy/hr

In Fig. 8.24, In the FTIR spectra of the GBFS/MKPC binders irradiated at the av. 17.7 kGy/hr dose rate, the intensity of the overlapping H–O–H band between 3600-2500 cm^{-1} appeared to remain the same (observed by directly overlapping the spectra) for the unirradiated control sample and the specimens exposed to gamma irradiation, up to ≈ 10 MGy in Figs. 8.24-8.25. This is supported by the GBFS/MKPC binders exposed to the av. dose rate of 10.7 kGy/hr (Fig. 8.25), which did not exhibit any reduced intensities for the crystalline water environments nor any other changes at up to a total dose 10.3 MGy. As in the FA/MKPC binders, no changes occurred in either Fig. 8.24 or Fig. 8.25 associated with the phosphate group of the metal – oxygen bond, signifying that struvite-K present in both blended binders is tolerant to gamma radiation doses up to 10 MGy with no dose rate dependencies observed.

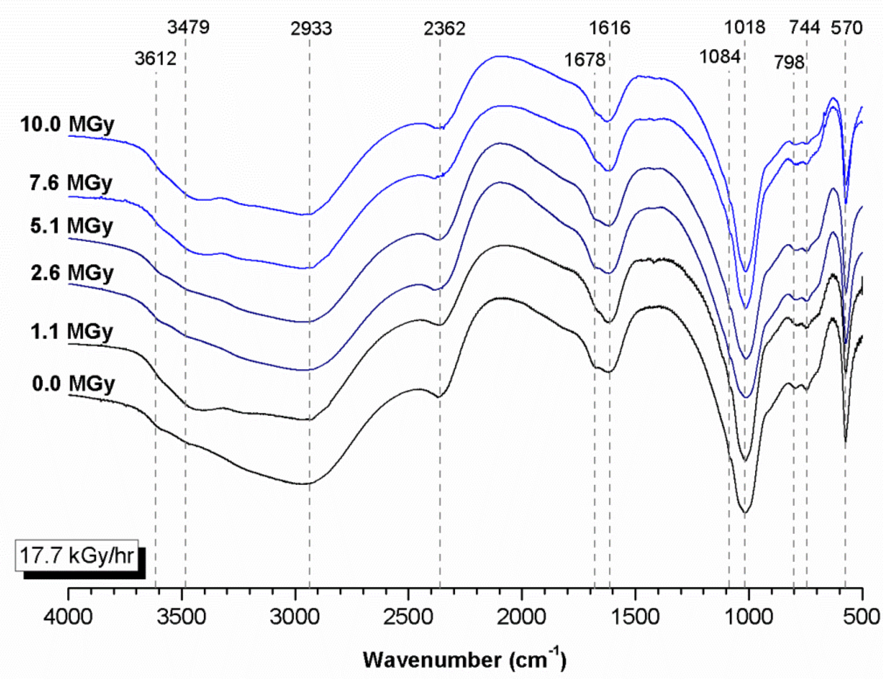

Fig. 8.24. Spectra of GBFS/MKPC specimens exposed to: 1.1, 2.6, 5.1, 7.6 and 10.0 MGy at 17.7 kGy/hr

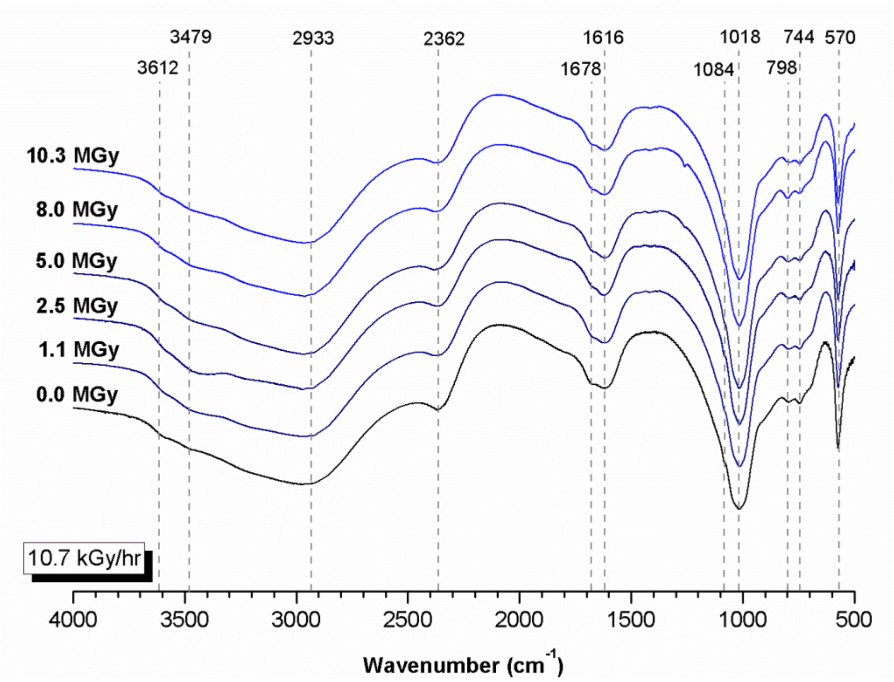

Fig. 8.25. Spectra of GBFS/MKPC specimens exposed to: 1.1, 2.5, 5.0, 8.0 and 10.3 MGy at 10.7 kGy/hr

8.3.2.3 Thermal analysis

The thermal behaviour of the FA/MKPC (Figs. 8.26-8.27) and GBFS/MKPC (Fig. 8.28-8.29) binders exposed to gamma irradiation were very similar to that of struvite-K (Chapters 5 and 8) and blended MKPC binders (Chapters 4, 7 and 8). A single dehydration event was identified between 50 - 150 °C. In the FA/MKPC binders irradiated at the av. dose rate 16.6 kGy/hr (Fig. 8.26), the mass loss was found to be 20 wt. % (measured at 150 °C) up to a total accumulated dose of 9.6 MGy. Concurrently, in the FA/MKPC samples irradiated at the av. dose rate 10.1 kGy/hr (up to 9.4 MGy), the mass loss was also observed to be 20 wt. % at 150 °C. These results are in agreement with the thermal analysis of unirradiated samples and the Cs-137 irradiated samples discussed in section 8.2.2.2. This indicates that these systems do not undergo the radiation dehydration described for PC grouts [169] and do not have a dose rate dependancy.

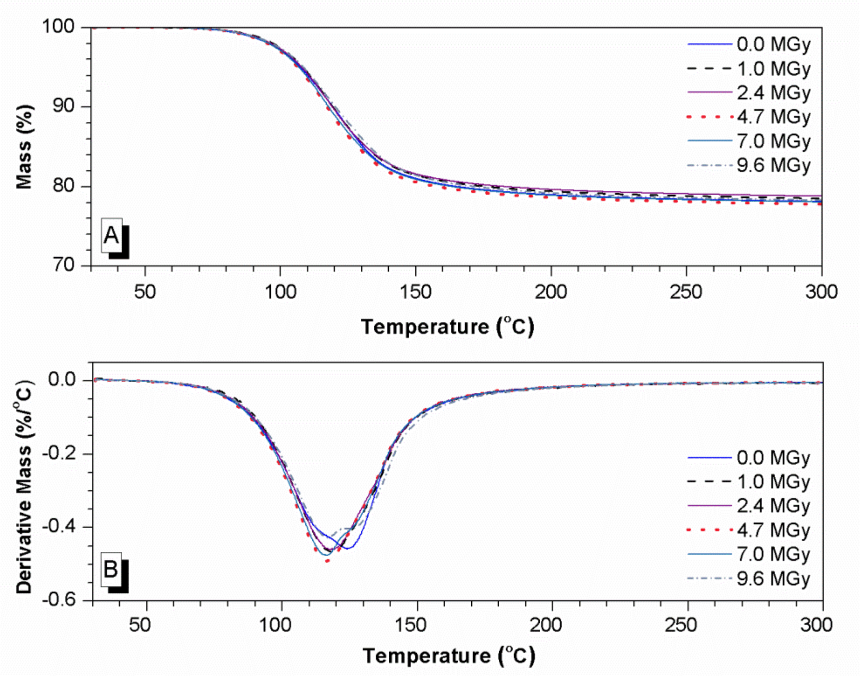

Fig. 8.26. TGA (A) and DTG (B) traces of FA/MKPC specimens exposed to: 1.0, 2.4, 4.7, 7.0 and 9.6 MGy at 16.6 kGy/hr

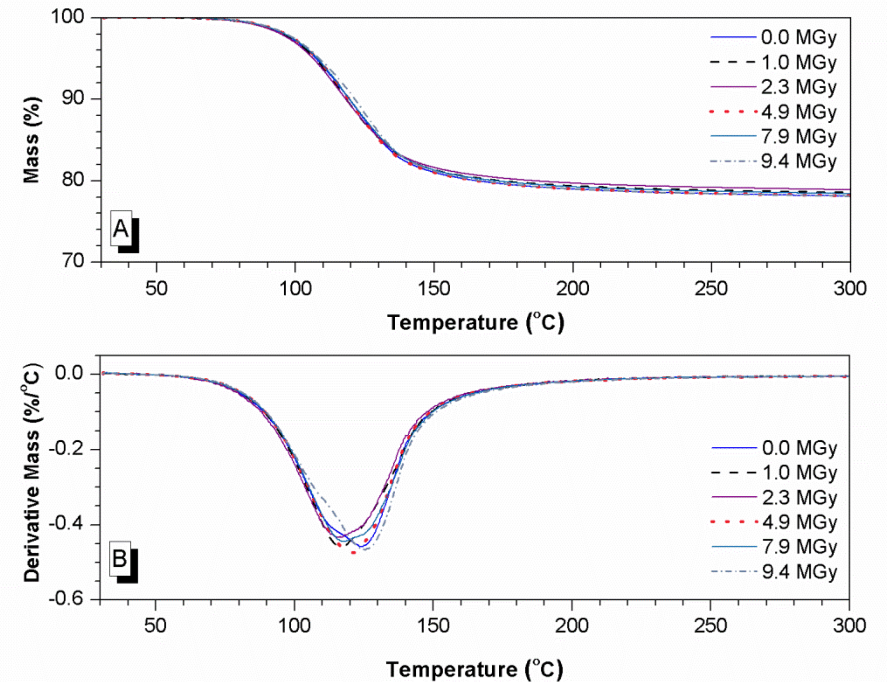

Fig. 8.27. TGA (A) and DTG (B) traces of FA/MKPC specimens exposed to: 1.0, 2.3, 4.9, 7.9 and 9.4 MGy at 10.1 kGy/hr

When compared to the thermal behaviour of the FA/MKPC binders, the irradiated GBFS/MKPC binders (at av. dose rates of 17.7 and 10.7 kGy/hr) appeared to have more variation in the mass loss associated with the dehydration of struvite-K (Figs. 8.28-8.29), however there is no clear pattern to this variation, which implies that there is no dose rate dependency in these systems. A single dehydration event (50 - 150 °C) was still identified however, the mass loss from the GBFS/MKPC binders varied from 22 to 18 wt. %, measured at 150 °C. In Fig. 8.28, the samples with the lowest mass loss (18 wt. %) were assigned to the 0.0 and 10.0 MGy samples, whilst in Fig. 8.29, an18 wt. % mass loss occurred in all samples, except those irradiated at 1.1 and 2.5 MGy. It is postulated that these differences are within statistical error of each other because there is no distinguishable pattern to varying mass loss. Therefore, this data indicated that gamma irradiation has little impact upon on the dehydration behaviour of GBFS/MKPC binders, which concurs with the FA/MKPC system.

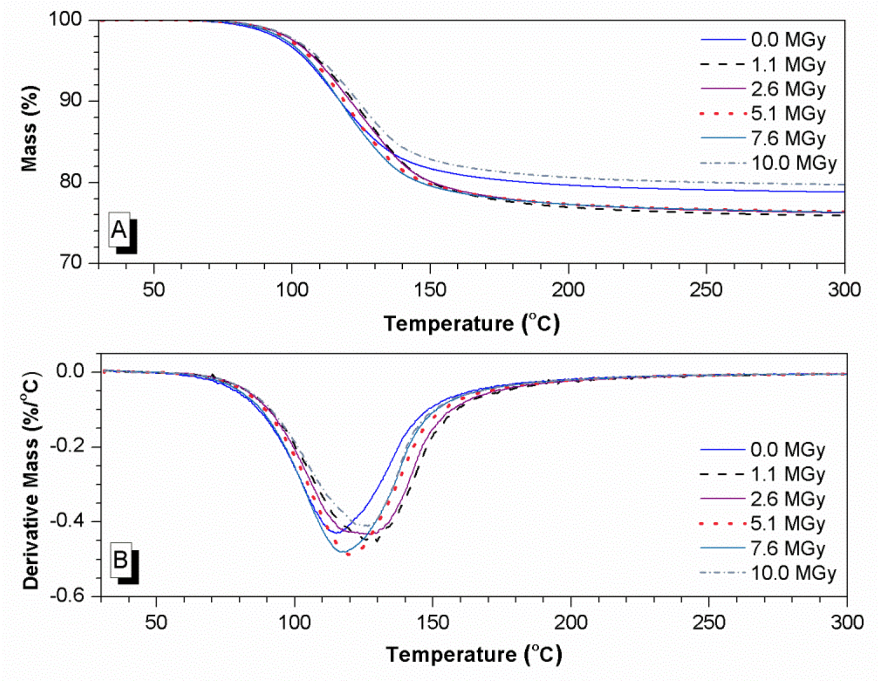

Fig. 8.28. TGA (A) and DTG (B) traces of GBFS/MKPC specimens exposed to: 1.1, 2.6, 5.1, 7.6 and 10.0 MGy at 17.7 kGy/hr

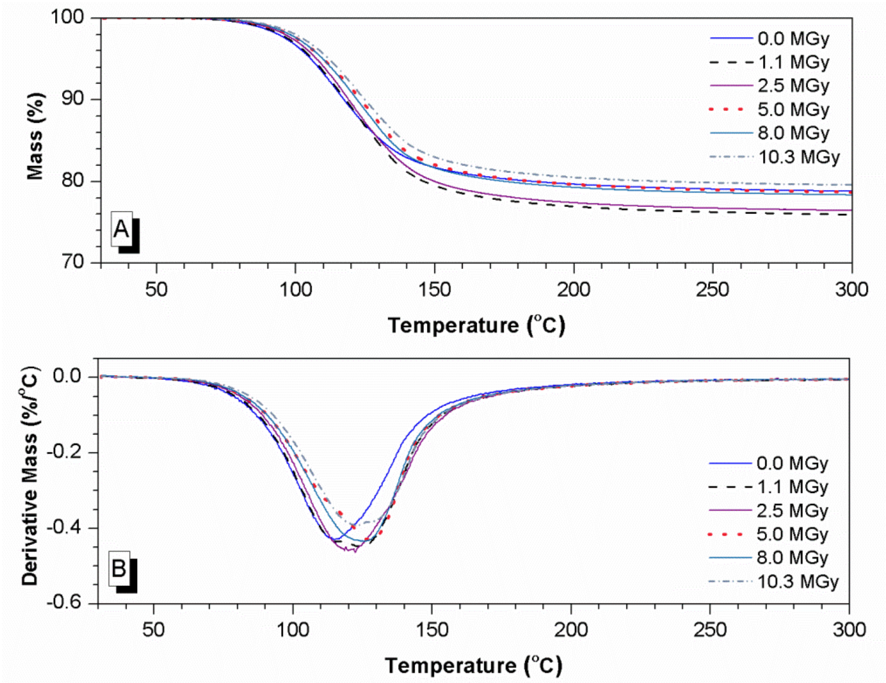

Fig. 8.29. TGA (A) and DTG (B) traces of GBFS/MKPC specimens exposed to: 1.1, 2.5, 5.0, 8.0 and 10.3 MGy at 10.7 kGy/hr

8.3.2.4 Nuclear magnetic resonance spectroscopy

The ^{27}Al MAS NMR spectra (Fig. 8.30A) of the FA/MKPC binders exposed to the av. dose rate 16.6 kGy/hr indicated the presence of two Al environments: Al^{IV} (47 ppm) and Al^{VI} (-3 ppm). The latter is assigned to mullite [150, 151] and the broad band centred at 47 ppm is associated with the tetrahedral resonance of mullite (reported to be at 46 ppm [151]) and the aluminosilicate glassy fraction present in the FA. At irradiation doses: 2.4, 4.7 and 9.0 MGy, no differences in the aluminium environments were identified, suggesting that these binders are tolerant to substantial levels of gamma irradiation. However, in the ^{27}Al MAS NMR spectrum (Fig. 8.30A) at 7.0 MGy and unexpected changes was observed in the Al^{VI} region. The resonance intensity significantly increased and the chemical shift was centred at 2 ppm, i.e. it became more shielded than in the other FA/MKPC spectra. It is postulated that this could be the artefact of sample contamination as no other changes were observed in the XRD, FTIR or SEM samples (discussed below), as such this analysis should be repeated in order to elucidate the cause of the difference observed.

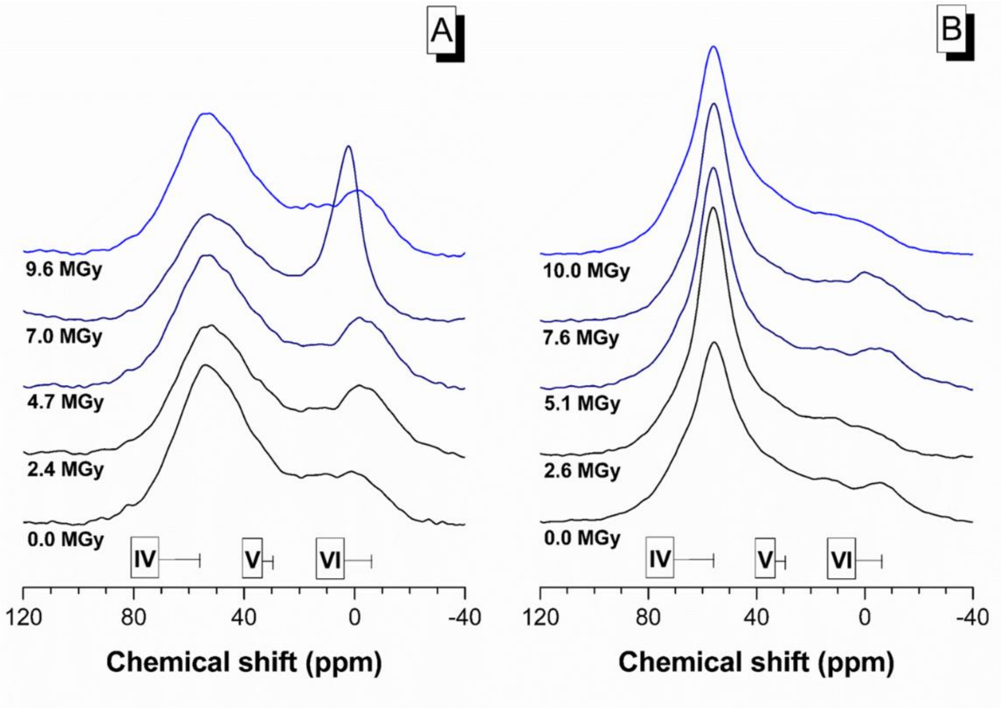

Fig. 8.30. Normalised ^{27}Al MAS NMR spectra of (A) FA/MKPC and (B) GBFS/MKPC specimens exposed to radiation at 16.6 and 17.7 kGy/hr, respectively

In the unreacted GBFS ^{27}Al MAS NMR spectrum (Fig. 8.30B), the broad Al^{IV} resonance centred at 56 ppm was assigned to the calcium aluminosilicate glassy fraction of the GBFS [141], whilst the minor band in the Al^{VI} region centred at 11 ppm is attributed to a minor octahedral Al environment in the GBFS glass. A third environment centred at -6 ppm in the Al^{VI} region (-10 to 15 ppm) region (discussed in Chapter 6) is thought to be associated with the formation of secondary reaction products, which are likely to be based on a potassium aluminate silicate phase and must be present at a substantial concentration to display such a clear NMR resonance. During gamma irradiation of the GBFS/MKPC binders at the av. dose rate of 17.7 kGy/hr, no differences were observed in the resonance intensity of the aluminium environments up to 7.6 MGy. However, in the 10.0 MGy ^{27}Al MAS NMR spectrum, the resonance associated with the glassy fraction broadened and the intensity of the resonance (secondary reaction product) appeared to decrease. This could suggest that a chemical change had begun to occur in the GBFS/MKPC as a result of radiation exposure.

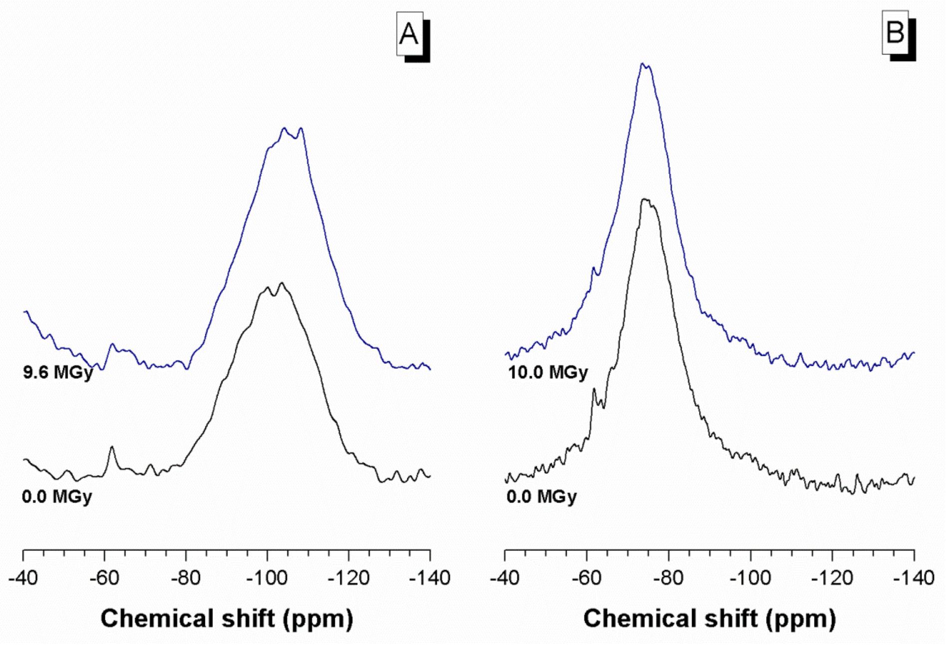

Fig. 8.31. Normalised ^{29}Si MAS NMR spectra of (A) FA/MKPC and (B) GBFS/MKPC specimens exposed to radiation at 16.6 and 17.7 kGy/hr, respectively

In Fig. 8.31A, the ^{29}Si MAS NMR spectrum of the unirradiated FA/MKPC binder (0.0 MGy) was typical of these systems (Chapter 6 and 7), where the broad asymmetric ^{29}Si MAS NMR resonance observed between -80 and -125 ppm (centred at -102 ppm) relates to the crystalline and poorly crystalline Si environments present in FA: a combination of quartz (107 ppm) [154], mullite (-86 ppm) [151], and the glassy fraction [155]. Comparable Si environments were observed in the ^{29}Si MAS NMR spectrum of the FA/MKPC binder irradiated at the av. dose rate 16.6 kGy/hr (Fig. 8.31A). In the ^{29}Si MAS NMR spectrum of the unirradiated GBFS/MKPC binder (Fig. 8.31B), a broad resonance centred at -75 ppm was observed, this is consistent with the glassy fraction and the minor åkermanite present in GBFS [141]. The resonance lineshape of the GBFS/MKPC binder exposed to 10.1 MGy at the av. dose rate 17.7kGy/hr was similar to that of the unirradiated control sample. The ^{29}Si MAS NMR spectra indicate that no chemical changes were identified in the Si environments as a result of exposure to gamma irradiation.

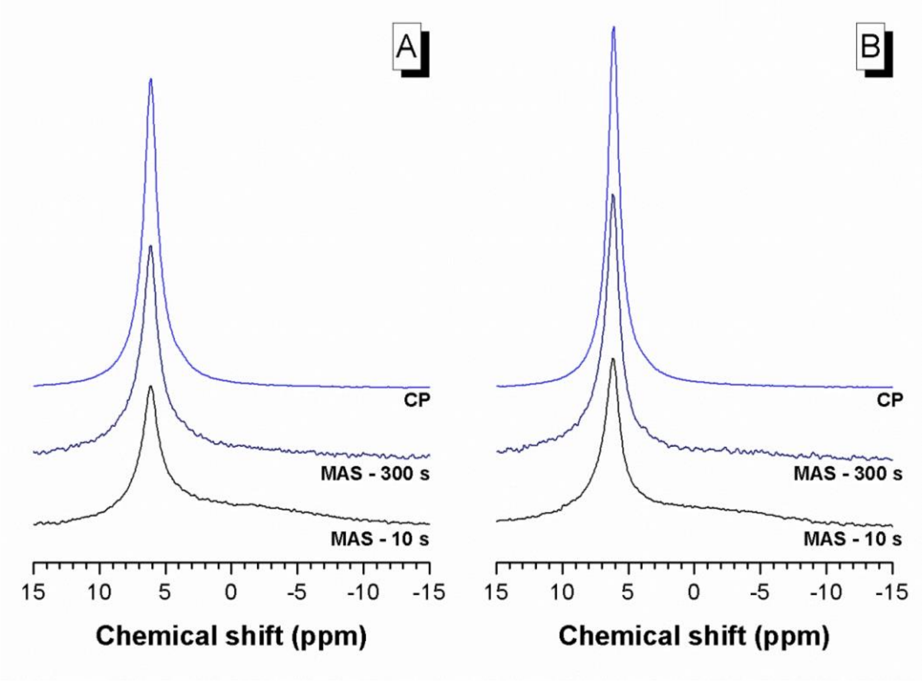

Fig. 8.32. ^{31}P MAS and ^{31}P[^{1}H] CP/MAS NMR spectra for (A) unirradiated FA/MKPC and (B) FA/MKPC specimen exposed to 9.6 MGy at 16.6 kGy/hr

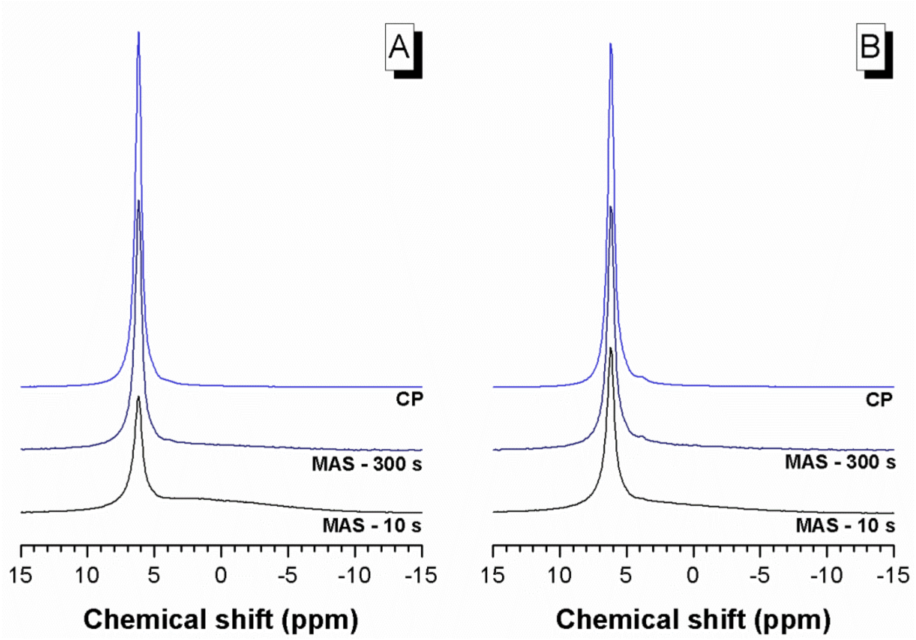

Fig. 8.33. ^{31}P MAS and $^{31}P[^{1}H]$ CP/MAS NMR spectra for (A) unirradiated GBFS/MKPC and (B) GBFS/MKPC specimen exposed to 9.6 MGy at 17.7 kGy/hr

The ^{31}P MAS NMR and $^{31}P[^{1}H]$ cross-polarisation (CP) MAS NMR of the FA/MKPC and GBFS/MKPC binders at 0.0 MGy (i.e. the control) and irradiated to ≈ 10.0 MGy at the av. dose rates 16.6 and 17.7 kGy/hr, respectively are shown in Figs. 8.32-8.33. A single sharp resonance at 6.2 ppm in the orthophosphate region was identified in both blended binders, which was associated with the main cementitious phase, struvite-K and concurred with data reported for struvite at 6.1 ppm [124]. The $^{31}P[^{1}H]$ CP MAS NMR enhanced the signal to noise ratio of the ^{31}P spectra, where it was found that all of the P-H interactions were related to the presence of struvite-K, in agreement with Chapter 4 and 6. Different relaxation times (10 s and 300 s) were utilised to investigate the present of any poorly crystalline phosphate phases, however, no evidence of these phases were identified in the control sample for either blended binder or the irradiated samples. The ^{31}P MAS NMR data conclusively show that there is no change in the phosphate environments resulting from exposure to gamma irradiation, which is a positive result for the application of blended MKPC binders in the encapsulation of ILW and storage/disposal in a geological repository setting.

8.3.2.5 Scanning electron microscopy

8.3.2.5.1 Elemental mapping - FA/MKPC

Backscattered electron micrographs and elemental maps of FA/MKPC binders subjected to gamma irradiation at the av. dose rates 16.6 and 10.1 kGy/hr are shown in Figs 8.34-8.44, with the Fig. 8.34 being the unirradiated control. The microstructure of the control sample is typical of FA/MKPC binders described in Chapter 6 and 7, where there is a continuous struvite-K matrix intermixed with large struvite-K crystalline and spherical particles of varying sizes and composition (Al/Si-rich and Fe-rich) associated with the unreacted FA. The grey angular particles relate to unreacted periclase, whilst the black spots are from the carbon coating process. The BSE/EDX maps highlight the association of Mg, K and P with the struvite-K matrix, whilst the spherical particles are associated with the aluminosilicate component of FA. The Fe-rich areas (Fig. 8.34.Fe) are ascribed to the Fe-rich phases present in FA particles (e.g. hematite) [140]. No microstructural differences were observed in the FA/MKPC binder (Figs. 8.35-8.44) as a result of exposure to gamma irradiation at the av. dose rates 16.6 and 10.1 kGy/hr, up to a total of ≈ 10.0 MGy.

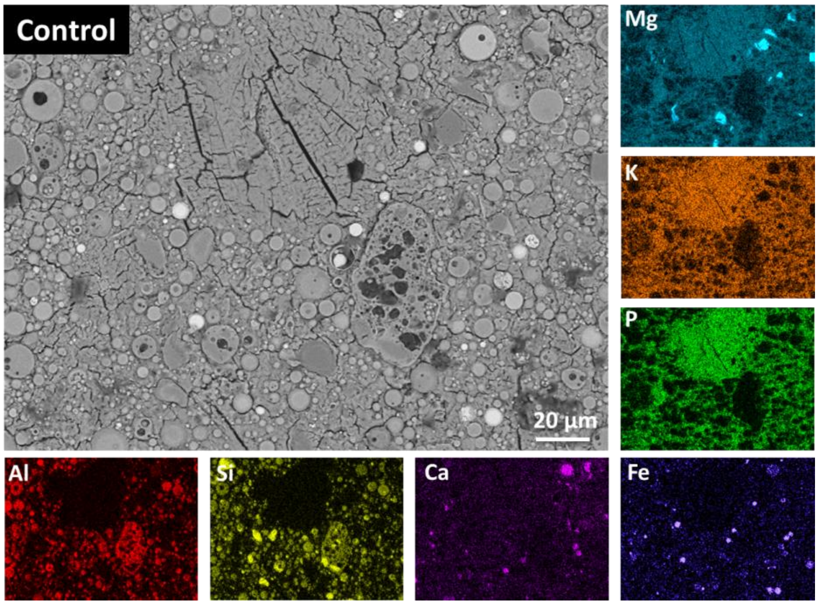

Fig. 8.34. Backscattered electron micrograph and elemental maps of an unirradiated FA/MKPC specimen

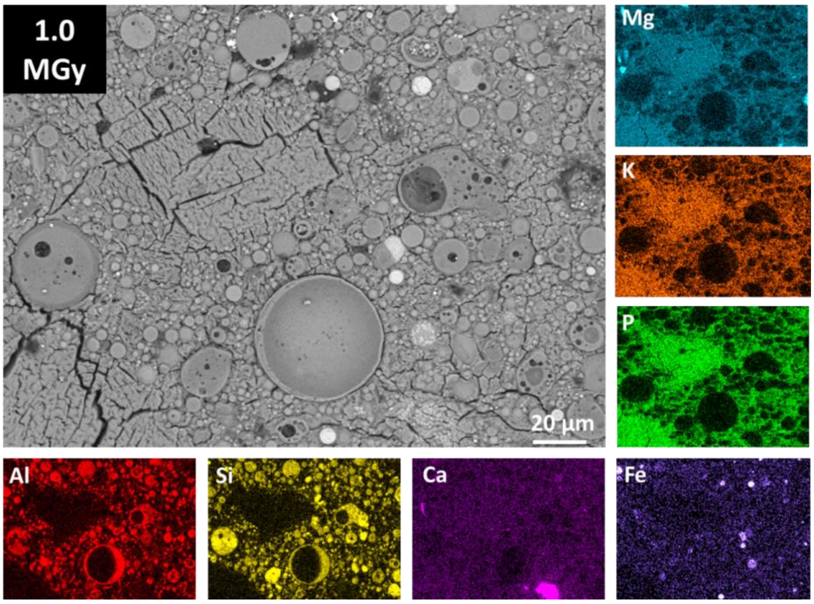

Fig. 8.35. Backscattered electron micrograph and elemental maps of a FA/MKPC specimen exposed to 1.0 MGy at 16.6 kGy/hr

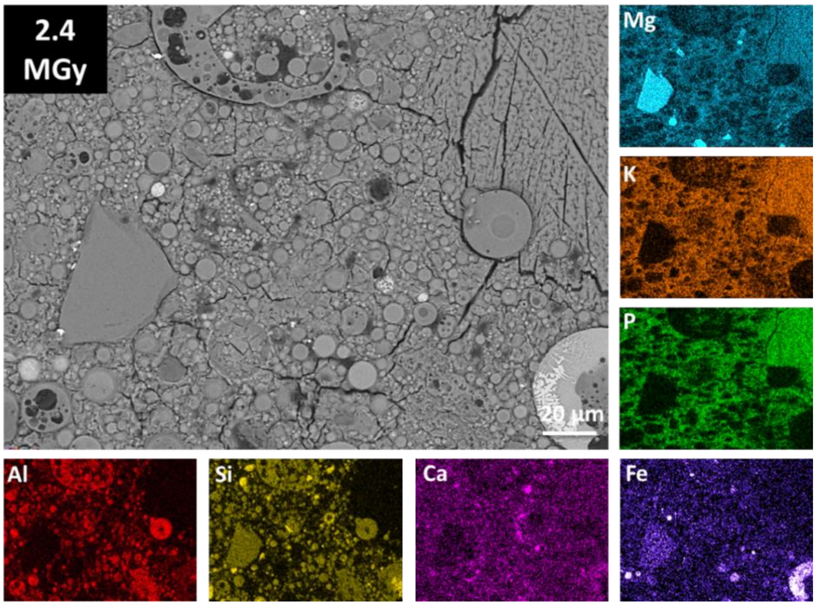

Fig. 8.36. Backscattered electron micrograph and elemental maps of a FA/MKPC specimen exposed to 2.4 MGy at 16.6 kGy/hr

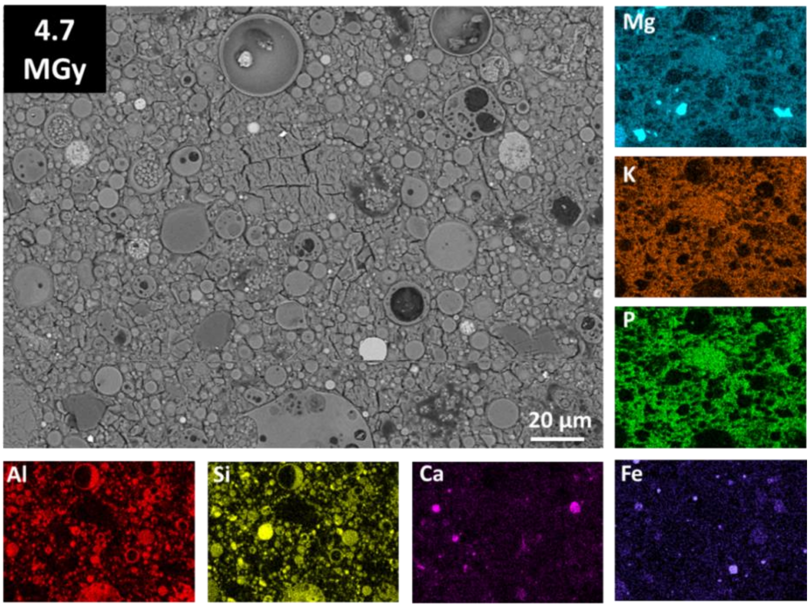

Fig. 8.37. Backscattered electron micrograph and elemental maps of a FA/MKPC specimen exposed to 4.7 MGy at 16.6 kGy/hr

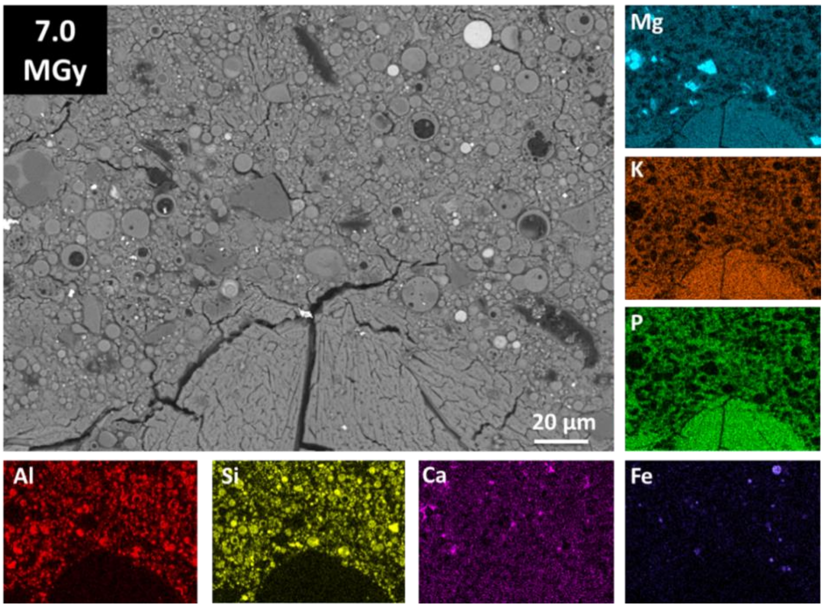

Fig. 8.38. Backscattered electron micrograph and elemental maps of a FA/MKPC specimen exposed to 7.0 MGy at 16.6 kGy/hr

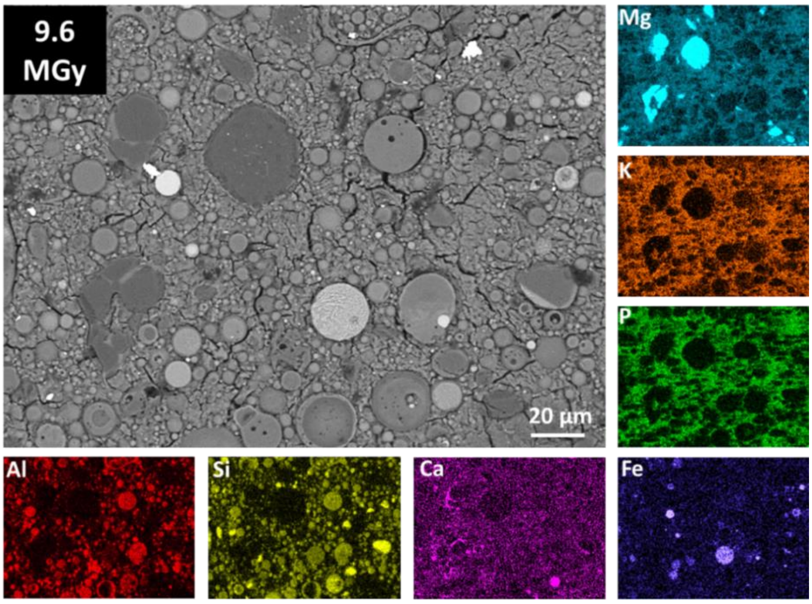

Fig. 8.39. Backscattered electron micrograph and elemental maps of a FA/MKPC specimen exposed to 9.6 MGy at 16.6 kGy/hr

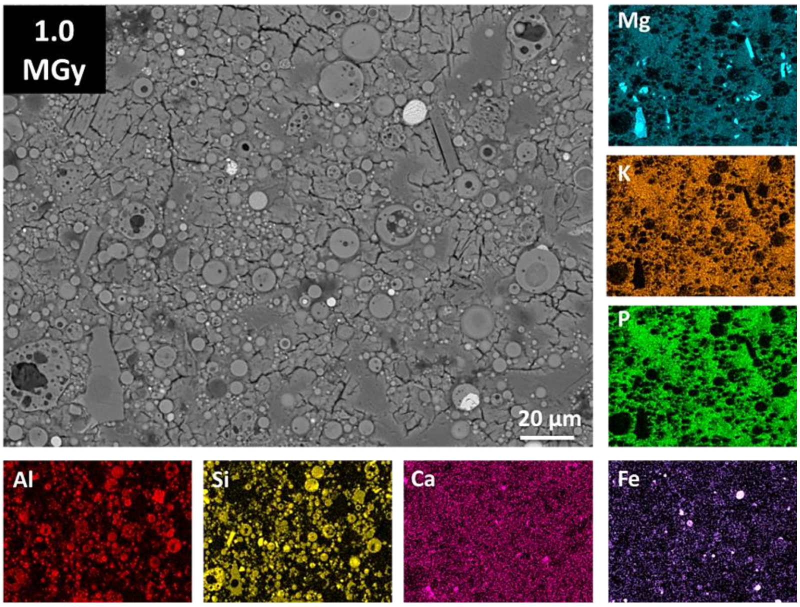

Fig. 8.40. Backscattered electron micrograph and elemental maps of a FA/MKPC specimen exposed to 1.0 MGy at 10.1 kGy/hr

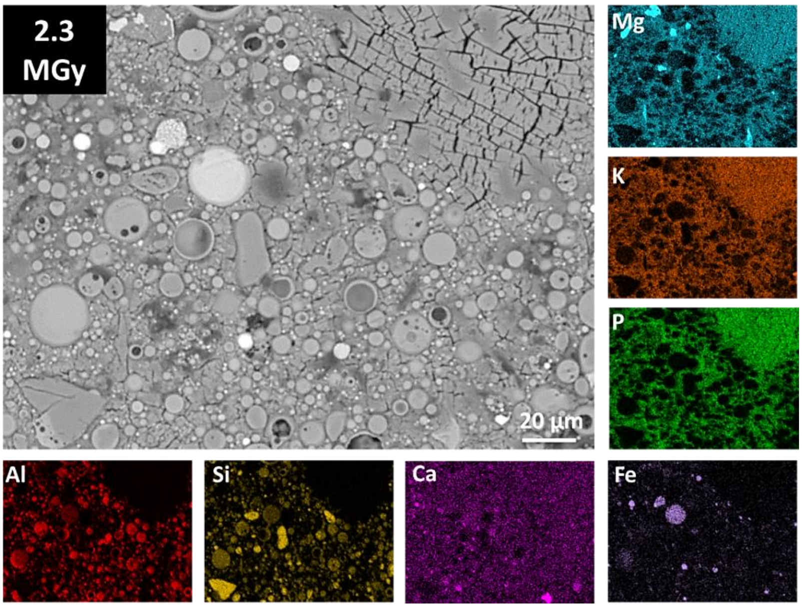

Fig. 8.41. Backscattered electron micrograph and elemental maps of a FA/MKPC specimen exposed to 2.3 MGy at 10.1 kGy/hr

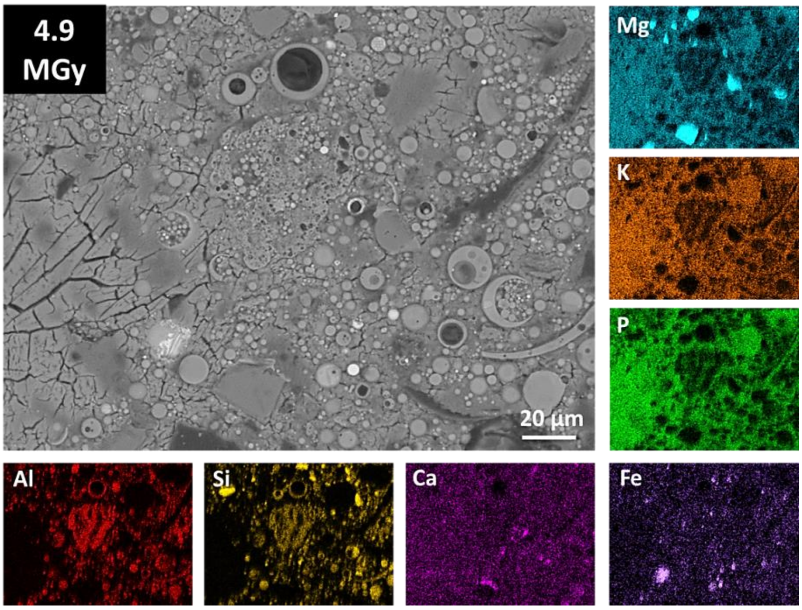

Fig. 8.42. Backscattered electron micrograph and elemental maps of a FA/MKPC specimen exposed to 4.9 MGy at 10.1 kGy/hr

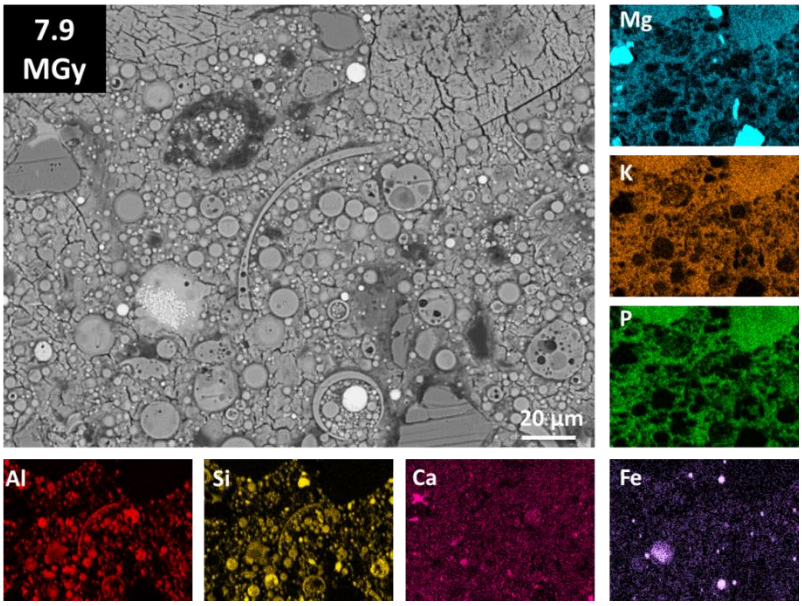

Fig. 8.43. Backscattered electron micrograph and elemental maps of a FA/MKPC specimen exposed to 7.9 MGy at 10.1 kGy/hr

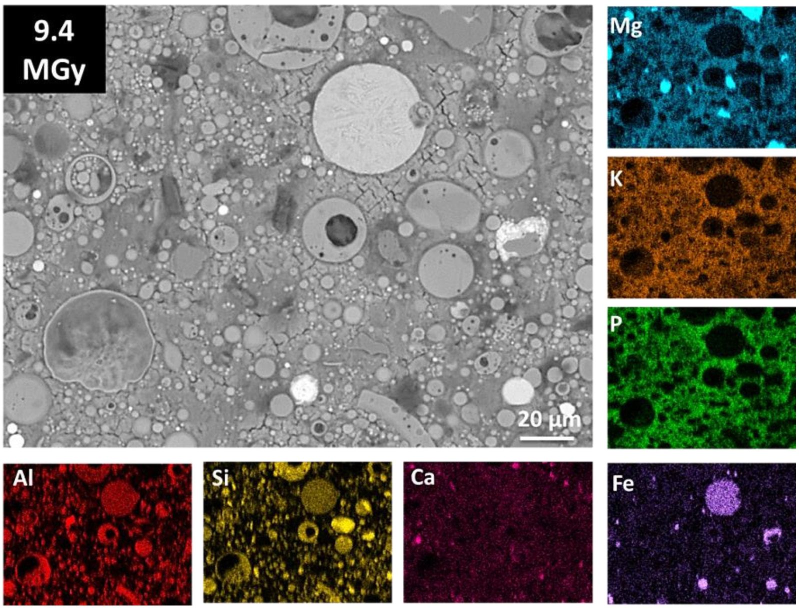

Fig. 8.44. Backscattered electron micrograph and elemental maps of a FA/MKPC specimen exposed to 9.4 MGy at 10.1 kGy/hr

8.3.2.5.2 Elemental mapping - GBFS/MKPC

Backscattered electron micrographs and elemental maps of GBFS/MKPC binders subjected to gamma irradiation at the av. dose rates 17.7 and 10.7 kGy/hr are shown in Figs. 8.45-8.55, with the Fig. 8.45 being the unirradiated control. The microstructure of the control sample is typical of GBFS/MKPC binders (shown in Chapter 6 and 7). The cementitious matrix consists of struvite-K usually with large crystallites intermixed with the matrix. The light grey angular particles are associated with the GBFS particles and are composed of a calcium aluminosilicate glassy fraction. The GBFS is a blend of fine and coarse ground materials (as observed in Fig. 8.45), which is designed for the UK nuclear industry. The grey angular particles relate to unreacted periclase, whilst the black spots are from the carbon coating process. The EDX maps in Fig. 8.45 clearly indicate the distinct relationship between Mg, K and P (struvite-K) with the Ca, Al and Si solely associated with the unreacted GBFS particles. In similar behaviour to the FA/MKPC binders, no microstructural differences were observed in GBFS/MKPC binders (Figs. 8.46-8.55) due to the effect of gamma irradiation. These results indicate that both blended MKPC binders are tolerant to the estimated 300 year gamma radiation exposure of 10.0 MGy [188], independent of the dose rate.

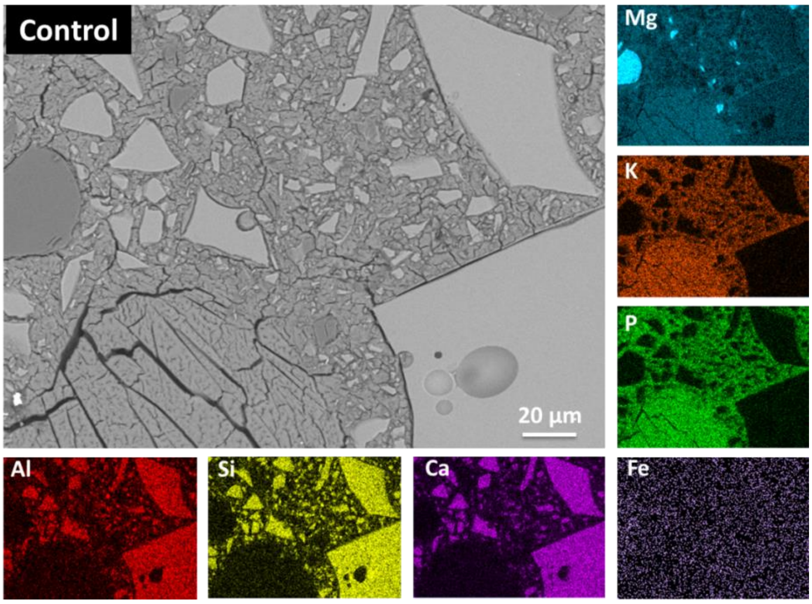

Fig. 8.45. Backscattered electron micrograph and elemental maps of an unirradiated GBFS/MKPC specimen

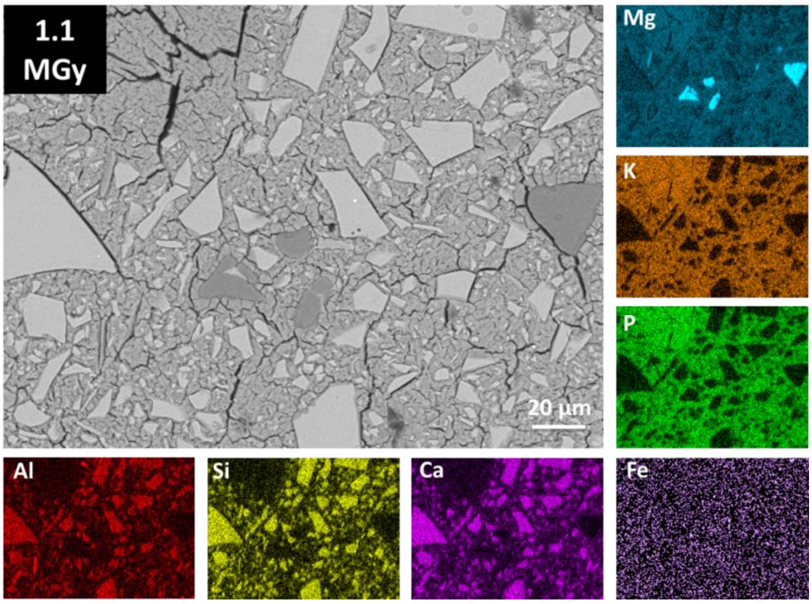

Fig. 8.46. Backscattered electron micrograph and elemental maps of a GBFS/MKPC specimen exposed to 1.1 MGy at 17.7 kGy/hr

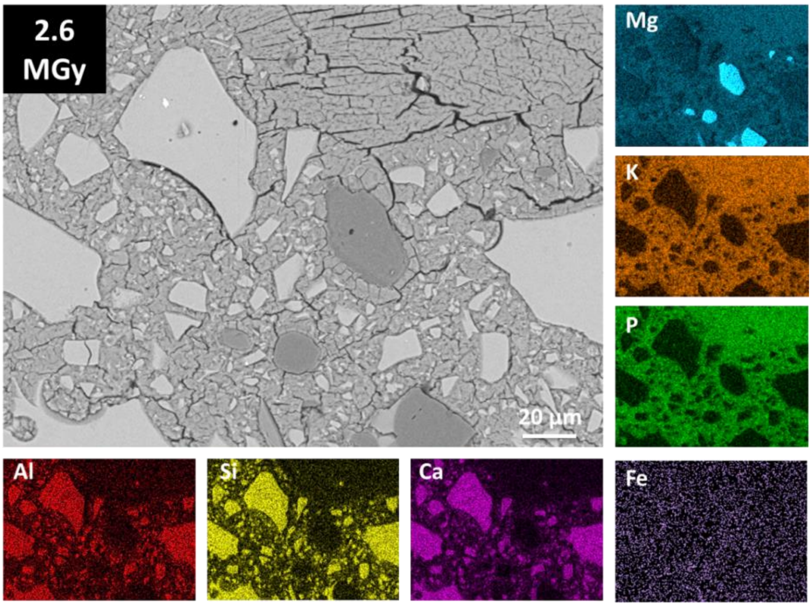

Fig. 8.47. Backscattered electron micrograph and elemental maps of a GBFS/MKPC specimen exposed to 2.6 MGy at 17.7 kGy/hr

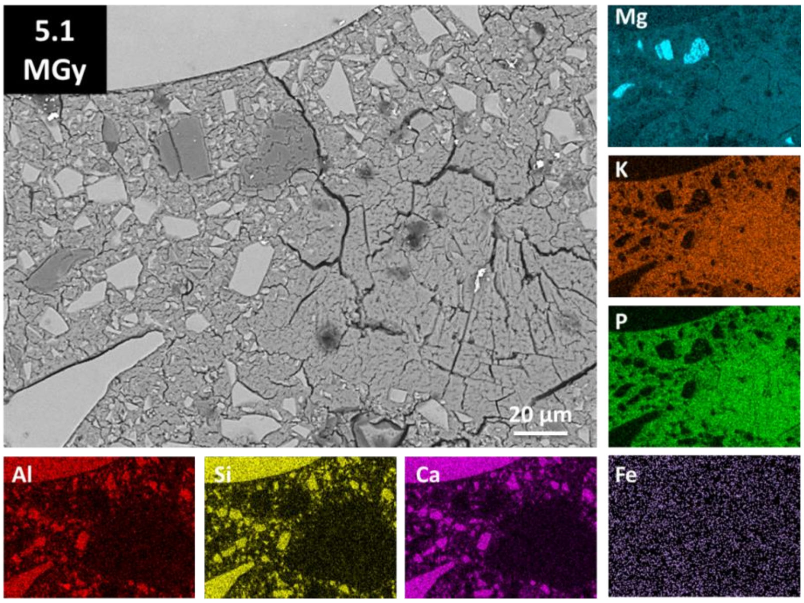

Fig. 8.48. Backscattered electron micrograph and elemental maps of a GBFS/MKPC specimen exposed to 5.1 MGy at 17.7 kGy/hr

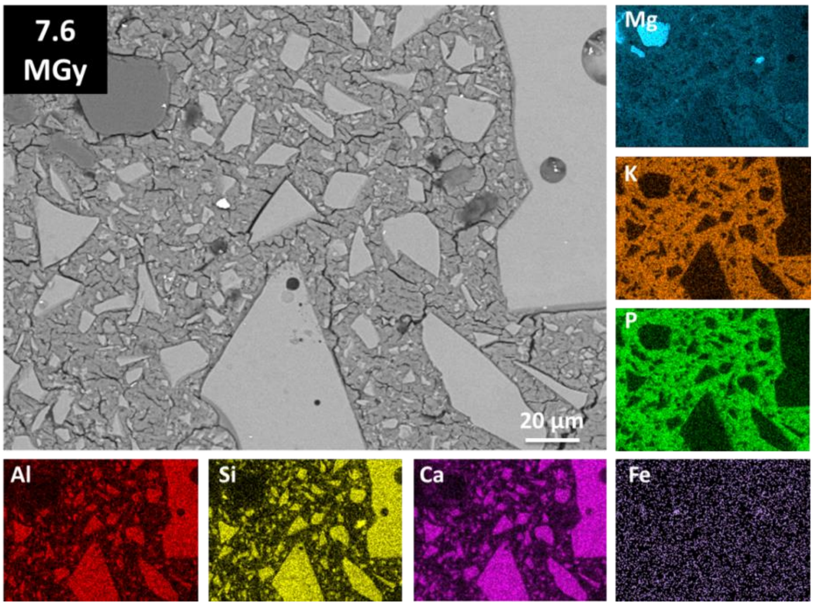

Fig. 8.49. Backscattered electron micrograph and elemental maps of a GBFS/MKPC specimen exposed to 7.6 MGy at 17.7 kGy/hr

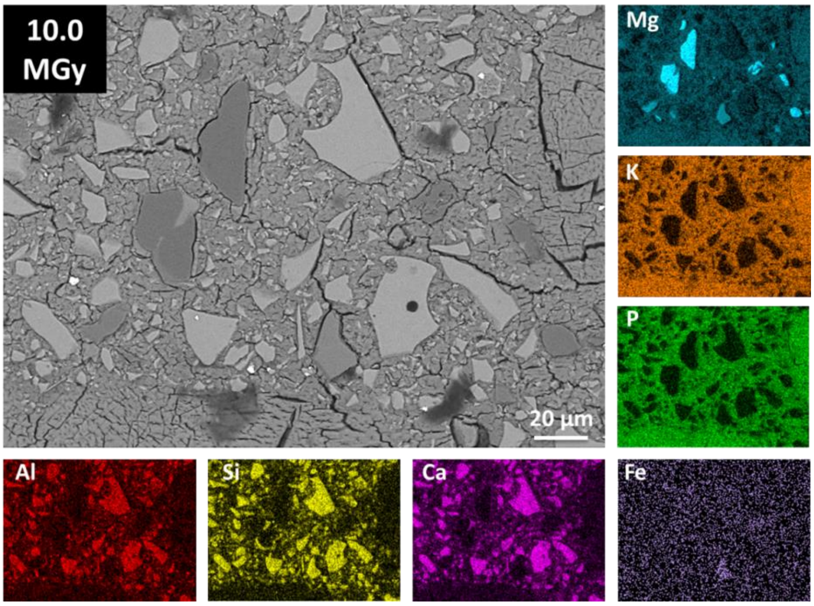

Fig. 8.50. Backscattered electron micrograph and elemental maps of a GBFS/MKPC specimen exposed to 10.0 MGy at 17.7 kGy/hr

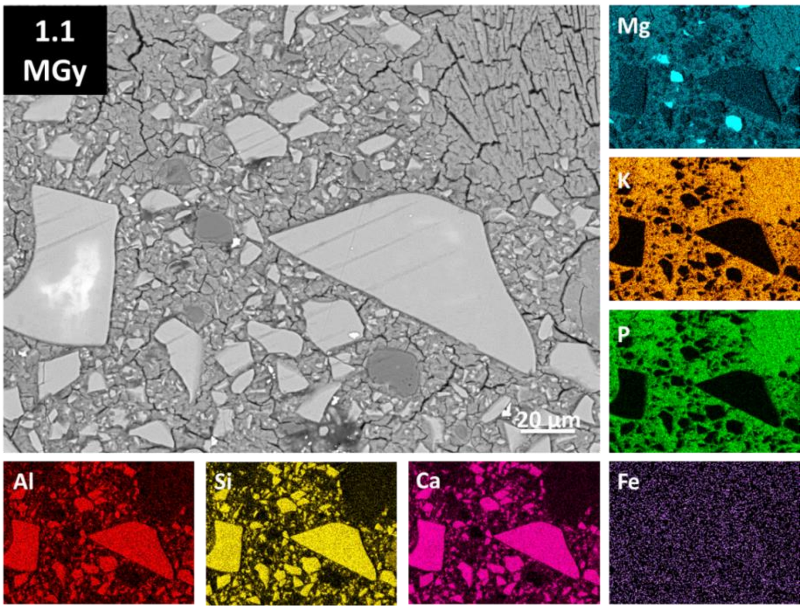

Fig. 8.51. Backscattered electron micrograph and elemental maps of a GBFS/MKPC specimen exposed to 1.1 MGy at 10.7 kGy/hr

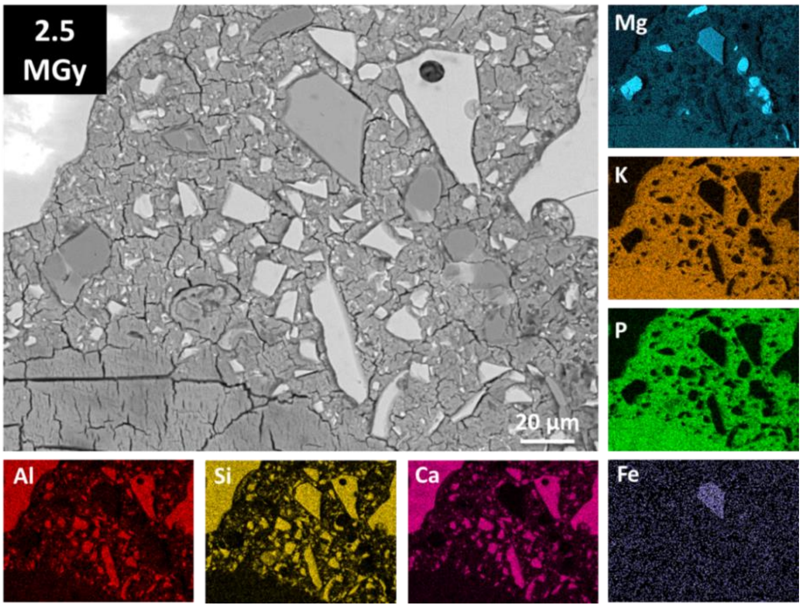

Fig. 8.52. Backscattered electron micrograph and elemental maps of a GBFS/MKPC specimen exposed to 2.5 MGy at 10.7 kGy/hr

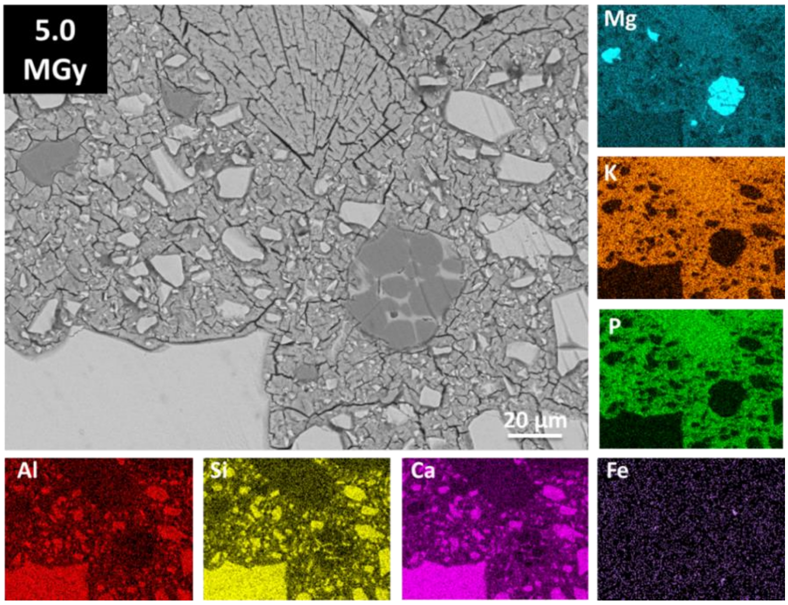

Fig. 8.53. Backscattered electron micrograph and elemental maps of a GBFS/MKPC specimen exposed to 5.0 MGy at 10.7 kGy/hr

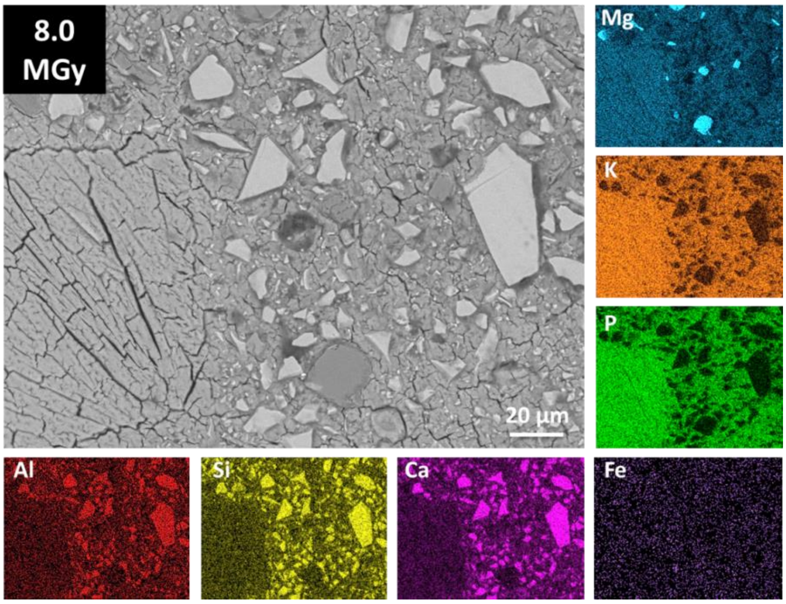

Fig. 8.54. Backscattered electron micrograph and elemental maps of a GBFS/MKPC specimen exposed to 8.0 MGy at 10.7 kGy/hr

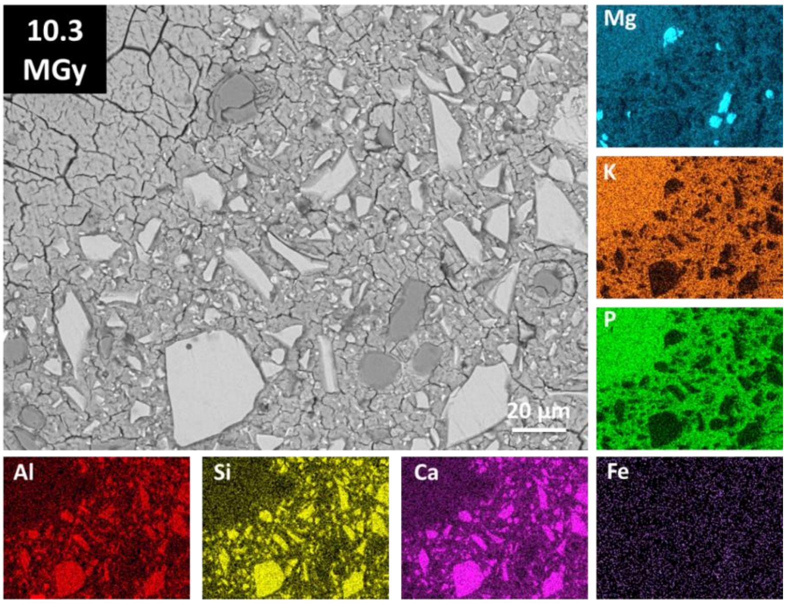

Fig. 8.55. Backscattered electron micrograph and elemental maps of a GBFS/MKPC specimen exposed to 10.3 MGy at 10.7 kGy/hr

8.4 Conclusions and Future work

Through the irradiation of FA/MKPC and GBFS/MKPC binders using Co-60, it was determined that no measurable effects of gamma irradiation could be detected using the experimental techniques used in this study. The typical radiation effects of PC encapsulants, for example, amorphisation of crystalline cement hydrated phases, and/or densification and decomposition of hydrated phases [194, 195] could not be distinguished within this study. An important distinction between PC grouts and blended MKPC binders are that the former undergo radiogenic dehydration of the hydrated phases [169]. This radiation effect was not exhibited in the blended MKPC binders within this study. Through the employment of four Co-60 dose rates (averaged) of 16.6, 10.7, 4.9 and 2.8 MGy/hr at total accumulated doses of: ≈ 0.5, 1.0, 2.5, 5.0, 7.5 and 10.0 MGy it has demonstrated that the chemical structure (through XRD, FTIR and NMR analysis) and microstructure (through SEM/EDX analysis) of blended MKPC binders show considerate radiation resistance up to ≈ 10.0 MGy. It should be noted that in the GBFS/MKPC spectrum at 10.0 MGy minor differences were observed in the ^{27}Al MAS NMR. However, these changes could not be substantiated with any other analyses. It is postulated that the differences could be the result post-data collection baseline corrections due to normalisation of the data. It is suggested that further work employing ^{27}Al MQMAS NMR experiments would help elucidate if any chemical changes as a result of gamma irradiation. In summary, the data presented in this study supports the employment of these alternative encapsulants for the use of nuclear waste immobilisation as no detrimental effects were observed up to the 300 year expected absorbed gamma dose of 10 MGy [188].

<u>Further work should be undertaken in the following areas:</u>

- Determine the physical properties of blended MKPC binders under gamma irradiation conditions.

- Determine the effect of alpha radiation using ion implantation and transmission electron microscopy (TEM) to monitor simulated alpha decay within the conditioned wasteforms. Alpha decay could arise from waste inventory for Magnox cladding, for example: Pu-238 and Pu-239 radionuclides [7, 8].
- Repeat the solid state MAS NMR experiments to elucidate the difference observed at 7.5 MGy in the FA/MKPC binder, including ^{27}Al MQMAS NMR experiments.

9 Conclusion

The objective of this thesis was to provide up-to-date research assessing the suitability of using magnesium potassium phosphate cements within the UK waste encapsulation clean-up process, focussing on the conceptual safety functions associated with the encapsulation of intermediate level waste streams [10]. It was identified that the currently preferred cement grout (GBFS/PC, 0.35 w/s) is not perfectly suited for the wide-ranging compositions present within the ILW inventory. One example is reactive metals, which can corrode in the high pH and/or high free water environment of GBFS/PC composite grouts leading to the generation of flammable hydrogen gas and expansive corrosion products. It is these scenarios where alterative cement grouts can be utilised. For the utilisation of MKPC binders in ILW encapsulation, they need to demonstrate several properties: chemical stability with the wastes (i.e. minimal corrosion), have a suitable accident performance (impact and thermal) and be radiation tolerant, there is very little information available regarding the fire performance and radiation stability of these binders. As such these properties were investigated alongside reducing the water content (to minimise the rate of corrosion within reactive metal wastes) and an in-depth understanding of the binder chemistry.

In Chapter 4, the optimum formulation of blended MKPC binders was determined through variation of the water to solids (w/s) ratio. The resulting formulation had an 8 % (by weight) reduction content compared to previous research [18], which should reduce the availability of water to partake in corrosion reaction of encapsulated reactive metals. Small scale two-year corrosion experiments using natural uranium revealed that the gas volume generated was consistently lower (by half) than the GBFS/PC (0.35 w/s) composite grout, which was a positive result for blended MKPC binders. In addition to varying the water content, it was found that the choice of SCM (FA or GBFS) has an effect on the early hydration behaviour of the MKPC binder (and thus, the exothermic output of the acid-base reaction) corresponding to a varied compressive strength values. This flexibility could be advantageous for waste encapsulation of legacy wastes, which have wide-ranging composition.

In Chapter 5, struvite-K was synthesised and the chemical environments investigated using high field solid-state ^{25}Mg and ^{39}K MAS NMR for the first time. The experimental NMR spectra were presented alongside their calculated quadrupolar parameters and simulated NMR spectra, in combination with X-ray diffraction and thermal analysis data.

In Chapter 6, the chemistry of struvite-K and blended MKPCs were assessed using a range of analytical techniques (compressive strength, XRD, SEM, NMR) to provide the first definitive evidence that dissolution of the glassy aluminosilicate phases of both FA and GBFS occurred under the pH conditions of MKPC. The principal role of FA and GBFS in blended MKPC binders is as a filler and diluent however, high-field solid-state NMR analysis indicated that in the GBFS/MKPC binder, the secondary reaction formed as a result of GBFS dissolution was likely to be a potassium-aluminosilicate phase.

In Chapter 7, the fire performance of blended MKPC binders was assessed up to 1200 °C, after high temperature exposure, it was found that the main binding phase in these cements, struvite-K, underwent dehydration to a poorly-crystalline α-$MgKPO_4$ phase, upon further heating the long-range order was re-established commensurate with polymorph transitions to the β and γ-$MgKPO_4$ phases. Between 1000 - 1200 °C, the formation of potassium aluminosilicate phases: leucite and kalsilite (feldspathoid minerals), were observed along with other magnesium silicates and calcium phosphate phases. This was the direct result of high temperature reactions between α-$MgKPO_4$ and the FA or GBFS, which supply the necessary Ca, Al and Si. The results indicate that the blended MKPC binders performed satisfactorily under the fire performance criteria, the struvite-K matrix was transformed into a combination of well-known stable mineral phases but without the loss of the structural integrity.

In Chapter 8, initial scoping irradiation experiments using Cs-137 revealed that the blended MKPC binders were stable up to 3.6 kGy gamma irradiation. After which, a compete irradiation programme was undertaken at the Dalton Cumbrian Facility (University of Manchester), where a matrix of samples was irradiated in order to elucidate the presence of any dose rate or total dose dependencies. It was found that the blended MKPC binders were radiation tolerant up to a total dose of 10 MGy, which is considered to be the 300 year dose of ILW conditioned waste packages in a GDF [188]. There were no apparent changes in the crystal structure or the microstructural properties of these binders, as such no dose rate dependencies exist, this suggest that blended MKPC binders are suitable encapsulants for the UK nuclear industry.

Areas of interest for the future research of MKPCs would be to improve the safety case for industrial deployment in nuclear waste encapsulation by: investigating the durability (leaching, radionuclide sorption) of these binders, the impact accident performance, large scale corrosion and fire accident performance trials. Investigation into the use of different filler materials (for example: sand, which is widely available) should be conducted as the FA/GBFS supply security cannot be guaranteed in the UK industry due to coal power plant closures and variable iron ores [12].

10 References

[1] M.I. Ojovan, W.E. Lee, *An introduction to nuclear waste immobilisation*, Elsevier, Oxford, UK, **2005**.

[2] Department of Energy and Climate Change, *Implementing geological disposal, a framework for the long-term management of higher activity radioactive waste*, **2014**.

[3] Pöyry Energy Limited, Amec plc, *2013 UK radioactive waste inventory: waste quantities from all sources, NDA/ST/STY(14)0010*, Prepared for Department of Energy and Climate Change and the Nuclear Decomissioning Authority, **2013**.

[4] B. Batchelor, Overview of waste stabilization with cement, *Waste Management*, **2006**, vol. 26, pp. 689-698.

[5] C.R. Wilding, The performance of cement based systems, *Cement and Concrete Research*, **1992**, vol. 22, pp. 299-310.

[6] Nuclear decommissioning Authority, *The Magnox operating programme (MOP 9)*, NDA, **2012**.

[7] Nuclear Decommissioning Authority, *Waste stream 2D22: Magnox cladding and miscellaneous solid waste*, NDA, **2014**.

[8] Nuclear Decommissioning Authority, *Waste stream 2D24: Magnox cladding and miscellaneous solid waste*, NDA, **2014**.

[9] Sellafield Ltd. *Magnox reprocessing*. www.sellafieldsites.com/solution/spent-fuel-management/magnox-reprocessing/ (accessed 18/03/2013), **n.d.**).

[10] NDA, *Geological Disposal Package evolution status report 2010, NDA Report no. NDA/RWMD/031*, **2010**.

[11] G.A. Fairhall, J.D. Palmer, The encapsulation of Magnox Swarf in cement in the United Kingdom, *Cement and Concrete Research*, **1992**, vol. 22, pp. 293-298.

[12] M.J. Angus, I.H. Godfrey, M. Hayes, S. Foster, Managing change in the supply of cement powders for radioactive waste encapsulation, *Waste Management*; AZ, USA, **2010**.

[13] A. Setiadi, N.B. Milestone, J. Hill, M. Hayes, Corrosion of aluminium and magnesium in BFS composite cements, *Advances in Applied Ceramics*, **2006**, vol. 105, pp. 191-196.

[14] A. Covill, *Novel encapsulants for intermediate level waste in the UK nuclear industry*, Unpublished thesis, Department of Materials Science and Engineering, University of Sheffield, **2010**.

[15] J.H. Sharp, N.B. Milestone, J. Hill, E.W. Miller, Cementitious systems for encapsulation of intermediate level waste, *The 9th International Conference on Radioactive Waste Management and Environmental Remediation*; Oxford, UK, Sept 21-25; **2003**, On-line/CD ROM proceedings.

[16] Pöyry Energy Limited, *The 2010 UK Radioactive Waste Inventory: Main Report NDA/ST/STY (11)0004*, Prepared for Department of Energy and Climate Change and the Nuclear Decomissioning Authority, **2011**.

[17] N.B. Milestone, Reactions in cement encapsulated nuclear wastes: need for toolbox of different cement types, *Advances in Applied Ceramics*, **2006**, vol. 105, pp. 13-20.

[18] A. Covill, N.C. Hyatt, J. Hill, N.C. Collier, Development of magnesium phosphate cements for encapsulation of radioactive waste, *Advances in Applied Ceramics*, **2011**, vol. 110, pp. 151-156.

[19] M. Hayes, I.H. Godfrey, Development of the use of alternative cements for the treatment of intermediate level waste, *Waste Management Conference*; AZ, USA, Feb 25 - Mar 1; **2007**, On-line/CD ROM proceedings.

[20] Nuclear Decommissioning Authority, *Geological disposal: Gas status report NDA/RWMD/037*, **2010**.

[21] F. Qiao, C.K. Chau, Z. Li, Property evaluation of magnesium phosphate cement mortar as patch repair material, *Construction and Building Materials*, **2010**, vol. 24, pp. 695-700.

[22] M. Mathew, L.W. Schroeder, Crystal structure of a struvite analogue, $MgKPO_4 \cdot 6H_2O$, *Acta Crystallographica: Section B Structural Crystallography and Crystal Chemistry*, **1979**, vol. 35, pp. 11-13.

[23] H.F.W. Taylor, *Cement Chemistry*, Second ed., Thomas Telford, London, UK, **1997**.

[24] E.M. Gartner, J.F. Young, D.A. Damidot, I. Jawad, *Hydration of Portland cement*, in: J. Bensted, P. Barnes (Eds.), Structure and Performance of Cements, Spon Press, London, UK, **2002,** pp. 57-114.

[25] F.P. Glasser, Progress in the immobilization of radioactive wastes in cement, *Cement and Concrete Research*, **1992**, vol. 22, pp. 201-216.

[26] E. Lang, *Blastfurnace cements* in: J. Bensted, P. Barnes (Eds.), Structure and Performance of Cements, Spon Press, London, UK, **2002,** pp. 310-325.

[27] K. Luke, *Pulverized fuel ash as a cement extender*, in: J. Bensted, P. Barnes (Eds.), Structure and Performance of Cements, Spon Press, London, UK, **2002,** pp. 353-369.

[28] Nuclear Decommissioning Authority, *Waste package specification and guidance documentation; WPS/300/02, specification for 500 litre drum waste package*, **2008**.

[29] P. Swift, H. Kinoshita, N.C. Collier, C.A. Utton, Phosphate modified calcium aluminate cement for radioactive waste encapsulation, *Advances in Applied Ceramics*, **2013**, vol. 112, pp. 1-8.

[30] Y. Bai, N.C. Collier, N.B. Milestone, C.H. Yang, Review: The potential of using slags activated with near neutral salts as immobilisation matrices for nuclear wastes containing reactive metals, *Journal of Nuclear Materials*, **2011**, vol. 413, pp. 183-192.

[31] W.D. Kingery, Fundamental study of phosphate bonding in refractories: I, literature review, *Journal of the American Ceramic Society*, **1950**, vol. 33, pp. 239-241.

[32] W.D. Kingery, Fundamental study of phosphate bonding in refractories: II, cold-setting properties, *Journal of the American Ceramic Society*, **1950**, vol. 33, pp. 242-246.

[33] D.M. Roy, New strong cement materials: chemically bonded ceramics, *Science Magazine*, **1987**, vol. 235, pp. 629-697.

[34] A.S. Wagh, *Ceramicrete: An alternative radioactive waste form*, in: R.D. Spence, C. Shi (Eds.), Stabilization and Solidification of Hazardous, Radioactive and Mixed Wastes, CRC Press, Boca Raton, FL, USA, **2004,** pp. 112-121.

[35] E. Banks, R. Chianelli, R. Korenstein, Crystal chemistry of struvite analogs of the type $MgMPO_4{\cdot}6H_2O$ ($M^+ = K^+, Rb^+, Cs^+, Tl^+, NH_4^+$), *Inorganic Chemistry*, **1975**, vol. 14, pp. 1634-1639.

[36] A.S. Wagh, *Chemically Bonded Phosphate Ceramics – 21st Century Material with Diverse Applications*, 1st ed., Elsevier Ltd, Oxford, UK, **2004**.

[37] E. Soudée, J. Péra, Mechanism of setting reaction in magnesia-phosphate cements, *Cement and Concrete Research*, **2000**, vol. 30, pp. 315-321.

[38] A.S. Wagh, S.Y. Jeong, Chemically bonded phosphate ceramics: I, a dissolution model of formation, *Journal of the American Ceramic Society*, **2003**, vol. 86, pp. 1838-1844.

[39] R. Neiman, A.C. Sarma, Setting and thermal reactions of phosphate investments, *Journal of Dental Research*, **1980**, vol. 59, pp. 1478-1485.

[40] A.K. Sarkar, Investigation of reaction/bonding mechanisms in regular and retarded magnesium ammonium phosphate cement systems, *Ceramic Transactions*, **1993**, vol. 40, pp. 281-288.

[41] E. Soudée, J. Péra, Influence of magnesia surface on the setting time of magnesia–phosphate cement, *Cement and Concrete Research*, **2002**, vol. 32, pp. 153-157.

[42] W.R. Eubank, Calcination studies of magnesium oxides, *Journal of the American Ceramic Society*, **1951**, vol. 34, pp. 225-229.

[43] D.A. Hall, R. Stevens, B. El-Jazairi, The effect of retarders on the microstructure and mechanical properties of magnesia–phosphate cement mortar, *Cement and Concrete Research*, **2001**, vol. 31, pp. 455-465.

[44] T. Sugama, L.E. Kukacka, Characteristics of magnesium polyphosphate cements derived from ammonium polyphosphate solutions, *Cement and Concrete Research*, **1983**, vol. 13, pp. 499-506.

[45] A.S. Wagh, D. Singh, S.-Y. Jeong, *Stabilization of hazardous asg waste with newberyite-rich chemically binded magnesium phosphate ceramic*, in: A.N.L. Energy Technology Division (Ed.) Argonne, IL, USA, **1995**.

[46] P.K.S. Gupta, G.H. Swihart, R. Dimitrijevic, The crystal structure of lünebergite, $Mg_3(H_2O)_6[B_2(OH)_6(PO_4)_2]$, *American Mineralogist*, **1991**, vol. 76, pp. 1400-1407.

[47] J. Formosa, J.M. Chimenos, A.M. Lacasta, M. Niubó, Interaction between low-grade magnesium oxide and boric acid in chemically bonded phosphate ceramics formulation, *Ceramics International*, **2011**, vol. 38, pp. 2483-2493.

[48] D.V. Ribeiro, M.R. Morelli, Influence of the addition of grinding dust to a magnesium phosphate cement matrix, *Construction and Building Materials*, **2009**, vol. 23, pp. 3094-3102.

[49] J.H. Cho, Y. Eom, T.G. Lee, Stabilization/solidification of mercury-contaminated waste ash using calcium sodium phosphate (CNP) and magnesium potassium phosphate (MKP) processes, *Journal of Hazardous Materials*, **2014**, vol. 278, pp. 474-482.

[50] D. Singh, M. Tlustochowicz, A.S. Wagh, Development of Zirconium/Magnesium Phosphate Composites for Immobilization of Fission Products, *Journal of the American Ceramic Society*, **1999**, vol. 82, pp. 43-49.

[51] K. Sasaki, S. Moriyama, Effect of calcination temperature for magnesite on interaction of MgO-rich phases with boric acid, *Ceramics International*, **2014**, vol. 40, pp. 1651-1660.

[52] B.E.I. Abdelrazig, J.H. Sharp, B. El-Jazairi, The chemical composition of mortars made from magnesia-phosphate cement, *Cement and Concrete Research*, **1988**, vol. 18, pp. 415-425.

[53] S.S. Seehra, S. Gupta, S. Kumar, Rapid setting magnesium phosphate cement for quick repair of concrete pavements — characterisation and durability aspects, *Cement and Concrete Research*, **1993**, vol. 23, pp. 254-266.

[54] Q. Yang, X. Wu, Factors influencing properties of phosphate cement-based binder for rapid repair of concrete, *Cement and Concrete Research*, **1999**, vol. 29, pp. 389-396.

[55] Q. Yang, B. Zhu, S. Zhang, X. Wu, Properties and applications of magnesia–phosphate cement mortar for rapid repair of concrete, *Cement and Concrete Research*, **2000**, vol. 30, pp. 1807-1813.

[56] D. Singh, A.S. Wagh, J.C. Cunnane, J.L. Mayberry, Chemically bonded phosphate ceramics for low-level mixed-waste stabilization, *Journal of Environmental Science and Health Part A: Environmental Science and Engineering and Toxicology*, **1997**, vol. 32, pp. 527-541.

[57] D. Singh, A.S. Wagh, M. Tlustochowicz, S.Y. Jeong, Phosphate ceramic process for macroencapsulation and stabilization of low-level debris wastes, *Waste Management*, **1998**, vol. 18, pp. 135-143.

[58] D. Singh, S.Y. Jeong, K. Dwyer, Ceramicrete: a novel ceramic packaging system for spent-fuel transport and storage, *Waste Management*; AZ, USA, **2000**.

[59] D. Singh, V.R. Mandalika, S.J. Parulekar, A.S. Wagh, Magnesium potassium phosphate ceramic for ^{99}Tc immobilization, *Journal of Nuclear Materials*, **2006**, vol. 348, pp. 272-282.

[60] A.S. Wagh, S.-Y. Jeong, D. Singh, Mercury stabilization in chemically bonded phosphate ceramics, *American Ceramic Society* San Antonio, TX, USA, **1997**.

[61] A.S. Wagh, R. Strain, S.Y. Jeong, D. Reed, T. Krause, D. Singh, Stabilization of Rocky Flats Pu-contaminated ash within chemically bonded phosphate ceramics, *Journal of Nuclear Materials*, **1999**, vol. 265, pp. 295-307.

[62] A.S. Wagh, M.D. Maloney, G.H. Thomson, A. Antink, Investigations in ceramicrete stabilization of hanford tank wastes, *Waste Management*; AZ, USA, **2003**.

[63] British Standard, *Fly ash for concrete*, in: Part 1: Definition, specifications and conformity criteria, BS EN 450-1, **2012**.

[64] British Standard, *Methods of testing cement*, in: Part 6: determination of fineness, BS EN 196-6, **2010**.

[65] S.E. Mouring, P.H. Miller, V.L. Burns, Investigation into the mechanical behaviour of ceramicrete, *Proceedings of 13th International Offshore and Polar Engineering Conference*; Honolulu, Hawaii, USA, **2003**.

[66] British Standard, *Testing hardened concrete*, in: Part 2: compressive strength of test specimens, BS EN 12390-3, **2009**.

[67] D.L. Pavia, G.M. Lampman, G.S. Kriz, J.R. Vyvyan, *Introduction to Spectroscopy*, Fourth ed., Brookes/Coele, CA, USA, **2009**.

[68] B.C. Smith, *Fundamentals of Fourier Transform Infrared Spectroscopy*, Second ed., CRC Press, FL, USA, **2011**.

[69] A.R. West, *Basic Solid State Chemistry*, Second ed., John Wiley & Sons, Ltd, Chichester, UK, **1999**.

[70] P.R. Griffiths, *Fourier Transform Infrared Spectroscopy*, Second ed., John Wiley & Sons, Inc., NJ, USA, **2007**.

[71] R.J. Wilson, *Calorimetry* in: P.J. Haines (Ed.) Principles of Thermal Analysis and Calorimetry, The Royal Society of Chemistry, Cambridge, UK, **2002,** pp. 129-161.

[72] D.L. Kantro, Influence of water-reducing admixtures on properties of cement paste - a miniature slump test, *Cement, Concrete and Aggregates*, **1980**, vol. 2, pp. 95-102.

[73] W.S. Rasband. ImageJ, U.S. National Institute of Health: Bethesda, Maryland, USA, **1997-2012**.

[74] K. Lagarec, D.G. Rancourt, Recoil - Mössbauer spectral analysis software for Windows, version 1.02, *Department of Physics, University of Ottawa, Ottawa*, **1998**, vol.

[75] P.J. Goodhew, J. Humphreys, R. Beanland, *Electron Microscopy and Analysis*, Third ed., Taylor & Francis, London, UK, **2001**.

[76] R.F. Egerton, *Physical Principles of Electron Microscopy: An Introduction to TEM, SEM and AEM*, Springer Science+Buisness Media, Inc., NY, USA, **2005**.

[77] J. Lilley, *Nuclear Physics: Principles and Applications*, John Wiley & Sons, Ltd., Chichester, UK, **2001**.

[78] K.J.D. MacKenzie, M.E. Smith, *Multinuclear Solid-State NMR of Inorganic Materials*, Elsevier Science Ltd, Oxford, UK, **2002**.

[79] D.C. Apperley, R.K. Harris, P. Hodgkinson, *Solid-State NMR: Basic Principles & Practice*, Momentum Press, LLC, NY, USA, **2012**.

[80] S.E. Ashbrook, S. Sneddon, New methods and applications in solid-state NMR spectroscopy of quadrupolar nuclei, *Journal of the American Chemical Society*, **2014**, vol. 136, pp. 15440-15456.

[81] D. Laurencin, C. Gervais, H. Stork, S. Krämer, D. Massiot, F. Fayon, ^{25}Mg solid-state NMR of magnesium phosphates: high magnetic field experiments and density functional theory calculations, *The Journal of Physical Chemistry C*, **2012**, vol. 116, pp. 19984-19995.

[82] P. Duxson, J.L. Provis, G.C. Lukey, J.S.J. van Deventer, F. Separovic, Z.H. Gan, ^{39}K NMR of free potassium in geopolymers, *Industrial & Engineering Chemistry Research*, **2006**, vol. 45, pp. 9208-9210.

[83] Bruker. *TopSpin 3.2*, **2013**.

[84] G.R. Heal, *Thermogravimetry and derivative thermogravitmetry* in: P.J. Haines (Ed.) Principles of Thermal Analysis and Calorimetry, The Royal Society of Chemistry, Cambridge, UK, **2002**.

[85] P.G. Laye, *Differential thermal analysis and differential scanning calorimetry* in: P.J. Haines (Ed.) Principles of Thermal Analysis and Calorimetry, The Royal Society of Chemistry, Cambridge, UK, **2002,** pp. 55-92.

[86] M.E. Brown, *Introduction to Thermal Analysis: Techniques and Applications*, Chapan and Hall Ltd, London, UK, **1988**.

[87] STOE and Cie GmbH. STOE WinXPOW, 2.10; Darmstadt, Germany, **2004**.

[88] R.E. Dinnebier, S.J.L. Billinge, *Principles of powder diffraction*, in: R.E. Dinnebier, S.J.L. Billinge (Eds.), Powder Diffraction: Theory and Practice, The Royal Society of Chemistry Cambridge, UK, **2008**.

[89] A. Covill, Cementing change in nuclear waste, *Materials World Magazine*, **2010**, vol. 18, pp. 23-25.

[90] D.A. Hall, R. Stevens, B.E. Jazairi, Effect of water content on the structure and mechanical properties of magnesia-phosphate cement mortar, *Journal of the American Ceramic Society*, **1998**, vol. 81, pp. 1550-1556.

[91] Z. Ding, B. Dong, F. Xing, N. Han, Z. Li, Cementing mechanism of potassium phosphate based magnesium phosphate cement, *Ceramics International*, **2012**, vol. 38, pp. 6281-6288.

[92] H. Ma, B. Xu, J. Liu, H. Pei, Z. Li, Effects of water content, magnesia-to-phosphate molar ratio and age on pore structure, strength and permeability of magnesium potassium phosphate cement paste, *Materials & Design*, **2014**, vol. 64, pp. 497-502.

[93] Nuclear Decommissioning Authority, *Waste package specification and guidance documentation: WPS/700 500 litre drum waste package specification: explantory material and design guidelines*, **2008**.

[94] P.D. Swift, *The development of calcium aluminate phosphate cement for radioactive waste encapsulationw*, Unpublished thesis, Department of Materials Science and Engineering, University of Sheffield, **2013**.

[95] Q. Yang, B. Zhu, X. Wu, Characteristics and durability test of magnesium phosphate cement-based material for rapid repair of concrete, *Materials and Structures*, **2000**, vol. 33, pp. 229-234.

[96] Z. Liu, G. Qian, J. Zhou, C. Li, Y. Xu, Z. Qin, Improvement of ground granulated blast furnace slag on stabilization/solidification of simulated mercury-doped wastes in chemically bonded phosphate ceramics, *Journal of Hazardous Materials*, **2008**, vol. 157, pp. 146-153.

[97] L.J. Gardner, S.A. Bernal, S.A. Walling, C.L. Corkhill, J.L. Provis, N.C. Hyatt, Characterisation of magnesium potassium phosphate cements blended with fly ash and blast furnace slag, *Cement and Concrete Research*, **2015**, vol. 74, pp. 78-87.

[98] S. Zhang, H. Shi, S. Huang, P. Zhang, Dehydration characteristics of struvite-K pertaining to magnesium potassium phosphate cement system in non-isothermal condition, *Journal of Thermal Analysis and Calorimetry*, **2013**, vol. 111, pp. 35-40.

[99] J.L. Provis, P. Duxson, J.S.J. van Deventer, The role of particle technology in developing sustainable construction materials, *Advanced Powder Technology*, **2010**, vol. 21, pp. 2-7.

[100] N.E. Hipedinger, A.N. Scian, E.F. Aglietti, Magnesia–phosphate bond for cold-setting cordierite-based refractories, *Cement and Concrete Research*, **2002**, vol. 32, pp. 675-682.

[101] F. Qiao, C. Chau, Z. Li, Calorimetric study of magnesium potassium phosphate cement, *Materials and Structures*, **2012**, vol. 45, pp. 447-456.

[102] A.D. Wilson, J.W. Nicholson, *Acid-base Cements: Their Biomedical and Industrial Applications*, Cambridge University Press, **1993**.

[103] R.M. Hazen, Effects of temperature and pressure on the cell dimension and X-ray temperature factors of periclase, *American Mineralogist*, **1976**, vol. 61, pp. 266-271.

[104] R.J. Angel, C.T. Prewitt, Crsytal structure of mullite: a re-examination of the average structure, *American Mineralogist*, **1986**, vol. 71.

[105] S.M. Antao, I. Hassan, J. Wang, P.L. Lee, B.H. Toby, State-of-the-art high resolution powder X-ray diffraction (HRPXRD) illustrated with Rietveld structure refinement of quartz, sodalite, tremolite, and meionite, *The Canadian Mineralogist*, **2008**, vol. 46, pp. 1501-1509.

[106] R.L. Blake, R.E. Hessevick, T. Zoltai, L.W. Finger, Refinement of the hematite structure, *American Mineralogist*, **1966**, vol. 51, pp. 123-129.

[107] J. west, A quantitative X-ray analysis of the structure of potassium dihydrogen phosphate (KH_2PO_4), *Zeitschrift fur Kristallographie*, **1930**, vol. 74, pp. 306-335.

[108] S. Popovics, N. Rajendran, M. Penko, Rapid hardening cements for repair of concrete, *Materials Journal*, **1987**, vol. 84, pp. 65-73.

[109] B.E.I. Abdelrazig, J.H. Sharp, B. El-Jazairi, The microstructure and mechanical properties of mortars made from magnesia-phosphate cement, *Cement and Concrete Research*, **1989**, vol. 19, pp. 247-258.

[110] A.G.d.l. Torre, R.N.d. Vera, A.J.M. Cuberos, M.A.G. Aranda, Crystal structure of low magnesiu-content alite: application to Rietveld quantitative phase analysis, *Cement and Concrete Research*, **2008**, vol. 38, pp. 1261-1269.

[111] E.N. Maslan, V.A. Streltsov, N.R. Streltsova, X-ray study of the electron density in calcite, $CaCO_3$, *Acta Crystallographica B49*, **1993**, vol. pp. 636-641.

[112] G.L. Ulex, CLXIII. On struvite, a new mineral, *Memoirs and Proceedings of the Chemical Society*, **1845**, vol. 3, pp. 106-110.

[113] R.W.E. MacIvor, On Australian bag guano and some minerals occuring therein, *The Chemical News*, **1887**, vol. 55, pp. 215-216.

[114] R.W.E. MacIvor, On minerals occuring in Australian bat guano, *The Chemical News*, **1902**, vol. 85, pp. 181-182.

[115] A. Whitaker, J.W. Jeffery, The crystal structure of struvite, $MgNH_4PO_4{\cdot}6H_2O$, *Acta Crystallographica: Section B Structural Crystallography and Crystal Chemistry*, **1970**, vol. 26, pp. 1429-1440.

[116] S. Graeser, W. Postl, H.-P. Bojar, P. Berlepsch, T. Armbruster, T. Raber, K. Ettinger, F. Walter, Struvite-(K), $KMgPO_4{\cdot}6H_2O$, the potassium equivalent of struvite – a new mineral, *European Journal of Mineralogy*, **2008**, vol. 20, pp. 629-633.

[117] K. Momma, F. Izumi, VESTA 3 for three-dimensional visualization of crystal, volumetric and morphology data, *Journal of Applied Crystallography*, **2011**, vol. 44, pp. 1272-1276.

[118] G.B. Sinclair, F.G. Barton, L.J. Kennedy, Military engineering in the Falkland Islands 1982-83, *Proceedings of Instiution of Civil Engineers, part 1*, **1984**, vol. 76, pp. 269-277.

[119] L.J. Gardner, V. Lejeune, C.L. Corkhill, S.A. Bernal, J.L. Provis, M.C. Stennett, N.C. Hyatt, Evolution of the phase assemblage in magnesium potassium phosphate cement binders at 200 and 1000 °C, *Advances in Applied Ceramics*, **2015**, vol. 114, pp. 386-392.

[120] G. Wallez, C. Colbeau-Justin, T. Le Mercier, M. Quarton, F. Robert, Crystal chemistry and polymorphism of potassium–magnesium monophosphate, *Journal of Solid State Chemistry*, **1998**, vol. 136, pp. 175-180.

[121] A.K. Sarkar, Hydration/dehydration characteristics of struvite and dittmarite pertaining to magnesium ammonium phosphate cement systems, *Journal of Materials Science*, **1991**, vol. 26, pp. 2514-2518.

[122] B.E.I. Abdelrazig, J.H. Sharp, Phase changes on heating ammonium magnesium phosphate hydrates, *Thermochimica Acta*, **1988**, vol. 129, pp. 197-215.

[123] M.I.H. Bhuiyan, D.S. Mavinic, F.A. Koch, Thermal decomposition of struvite and its phase transition, *Chemosphere*, **2008**, vol. 70, pp. 1347-1356.

[124] S.N. Scrimgeour, J.A. Chudek, G.A. Cowper, C.H. Lloyd, ^{31}P solid-state MAS-NMR spectroscopy of the compounds that form in phosphate-bonded dental casting investment materials during setting, *Dental Materials*, **2007**, vol. 23, pp. 934-943.

[125] N. Ma, A.A. Rouff, B.L. Phillips, A ^{31}P NMR and TG/DSC-FTIR investigation of the influence of initial pH on phosphorus recovery as struvite, *ACS Sustainable Chemistry & Engineering*, **2014**, vol. 2, pp. 816-822.

[126] M.C. Connaway-Wagner, W.G. Klemperer, J.F. Young, *A comparative study of magnesia-orthophosphate and magnesia-tripoyphosphate cements*, in: S. Mindess (Ed.) Advances in Cementitious Materials, The American Ceramic Society. Ceramic Transactions, Westerville, OH, **1991**.

[127] T.F. Kemp, M.E. Smith, QuadFit—A new cross-platform computer program for simulation of NMR line shapes from solids with distributions of interaction parameters, *Solid State Nuclear Magnetic Resonance*, **2009**, vol. 35, pp. 243-252.

[128] G. Mestres, M.P. Ginebra, Novel magnesium phosphate cements with high early strength and antibacterial properties, *Acta Biomaterialia*, **2011**, vol. 7, pp. 1853-1861.

[129] A.S. Wagh, S.Y. Jeong, D. Singh, *High strength phosphate cement using industrial byproduct ashes*, in: Proceedings of 1st International Conference on High Strength Concrete, United Engineering Foundation, Inc, HI, USA, **1997**, pp. 542-553.

[130] Y. Li, B. Chen, Factors that affect the properties of magnesium phosphate cement, *Construction and Building Materials*, **2013**, vol. 47, pp. 977-983.

[131] Z. Ding, Z. Li, Effect of aggregates and water contents on the properties of magnesium phospho-silicate cement, *Cement and Concrete Composites*, **2005**, vol. 27, pp. 11-18.

[132] F. Xing, Z. Ding, Z. Li, Study of potassium-based magnesium phosphate cement, *Advances in Cement Research*, **2011**, vol. 23, pp. 81-87.

[133] F. Xing, Z. Ding, Z. Li, Effect of additives on properties of magnesium phosphosilicate cement, *Advances in Cement Research*, **2011**, vol. 23, pp. 69-74.

[134] L. Johansson, J.P. Gustafsson, Phosphate removal using blast furnace slags and opoka-mechanisms, *Water Research*, **2000**, vol. 34, pp. 259-265.

[135] N.M. Agyei, C.A. Strydom, J.H. Potgieter, The removal of phosphate ions from aqueous solution by fly ash, slag, ordinary Portland cement and related blends, *Cement and Concrete Research*, **2002**, vol. 32, pp. 1889-1897.

[136] S. Lu, S. Bai, H. Shan, Mechanisms of phosphate removal from aqueous solution by blast furnace slag and steel furnace slag, *Journal of Zhejiang University - Science A*, **2008**, vol. 9, pp. 125-132.

[137] C.K. Chauhan, P.M. Vyas, M.J. Joshi, Growth and characterization of struvite-K crystals, *Crystal Research and Technology*, **2011**, vol. 46, pp. 187-194.

[138] S. Diamond, Particle morphologies in fly ash, *Cement and Concrete Research*, **1986**, vol. 16, pp. 569-579.

[139] R.R. Lloyd, J.L. Provis, Microscopy and microanalyis of inorganic polymer cements. 1: remnant fly ash particles, *Journal of Materials Science*, **2009**, vol. 44, pp. 608-619.

[140] B.G. Kutchko, A.G. Kim, Fly ash characterization by SEM–EDS, *Fuel*, **2006**, vol. 85, pp. 2537-2544.

[141] R.J. Kirkpatrick, *MAS NMR Spectroscopy of Minerals and Glasses* in: F.C. Hawthorne (Ed.) Spectroscopic Methods in Mineralogy and Geology, The Society, **1988,** pp. 341-403.

[142] R.J. Myers, S.A. Bernal, R. San Nicolas, J.L. Provis, Generalized Structural Description of Calcium–Sodium Aluminosilicate Hydrate Gels: The Cross-Linked Substituted Tobermorite Model, *Langmuir*, **2013**, vol. 29, pp. 5294-5306.

[143] S.A. Bernal, J.L. Provis, B. Walkley, R. San Nicolas, J.D. Gehman, D.G. Brice, A.R. Kilcullen, P. Duxson, J.S.J. van Deventer, Gel nanostructure in alkali-activated binders based on slag and fly ash, and effects of accelerated carbonation, *Cement and Concrete Research*, **2013**, vol. 53, pp. 127-144.

[144] J. Schneider, M.A. Cincotto, H. Panepucci, ^{29}Si and ^{27}Al high-resolution NMR characterization of calcium silicate hydrate phases in activated blast-furnace slag pastes, *Cement and Concrete Research*, **2001**, vol. 31, pp. 993-1001.

[145] S. Wang, K.L. Scrivener, ^{29}Si and ^{27}Al NMR study of alkali-activated slag, *Cement and Concrete Research*, **2003**, vol. 33, pp. 769-774.

[146] S. Murgier, H. Zanni, D. Gouvenot, Blast furnace slag cement: a ^{29}Si and ^{27}Al NMR study, *Comptes Rendus Chimie*, **2004**, vol. 7, pp. 389-394.

[147] J. McManus, S.E. Ashbrook, K.J.D. MacKenzie, S. Wimperis, ^{27}Al multiple-quantum MAS and ^{27}Al{^{1}H} CPMAS NMR study of amorphous aluminosilicates, *Journal of Non-Crystalline Solids*, **2001**, vol. 282, pp. 278-290.

[148] E. Lippmaa, A. Samoson, M. Mägi, High-resolution ^{27}Al NMR of aluminosilicates, *Journal of the American Chemical Society*, **1986**, vol. 108, pp. 1730-1735.

[149] J. Skibsted, E. Henderson, H.J. Jakobsen, Characterization of calcium aluminate phases in cements by ^{27}Al MAS NMR spectroscopy, *Inorganic Chemistry*, **1993**, vol. 32, pp. 1013-1027.

[150] H. He, J. Guo, J. Zhu, P. Yuan, C. Hu, ^{29}Si and ^{27}Al MAS NMR spectra of mullites from different kaolinites, *Spectrochimica Acta Part A: Molecular and Biomolecular Spectroscopy*, **2004**, vol. 60, pp. 1061-1064.

[151] L.H. Merwin, A. Sebald, H. Rager, H. Schneider, ^{29}Si and ^{27}Al MAS NMR spectroscopy of mullite, *Physics and Chemistry of Minerals*, **1991**, vol. 18, pp. 47-52.

[152] T. Georgelin, M. Jaber, T. Onfroy, A.-A. Hargrove, F. Costa-Torro, J.-F. Lambert, Inorganic Phosphate and Nucleotides on Silica Surface: Condensation, Dismutation, and Phosphorylation, *The Journal of Physical Chemistry C*, **2013**, vol. 117, pp. 12579-12590.

[153] G. Engelhardt, D. Michel, *High-resolution solid-state NMR of silicates and zeolites*, John Wiley & Sons, Chichester, **1987**.

[154] E. Lippmaa, M. Mägi, A. Samoson, G. Engelhardt, A.R. Grimmer, Structural studies of silicates by solid-state high-resolution ^{29}Si NMR, *Journal of the American Chemical Society*, **1980**, vol. 102, pp. 4889-4893.

[155] Á. Palomo, S. Alonso, A. Fernandez-Jiménez, I. Sobrados, J. Sanz, Alkaline activation of fly ashes: NMR study of the reaction products, *Journal of the American Ceramic Society*, **2004**, vol. 87, pp. 1141-1145.

[156] P.J. Pallister, I.L. Moudrakovski, J.A. Ripmeester, Mg-25 ultra-high field solid state NMR spectroscopy and first principles calculations of magnesium compounds, *Physical Chemistry Chemical Physics*, **2009**, vol. 11, pp. 11487-11500.

[157] V.F.F. Barbosa, K.J.D. MacKenzie, Synthesis and thermal behaviour of potassium sialate geopolymers, *Materials Letters*, **2003**, vol. 57, pp. 1477-1482.

[158] J.F. Stebbins, L.-S. Du, S. Kroeker, P. Neuhoff, D. Rice, J. Frye, H.J. Jakobsen, New opportunities for high-resolution solid-state NMR spectroscopy of oxide materials at 21.1- and 18.8-T fields, *Solid State Nuclear Magnetic Resonance*, **2002**, vol. 21, pp. 105-115.

[159] L. Sánchez-Muñoz, J. Sanz, I. Sobrados, Z. Gan, Medium-range order in disordered K-feldspars by multinuclear NMR, *American Mineralogist*, **2013**, vol. 98, pp. 2115-2131.

[160] S.A. Walling, J.L. Provis, Magnesia based cements – a journey of 150 years, and cements for the future?, *Chemical Reviews*, **2016**, vol. Accepted.

[161] Nuclear Decommissioning Authority, *Geological Disposal: Waste package accident performance status report, NDA/RWMD/032*, **2010**.

[162] U.S Department of Energy, *Waste isolation pilot plant recovery plan, revision 0*, **2014**.

[163] F. Delhomme, J. Ambroise, A. Limam, Effects of high temperatures on mortar specimens containing Portland cement and GGBFS, *Materials and Structures*, **2012**, vol. 45, pp. 1685-1692.

[164] D. Matesová, D. Bonen, S. Shah, Factors affecting the resistance of cementitious materials at high temperatures and medium heating rates, *Materials and Structures*, **2006**, vol. 39, pp. 455-469.

[165] R.W. Limes, D. Ponzani. *Basic refractory compositions for intermediate temperature zones*, U.S. Patent 3285758, **1966**.

[166] R.W. Limes, R.O. Russell. *Process for preparing fast-setting aggregate compositions and products for low porosity produced therewith*, U.S. Patent 3879209, **1975**.

[167] N.E. Hipedinger, A.N. Scian, E.F. Aglietti, Magnesia–ammonium phosphate-bonded cordierite refractory castables: phase evolution on heating and mechanical properties, *Cement and Concrete Research*, **2004**, vol. 34, pp. 157-164.

[168] T. Sugama, L.E. Kukacka, Magnesium monophosphate cements derived from diammonium phosphate solutions, *Cement and Concrete Research*, **1983**, vol. 13, pp. 407-416.

[169] Y. Li, T. Shi, B. Chen, Y. Li, Performance of magnesium phosphate cement at elevated temperatures, *Construction and Building Materials*, **2015**, vol. 91, pp. 126-132.

[170] International Atomic Energy Agency, *Advisory material for the IAEA regulations for the safe transport of radioactive material; 2012 edition, specific safety guide No. SSG-26*, Vienna, **2014**.

[171] T. Bakharev, Thermal behaviour of geopolymers prepared using class F fly ash and elevated temperature curing, *Cement and Concrete Research*, **2006**, vol. 36, pp. 1134-1147.

[172] X. Li, X. Wang, D. He, J. Shi, Synthesis and characterization of mesoporous CaO-MO-SiO_2-P_2O_5 (M = Mg, Zn, Cu) bioactive glasses/composites, *Journal of Materials Chemistry*, **2008**, vol. 18, pp. 4103-4109.

[173] B.L. Phillips, R.J. Kirkpatrick, Short-range Si-Al order in leucite and analcime: determination of the configurational entropy from ^{27}Al and variable-temperature ^{29}Si NMR spectroscopy of leucite, its Cs and Rb-exchanged derivatives, and analcime, *American Mineralogist*, **1994**, vol. 79, pp. 1025-1031.

[174] B.L. Phillips, R.J. Kirkpatrick, A. Putnis, Si,Al ordering in leucite by high-resolution ^{27}Al MAS NMR spectroscopy, *Physics and Chemistry of Minerals*, **1989**, vol. 16, pp. 591-598.

[175] A.I. Becerro, M. Mantovani, A. Escudero, Hydrothermal synthesis of kalsilite: a simple and economical method, *Journal of the American Ceramic Society*, **2009**, vol. 92, pp. 2204-2206.

[176] G.L. Hovis, D.R. Spearing, J.F. Stebbins, J. Roux, A. Clare, X-ray powder diffraction and ^{23}Na, ^{27}Al, and ^{29}Si MAS-NMR investigation of nepheline-kalsilite crystalline solutions, *American Mineralogist*, **1992**, vol. 77, pp. 19-29.

[177] I.W.M. Brown, C.M. Cardile, K.J.D. MacKenzie, M.J. Ryan, R.H. Meinhold, Natural and synthetic leucites studied by solid state 29-Si and 27-Al NMR and 57-Fe Mossbauer spectroscopy, *Physics and Chemistry of Minerals*, **1987**, vol. 15, pp. 78-83.

[178] L.H. Merwin, A. Sebald, F. Seifert, The incommensurate-commensurate phase transition in akermanite, $Ca_2MgSi_2O_7$, observed by in-situ ^{29}Si MAS NMR spectroscopy, *Physics and Chemistry of Minerals*, **1989**, vol. 16, pp. 752-756.

[179] J.A. Tangeman, B.L. Phillips, A. Navrotsky, J.K.R. Weber, A.D. Hixson, T.S. Key, Vitreous forsterite (Mg_2SiO_4): synthesis, structure, and thermochemistry, *Geophysical Research Letters*, **2001**, vol. 28, pp. 2517-2520.

[180] M. Mägi, E. Lippmaa, A. Samoson, G. Engelhardt, A.R. Grimmer, Solid-state high-resolution silicon-29 chemical shifts in silicates, *The Journal of Physical Chemistry*, **1984**, vol. 88, pp. 1518-1522.

[181] J.F. Stebbins, J.B. Murdoch, I.S.E. Carmichael, A. Pines, Defects and short-range order in nepheline group minerals: a silicon-29 nuclear magnetic resonance study, *Physics and Chemistry of Minerals*, **1986**, vol. 13, pp. 371-381.

[182] J.V. Smith, O.F. Tuttle, The nepheline-kalsilite system; Part I, X-ray data for the crystalline phases, *American Journal of Science*, **1957**, vol. 255, pp. 282-305.

[183] J.R. Smyth, Experimental study on the polymorphism of enstatite, *American Mineralogist*, **1974**, vol. 59, pp. 345-352.

[184] S.E. Ashbrook, A.J. Berry, D.J. Frost, A. Gregorovic, C.J. Pickard, J.E. Readman, S. Wimperis, ^{17}O and ^{29}Si NMR parameters of $MgSiO_3$ phases from high-resolution solid-state NMR spectroscopy and first-principles calculations, *Journal of the American Chemical Society*, **2007**, vol. 129, pp. 13213-13224.

[185] S.A. Jones, J.M. Burlitch, J.C. Duchamp, T.M. Duncan, Sol-gel synthesis of protoenstatite and a study of the factors that affect crystallisation, *Journal of Sol-Gel Science and Technology*, **1999**, vol. 15, pp. 201-209.

[186] P.J. Schilling, L.G. Butler, A. Roy, H.C. Eaton, 29Si and 27Al MAS-NMR of NaOH-activated blast furnace slag, *Journal of American Ceramic Society*, **1994**, vol. 77, pp. 2363-2368.

[187] S. Gomes, M. François, M. Abdelmoula, P. Refait, C. Pellissier, O. Evrard, Characterization of magnetite in silico-aluminous fly ash by SEM, TEM, XRD, magnetic susceptibility, and Mössbauer spectroscopy, *Cement and Concrete Research*, **1999**, vol. 29, pp. 1705-1711.

[188] Nuclear Decommissiong Authority, *WPS/800: wasteform specification for 500 litre drum waste package - explantory material and design guidelines*, NDA, **2008**.

[189] Nirex, *Generic repository studies: generic waste package specification: volume 2 - justification* UK Nirex Ltd, Oxford, UK, **2007**.

[190] D. Delacroix, J.P. Guerre, P. Leblanc, C. Hickman, *Radionuclide and Radiation Protection Data Handbook*, Second ed., Nuclear Technology Publishing, Kent, UK, **2002**.

[191] W.D. Loveland, D.J. Morrissey, G.T. Seaborg, *Modern Nuclear Chemistry*, John Wiley & Sons, Inc., NJ, USA, **2006**.

[192] O. Kontani, Y. Ichikawa, A. Ishizawa, M. Takizawa, O. Sato, Irradiation effects on concrete structure, *4th International Symposium on the Ageing Management & Maintenance of Nuclear Power Plants*; Tokyo, Japan, **2010**.

[193] P. Bouniol, A. Aspart, Disappearance of oxygen in concrete under irradiation: the role of peroxides in radiolysis, *Cement and Concrete Research*, **1998**, vol. 28, pp. 1669-1681.

[194] A. Lowinska-Kluge, P. Piszora, Effect of gamma irradiation on cement composites observed with XRD and SEM methods in the range of radiation dose 0-1409 MGy, *7th National Meeting og Synchrotron Radiation Users*; Poznan, Poland, **2007**.

[195] P. Soo, L.M. Milian, The effect of gamma radiation on the strength of portland cement mortars, *Journal of Materials Science Letters*, **2001**, vol. 20, pp. 1345-1348.

[196] C.R. Wilding, D.C. Phillips, C.E. Lyon, S.G. Burnay, J.A. Winter, W.E. Spindler, *The effects of radiation on intermediate-level waste forms*, Commission of the Europeon Communities, Luxembourg, **1991**.

[197] V. Stefov, B. Šoptrajanov, F. Spirovski, I. Kuzmanovski, H.D. Lutz, B. Engelen, Infrared and Raman spectra of magnesium ammonium phosphate hexahydrate (struvite) and its isomorphous analogues. I. spectra of protiated and partially deuterated magnesium potassium phosphate hexahydrate, *Journal of Molecular Structure*, **2004**, vol. 689, pp. 1-10.

[198] E.R. Lippincott, A.V. Valkenburg, C.E. Weir, E.N. Bunting, Infrared studies on polymorphs of silicon dioxide and germanium dioxide, *Journal of Research of the National Bureau of Standards*, **1958**, vol. 61, pp. 61-70.

[199] University of Manchester. *Dalton Cumbrian Facility - Co-60 irradiator*. www.dalton.manchester.ac.uk/discover/daltoncumbrianfacility/discover/facilities/co-60irradiator/ (accessed 01/09/2014), **n.d.**).

Appendix A: List of Figures

Appendix B: List of Tables

Appendix C: Formulation optimisation of MKPC binders

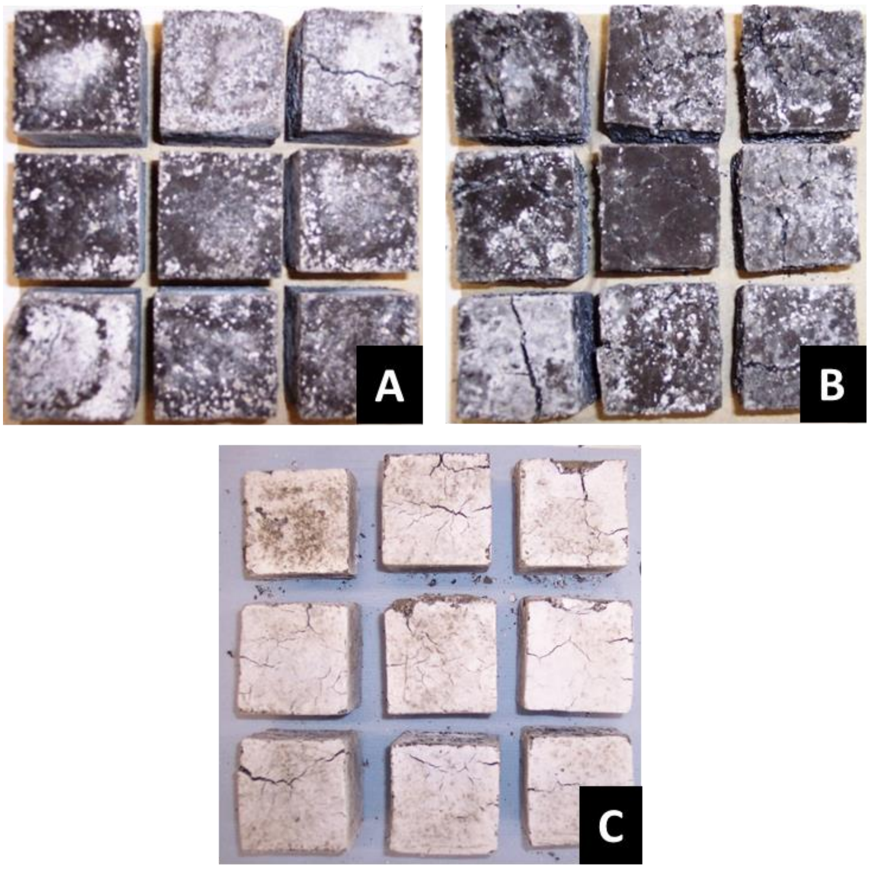

Fig. C1. Examples of compressive strength cubes that significantly cracked by curing day 3: (A) FA/MKPC (0.26 w/s) with 40 wt. % FA, (B) FA/MKPC (0.26 w/s) with 40 wt. % FA and (C) GBFS/MKPC 0.24 w/s

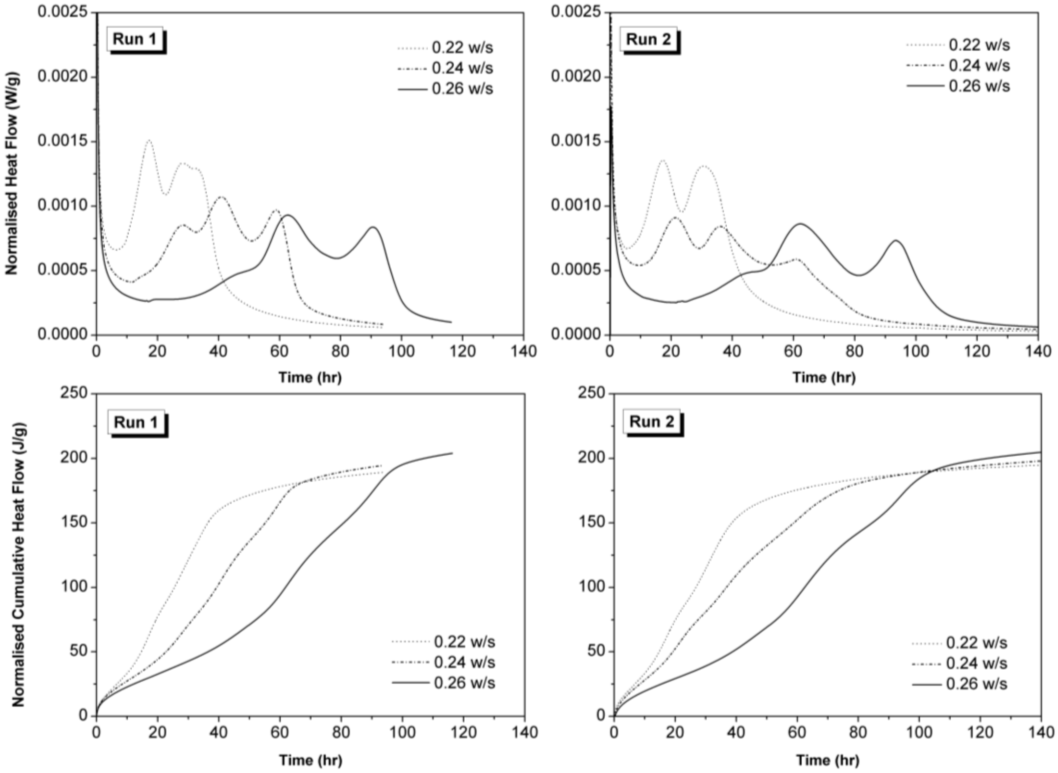

Fig. C2. Two sets of calorimetry data for GBFS/MKPC binders with w/s ratios 0.22, 0.24 and 0.26 to highlight the reproducibility of this characteristic hydration behaviour

Appendix D: Synthesis of struvite-K

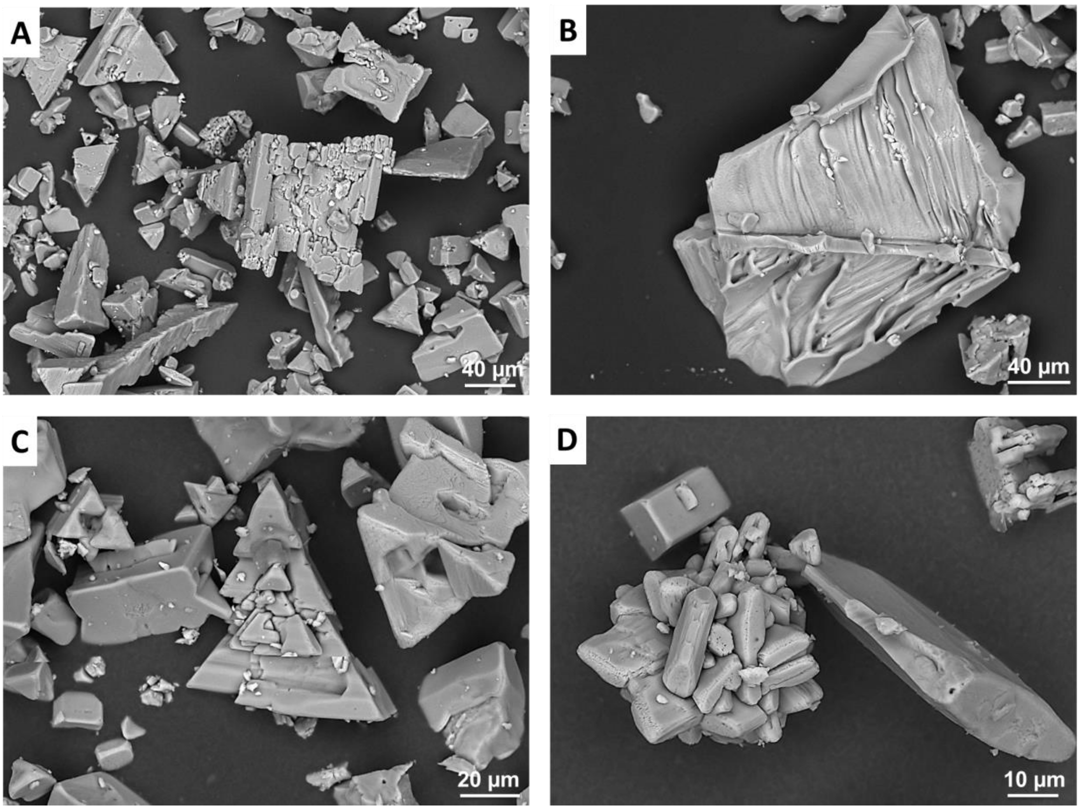

Fig. D1. Scanning electron micrographs of struvite-K at different magnifications; (A) x400, (B) x500, (C) x1000 and (D) x1500

Appendix E: High temperature stability of MKPC binders

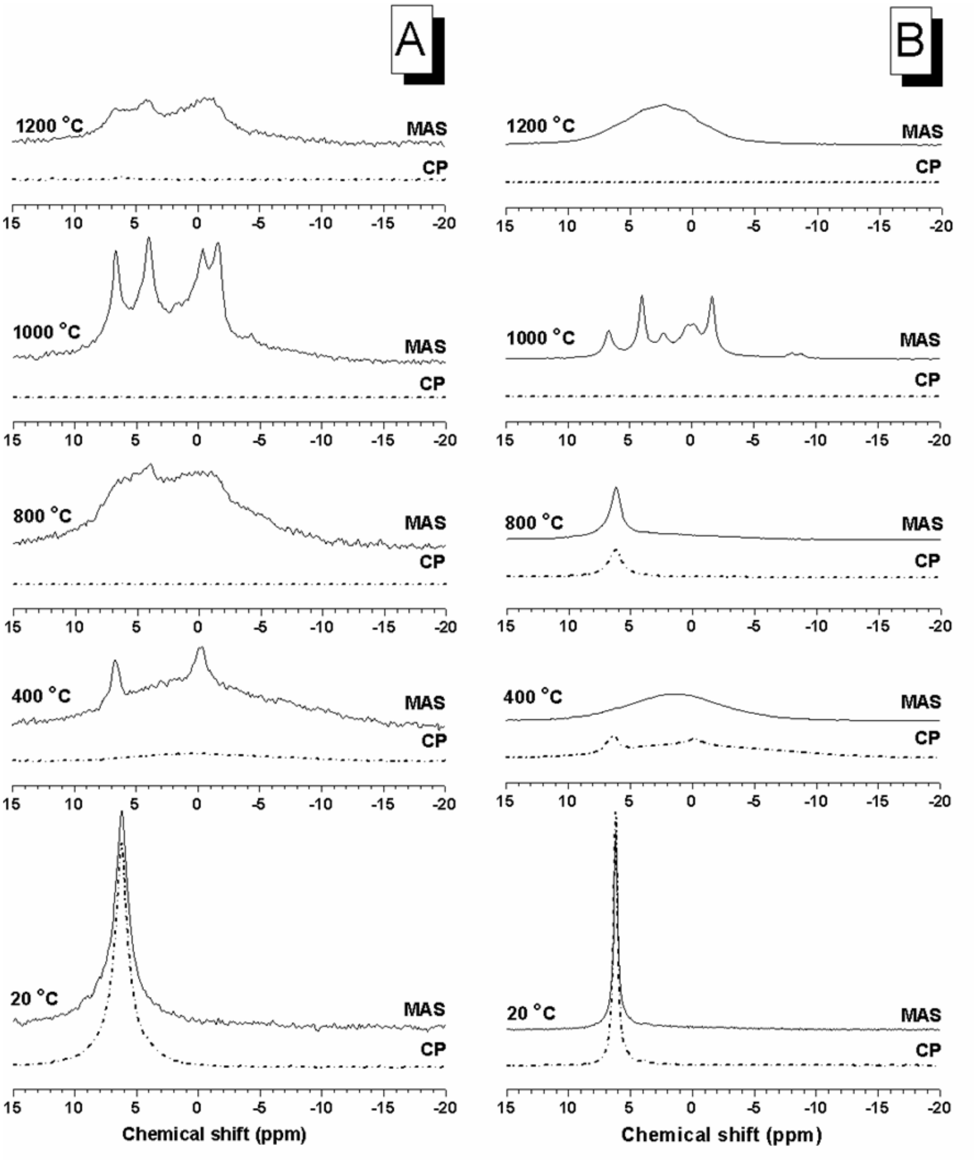

Fig. E1. Normalised ^{31}P MAS NMR spectra and ^{31}P-^{1}H CP MAS NMR spectra of hardened FA/MKPC (A) and GBFS/MKPC (B) binders heated between 20 - 1200 °C

Appendix F: Co-60 radiation tolerance of MKPC binders

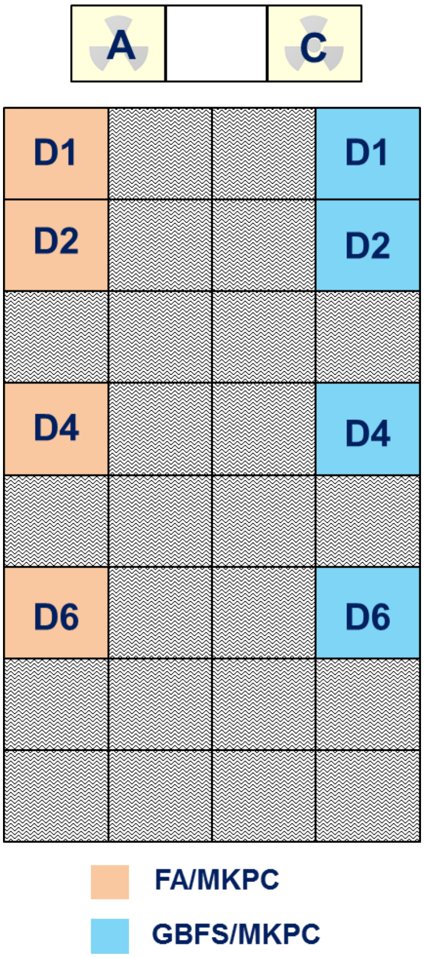

Fig. F1. Schematic of the Co-60 irradiation positions, Co-60 rods are labelled A-C

Table. F1. Dose summary of the Co-60 irradiated FA/MKPC binders

Sample No.	Co-60 Position	Time (hr)	Dose Rate (kGy/hr)	Dose (MGy)
1	Control	0.0	0.0	0.0
2	D1	57.0	17.7	1.0
3	D1	146.0	16.2	2.4
4	D1	291.0	16.1	4.7
5	D1	438.0	16.0	7.0
6	D1	559.5	17.2	9.6
7	D2	96.0	10.6	1.0
8	D2	238.0	9.8	2.3
9	D2	495.0	9.9	4.9
10	D2	775.0	10.2	7.9
11	D2	921.0	10.2	9.4
12	D4	94.0	5.2	0.5
13	D4	221.0	4.5	1.0
14	D4	323.0	4.5	1.5
15	D4	467.5	5.1	2.4
16	D4	969.0	5.0	4.8
17	D6	172.0	2.9	0.5
18	D6	348.0	2.8	1.0
19	D6	539.0	2.7	1.5
20	D6	914.0	2.7	2.5

Table. F2. Dose summary of the Co-60 irradiated GBFS/MKPC binders

Sample No.	Co-60 Position	Time (hr)	Dose Rate (kGy/hr)	Dose (MGy)
1	Control	0.0	0.0	0.0
2	D1	57.0	18.5	1.1
3	D1	146.0	17.6	2.6
4	D1	291.0	17.4	5.1
5	D1	438.0	17.3	7.6
6	D1	559.5	17.9	10.0
7	D2	96.0	11.5	1.1
8	D2	238.0	10.6	2.5
9	D2	495.0	10.1	5.0
10	D2	775.0	10.3	8.0
11	D2	921.0	11.2	10.3
12	D4	94.0	5.3	0.5
13	D4	221.0	4.6	1.0
14	D4	323.0	4.6	1.5
15	D4	467.5	5.3	2.5
16	D4	969.0	5.2	5.0
17	D6	172.0	2.9	0.5
18	D6	348.0	3.0	1.0
19	D6	539.0	2.8	1.5
20	D6	914.0	2.8	2.6

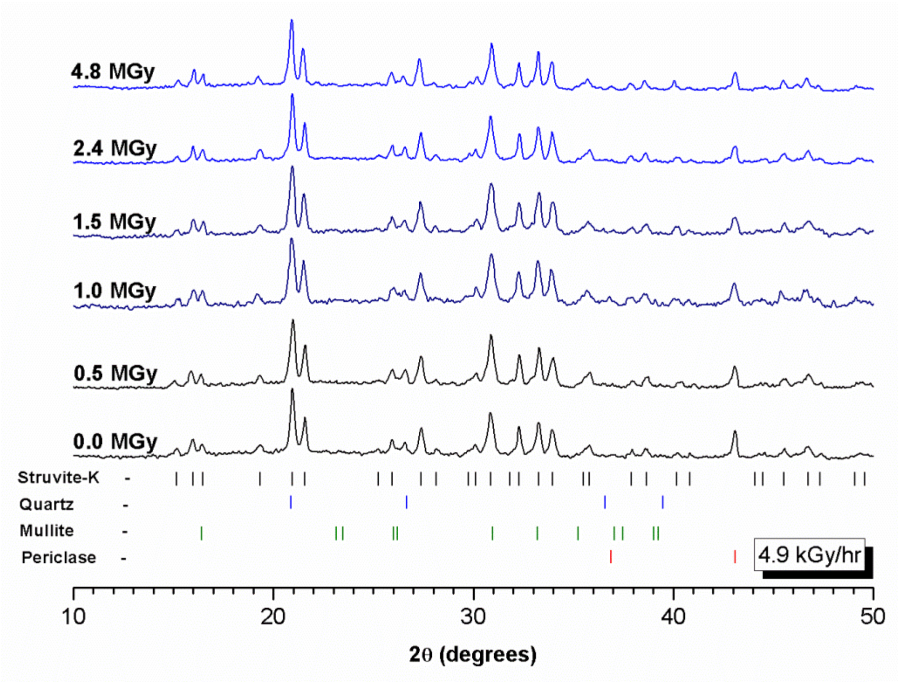

Fig. F2. Diffraction patterns of FA/MKPC exposed to: 0.0, 0.5, 1.0, 2.5 and 5.0 MGy at 4.9 kGy/hr

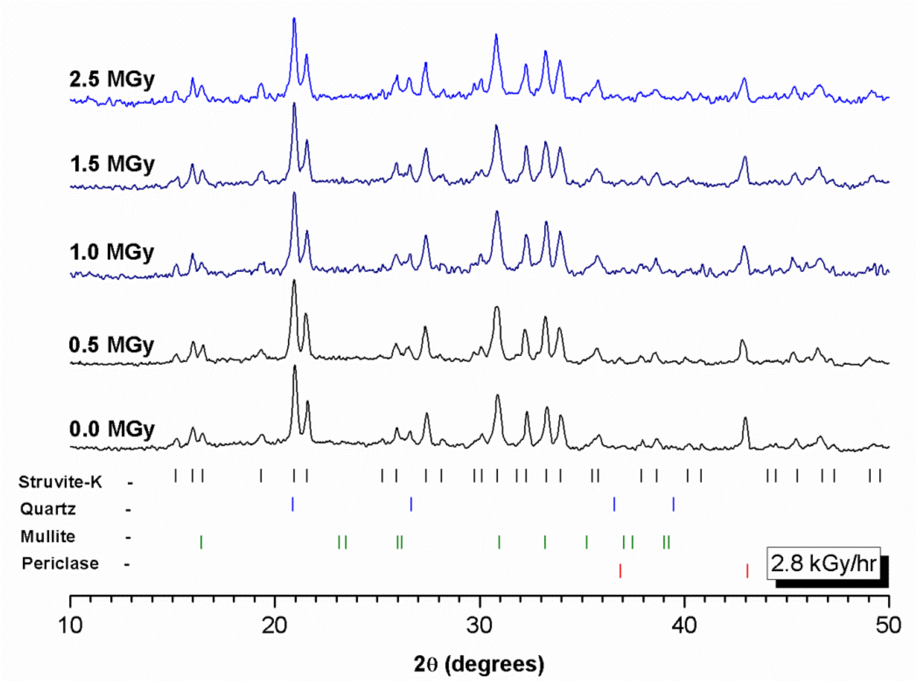

Fig. F3. Diffraction patterns of FA/MKPC exposed to: 0.0, 1.0, 1.5 and 2.5 MGy at 2.8 kGy/hr

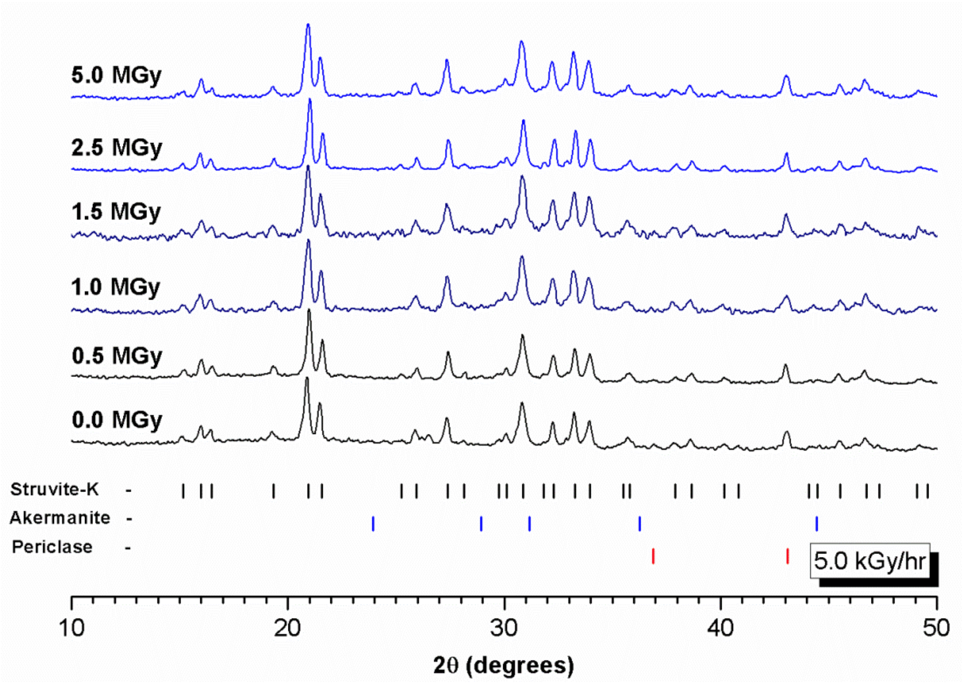

Fig. F4. Diffraction patterns of GBFS/MKPC exposed to: 0.0, 0.5, 1.0, 2.5 and 5.0 MGy at 5.0 kGy/hr

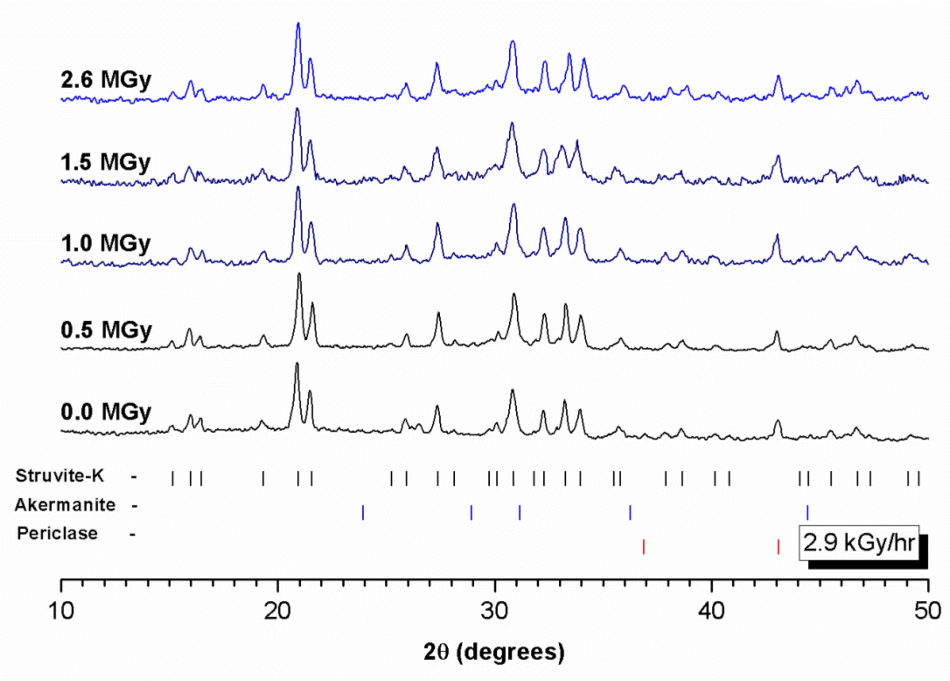

Fig. F5. Diffraction patterns of GBFS/MKPC exposed to: 0.0, 1.0, 1.5 and 2.5 MGy at 2.9 kGy/hr

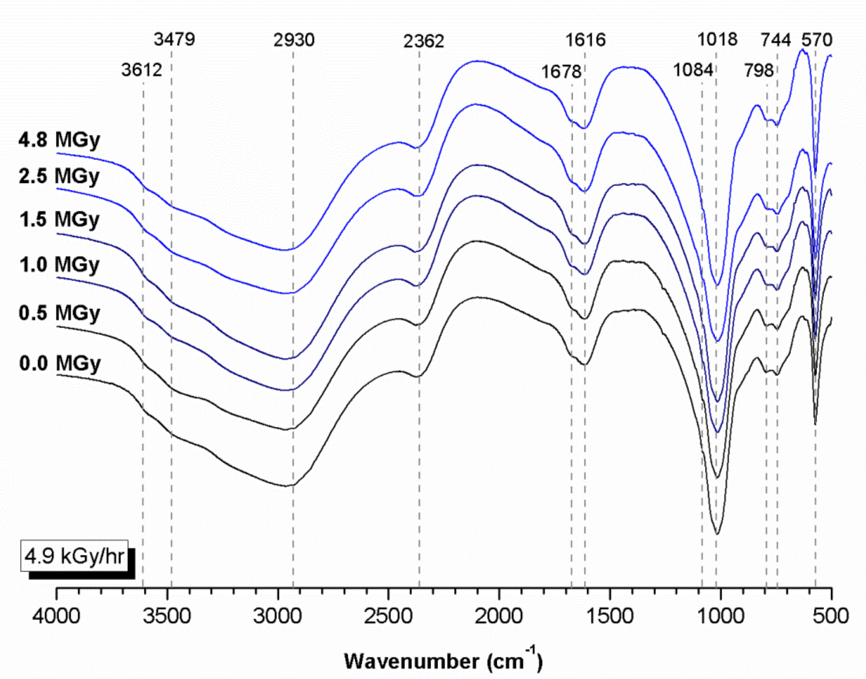

Fig. F6. Spectra of FA/MKPC specimens exposed to: 0.5, 1.0, 1.5, 2.5 and 4.8 MGy at 4.9 kGy/hr

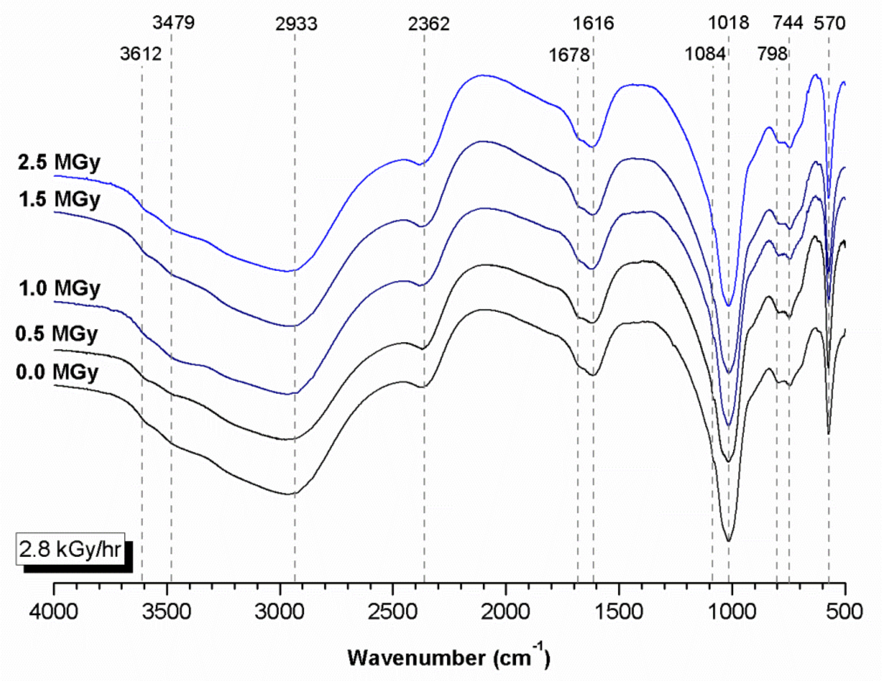

Fig. F7. Spectra of FA/MKPC specimens exposed to: 0.5, 1.0, 1.5 and 2.5 MGy at 2.8 kGy/hr

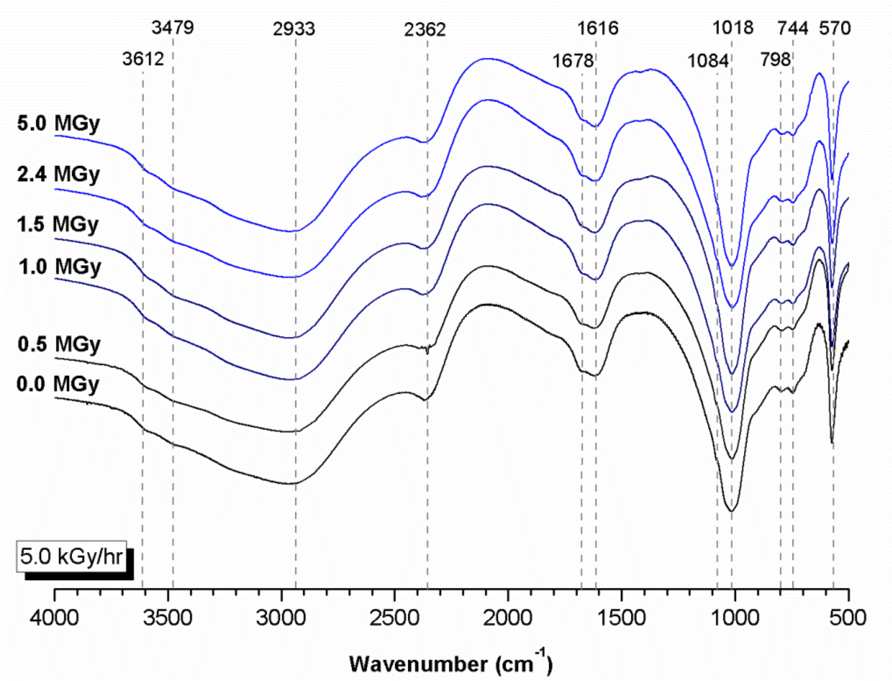

Fig. F8. Spectra of GBFS/MKPC specimens exposed to: 0.5, 1.0, 1.5, 2.4 and 5.0 MGy at 5.0 kGy/hr

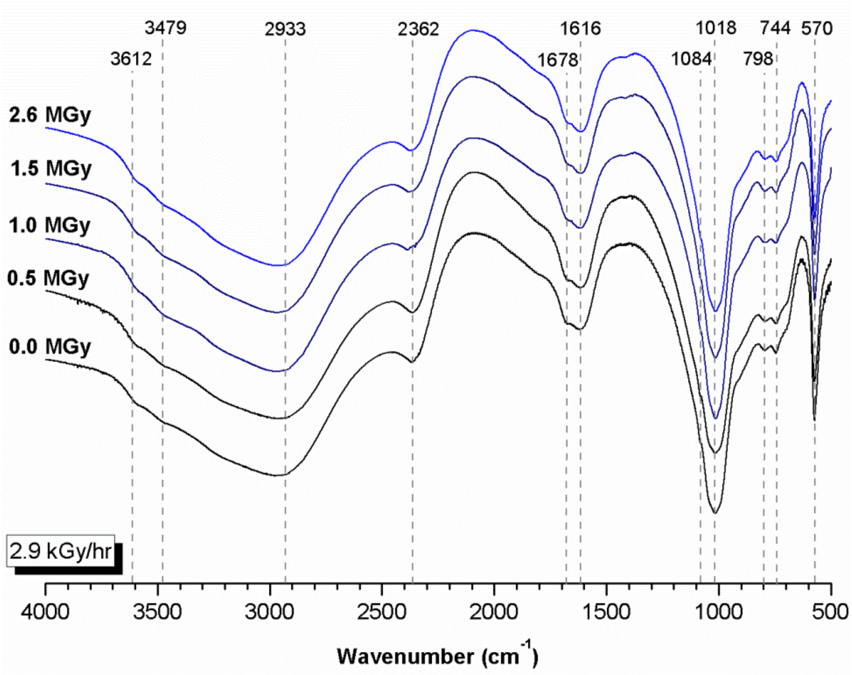

Fig. F9. Spectra of GBFS/MKPC specimens exposed to: 0.5, 1.0, 1.5 and 2.6 MGy at 2.9 kGy/hr

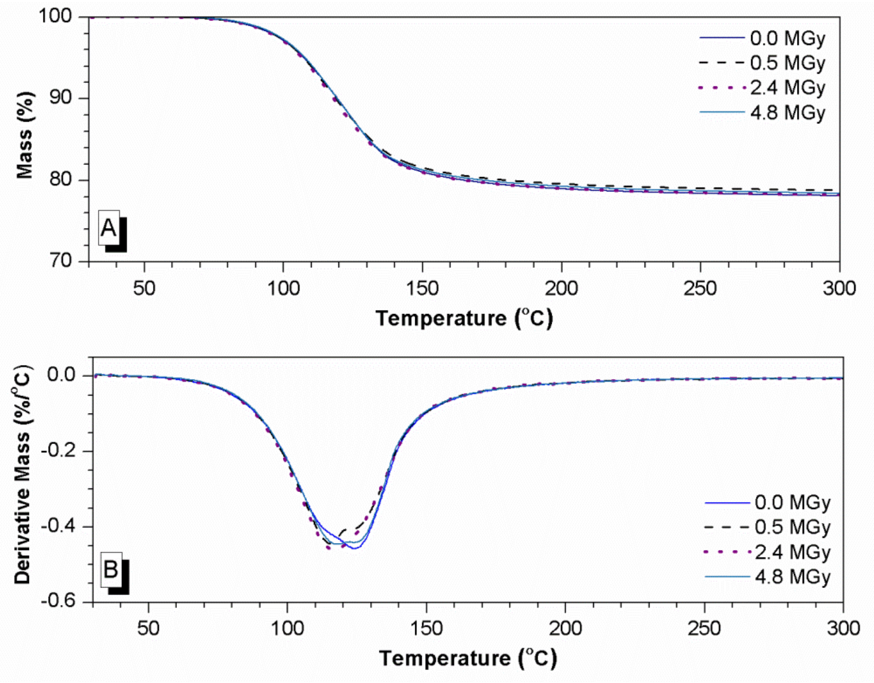

Fig. F10. TGA (A) and DTG (B) traces of FA/MKPC specimens exposed to: 0.5, 2.4 and 4.8 MGy at 4.9 kGy/hr

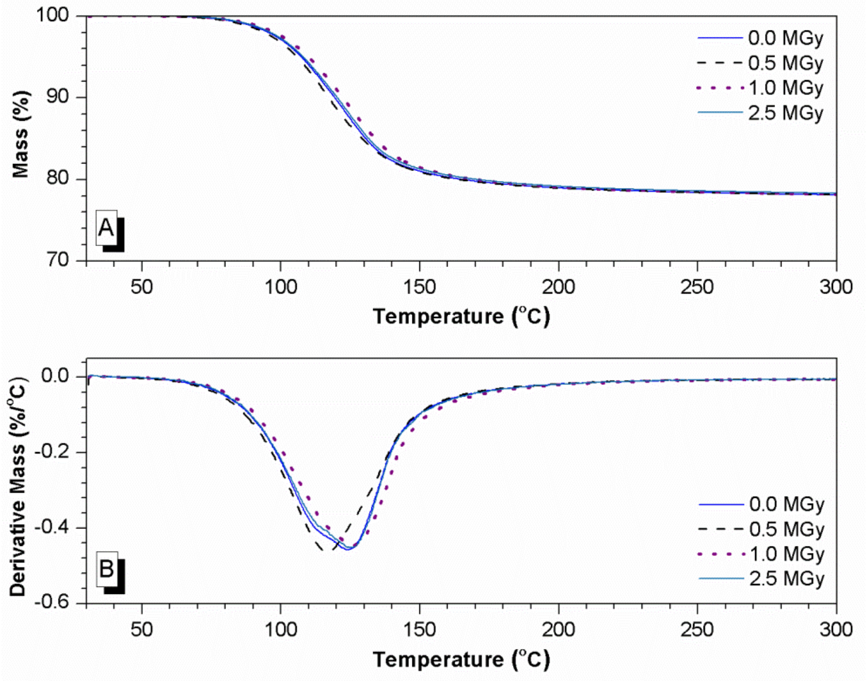

Fig. F11. TGA (A) and DTG (B) traces of FA/MKPC specimens exposed to: 0.5, 1.0 and 2.5 MGy at 2.8 kGy/hr

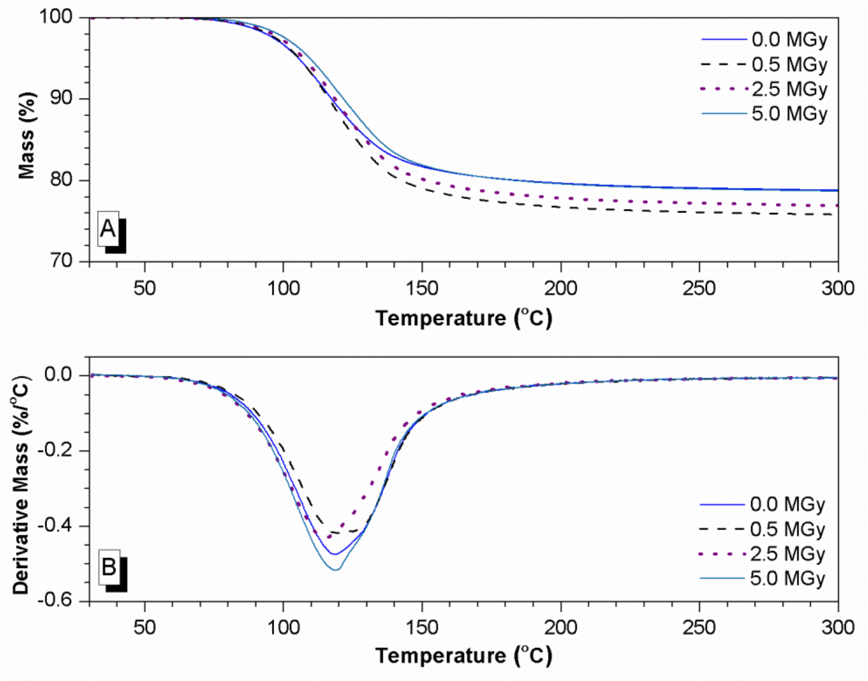

Fig. F12. TGA (A) and DTG (B) traces of GBFS/MKPC specimens exposed to: 0.5, 2.5 and 5.0 MGy at 5.0 kGy/hr

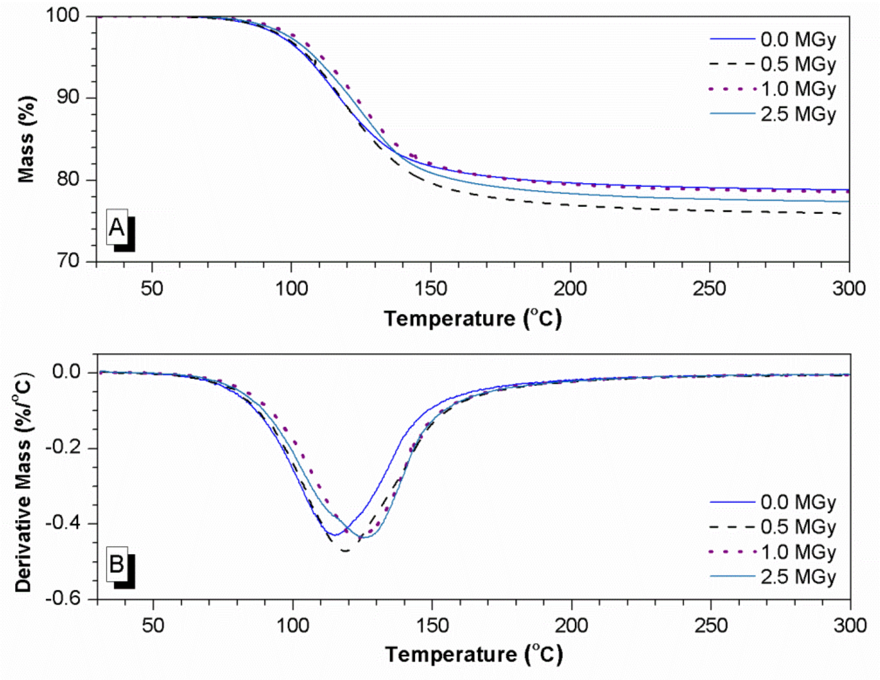

Fig. F13. TGA (A) and DTG (B) traces of GBFS/MKPC specimens exposed to: 0.5, 1.0 and 2.5 MGy at 2.9 kGy/hr

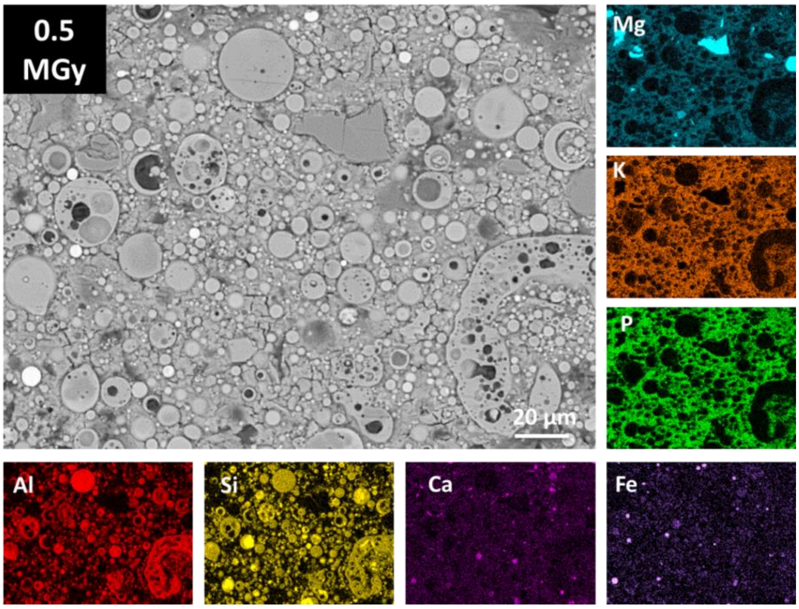

Fig. F14. Backscattered electron micrograph and elemental maps of a FA/MKPC specimen exposed to 0.5 MGy at 4.9 kGy/hr

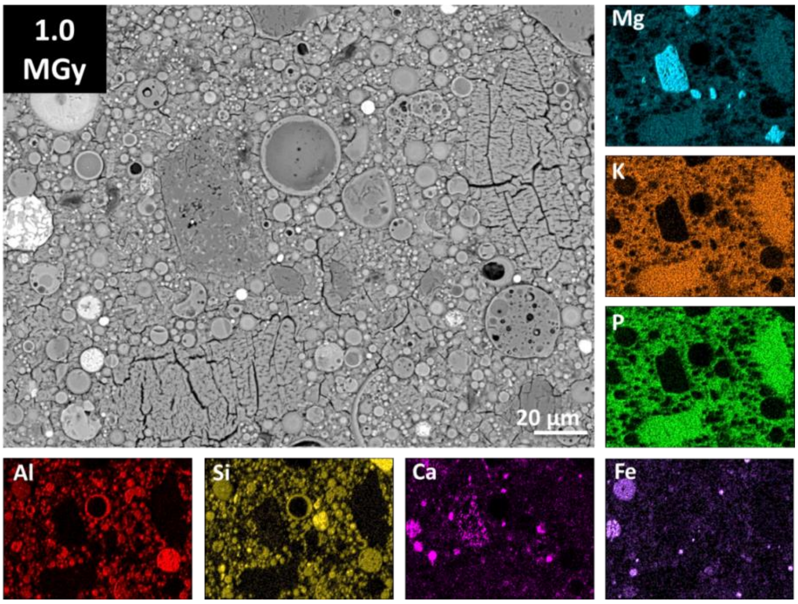

Fig. F15. Backscattered electron micrograph and elemental maps of a FA/MKPC specimen exposed to 1.0 MGy at 4.9 kGy/hr

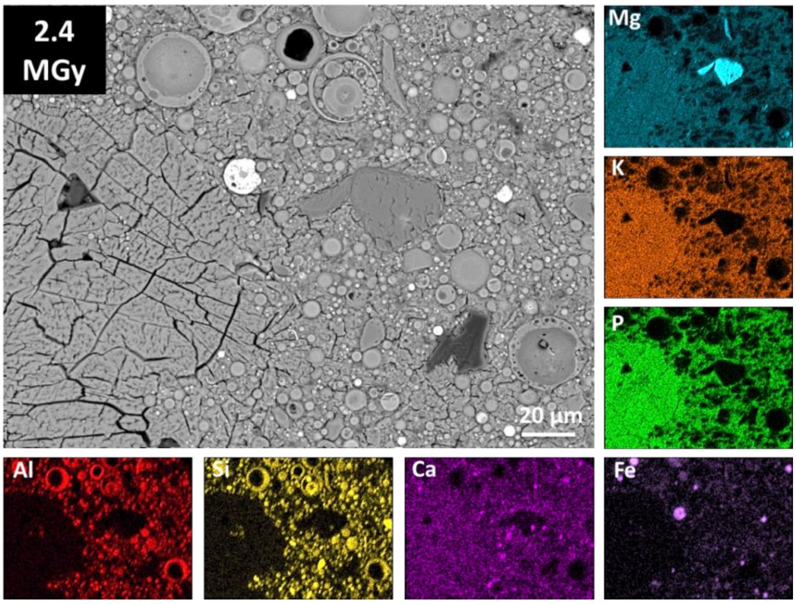

Fig. F16. Backscattered electron micrograph and elemental maps of a FA/MKPC specimen exposed to 2.4 MGy at 4.9 kGy/hr

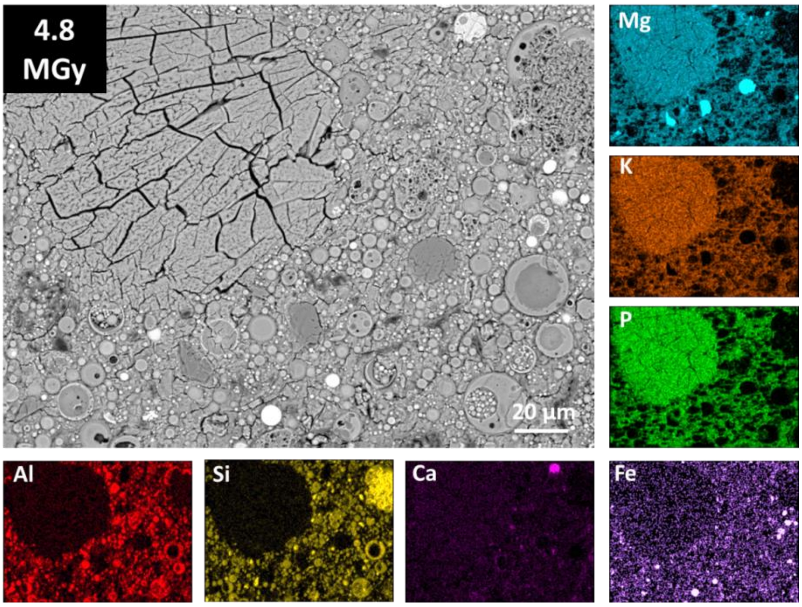

Fig. F17. Backscattered electron micrograph and elemental maps of a FA/MKPC specimen exposed to 4.8 MGy at 4.9 kGy/hr

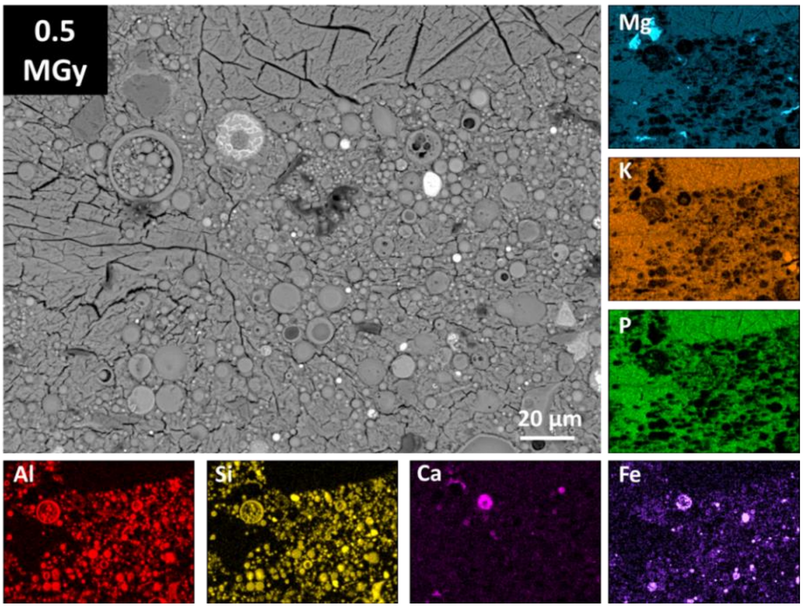

Fig. F18. Backscattered electron micrograph and elemental maps of a FA/MKPC specimen exposed to 0.5 MGy at 2.8 kGy/hr

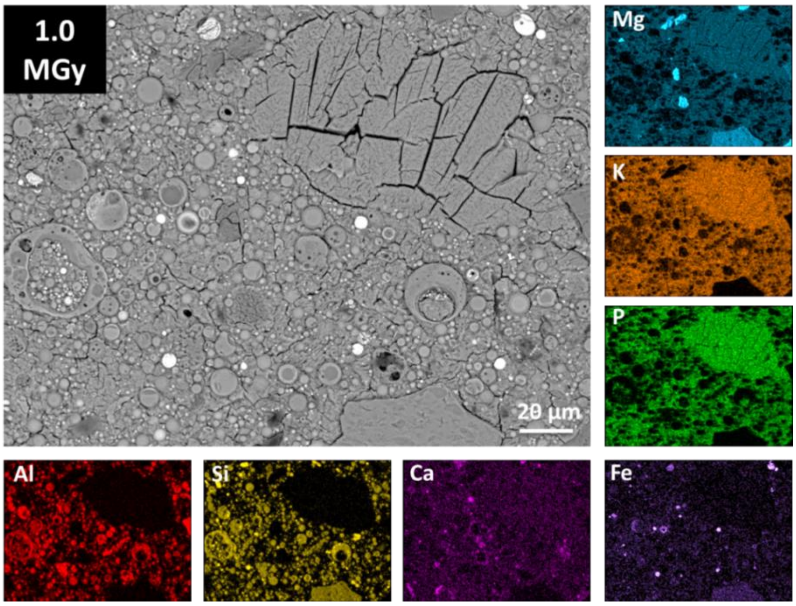

Fig. F19. Backscattered electron micrograph and elemental maps of a FA/MKPC specimen exposed to 1.0 MGy at 2.8 kGy/hr

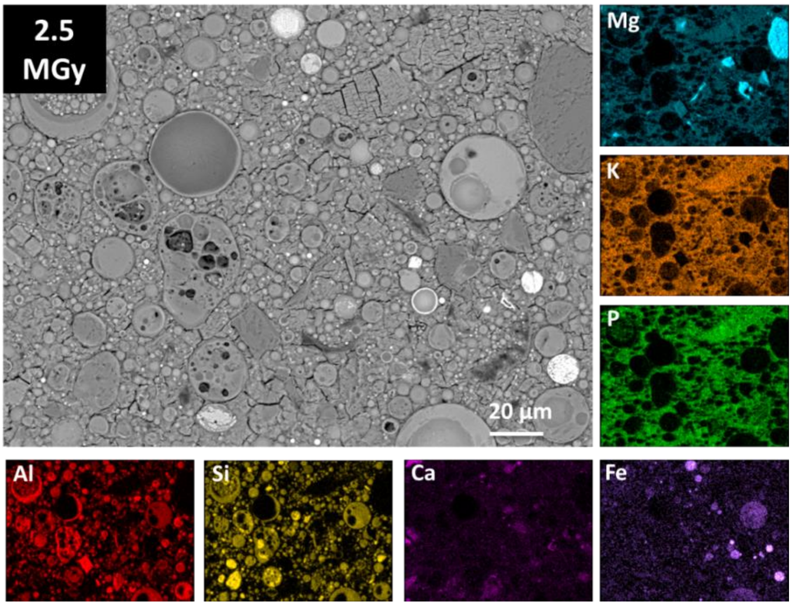

Fig. F20. Backscattered electron micrograph and elemental maps of a FA/MKPC specimen exposed to 2.5 MGy at 2.8kGy/hr

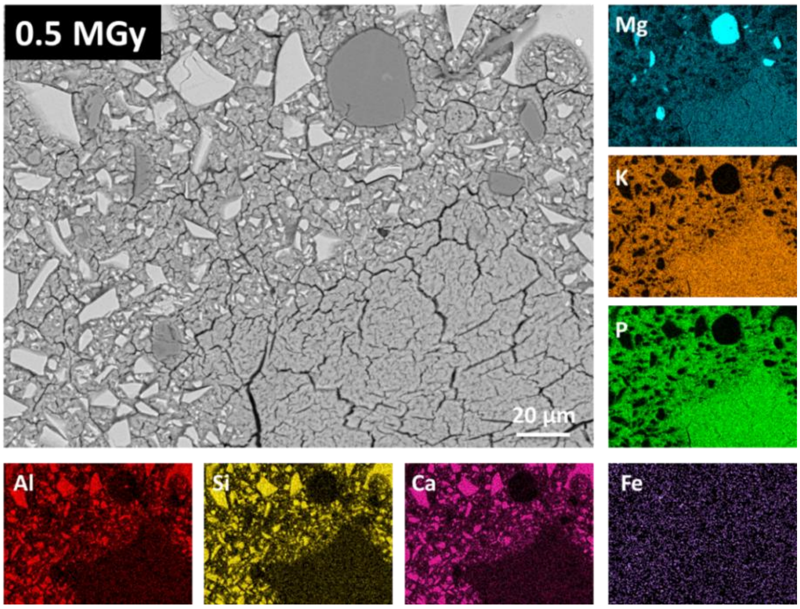

Fig. F21. Backscattered electron micrograph and elemental maps of a GBFS/MKPC specimen exposed to 0.5 MGy at 5.0 kGy/hr

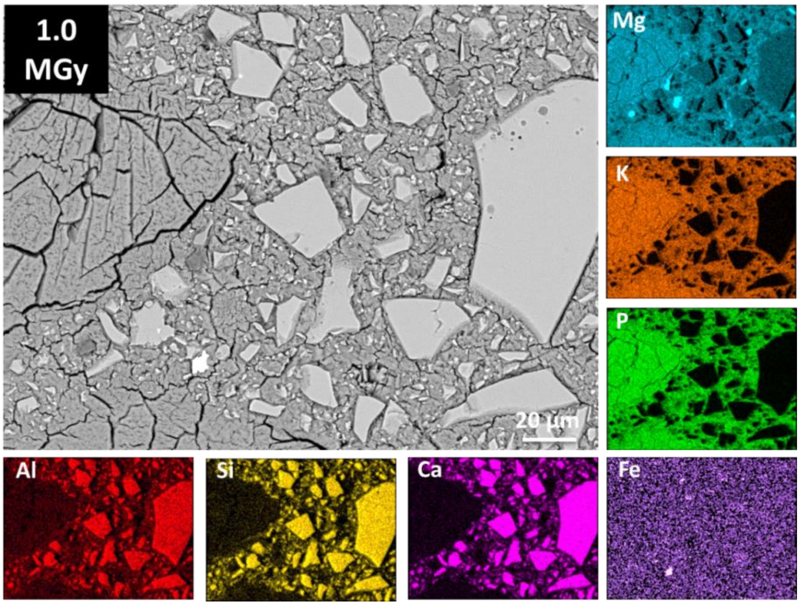

Fig. F22. Backscattered electron micrograph and elemental maps of a GBFS/MKPC specimen exposed to 1.0 MGy at 5.0 kGy/hr

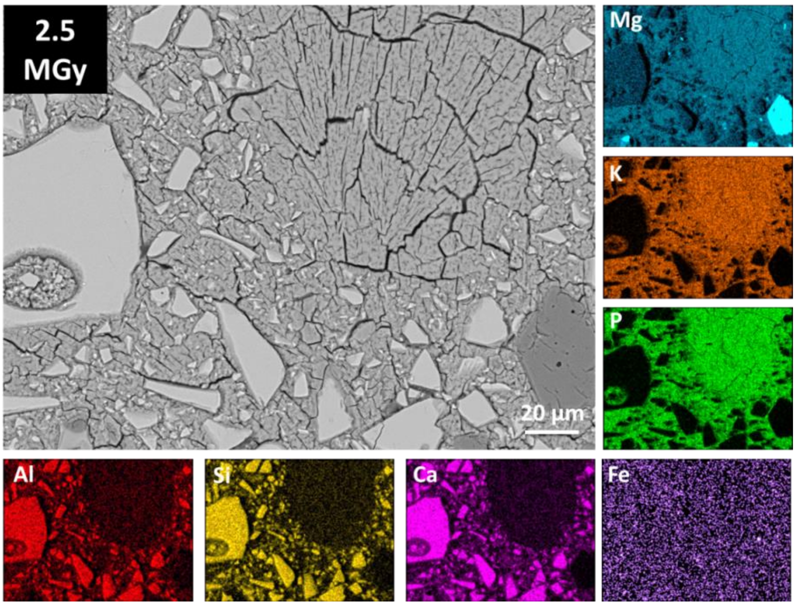

Fig. F23. Backscattered electron micrograph and elemental maps of a GBFS/MKPC specimen exposed to 2.5 MGy at 5.0 kGy/hr

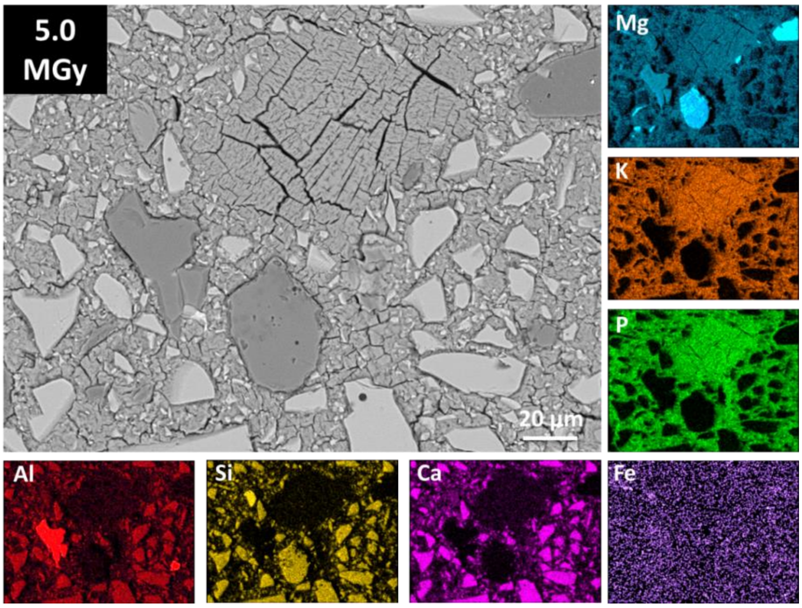

Fig. F24. Backscattered electron micrograph and elemental maps of a GBFS/MKPC specimen exposed to 5.0 MGy at 5.0 kGy/hr

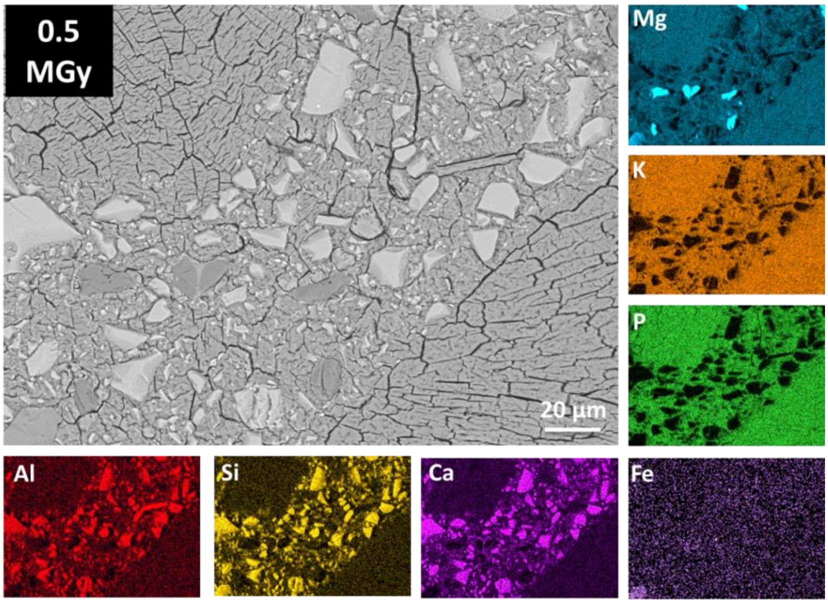

Fig. F25. Backscattered electron micrograph and elemental maps of a GBFS/MKPC specimen exposed to 0.5 MGy at 2.9 kGy/hr

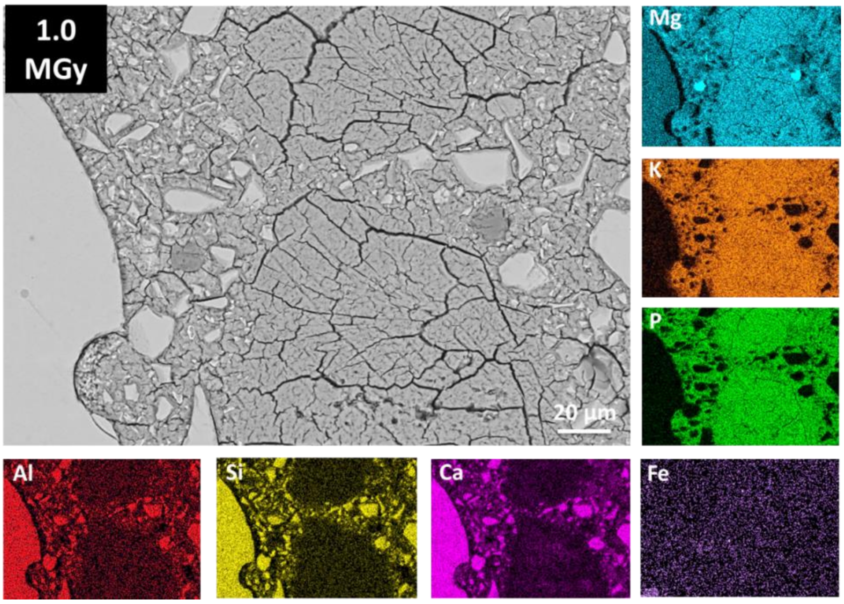

Fig. F26. Backscattered electron micrograph and elemental maps of a GBFS/MKPC specimen exposed to 1.0 MGy at 2.9 kGy/hr

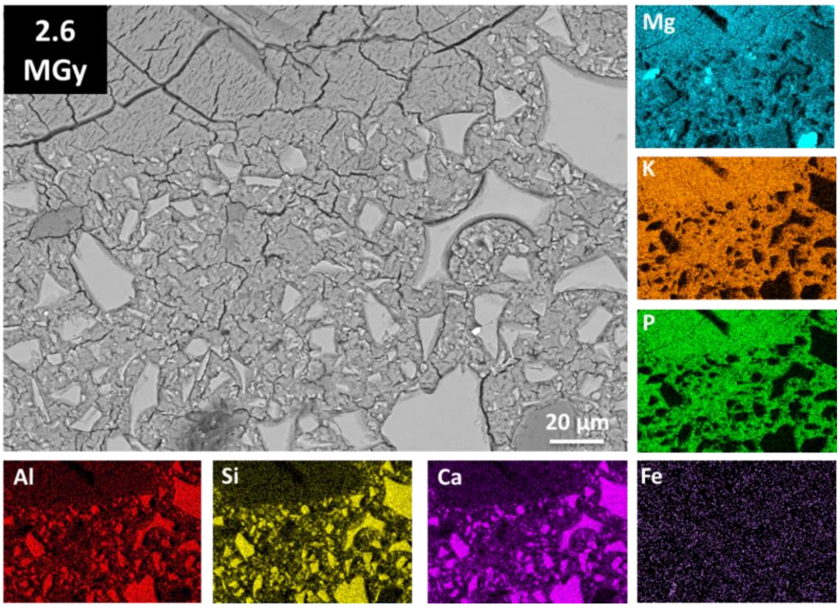

Fig. F27. Backscattered electron micrograph and elemental maps of a GBFS/MKPC specimen exposed to 2.6 MGy at 2.9 kGy/hr